Modeling Hemostasis and Thrombosis - In Silico Prediction of Dynamics of Blood Clotting

Ph.D. Dissertation

Doctoral thesis
for
the award of the doctoral degree
of the Faculty of Mathematics and Natural Sciences
of the University of Cologne
submitted by
Alper Topuz

in the year 2026

Contents

List of Figures

List of Tables

Abstract

Hemostasis is an essential physiological process that prevents blood loss following vascular injury, yet its dysregulation can lead to severe pathological outcomes. Thrombosis refers to clot formation in the absence of vascular injury and can lead to lethal consequences. These processes arise from a complex interplay between hydrodynamics, deformable blood cells, polymeric blood proteins, and force-dependent adhesive interactions occurring across multiple length and time scales. In this thesis, we develop and apply large-scale particle-based simulations to investigate the physical mechanisms governing blood clot and thrombus formation under flow, with particular emphasis on the coupling between hydrodynamics, cellular mechanics, and adhesive bond kinetics. Blood plasma is modeled as a viscous fluid; red blood cells and platelets as deformable or rigid particles; and von Willebrand factor (vWF) as a polymeric macromolecule whose conformation and adhesive activity are regulated by hydrodynamic forces. By explicitly resolving individual blood components, the simulations enable a multi-scale investigation of how microscale interactions give rise to emergent collective macro-scale behavior in flowing blood.

The first part of this work focuses on the formation and dynamics of platelet–vWF aggregates in blood flow. We examine the conditions under which aggregates form, migrate, remain stable, or dissociate, and distinguish between reversible and irreversible aggregation mechanisms. The results demonstrate that aggregate behavior is governed by the combined effects of hydrodynamic interactions, margination, and force-dependent bond lifetimes. In particular, bond kinetics play a decisive role in controlling whether aggregates persist as they migrate away from the vessel wall toward the channel center, where shear rates are reduced, or undergo dissociation. By systematically comparing different adhesive bond models, including catch-slip and slip-only kinetics, we identify physical regimes in which transient or stable aggregates emerge in flowing blood.

Building on these insights, the second part of the thesis presents an in silico model of primary hemostasis at a site of vascular injury. The simulations capture the accumulation of platelets and vWF at a hemostatic site that mimics a damaged vessel wall and follow the time-dependent formation, growth, and embolization of a hemostatic plug under physiologically relevant high-shear flow conditions. We analyze clot geometry, internal structure, and mechanical stability, and characterize distinct phases of clot evolution, including growth, deformation, and embolization events. The results highlight early stages of primary hemostasis that remain poorly understood. Overall, this work provides a mechanistic, physics-based perspective on blood clotting dynamics and demonstrates how mesoscale simulations can bridge microscopic interactions and macroscopic hemostatic outcomes.

1 Introduction

Blood is a complex fluid composed of blood plasma and cellular components such as red blood cells (RBCs), white blood cells (WBCs), platelets, and von Willebrand factor (vWF). Blood plasma makes up approximately 55% of whole blood and contains soluble proteins, minerals, and other elements essential for metabolism. In addition, it serves as a transport medium for the various blood components [230]. Together, plasma and blood components constitute blood, an essential fluid for human life.

Blood has many fundamental functions in the human body, including the transport of oxygen and nutrients, blood clotting in the case of injury, the delivery of hormones and immune components to different parts of the body, the removal of waste products resulting from metabolic processes, and the regulation of body temperature. These tasks are of utmost importance, as losing a significant amount of blood over a short period of time has lethal consequences for human life [24, 79]. Therefore, it is essential to understand the nature of blood and blood flow in both health and disease, at physical as well as biological levels, in order to gain deeper insight into this central element.

In order to fully understand and characterize various physiological phenomena and diseases, it is essential to develop a solid understanding of blood flow and its components. With advances in imaging techniques, measurement tools, and experimental equipment in the late 20th and early 21st centuries, significant progress has been made in elucidating the physiology of the human cardiovascular system, the morphology of blood components, and their properties. Based on the extensive literature produced during this period, a few key insights are worth highlighting. First, blood flow is inherently a multiscale phenomenon. Second, the length scales of the cardiovascular system through which blood flows are extremely heterogeneous and span several orders of magnitude. In this context, the term *grotesque* is borrowed from architecture to describe structures with highly unusual geometric ratios and characteristic lengths; while the circulatory system indeed exhibits such properties, any aesthetic judgment is left to the reader.

As mentioned earlier, blood is a complex fluid. This can be understood in simple terms as follows: blood is a suspension composed of soft capsules and polymers that can deform and stretch when external forces are applied. The soluble components of blood plasma (i.e. fibrinogen, immunoglobulins, high- and low-density lipoprotein cholesterol, triglycerides, glucose, clotting factors, electrolytes, hormones, carbon dioxide, oxygen, etc. [230]) do not significantly affect the hydrodynamic characteristics of blood. Instead, they primarily participate in biochemical processes occurring at smaller length and time scales. In contrast, red blood cells, which constitute approximately 42.5% of blood volume (a value that varies throughout the cardiovascular system and depends on factors such as sex, environmental conditions, and tem-

perature), largely determine the flow behavior of blood. The influence of platelets, white blood cells (WBCs), and other large components is comparatively minor. As a simple rule of thumb, for every 1000 RBCs there is approximately one WBC, and for every 15 RBCs there is one platelet [76]. On average, human blood contains about 4.72×10^6 red blood cells per μl (averaged over males and females), and the total blood volume in an adult human cardiovascular system is approximately 5.5 L [68, 158, 187]. This complex fluid is continuously pumped by the heart through the cardiovascular system in order to fulfill the aforementioned physiological functions.

Red blood cells are highly specialized cells whose mechanical properties are closely tied to their unique internal organization. They possess an internal cytoskeletal network composed primarily of actin filaments that is anchored to the inner surface of the cell membrane. This cytoskeleton provides structural support and helps maintain the characteristic shape of the cell as it circulates through the vascular system. The membrane of a red blood cell therefore consists of a lipid bilayer that is mechanically coupled to an underlying protein scaffold, forming a composite structure that is both flexible and resilient. Under physiological conditions, red blood cells adopt a distinctive biconcave disc shape, with a typical diameter of approximately 8 μm and a thickness of about 2 μm. A typical red blood cell shape and its internal structure are shown in Figure 2(b)–(c). Figure 3(b) shows electron microscope images of a red blood cell, an activated platelet, and a white blood cell. Platelets play an essential role in hemostasis and thrombosis, whereas white blood cells are responsible for immune responses.

As blood circulates through the cardiovascular system, it experiences a wide range of length scales, which in turn dictate the flow rates and hydrodynamic forces acting on blood components. The total length of the cardiovascular network in an adult human is approximately 100,000 km [187]. This extensive vessel network can be broadly classified into three main categories based on the oxygen content of the blood they carry: arteries, veins, and capillaries. The smallest vessel diameters in the human body are on the order of 4–5 μm, comparable to about half the diameter of a red blood cell, whereas the largest artery, the aorta, has a diameter of approximately 32 mm [112, 166].

Furthermore, the cardiovascular system forms a highly interconnected network of vessels with numerous bifurcations and branches. After each bifurcation, the flow is disturbed and subsequently redevelops over characteristic length and time scales, during which blood experiences additional accelerations and forces that redistribute blood components across the vessel diameter, induce plasma skimming, and generate other secondary effects [166, 188]. Figure 1 presents a schematic overview of the cardiovascular system, illustrating the major vessel types and their interconnections. Blood leaves the heart through the aorta, the largest artery, and subsequently flows into progressively smaller arteries, then arterioles, and finally capillaries.

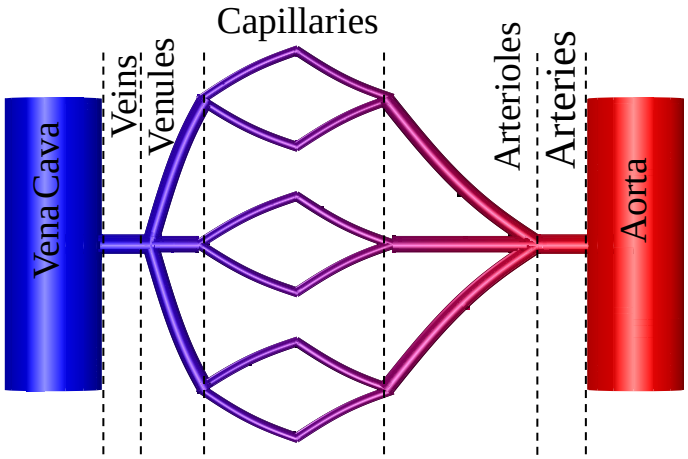

Figure 1: A simple schematic illustrating the different types of vessels and their interconnections. The color code (from red to blue) represents the oxygen content of a red blood cell during its journey from the aorta to the vena cava.

The capillaries merge into venules, which in turn form veins that return blood to the heart via the vena cava, thereby completing the circulatory loop. The color code in Figure 1 (from red to blue) indicates the oxygen content of the blood. Figure 3(a) shows blood samples taken from different parts of the circulatory system, where the brightness of the blood reflects oxygen presence.

By its nature, blood flow is oscillatory due to the periodic motion of the heart. A cardiac cycle, corresponding to one complete contraction and relaxation of the heart, lasts approximately one second (or equivalently 1 Hz) and persists continuously throughout the human lifespan [241]. Each cycle consists of two main phases: systole, during which blood is actively pumped out of the heart, and diastole, a resting phase [112]. The oscillatory nature of blood flow is prominent in arteries and venules with relatively large diameters but gradually diminishes as blood enters smaller vessels. In capillaries, the oscillatory component largely disappears, as the majority of the pressure drop in the cardiovascular system occurs at this scale [112].

In the case of vascular damage to a vessel wall, the body's response to prevent blood loss is referred to as hemostasis. It is a tightly regulated physiological process that enables rapid and localized clot formation following vascular injury, thereby preventing excessive blood loss. Hemostasis relies on a delicate balance between procoagulant and anticoagulant mechanisms, such that disruption of this balance can result in either bleeding or pathological thrombosis.

Functionally, hemostasis involves coordinated interactions between the vascular endothelium, circulating platelets, plasma coagulation factors, and adhesive proteins, most notably von Willebrand factor. These interactions ensure both the rapid sealing of damaged vessels and the subsequent stabilization and dissolution of the clot as tissue repair proceeds. Figure 3(c) shows a fresh wound initiating the hemostatic process.

Hemostasis is commonly described as a two-stage process consisting of primary and secondary hemostasis, with primary hemostasis preceding and enabling the secondary stage. Primary hemostasis is governed predominantly by mechanical and hydrodynamic interactions, involving platelet margination, adhesion, and aggregation at the site of vascular injury under flow. In contrast, secondary hemostasis is driven by a cascade of biochemical reactions that lead to fibrin generation and clot stabilization. Importantly, the mechanisms underlying primary hemostasis depend strongly on the local shear environment. At relatively low shear rates, platelet adhesion is mediated primarily by direct platelet–substrate and platelet–platelet interactions, whereas at high shear rates an additional mechanism becomes dominant through the activation of the shear-sensitive protein von Willebrand factor. Upon exposure to elevated shear, vWF undergoes conformational changes that promote platelet binding and enable robust clot formation under conditions where platelet adhesion would otherwise be suppressed by hydrodynamic forces.

Despite extensive experimental and computational efforts to characterize platelet adhesion and aggregation under flow, many existing studies probe dynamical regimes that evolve on time scales significantly longer than those associated with primary hemostasis *in vitro*. In particular, a large body of work focuses on transient platelet capture, long-lived adhesive events, or rapid aggregate formation under controlled, very high shear conditions, often spanning minutes [19, 27, 93, 216, 216–218, 245], whereas primary hemostasis takes place within seconds. While such studies have provided valuable insight into microscopic binding mechanisms and long-time hydrodynamic responses, they do not fully capture the sustained, collective dynamics required for the development of a stable hemostatic plug at short time scales. As a result, the temporal evolution of material accumulation, restructuring, and force balance during primary hemostasis remains incompletely understood.

In Chapter 5, we perform multiscale simulations of primary hemostasis using a mesoscale model that explicitly resolves red blood cells, platelets, and von Willebrand factor under flow. The simulations are designed to capture the early stages of clot formation, focusing on the mechanical and hydrodynamic processes that govern platelet adhesion and aggregation prior to the onset of biochemical coagulation. By accounting for cell–cell interactions, fluid–structure coupling, and shear-dependent vWF activity, this approach enables us to investigate the long-time evolution of primary hemostasis under physiologically relevant flow conditions.

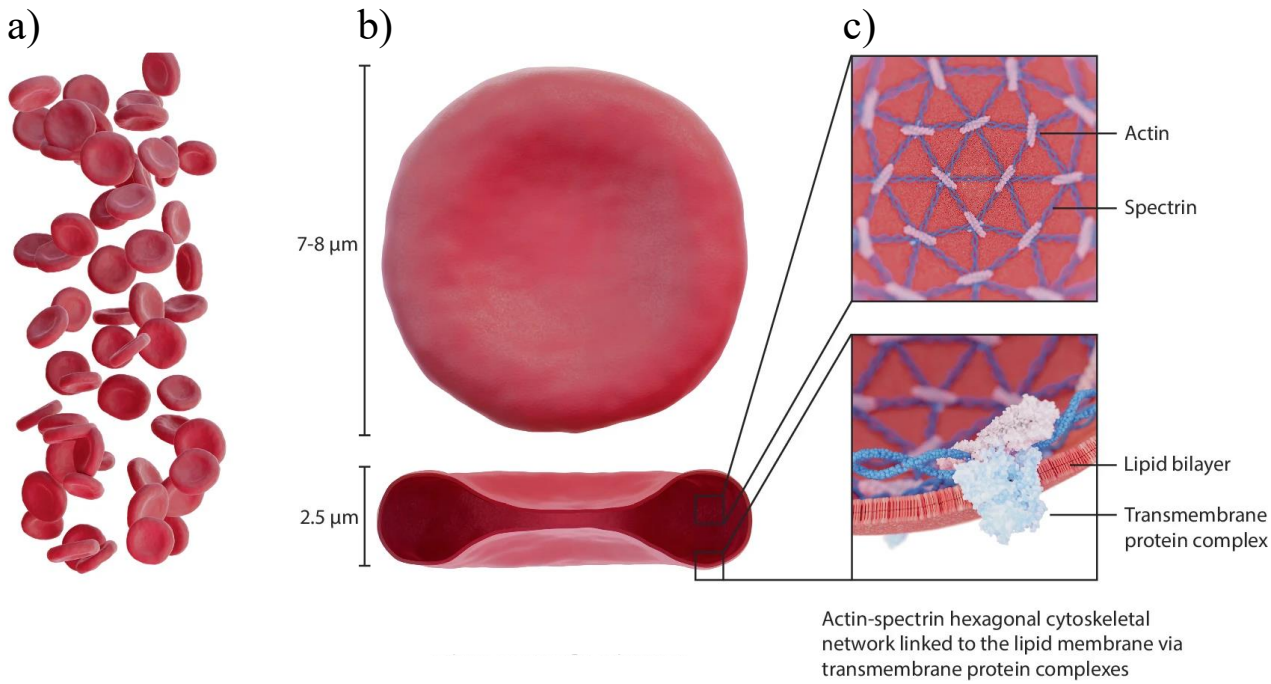

Figure 2: (a) Collection of red blood cells. (b) Geometric dimensions of a typical red blood cell, which exhibits a biconcave shape with a diameter of 7–8 μm and a thickness of approximately 2.5 μm. (c) Composition of the inner leaflet of the lipid bilayer, showing a cytoskeleton attached to the membrane. The cytoskeleton consists of an actin–spectrin hexagonal network that is coupled to the bilayer via transmembrane proteins. The figure is reproduced from [234] under a Creative Commons license.

Thrombosis refers to pathological clot formation within the vasculature that occurs in the absence of overt vessel rupture and can lead to vessel occlusion and severe clinical consequences. While hemostasis is a tightly regulated response to vascular injury, thrombosis represents the inappropriate activation of the same molecular pathways under conditions of intact but dysfunctional endothelium and altered blood flow.

Thrombosis is a leading contributor to global morbidity and mortality. It underlies most myocardial infarctions, ischemic strokes, and venous thromboembolic events, collectively accounting for approximately one quarter of all deaths worldwide. The high prevalence of thrombotic disease highlights that thrombosis is not merely a pathological endpoint, but rather reflects dysregulation of physiological mechanisms that operate continuously under diverse flow and vascular conditions. Ageing, inflammation, and alterations in blood composition or vessel geometry can shift this regulation toward pathological outcomes, emphasizing the need for precise control mechanisms that adapt thrombus formation to local hemodynamic environments. Understanding thrombosis as a dynamic, flow-regulated process is therefore essential for elucidating how vascular integrity is preserved under normal conditions and how this balance fails

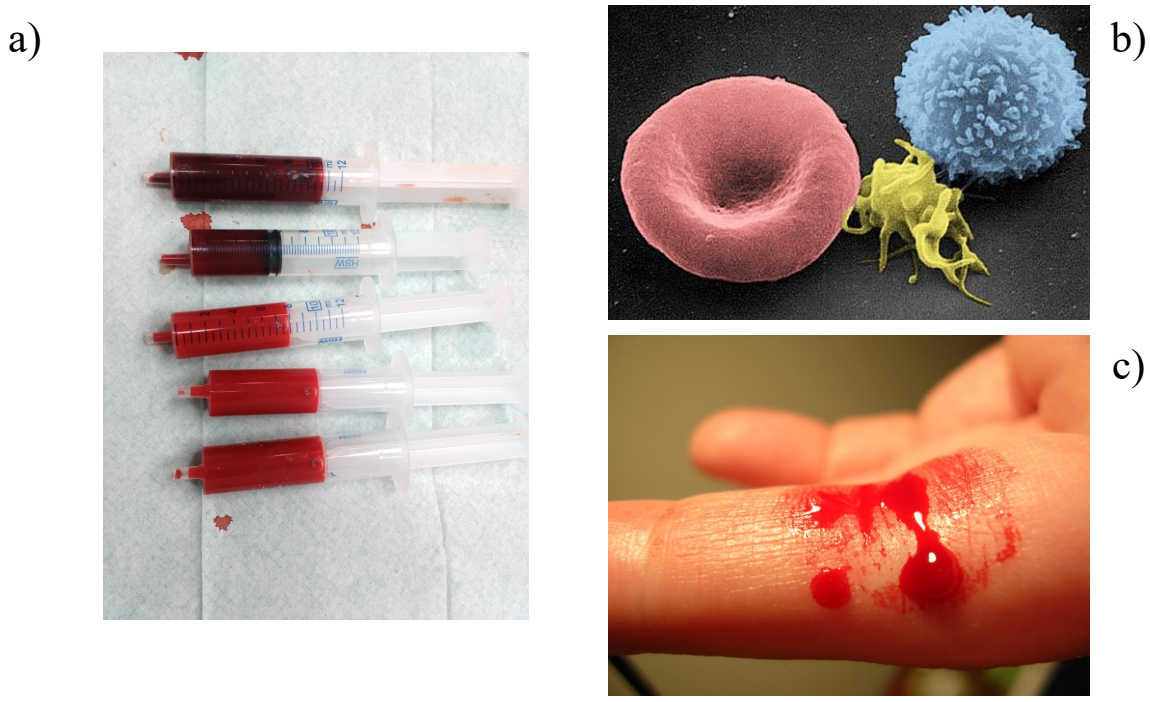

Figure 3: (a) Blood samples obtained from different locations of the circulatory system. Arterial blood appears brighter, whereas venous blood appears darker. (b) Scanning electron microscope (SEM) images of a red blood cell, an activated platelet, and a white blood cell (from left to right). (c) A fresh wound. All images are reproduced from Wikimedia Commons (public domain).

in disease [240].

Two additional points are worth mentioning in order to distinguish related but distinct pathological conditions. Thrombosis refers to the formation of a blood clot (thrombus) at its site of origin within the vasculature or heart, leading to local obstruction of blood flow. The formation of thrombi is the subject of Chapter 4. In contrast, thromboembolism describes vascular occlusion caused by thrombotic material that detaches from its original site, travels through the circulation, and subsequently lodges in a distant vessel. The formation of thromboembolic material and its relevance to hemostasis are discussed in Chapter 5. While thrombosis and thromboembolism are often discussed together in clinical contexts, they represent distinct processes: thrombosis concerns the local mechanisms of clot formation, whereas thromboembolism reflects the downstream consequences of thrombus fragmentation and transport.

The molecular and cellular components involved in thrombosis are well characterized. The roles of platelets, plasma coagulation factors, fibrin formation, and key adhesive proteins such as von Willebrand factor have been extensively studied, and many of the biochemical pathways governing clot initiation and stabilization are known. Classical risk factors for thrombosis are also well established and are commonly summarized by Virchow's triad. At this level, thrombo-

sis is not an unknown process, but rather a regulated—albeit pathological—machinery whose components and individual interactions have been identified and experimentally characterized.

However, despite this detailed knowledge, the mechanisms by which thrombosis emerges as a macroscopic pathological event remain incompletely understood. In particular, how local hydrodynamic conditions, cellular transport phenomena, and force-dependent molecular interactions dynamically couple to initiate, sustain, or terminate thrombus formation under physiological flow conditions is still an open question. Small changes in local shear rate or adhesive bond kinetics can lead to qualitatively different outcomes, ranging from transient and reversible aggregation to stable thrombus growth. As a result, while the building blocks of thrombosis are known, predicting when and where thrombosis will occur—and whether it will remain intact—remains a major challenge.

In Chapter 4, we argue that a physically consistent pathway exists by which platelet–von Willebrand factor aggregation (a pathway to physiologically high-shear thrombus formation) can remain reversible under physiological conditions or transition toward effectively irreversible growth. We show that this behavior can emerge from coupled effects of blood flow, cellular margination, and force-dependent molecular adhesion.

The material covered in this thesis requires a solid understanding of the physical mechanisms governing blood flow, such as the formation of the cell-free layer, which appears in both core chapters. Furthermore, the mechanistic models and fluid-dynamical descriptions employed are inherently rigorous. Therefore, the physiological aspects of blood flow, along with the materials and methods used in this work, are explained in detail in the following chapter. Due to the complexity of the models and numerical approaches, a large number of simulation parameters appear in the subsequent chapters addressing hemostasis and thrombosis. Relevant parameters are provided and discussed in the corresponding chapters.

In what follows, we first present a historical background, followed by a detailed discussion of the physiology of blood flow, with an emphasis on its fluid-mechanical aspects and the emergent collective phenomena of blood constituents. Finally, the materials and methods used in this thesis are described, followed by an outline of the core chapters.

2 Background

2.1 Historical Background

In modern medical sciences, the study of blood and blood disorders is called hematology, and the field that examines blood flow is referred to as hemodynamics. The study of blood disorders, the cardiovascular system, and blood flow dates back to ancient times. Ancient civilizations were aware of the importance of blood for human health, but the first written accounts emphasizing the significance of blood for human life date back to Homeric times (8th century B.C.) in ancient Greece. All blood-related disorders, components, and terms beginning with the prefixes "hemo-" or "haemo-"—the former used in American English and the latter in British English—originate from the Greek word *haema* ($\alpha\acute{\iota}\mu\alpha$), meaning "hot" or "incandescent". For many ancient savants and philosophers—such as Aristotle (384–322 B.C.)—blood was regarded as the physical essence of life, as it was believed to transport nutrients to different parts of the body. Hippocrates (460–370 B.C.) already recognized that blood undergoes a periodic motion through the body driven by the heart and believed that blood was produced in the spleen. However, it was Erasistratus (330–255 B.C.) who understood that the heart functions as a pump driving blood through the body and that different vessels serve distinct roles [125]. The idea that the human body contains four types of fluids (blood, phlegm, black bile, and yellow bile) also originated in ancient Greece (with early accounts in the works of Hippocrates) and persisted through the Middle Ages into the Islamic era. Furthermore, scholars commonly attributed certain diseases and human behaviors to imbalances among these fluids. A major milestone during late antiquity was achieved by Galen (129–216), who demonstrated that arteries carry blood rather than air, contrary to earlier theories [160]. Nevertheless, Galen maintained the idea that air reached the heart through the lungs without dissolving in the blood, and this view persisted for nearly a thousand years until Ibn Nafis (1210–1288) first described pulmonary circulation [92], although the notion of air flowing within vessels remained influential. The concept that the human circulatory system is filled exclusively with liquid blood, rather than gaseous air, had to wait until Colombo (1515–1559), who proposed that air mixes with blood in the lungs. In 1628, Harvey (1578–1657) introduced the concept of a closed cardiovascular system, which closely resembles our modern understanding. According to Harvey, the entire cardiovascular system, including the pulmonary circulation, is a closed loop filled with liquid blood that circulates through the body via the heart. Finally, Malpighi (1629–1694) completed the classification of vessel types by observing the capillary network [160]. Over the course of more than 3000 years, our understanding of the cardiovascular system, blood, and blood-related diseases has evolved and reached its present form.

The identification of blood components required the invention of the microscope in the 16th century. The first detailed and reliable descriptions of red blood cells were provided by Jan Swammerdam (1637–1680) and Antoni van Leeuwenhoek (1632–1723). The first illustration of

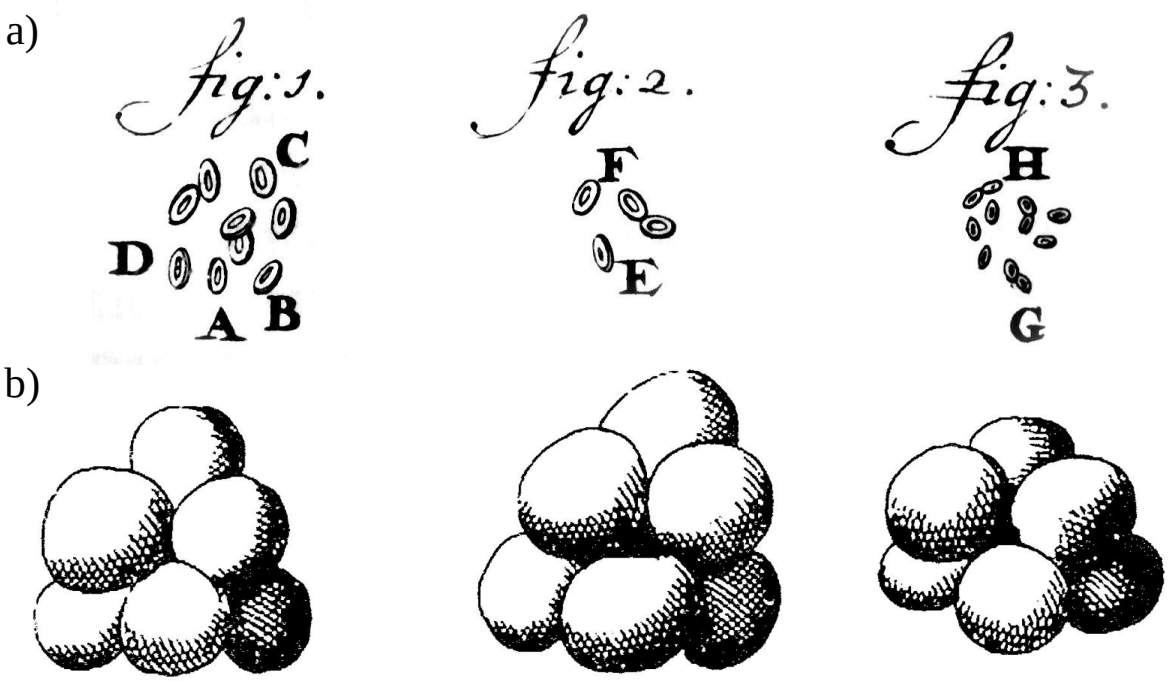

Figure 4: Early illustrations of red blood cells from the work of A. van Leeuwenhoek. (a) Illustration of red blood cells in salmon fish's blood. Work of Leeuwenhoek in 1719.Reproduced from Wikimedia Commons (public domain).(b) Illustration of 'red corpuscles' in human blood. Same author's work from his letters in 1695 [227].

red cells as spherical capsules, or in Leeuwenhoek's words "red corpuscles", was published in 1695 [92]. Figure 4(b) shows the earliest illustrations published in the work of Leeuwenhoek, while Figure 4(a) presents his observations of salmon blood.

William Hewson (1739–1774), often referred to as the father of hematology, was the first to identify that red blood cells are not solid corpuscles but instead possess a biconcave shape [44]. He was also the first to report the presence of colorless cells in blood—later identified as white blood cells—during the years 1770–1774. Nevertheless, major breakthroughs in the observation and characterization of blood components did not occur until the second half of the 19th century and the early 20th century. Gabriel Andral (1797–1876) and William Addison (1802–1881) were among the first to report systematic studies on leukocytes (WBCs). Max Schütze (1825–1874) proposed the first description of platelets, although they were first properly observed under a microscope by Giulio Bizzozero (1846–1901) in 1882. Bizzozero was also the first scientist to report the role of platelets in blood coagulation [92, 116]. Between 1852 and 1876, early studies on white and red blood cell counts using a hemocytometer were developed as a result of these collective efforts [39]. In 1845, Rudolf Virchow (1821–1902)—after whom Virchow's triad, which establishes the fundamental principles of blood clotting, is named—provided detailed descriptions of leukemia and introduced its modern name [92]. Later, in 1868, Virchow completed his work on thrombosis and embolism. Von Willebrand

factor is named after Erik von Willebrand (1870–1949), who identified the bleeding disorder associated with this factor—now known as von Willebrand disease—in 1926. The study of blood flow (i.e., hemodynamics), although rooted in antiquity, accelerated significantly in the early 20th century with the work of Fåhræus and Lindqvist in 1928 and 1931. They were the first to measure the apparent viscosity of blood in glass tubes and to relate discharge hematocrit to tube hematocrit as a consequence of apparent viscosity [188].

There exists a vast body of historical work that is not discussed here in order to keep this overview concise. The present section aims to convey a broad impression of the numerous efforts and monumental contributions of early scientists, on whose shoulders we stand, as famously noted by Newton. For further historical details, interested readers are referred to [39, 44, 92, 116, 125, 160, 173, 188].

2.2 Physiological Background : Blood Flow, Blood Agonists in Cannonical Flows and Complex Flows, Cell-Free Layer

Several key dimensionless numbers govern the motion of blood and the deformation and transport of its components. The Reynolds number characterizes the ratio of inertial to viscous forces and is defined as

$$\mathrm{Re} = \frac{\rho \bar{\mathrm{u}} \mathrm{R}}{\eta}, \tag{1}$$

where ρ is the fluid density, η the viscosity, R the characteristic length scale, and $\bar{u}$ the mean velocity. Large Reynolds numbers (i.e. $Re > 0.1$) (in the context of blood flow) indicate flows where inertial effects are significant, whereas for small Reynolds numbers (i.e. $Re < 0.1$) inertial effects can be neglected and viscous forces dominate. In this latter regime, the Stokes flow approximation applies, leading to a simplified set of governing equations. As will be discussed in subsequent chapters, blood flow exhibits a wide range of Reynolds numbers across the cardiovascular system (see Figure 5, blue curve). In general, Reynolds numbers are higher in vessels with large mass transport and lower in vessels with reduced transport. While this rule of thumb holds at larger length scales, it cannot be universally applied, as the flow rate—and thus the Reynolds number—depends on vessel diameter in a nontrivial manner (see Figure 6(a)). At small scales, smaller diameters typically imply reduced transport, but at finer resolutions this relationship may break down. Typical Reynolds numbers encountered in the human cardiovascular system are summarized in Figure 5.

The next dimensionless number that characterizes the flow is the Womersley number, which

quantifies the ratio of transient inertial forces to viscous forces and is defined as

$$\mathrm{Wo} = \mathrm{R}\sqrt{\frac{2\pi\omega\rho}{\eta}}. \tag{2}$$

Here, R, η, and ρ denote the characteristic length scale, viscosity, and density, respectively, while ω represents the characteristic frequency of the oscillation. A large Womersley number corresponds to a flow dominated by oscillatory effects, that is, by temporal variations in forces and accelerations. In contrast, for small Womersley numbers these effects are negligible, and the flow is dominated by viscous forces. In general, blood flow in larger vessels is governed by periodic oscillations, whereas in capillaries the influence of periodic motion diminishes and the flow can be approximated as steady, in terms of the driving forces, and laminar, since the Reynolds number is small. The impact of unsteady flow on blood-related phenomena such as thrombosis, hemostasis, and oxygen transport remains an active area of research. Nevertheless, as a practical rule of thumb, for capillaries and the capillary segments of the arterial and venular circulatory system (i.e. $Wo < 10$ [112]), the flow can be considered non-oscillatory. Assuming a blood density of $1060\,\mathrm{kg/m^3}$, a viscosity of $3.5 \times 10^{-3}\,\mathrm{Pa \cdot s}$, and a characteristic frequency of $1\,\mathrm{Hz}$, which are typical values for an adult human, a Womersley number of 10 corresponds to a vessel diameter of approximately $0.4\,\mathrm{mm}$. Below this diameter, blood flow can be assumed to be effectively non-oscillatory. Typical Womersley numbers encountered in the human cardiovascular system are shown in Figure 5.

In addition to these flow characteristics, the cardiovascular system comprises a vast number of branches and bifurcations. Moreover, moving valves, particularly in the venular part of the circulatory system, enforce unidirectional flow. Pathological conditions can further modify vessel geometry through constrictions (stenosis) or expansions (aneurysms), thereby altering the flow field. Such geometric variations can induce secondary flows within the cardiovascular system. Even in the absence of pathological changes, the complex network topology itself continuously influences blood flow. Following a bifurcation or a bend in a vessel, the flow undergoes a development process, during which it experiences accelerations that are absent in fully developed flow. Within this developing region, both the velocity field and the spatial distribution of suspended particles, including RBCs, WBCs, and platelets, are affected. A conservative rule of thumb adopted in both experimental and numerical studies is to assume an undisturbed entrance length ranging from $500\,\mu\mathrm{m}$ to several centimeters [187].

Another important dimensionless parameter is the capillary number, defined as the ratio of hydrodynamic forces to membrane mechanical forces.

$$\mathrm{Ca} = \frac{\eta\dot{\gamma}\mathrm{R}^3}{\kappa}, \tag{3}$$

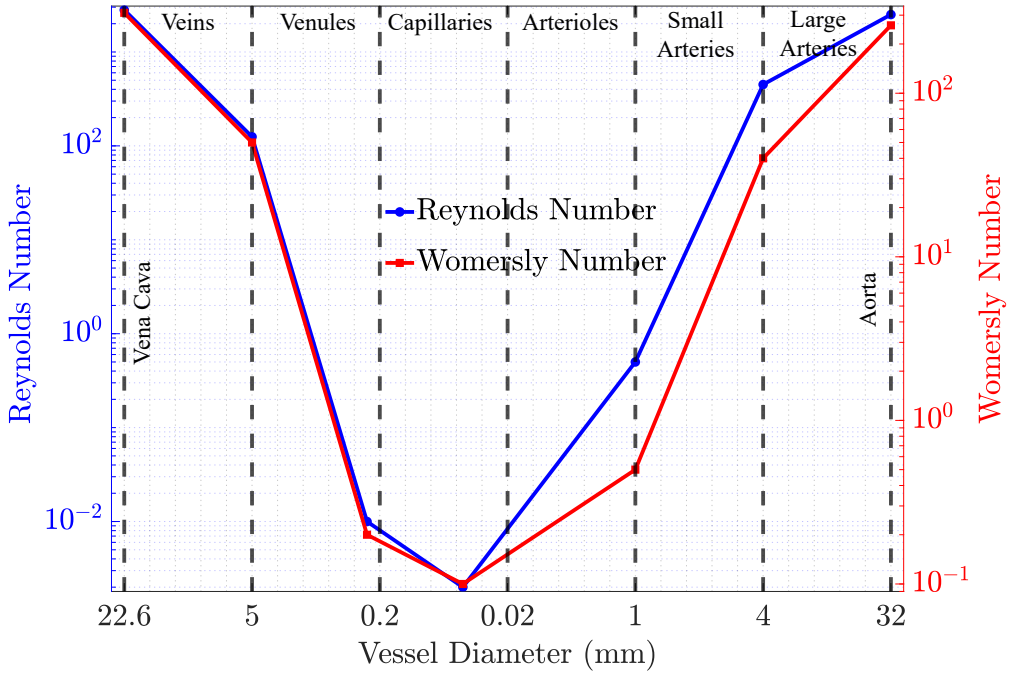

Figure 5: Reynolds number (to be read from the left hand side axis) and Womersly number (to be read from the right hand side axis) of typical vessels. The partitioning of the vessel diameters to vessel types is from [187]. The corresponding Reynolds numbers and the Womersly numbers are from [241].

where η is the fluid viscosity, $\dot{\gamma}$ is the shear-rate, R is the characteristic dimension of the red blood cell, and κ is the bending elasticity of the membrane.

At high capillary numbers, viscous forces dominate over membrane forces. This parameter plays a central role in the dynamics of elastic capsules suspended in a flow, as it characterizes their modes of motion and deformation, such as tank-treading, tumbling, and swinging. As discussed earlier, blood consists of elastic capsules or shells suspended in a liquid medium, namely blood plasma. In contrast to the Reynolds and Womersley numbers, the capillary number typically attains its largest values in capillaries, where the velocity field varies strongly over small length scales. In this regime, the capsules undergo significant deformation. Conversely, in vessels with high material transport, the capillary number is relatively small, and capsule deformation is modest when compared with that observed in capillary flow. Typical capillary numbers relevant to the human cardiovascular system are shown in Figure 6(b).

As mentioned earlier, blood is a complex fluid composed of soft elastic capsules, namely red blood cells. Consequently, the characteristic properties of blood (e.g. its rheology) are largely determined by the behavior of these elastic capsules and their interaction with the surrounding flow environment. In this sense, blood is considered a heterogeneous fluid at small length scales. At scales smaller than $200\,\mu$m, the motion and deformation of individual red blood cells play

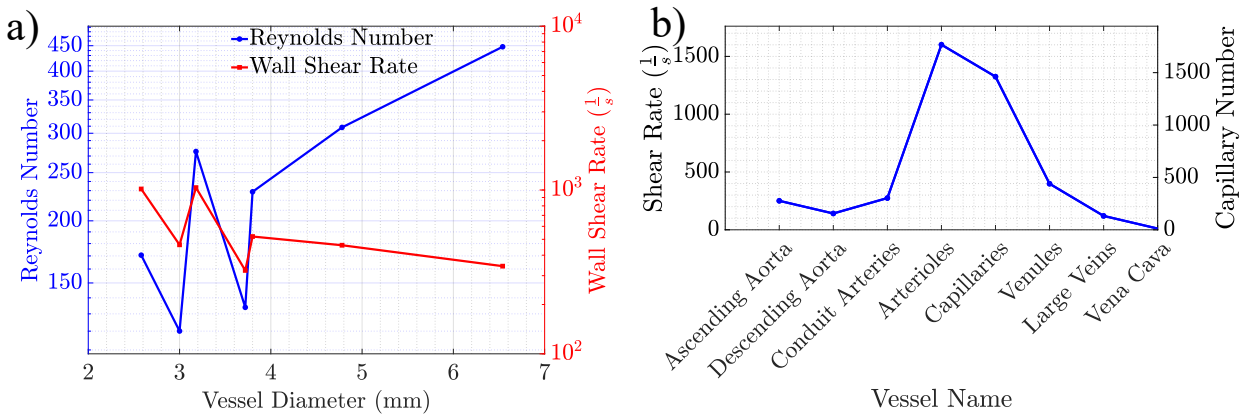

Figure 6: Characteristic Reynolds number and wall shear rates for typical vessels. (a) Shows the Reynolds number (left axis) for the large arteries in human's body. From left to right each point corresponds to; Anterior Cerebral,Posterior Cerebral ,Middle Cerebral, Vertebral, Basilar, Internal Cartoid and Common Cartoid. Data is from [198]. (b) Typical shear rates and corresponding capillary number of the blood flow in different parts of the human body. Data is from [164]

a significant role in the hydrodynamics of the system. Moreover, when complex phenomena such as hemostasis or thrombosis are modeled in addition to hydrodynamics, the dynamics and deformation of red blood cells are, in most cases, essential. Therefore, at these scales, blood must be modeled by treating red blood cells and other agonists as discrete constituents of the fluid.

This description can be simplified at larger length scales, where the characteristic size of red blood cells is no longer comparable to the length scale of the problem. For blood flow in vessels with diameters larger than 200 μm, the fluid can be assumed to be homogeneous [68, 166]. Above this threshold, blood flow can be modeled using the Navier–Stokes equations together with a phenomenological constitutive relation for the viscosity. Fluids whose viscosity depends on hydrodynamic parameters or time are referred to as non-Newtonian fluids. Numerous constitutive models have been proposed for blood under different assumptions and conditions, such as varying shear rates or hematocrit levels, where hematocrit denotes the volume fraction of red blood cells in the suspending medium. A widely used example is the Carreau–Yasuda model, which is implemented in many continuum-based solvers employing finite element or finite volume methods to solve the Navier–Stokes equations.

The non-Newtonian description can be further simplified at even larger length scales. When the characteristic length scale is much larger than 200 μm, typical in vivo shear rates increase (see Figure 6(a) and (b)), and the effective viscosity of blood approaches a nearly constant value [67]. At this scale, variations in the red blood cell distribution across the vessel diameter can be assumed to be uniform [112, 166], allowing blood to be approximated as a Newtonian

fluid. In summary, blood flow in large arteries and venules with diameters on the order of millimeters can be treated as Newtonian and governed by the Navier–Stokes equations. For smaller arteries and venules, blood must be modeled as a non-Newtonian fluid, again within the Navier–Stokes framework. When vessel diameters fall below 200 μm, corresponding to capillaries and the capillary regions of the arterial and venular systems, the characteristic size of red blood cells becomes comparable to the vessel diameter. At this scale, solutions of the Navier–Stokes equations begin to show discrepancies with experimental observations, both in vivo and in vitro [64, 68, 76]. Consequently, the assumption of homogeneity is no longer valid, and direct numerical simulations that explicitly resolve individual cells are required. A comprehensive review of blood flow simulation techniques is provided in [76].

Below length scales of approximately 100 μm, the computation of local hydrodynamic variables requires special care. At these scales, the spatial distribution of red blood cells, arising from various mechanisms discussed later in this chapter, violates the locality assumption. As a result, quantities such as shear stress can no longer be expressed solely in terms of local hydrodynamic variables [63]. It is important to note that this does not imply a breakdown of the continuum hypothesis itself, but rather a breakdown of the local action principle. Even in capillaries with diameters as small as 4–5 μm.

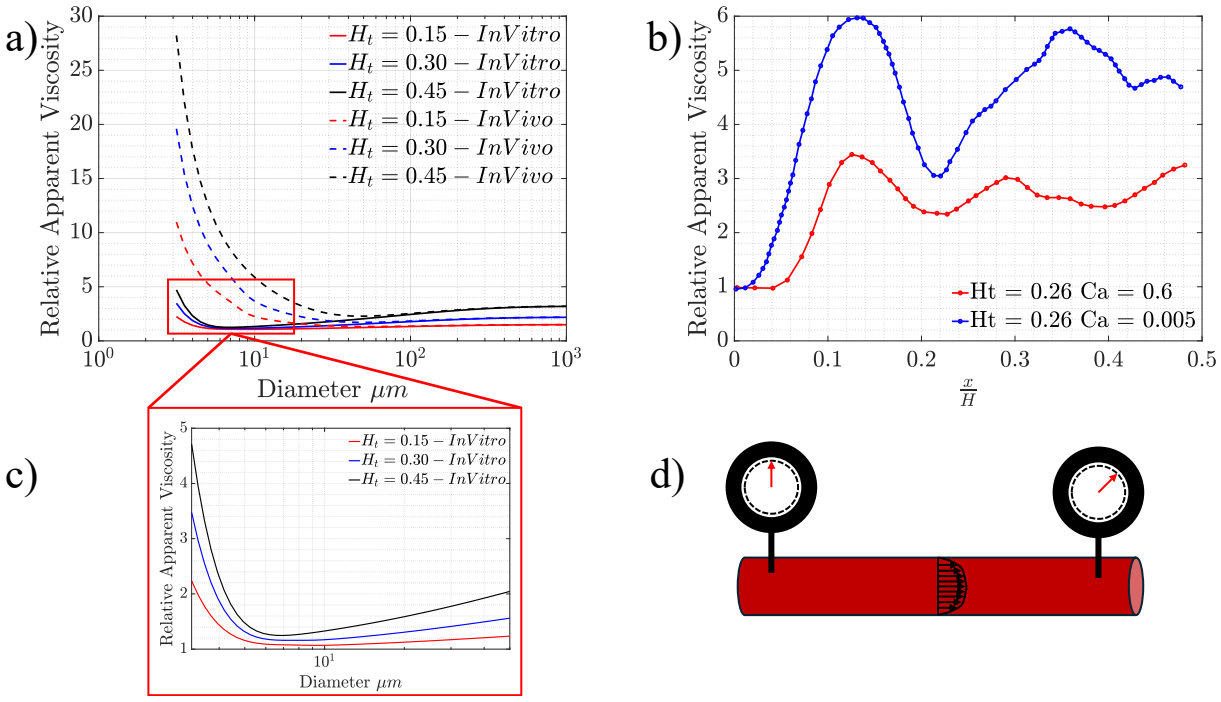

Figure 7: Relative apparent viscosity (i.e., the ratio of the measured viscosity over the viscosity of the blood plasma η/η_0) measures for blood and a schematic for pressure drop measurement in a tube. (a) Shows the relative apparent in vitro and in vivo measurements blood viscosity. The measurement is done against varying hematrocit and vessel/tube diameter. This viscosity is used to calculate pressure drop for zero dimensional models for complex networks. The data is from [168]. (b) Averaged apparent viscosity over a channel for a given diameter and percentage hematrocit. This viscosity is obtained by averaging the ratio of instantaneous shear-stress over instantaneous shear-rate over the cross-section of the channel. Further averaging this viscosity results a data point on panel (a). Data is from [11]. (c) The turning points of the viscosity curves for in vitro measurements. Approximately around $8\mu m$ the decreasing apperant viscosity, starts to increase. The diameter of the red blood cell matches the diameter of the tube, therefore further decrease in the tube diameter results with increased viscosity. The turning point appears early in case of in vivo measurement. This is due to glycolax layer on the vessel walls. (d) A schematic of a blood vessel and measurement of pressure drop across a certain length. At a cross-section the apparent viscosity is similar to panel (b). The pressure drop is estimated using the data in panel (a).

One of the most important parameters characterizing blood flow is its viscosity. It is therefore not surprising that either the plasma viscosity or the effective viscosity of whole blood appears in the characteristic dimensionless numbers discussed earlier. Long-term research efforts on blood viscosity—dating back to the seminal work of Fåhræus and Lindqvist—have led to several complementary descriptions of this property. Among these, the easiest quantity to characterize is the viscosity of blood plasma, which remains nearly constant over a wide range of shear rates and can thus be treated as a Newtonian fluid. In the case of extensional flows, however, this assumption may break down [230]. When red blood cells and other agonists are suspended in plasma, the resulting fluid exhibits non-Newtonian behavior. As a simple rule

of thumb, the presence of these elastic capsules increases the effective viscosity of blood. The early work of Fåhræus and Lindqvist established a relationship between the apparent viscosity of whole blood and the pressure drop measured in glass tubes of a given diameter. This apparent viscosity can be interpreted as an engineering quantity that is useful, for example, for estimating pressure drops in specific parts of the circulatory system. Relative apparent viscosity measurements obtained in vivo and in vitro are shown in Figure 7(a).

Another relevant measure is the bulk viscosity, commonly referred to as the Couette-flow viscosity of blood. In this case, the distribution of red blood cells across the slit in a Couette-flow experiment is assumed to be uniform, either because cells are sufficiently far from the walls or because the experimental conditions enforce a homogeneous red blood cell distribution. The resulting resistance of whole blood to shear is then measured, and the corresponding parameter is termed the whole-blood or Couette-flow viscosity. This quantity has been determined both experimentally and numerically using simulations [67].

In reality, for a given vessel diameter and hematocrit level, red blood cells are distributed non-uniformly across the vessel cross-section and are subjected to a range of local shear rates. Consequently, the hydrodynamic viscosity—understood as the local resistance to flow—varies across the channel diameter. The apparent viscosity effectively averages these spatial variations into a single scalar quantity. This single-parameter description has proven useful and has been widely employed in simulations of large-scale cardiovascular networks.

As in the Couette-flow case, the apparent viscosity depends on both hematocrit and shear rate. Although both measures provide valuable characterizations of flow resistance, blood viscosity is inherently a complex and spatially varying quantity. It depends sensitively on the local red blood cell concentration and the local shear rate, both of which fluctuate in time under physiological conditions. Nevertheless, when long-time averages of the local red blood cell density and shear rate are considered, the resulting effective viscosity is well described by the Couette-flow viscosity corresponding to the same hematocrit. This fluctuating quantity—whose time-averaged profile is shown in Figure 7(b)—represents the local shear viscosity of blood at a given point within the vessel. When the spatial distribution of this local viscosity is examined, a pronounced peak is often observed at the interface between the cell-rich core and the cell-depleted layer near the vessel wall (these regions are discussed in more detail in subsequent sections). This peak promotes irreversible platelet aggregation by generating a viscous stress barrier for blood agonists to not to re-enter the cell rich zone and plays an important role in the margination, which refers to the hydrodynamically driven redistribution in flowing blood whereby deformable red blood cells migrate toward the vessel center, creating a cell-free layer that passively displaces platelets and other smaller or stiffer constituents toward the vessel wall. Here A substantial body of literature, spanning in vivo, in vitro, and in silico studies, has in-

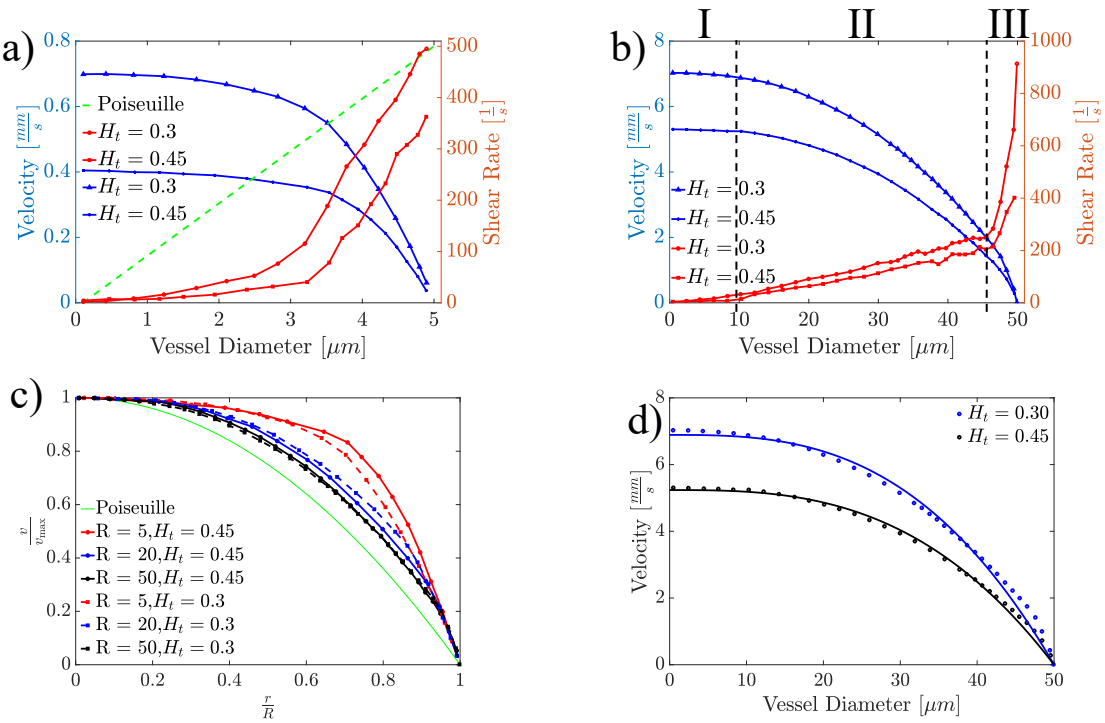

Figure 8: Velocity profiles and shear rates in a typical vessel. (a) Shows the velocity profiles in $10\mu m$ vessel with 0.3 and 0.45 percent hematrocits. Corresponding shear rates are drawn on the right hand side of the graph together with the Poiseuille flow shear rate that satisfies the same wall shear rate with 0.3 percent hematrocit. Data is from [57].(b) Typical velocity profiles in a larger vessel of diameter $100\mu m$. Corresponding shear rates can be read from the right hand side axis. The three distinct regimes where the shear rate behaves differently is shown with I,II and III. Data is from [63] .(c) Non-dimensional velocity profiles for different channel sizes and percentage hematrocits. Data is from both [57, 63].(d) Curve fit of the form $v_{max}(1-(x/R)^k)$ to the same velocity profiles for the geometry given in panel (b). The corresponding parameter sets (v_{max}, k) for the fit are (6.8896,2.8734) and (5.2360,2.8837) for 30 and 45 percent hematrocits respectively. Data is from [64]

vestigated blood viscosity under a wide range of physical conditions. However, the complexity of the circulatory system and the interactions among blood components give rise to significant discrepancies. For instance, the influence of the endothelial glycocalyx layer cannot be captured in glass-tube experiments, while marginating white blood cells, as well as vessel bifurcations and merging points that strongly affect local hematocrit distributions, must also be taken into account. Figure 7(a) shows the discrepancies between in vivo and in vitro measurements of apparent viscosities of blood. Furthermore, the role of the extensional viscosity of blood plasma remains poorly understood [230].

As mentioned earlier, when the vessel diameter is sufficiently large and flow rates are high, blood can be approximated as a Newtonian fluid. At this scale, the velocity profile is parabolic and is given by the classical Poiseuille solution of the Navier–Stokes equations. As the vessel diameter is reduced, the non-Newtonian nature of blood begins to manifest itself, and the ve-

locity profile in typical venules or arterioles becomes increasingly blunted. This non-Newtonian behavior originates from the heterogeneous composition of blood. In principle, the suspending fluid, namely blood plasma, is a Newtonian fluid with a viscosity of approximately $0.0012\,\mathrm{Pa}\cdot\mathrm{s}$ [230]. However, when red blood cells are suspended in plasma, their deformability becomes a key factor. This can be understood through an energy-based argument. In the cardiovascular system, blood motion is driven by pressure differences generated by the heart, which act as an external energy input. Part of this energy is stored elastically through the deformation of red blood cells, while another part is dissipated through viscous fluid motion and through collisions among the constituents of this complex fluid. The stored elastic energy can subsequently be released, perturbing the surrounding fluid, while collisions further contribute to fluid motion. This mechanism is absent in simple fluids that do not contain deformable or rigid inclusions. As a result, blood viscosity is no longer a simple function of shear rate but instead exhibits a more complex dependence. In addition, this cascade of energy transfer occurs within the intricate geometry of the circulatory system, which features composite and multiplex junctions, further contributing to the development of complex velocity profiles. As discussed earlier, the pressure difference generated by the heart is oscillatory, rendering this energy cascade inherently unsteady. Moreover, in small vessels, the non-uniform spatial distribution of red blood cells further enhances the non-Newtonian character of blood. In summary, the non-Newtonian behavior of blood primarily arises from the presence and deformability of red blood cells, which constitute the dominant cellular component of blood.

A representative simulation illustrating velocity profiles under physiological conditions is shown in Figure 8. Panel (a) presents velocity profiles in a vessel of diameter $10\,\mu\mathrm{m}$ at hematocrit values of 30% and 45%, respectively, driven by a constant pressure gradient. For a Newtonian fluid under the same conditions, the velocity profile would be parabolic at the corresponding Reynolds number. In these examples, as in typical microvascular blood flow, red blood cells accumulate near the center of the channel, leaving a cell-depleted region close to the vessel wall. This region is commonly referred to as the cell-free layer and is characteristic of bounded flows containing deformable particles. The combination of this uneven cell distribution, red blood cell deformability, and intercellular collisions gives rise to non-Newtonian behavior and results in a blunted velocity profile. A closer inspection of panel (a) reveals that increasing the hematocrit leads to stronger bluntness of the velocity profile. This is a classical feature of flows containing deformable bodies, where non-Newtonian effects become increasingly pronounced. In contrast, in a hypothetical situation where only blood plasma is present—such as may occur locally in microcirculation due to plasma skimming at bifurcations—the velocity profile follows the Poiseuille solution and remains parabolic, consistent with the Newtonian nature of plasma [230].

The shear-rate distributions corresponding to these velocity profiles are shown on the right-

hand axis of panel (a). For Poiseuille flow, the shear rate varies linearly across the channel, leading to a linear shear-stress distribution. In contrast, blood flow exhibits a highly non-linear shear-rate profile. In the Poiseuille reference case, a hypothetical flow producing the same wall shear stress (approximately $500\,\mathrm{s}^{-1}$) is considered. When blood plasma alone is driven by the same pressure gradient, it generates a similar wall shear-rate but maintains a higher flow rate. As the hematocrit increases, the flow rate decreases for a fixed pressure drop, consistent with the energy-based arguments discussed above. Panel (b) of the same figure shows blood flow in a vessel of larger diameter ($100\,\mu$m). The previously discussed trends regarding hematocrit dependence and velocity-profile bluntness remain valid. However, examination of the shear-rate distribution reveals three distinct regions. Region I corresponds to a highly non-Newtonian core, where the shear rate is nearly zero and the velocity profile is maximally blunted. Region II exhibits a nearly linear increase in shear rate, indicating a quasi-Newtonian regime where the velocity profile approaches its Poiseuille counterpart. Region III, located in a narrow layer adjacent to the vessel wall, shows a sharp and linear increase in shear rate. This region coincides with the cell-free layer, where red blood cells are absent and the flow is dominated by plasma, resulting in strongly damped non-Newtonian effects. A similar behavior is present in smaller vessels, as seen in panel (a), but it becomes more pronounced at larger diameters.

Panel (c) of Figure 8 summarizes simulation results for various hematocrit values and vessel diameters. All velocity profiles deviate from the Poiseuille solution, with the strongest deviations observed at the smallest diameters and highest hematocrits. As the vessel diameter increases, non-Newtonian effects persist but gradually weaken, and the velocity profiles approach the parabolic Poiseuille form. At sufficiently large diameters, on the order of millimeters, blood viscosity can be approximated as constant and inertial effects may also become relevant. Panel (d) presents curve fits to the velocity profiles shown in panel (b), using the functional form $v_{\max}\big(1-(x/R)^k\big)$. This ansatz arises from analytical solutions for power-law fluids, which capture certain classes of non-Newtonian behavior relevant to suspensions of elastic capsules. For vessel diameters of $100\,\mu$m, continuum descriptions with appropriate viscosity laws yield excellent agreement, with coefficients of determination $R^2 = 0.9916$ and 0.9945 for hematocrits of 30% and 45%, respectively. Such fits fail for vessels of diameter $10\,\mu$m, where a more elaborate multiphase description distinguishing the red-cell-rich core and the cell-free layer is required. This limitation arises from the comparable length scales of red blood cells and the vessel diameter, necessitating direct numerical simulations that explicitly resolve cells and the surrounding fluids. Although the continuum hypothesis remains valid, red blood cells and other blood agonists must be modeled as distinct entities, rendering blood a heterogeneous rather than homogeneous fluid at this scale.

Having established the governing dimensionless numbers and the collective rheological behavior of blood, a bottom-up approach is required to identify the fundamental building blocks

of blood flow. This motivates a detailed examination of single-cell dynamics and of dilute suspensions of red blood cells. A blood cell, consisting of a lipid bilayer membrane coupled to an internal cytoskeleton, is already a complex object. Simpler deformable entities exist between rigid particles and red blood cells, such as droplets, vesicles, and capsules. Understanding the dynamics and rheology of these simpler systems provides essential insight into the mechanisms governing blood flow. For brevity, the dynamics of droplets are not discussed here; interested readers are referred to the relevant literature.

2.2.1 Dynamics of Red Blood Cells, Vesicles and Capsules in Canonical Flows

Within the scope of this thesis, red blood cells, platelets, and von Willebrand factor are of primary interest. To understand blood-flow characteristics, it is essential to study the dynamics of individual entities under canonical flow conditions, such as Couette and Poiseuille flows in bounded and unbounded geometries, as well as their collective behavior in suspension. A single red blood cell behaves as a capsule whose membrane resists bending and shear deformations and is effectively inextensible, while volume conservation is ensured by the incompressibility of the internal fluid. Platelets are significantly smaller than red blood cells, and they are, under healthy conditions, at least an order of magnitude stiffer, allowing them to be modeled as rigid oblate particles. Von Willebrand factor appears as short- and long-chain polymers that play a crucial role in hemostatic processes. Because the volume fractions of platelets and von Willebrand factor are much smaller than that of red blood cells, the overall blood flow is predominantly governed by red blood cell dynamics. Consequently, understanding red blood cell behavior in canonical flows is of central importance.

In the following sections, the dynamics of vesicles, capsules, and red blood cells in canonical flows are discussed. Viscous fluid entities enclosed by membranes or interfaces are traditionally classified into three categories: liquid droplets, vesicles, and capsules. In each case, an interface or membrane separates an internal fluid from an external one, which may be identical or distinct. Depending on the mechanical properties of this interface, different levels of complexity arise. This hierarchy progresses from liquid droplets to vesicles and finally to capsules and red blood cells. It is therefore natural to begin with the simplest systems and progressively move toward more complex ones [121, 132, 134, 141, 143, 193].

For brevity, liquid droplet dynamics are omitted. The discussion therefore follows a path from vesicles to capsules and ultimately to red blood cells. Topics include the dynamics of single entities in canonical bounded and unbounded flows, symmetry breaking and associated lift forces, shear-induced diffusion in suspensions, and finally the formation of the cell-free layer.

This framework is essential for the present thesis, as all simulations are initialized from a

state in which a well-developed cell-free layer is already present, devoid of red blood cells but enriched with hemostatic components. A detailed understanding of the physical mechanisms leading to the emergence of the cell-free layer is therefore necessary to justify the initial conditions and to correctly interpret the subsequent simulation results.

This pathway requires synthesizing a wide range of terminology used variably (e.g., different terms for same mode of motion) across the literature. Accordingly, specific conventions are adopted here. The term "early" refers to studies published before 2011, while "later" or "recent" denotes work published after 2011. Additional conventions relevant to deformation modes and dynamical states of soft particles are introduced as needed.

The membranes of vesicles and red blood cells consist of lipid bilayers, and capsules are often enclosed by similar structures. A lipid bilayer is formed by two monolayers composed of lipid molecules, each consisting of a hydrophilic head and a hydrophobic tail, rendering lipids amphiphilic. When dispersed in aqueous environments, lipid molecules spontaneously assemble into structures such as micelles, bilayers, or tubular formations, depending on concentration and temperature. In bilayers, hydrophilic heads remain in contact with water, effectively shielding hydrophobic tails within the membrane interior. Strong noncovalent interactions maintain bilayer integrity, making membrane rupture energetically costly and intermonolayer lipid transport extremely slow. As a result, both the total membrane area and the number of lipids per monolayer are effectively conserved, leading to membrane incompressibility and bending elasticity. Artificial vesicles differ from living cells in that biological membranes are decorated with proteins, pores, and receptors involved in metabolism and active transport. Living cells actively regulate osmotic pressure, whereas vesicles lack such mechanisms. Due to fluid incompressibility, vesicles, capsules, and red blood cells all conserve volume [190].

Vesicles are more complex than liquid droplets because of their bending rigidity and area incompressibility. Droplets are separated from the surrounding fluid by an interface characterized solely by surface tension and do not conserve surface area or volume. Their dynamics are therefore governed primarily by surface tension, rendering them simpler than vesicles within this hierarchy [190].

Capsules represent the closest analogues to red blood cells. They share many properties with vesicles but possess membranes formed by cross-linked polymers, which confer resistance to shear deformations. Capsules are typically artificial constructs produced under laboratory conditions. Due to their membrane shear elasticity, capsules cannot undergo the large shape changes characteristic of vesicles when subjected to external flows or thermal fluctuations [194].

Red blood cells contain an internal cytoskeleton composed of actin filaments anchored to

the inner membrane surface. This structure introduces shear elasticity, making red blood cells more complex than vesicles. They combine constant surface area, constant volume, bending rigidity, and shear elasticity. Under physiological conditions, red blood cells exhibit a biconcave shape with a diameter of approximately $8\,\mu$m and a thickness of about $2\,\mu$m [189]. The lipid bilayer thickness is less than 10 nm, and the bending rigidity is estimated to lie between 5 and $70\,k_{\mathrm{B}}T$ [76]. For comparison, vesicle bending rigidities typically range from 10 to $25\,k_{\mathrm{B}}T$, with shapes and dynamics strongly influenced by membrane composition and temperature [190].

Figure 9(c) illustrates the membrane layout of (i) vesicles, (ii) capsules, and (iii) red blood cells. Panel (b) of the same figure shows scanning electron microscopy (SEM) images of red blood cells.

Artificial vesicles and capsules typically enclose the same fluid as their surroundings, and the viscosity contrast between internal and external fluids is controlled experimentally, often by adding polymers such as dextran to the external medium [4, 5]. In contrast, red blood cells contain a hemoglobin solution that binds and releases gases and is approximately five times more viscous than blood plasma [50, 76, 112, 187, 188].

Modeling vesicles, capsules, and red blood cells in external flows constitutes a coupled multiphysics problem involving internal and external fluid dynamics as well as membrane mechanics. The challenge arises from the fact that membrane shape is not known *a priori* and must be determined self-consistently. The resulting problem is a strongly coupled fluid–structure interaction system with a free boundary. Membrane forces arise from resistance to bending and stretching and are typically derived from a membrane elastic energy, most commonly expressed through the Helfrich functional. Taking functional derivatives of this energy yields the corresponding force densities. Given the Helfrich formulation, membrane shapes can be obtained either by energy minimization under constraints or by coupling elastic forces to hydrodynamic stresses and solving the resulting force-balance equations. The Helfrich elastic energy is typically written as follows:

$$\mathcal{H} = \int_A \left(\frac{\kappa}{2}(2H - C_0)^2 + \kappa_G K \right) dA. \tag{4}$$

The above equation is the Hamiltonian for a lipid bilayer membrane proposed by Helfrich [193]. Here, $\mathcal{H}$ denotes the Helfrich potential (Hamiltonian), H and K are the mean and Gaussian curvatures, and κ and κ_G are the corresponding bending moduli to bending and Gaussian curvatures. The parameter C_0 is the spontaneous curvature, which penalizes deviations of the mean curvature from C_0. For fully enclosed vesicles, capsules, and RBCs without holes, the integral of the Gaussian-curvature term is a topological invariant and thus remains constant; consequently, only the first term contributes to shape changes. In practice, the Gaussian term

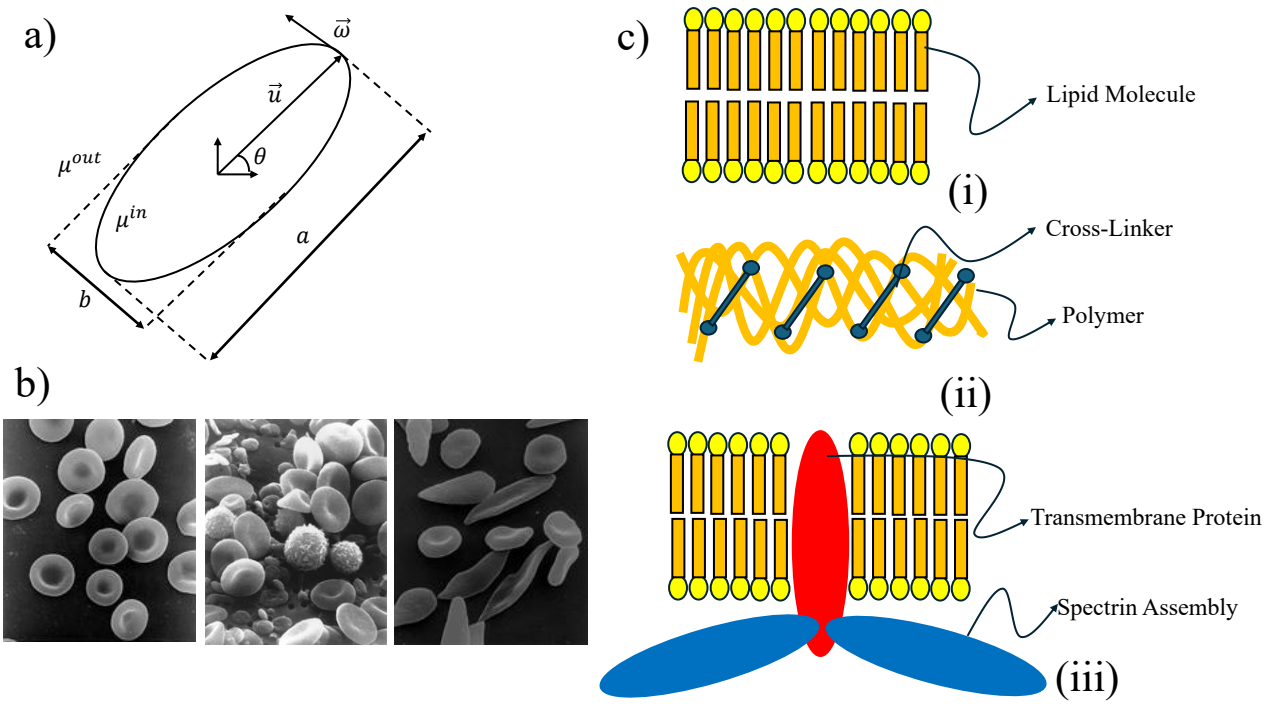

Figure 9: (a) Schematic of an ellipsoidal vesicle or capsule in shear flow. The unit vector **u** denotes the orientation of the entity also referred as inclination vector in the text, and the angle θ between **u** and the flow direction defines the tank–treading inclination angle. The semi–major and semi–minor axes of the ellipsoid are denoted by a and b, respectively which is used to calculate the Taylor deformation parameter. The entity separates an internal and an external fluid with viscosities μ^{in} and μ^{out}. (b) Scanning electron microscopy (SEM) image of red blood cells. Reproduced from Wikimedia Commons (public domain). (c) Schematic representation of the membrane composition of (i) vesicles, (ii) capsules, and (iii) red blood cells. Vesicles are enclosed by a lipid bilayer. In capsules, lipid molecules are cross–linked by polymer networks, imparting shear elasticity to the membrane. In red blood cells, the lipid bilayer is coupled to an underlying spectrin cytoskeleton, which is anchored to the membrane via transmembrane proteins.

is often omitted and additional constraints, such as local area incompressibility (or an effective surface tension), are imposed.

The governing potentials for capsule membranes are typically formulated as strain-energy functions. In the literature, two forms are particularly prevalent for modeling capsules and RBCs. These functions relate the energy stored in the membrane to its deformation through the principal stretch ratios λ_1 and λ_2. The associated material parameters include elastic moduli related to bending and a shear modulus associated with in-plane shear deformations. The neo-Hookean (NH) law is often used to model polymerized membranes and corresponds to the infinitely thin limit of an incompressible, homogeneous three-dimensional solid [212]. The NH law exhibits strain-softening under uniaxial stretching [22]. A typical form of the NH

potential is

$$\mathcal{W} = \frac{G_s}{2}\left(I_1 - 1 + \frac{1}{I_2 + 1}\right), \tag{5}$$

where I_1 and I_2 are invariants of the deformation expressed in terms of λ_1 and λ_2, and G_s is the shear modulus. This potential does not penalize area dilation and is therefore not suitable for RBC membranes. A widely used alternative devised for RBCs is the Skalak (SK) law, which strongly enforces area conservation. A typical form is

$$\mathcal{W} = \frac{G_s}{4}\left(\frac{1}{2}I_1^2 + I_1 - I_2\right) + \frac{G_A}{8}I_2^2. \tag{6}$$

Here, G_A is the surface dilatation modulus. This model is commonly used for red blood cell membranes and other biological membranes, as it captures resistance to both shear deformation and area dilatation [174].

The governing equations of fluid motion are discussed in detail in upcoming chapters. In this thesis, a multiscale mechanical model is employed for the membrane of an RBC; details are provided in the following sections. For continuum approximations of lipid bilayer membranes, the interested reader is referred to [22]. An early review of vesicle membrane mechanics is [191]. For RBC membranes, [76] is particularly useful, especially with regard to continuum-based approximations.

Two canonical flows are primarily relevant to this chapter: Couette and Poiseuille flows. Both can be considered in bounded or unbounded configurations to incorporate the effects of confining walls. Throughout this chapter, the viscous forces are assumed to dominate inertial forces; thus, the flow is effectively inertia-less (i.e., low-Reynolds-number flow). The corresponding velocity fields are

$$\mathbf{v}_{\text{Couette}} = \dot{\gamma}\, y\, \mathbf{e}_x, \tag{7}$$

$$\mathbf{v}_{\text{Poiseuille, plane}} = v_{\max}\left(1 - \left(\frac{2y}{W}\right)^2\right)\mathbf{e}_x, \tag{8}$$

$$\mathbf{v}_{\text{Poiseuille, pipe}} = v_{\max}\left(1 - \left(\frac{r}{R}\right)^2\right)\mathbf{e}_x = v_{\max}\left(1 - \alpha^2(y^2 + z^2)\right)\mathbf{e}_x, \tag{9}$$

where $\dot{\gamma}$ is the shear rate, $v_{\max}$ is the maximum centerline velocity in Poiseuille flow, W is the slit width, R is the pipe radius, $r = \sqrt{y^2 + z^2}$, and $\alpha = 1/R$ is the curvature parameter. Several dimensionless numbers arise in these settings and govern the dynamics; these are discussed next.

The dimensionless groups constitute the control parameters of numerical simulations and experimental studies. They can be grouped into six categories, three of which are typically considered essential control parameters in numerical, experimental, or analytical setups.

The first essential parameter is the reduced volume v. It is a dimensionless geometric measure that quantifies the deviation of an entity from a sphere and determines its equilibrium shape in the absence of external forcing. Given the surface area A of a vesicle, the area-based radius R_A is defined as $R_A = \sqrt{A/(4\pi)}$, which corresponds to a reference volume $V_A = \frac{4}{3}\pi R_A^3$. The reduced volume is then $v = V/V_A$. A perfect sphere has $v = 1$, whereas RBCs typically have $v \approx 0.65$. Smaller v implies more excess area and thus more room to deform. In the literature, an equivalent measure is the excess area,

$$\Delta = 4\pi \left(\frac{A}{4\pi R_V^2} - 1 \right), \tag{10}$$

where R_V is defined via $V = \frac{4}{3}\pi R_V^3$. The relation between these measures is $\Delta = 4\pi \left(v^{-2/3} - 1 \right)$, and $\Delta = 0$ for a sphere.

The second essential control parameter is the capillary number, which measures the ratio of viscous forces to membrane elastic forces. For vesicles dominated by bending elasticity, a common definition is

$$Ca = \frac{\dot{\gamma}\, \eta_{\text{out}}\, R_0^3}{\kappa}, \tag{11}$$

where η_{out} is the external fluid viscosity, R_0 is a characteristic size (e.g., R_A or R_V), and κ is the bending rigidity. Large Ca indicates viscous-force-dominated dynamics, whereas small Ca indicates elasticity-dominated dynamics. For capsules and RBCs with shear elasticity, Ca is often defined relative to the shear modulus,

$$Ca = \frac{\dot{\gamma}\, \eta_{\text{out}}\, R_0}{\mu}, \tag{12}$$

where μ is the shear-elastic modulus.

The third essential control parameter is the viscosity contrast,

$$\lambda = \frac{\eta_{\text{in}}}{\eta_{\text{out}}}, \tag{13}$$

the ratio of internal to external fluid viscosities. Large λ corresponds to highly viscous interiors, making the entity behave more like a weakly deformable solid. For RBCs, a typical value is $\lambda \approx 5$, while in certain diseases (e.g. malaria) λ may be significantly higher.

An attempt has been made to reduce the three-parameter space (v, Ca, λ) to two self-similar variables, S (related to shear strain) and Λ (both involving excess area) [113], with the claim that phase boundaries remain invariant under changes in excess area, therefore effectively reducing the phase space from three variables to two variables. This assertion is not fully correct:

a complete representation of dynamical regimes generally requires retaining the third axis, typically expressed as the reduced volume (or equivalently the excess area) [15, 134, 193].

The ratio of inertial to viscous forces is measured by the Reynolds number,

$$Re = \frac{\rho\,\dot{\gamma}\,R_0^2}{\eta_{\text{out}}}, \tag{14}$$

where ρ is the fluid density. For vesicles, most studies focus on the low-Re regime (typically $Re < 0.1$), while inertial effects become significant beyond this range [121].

In bounded flows, the confinement number characterizes the influence of walls. For a planar channel of width W it is often defined as $C_n = 2R_0/W$, while for circular channels it can be defined as $C_n = R_0/R$. This parameter is particularly relevant for near-wall migration.

If the membrane is viscous, then the ratio of membrane viscosity to external viscosity becomes relevant, typically expressed as $\eta_{\text{mb}}/\eta_{\text{out}}$. This parameter matters only when membrane viscosity is comparable to the external viscosity. Measuring RBC membrane viscosity is challenging; values on the order of 10^{-3} to $10^{-2}\,\text{dyn}\cdot\text{s/cm}$ have been reported [189]. However, more recent thermal-flickering experiments suggest that membrane viscosity may be negligible, and many recent simulations neglect RBC membrane viscosity [76, 188].

For capsules and RBCs with shear elasticity, an additional dimensionless bending rigidity compares bending and shear-elastic contributions,

$$\frac{\kappa}{R_0^2\mu}, \tag{15}$$

where κ is the bending rigidity and μ the shear-elastic modulus. For RBCs, κ is typically on the order of $10^{-19}\,\text{J}$ [188], while μ is on the order of $10^{-6}\,\text{N/m}$ [76], yielding $\kappa/(R_0^2\mu) \sim 10^{-1}$. This ratio is also called as Föplle - von Karman number.

The "periodic table" of dynamical modes for vesicles, capsules, and RBCs is diverse. The mode of motion depends primarily on the phase-space variables (λ, Ca, v). These modes are commonly characterized using a shared set of observables. For a prolate ellipsoid, the inclination angle between the major axis and the flow direction is denoted by θ. A material marker on the membrane defines an additional angle ψ, and its time derivative defines the tank-treading frequency ω. A characteristic tank-treading velocity scale is ωR. Deformation is often quantified by the Taylor deformation parameter,

$$D = \frac{a-b}{a+b}, \tag{16}$$

where a and b denote the lengths of the major and minor axes, respectively. Figure 9(a) shows the relevant measured parameters on a typical vesicle model.

Several common in-plane modes (with the major axis remaining in the shear plane) include: tank-treading, tumbling, vascillating–breathing (often also termed trembling), swinging.There also exist intrinsically three-dimensional modes, where the orientation vector deviates from the shear plane, including: kayaking, rolling and precession.These three-dimensional motions are often characterized by tracking the trajectory of the orientation vector on the unit sphere; closed periodic trajectories are commonly referred to as Jeffery orbits.

In bounded Poiseuille flows, vesicles, capsules, and RBCs can attain characteristic steady shapes such as : parachute, bullet, slipper, rocketlike, snaking and swirling.

Specific to RBCs, multilobed shapes may occur under strong flows: depending on flow strength, discocyte and stomatocyte-like shapes can also be observed and are typically quantified using suitable asphericity measures. The corresponding observables and their behavior are discussed in the following sections.

The simplest flow field of interest is linear shear flow, which generates a constant shear rate throughout the domain. Under constant shear, vesicles, capsules, or RBCs typically exhibit three broad categories of dynamics: tank-treading, tumbling, and all other modes which are not tumbling or tank-treading.

Figure 10(a-h) includes some of the configurations which are discussed in the upcoming chapters. For intrinsically three dimensional mode of motions where the inclination vector leaves the shear plane, reader is referred to the corresponding publications cited in the text.

Tank-treading is characterized by a steady rotation of the membrane around the enclosed fluid with a characteristic tank-treading frequency ω, together with a constant positive inclination angle of the vesicle with respect to the flow direction, denoted by θ. Figure 9(a) shows relevant metrics for an ellipsoidal vesicle.

This motion was first observed experimentally for red blood cells [74]. Building on Jeffrey's classical solution for the motion of a rigid ellipsoid in unbounded shear flow [103], Keller and Skalak extended the analysis to an undeformable ellipsoid undergoing tank-treading in an unbounded shear flow, known as the KS model [204]. Their solution is based on a torque balance between the internal and external fluids. An equivalent interpretation follows from an energy viewpoint: the energy injected by the external shear is dissipated by the internal fluid and by the disturbance generated in the surrounding fluid due to the membrane tank-treading motion

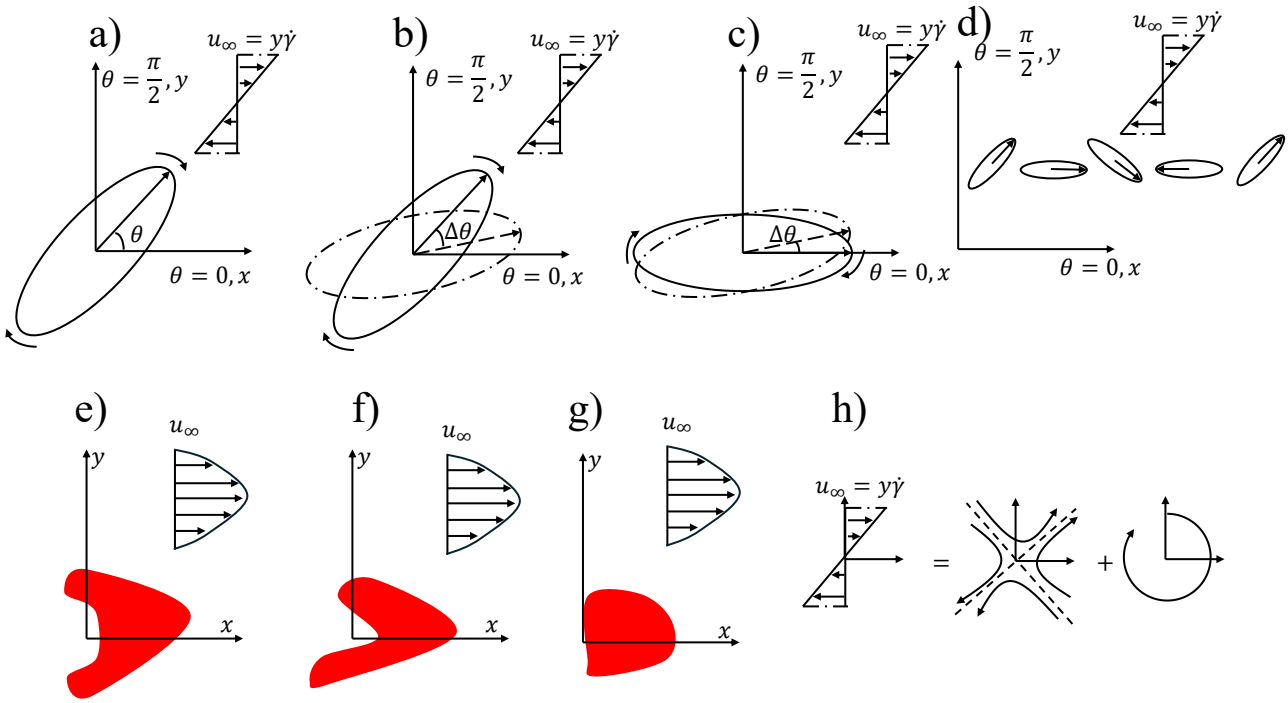

Figure 10: Different modes of motion of vesicles/capsules/red blood cells and decomposition of shear flow into elongational and rotational flow. Curved arrows show the tank-treading direction of the membrane. Straight arrows are used to indicate the inclination vector. (a-d) indicates modes of motion occurring in shear flow. (e-g) shows the modes of motion occurring in Poiseuille flow. (a) Tank-treading motion. Characterized by constant inclination angle θ. (b) Swinging or Trembling motion. Characterized by oscillations around positive mean angle θ. The oscillation amplitude is indicated by $\Delta\theta$. (c) Vascillating-breathing motion. The mean angle θ is zero. The vesicle oscillates between positive and negative θ values. (d) Tumbling motion. (e) Parachute shape. (f) Slipper shape. (g) Bullet shape. (h) Decomposition of shear-flow into elongational and rotational parts. The elongoation is maximal when $\theta = \frac{\pi}{4}, \frac{5\pi}{4}$ and the compression is maximal when $\theta = \frac{3\pi}{4}, \frac{7\pi}{4}$.

[132]. If the dissipation cannot cancel the injected energy by shearing then a transition from tank-treading to tumbling happens. A representative schematic for tank–treading motion can be seen in Figure 10(a).

This theory successfully predicts the transition from tank-treading to tumbling as a function of the viscosity contrast λ. The transition occurs at a critical value λ_c. At low internal viscosity, the membrane tank-treads around the enclosed fluid such that the energy injected by the shear flow is dissipated through internal viscous dissipation and through the disturbance flow generated in the external fluid. As the internal viscosity increases, the shear flow can no longer sustain membrane tank-treading, and a transition from tank-treading to tumbling occurs [132]. In the tank-treading regime, the equation of motion for the inclination angle reads

$$\frac{d\theta}{dt} = A_1 + A_2 \cos(2\theta), \tag{17}$$

where θ is the inclination angle (i.e., the stationary angle between the ellipsoid's major axis and the flow direction). Here, $A_1 = -\dot{\gamma}/2$, while A_2 is a geometry-dependent parameter. For explicit expressions for A_1 and A_2, the interested reader is referred to the appendix of [86]. In this formulation, A_1 corresponds to the torque arising from the elongational component of the shear flow, whereas A_2 corresponds to the torque associated with the rotational component. Figure 10(h) shows the decomposition of the linear shear flow into elongational and rotational components. In the tank-treading regime, a steady inclination angle satisfies $\dot{\theta} = 0$, and the ratio $|A_1/A_2|$ determines the existence of a stable stationary solution. Since the viscosity contrast λ enters only through A_2, the KS model predicts that the tank-treading–to–tumbling transition depends solely on λ. This is not strictly true in practice because the KS model assumes a fixed, undeformable ellipsoidal shape and an ellipsoidal membrane velocity field that does not conserve local membrane area. The latter constitutes a major source of discrepancy with experiments [4].

Nevertheless, early experimental studies and numerical simulations of vesicles and RBCs were broadly consistent with the KS model in regimes where RBCs adopt nearly ellipsoidal shapes, particularly at high capillary numbers and low viscosity contrasts where deformation is limited once a stationary shape is reached. The theory correctly predicts the experimentally observed linear relationship between the tank-treading frequency (i.e., the angular velocity of the membrane relative to the center of mass) and the imposed shear rate [71, 225]. It also captures the transition from tank-treading to tumbling for vesicles with sufficiently large reduced volumes [104]. Early numerical studies likewise showed good agreement with KS predictions, especially for large reduced volumes or high capillary numbers, where shape deformation remains small, if the viscosity ratio is small [133, 195].

For vesicles and capsules, membrane viscosity may play a role depending on membrane composition. Membrane viscosity effectively acts as an additional contribution to the internal dissipation and reduces both the inclination angle and the tank-treading frequency. It also lowers the critical viscosity contrast predicted by KS theory. Thermal fluctuations, which are particularly important for microscale vesicles, smooth the transition between tank-treading and tumbling by shifting the transition to larger viscosity contrasts. They can also induce occasional tumbling events even when λ is below the nominal critical value [85].

Perhaps the most accurate quantitative prediction of the KS model is that the inclination angle θ decreases with increasing viscosity contrast λ. High-fidelity simulations have consistently confirmed this trend, showing that increasing the internal viscosity reduces θ until it eventually vanishes [15, 134, 200, 201].

At sufficiently high shear rates, and for fixed reduced volume and viscosity contrast, the tank-treading inclination angle θ becomes essentially independent of the capillary number, in

agreement with the KS model. Physically, θ is set by a balance between the elongational and rotational components of the imposed shear flow. Since an increase in shear rate strengthens both components proportionally, the inclination angle remains nearly constant with respect to Ca. Analytical and experimental extensions of the KS model have supported this behavior [5, 132, 233]. More recent high-fidelity simulations, however, reveal a weak dependence of θ on Ca, particularly in intermediate and low-Ca regimes where vesicle deformation is appreciable; in these regimes, shape changes can slightly modify the steady inclination angle [15, 201].

The inclination angle θ is also highly sensitive to the reduced volume v, which strongly influences vesicle shape and quantifies the available excess area for deformation. For a given Ca and viscosity contrast λ, θ typically decreases as v decreases. In the spherical limit ($v = 1$), a deformable object in shear flow exhibits neither deformation nor a preferred orientation due to symmetry. For small deviations from sphericity ($v < 1$), the vesicle deforms and the inclination angle approaches $\pi/4$, corresponding to alignment with the elongational axis of the shear flow. As v decreases further, θ decreases steadily and eventually vanishes. This behavior arises because the vesicle's in-plane aspect ratio increases with nonsphericity, enhancing flow alignment and driving θ toward smaller values [15, 201]. The same trend was captured in early analytical extensions of the KS model to deformable vesicles [129].

Once the inclination angle vanishes, the transition from tank-treading to tumbling occurs. The corresponding critical viscosity contrast λ_c is a function of the reduced volume. As noted above, vesicles with smaller reduced volume tend to adopt smaller inclination angles, and therefore an increase in internal viscosity drives them to $\theta = 0$ more rapidly, leading to a lower critical viscosity contrast [16].

The deformation measure, i.e. the Taylor deformation parameter, remains approximately constant when the reduced volume v and capillary number Ca are fixed and the internal viscosity is varied [15, 201]. The internal viscosity strongly affects the inclination angle by favoring the rotational component of the shear flow, but it has little influence on the deformation. In the extreme limit $\lambda \to \infty$, deformation becomes negligible as the vesicle effectively rigidifies.

Within the tank-treading regime, if λ and v are held fixed, the deformation parameter D depends only weakly on Ca. The vesicle reaches a steady shape constrained by membrane inextensibility. At low and intermediate Ca, modest changes in D can be observed, whereas at high Ca further deformation is strongly limited [201].

Numerical studies indicate that D is a strong function of reduced volume, since v measures the available excess area for deformation. In the intermediate- and large-Ca regime, analytical

approaches predict

$$D = \sqrt{\frac{15\Delta}{32\pi}}, \tag{18}$$

where Δ is the excess area [191]. Numerical simulations show good agreement with this prediction [15]. Overall, smaller reduced volume implies more excess area and thus larger attainable deformation, leading to larger values of D.

The final parameter characterizing tank-treading is the tank-treading frequency ω, defined as the time derivative of the membrane marker angle. For fixed viscosity contrast and reduced volume, the KS model predicts a linear relationship between ω and the applied shear rate (equivalently, between ω and Ca) [204]. Both simulations and experiments support this linear scaling [122, 123, 201].

Once the inclination angle reaches zero, the vesicle transitions to tumbling. Tumbling is an unsteady motion in which the inclination angle θ spans the interval $[-\pi/2, \pi/2]$, and the tumbling rate $\dot{\theta}$ is periodically modulated [4]. The angular velocity is slowest when the vesicle is aligned with the flow direction (i.e., $\theta = 0$) and fastest when it is perpendicular to the flow (i.e., $\theta = \pm\pi/2$).

Since a second mode of motion is introduced over tank–treading, reader can now follow the different phase behaviors of the vesicle for $v = 0.6$ from Figure 11.

The transition from tank-treading to tumbling is a consequence of torque balance. As the internal viscosity increases, viscous resistance prevents the membrane from sustaining tank-treading, and tumbling becomes the preferred mode [204]. While the original KS model assumes a fixed shape, later analytical theories and modern numerical simulations show that shape deformation and oscillation are integral features of the tumbling regime, especially at higher capillary numbers [129, 193]. In tumbling, vesicles undergo periodic shape deformations and may exhibit large-amplitude shape oscillations [151, 233]. Moreover, a weak residual tank-treading component persists on the membrane, typically an order of magnitude smaller than in the pure tank-treading regime [133]. These deformation-driven deviations from rigid-body dynamics lead to systematic departures from KS predictions. In particular, at low capillary numbers (e.g., $Ca < 1$) and for low viscosity contrasts, where vesicles are more deformable, KS-based predictions for $\theta(t)$ can deviate noticeably from numerical results [134]. A representative schematic for tumbling motion can be seen in Figure 10(d).

During tumbling, the vesicle continually samples both the elongational and rotational components of the imposed shear flow. The elongational component tends to stretch the vesicle into an elongated shape, with maximal deformation occurring when the long axis is close to the

extensional direction of the flow, typically near $\theta = \pi/4$ [4, 86]. Such deformations effectively renormalize the KS parameters (often denoted A_1 and A_2), which slows tumbling relative to a rigid body, particularly at large Ca [151]. Conversely, when the deformation is compressive, the effective coefficients are modified in the opposite direction. In both cases, deformation alters the instantaneous rotational velocity, producing a rotation that is slower than that of a rigid ellipsoid. This continuous alternation between elongation and compression also underlies the residual tank-treading component on the membrane. The decomposition of the shear flow into elongational and rotational components and the direction of maximum extension and compression is displayed in Figure 10(h).

Early phase diagrams for the tank-treading and tumbling regimes include three-dimensional vesicle results for reduced volumes $v = 0.78$, 0.80, and 0.90 [88], as well as two-dimensional results for $v = 0.7$ [84]. An analytical phase diagram for a related setting is given in [113]. Although these phase boundaries have been refined by subsequent analytical developments and higher-fidelity simulations, they qualitatively capture the tank-treading and tumbling domains. Both types of phase diagrams also include an intermediate regime, often termed vacillating–breathing; in this chapter, it is referred to as trembling, as discussed next.

An intermittent dynamical state arises for vesicles in shear flow at intermediate capillary numbers and intermediate-to-high viscosity contrasts λ. This regime has been referred to as vacillating–breathing, swinging, or trembling. Here, the term trembling is adopted. The term swinging is reserved for capsules that exhibit inclination-angle oscillations around positive θ while remaining in a tank-treading-like state. Figure 10(c) shows characteristics of trembling/vacillating–breathing motion. Corresponding outlay of this mode of motion in (Ca-λ) space can be seen from Figure 11 for ($v = 0.6$).

Trembling was first observed experimentally in [105], where it was characterized by $\theta \approx 0$ together with periodic shape deformations, visible as oscillations in the deformation parameter D. Early analytical descriptions for nearly spherical vesicles can be found in [129]. Trembling is essentially an intermediate regime between tank-treading and tumbling: the inclination angle oscillates but does not reach $\pm\pi/2$, and therefore the vesicle does not complete full tumbling rotations. When the dynamics are represented in the D–θ plane, trembling appears as a closed orbit (often a deformed cycle) [15]. In contrast, pure tank-treading corresponds to a fixed point in the D–θ plane [201], whereas tumbling produces an almost line-like trajectory.

Trembling arises from the nonlinear interplay between membrane elasticity and hydrodynamic forcing, which contains both elongational and rotational components. Since the KS theory neglects membrane elasticity, it cannot predict this intermediate state. When the vesicle's long axis lies in the range $0 < \theta < \pi/2$, near the extensional quadrant, the vesicle is elongated;

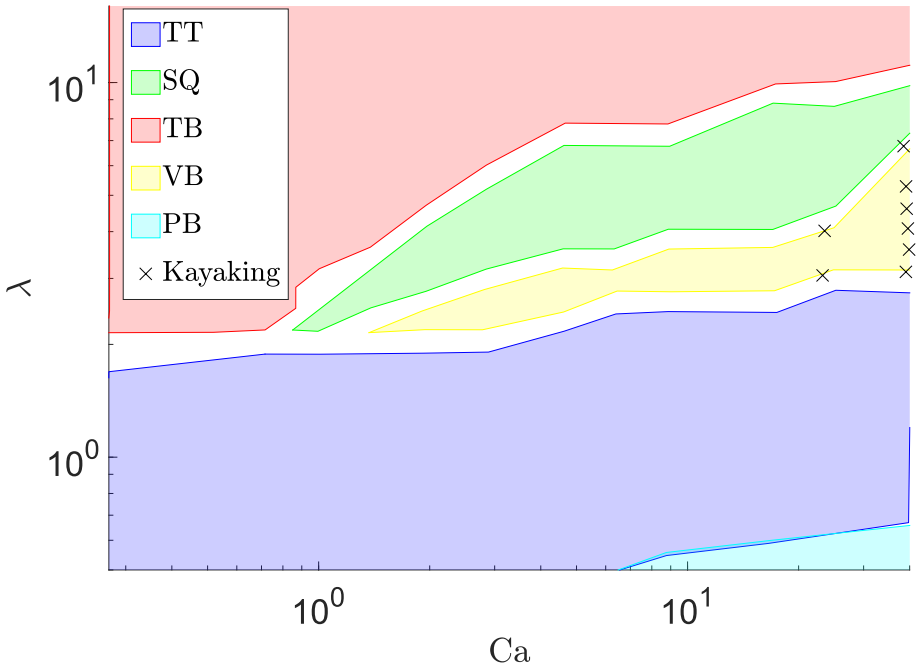

Figure 11: A phase space representation for mode of motions of a vesicle with reduced volume $v = 0.6$. The x-axis is the Ca number and y-axis is the viscosity contrast. (TT:tank–treading,SQ:squaring,TB:tumbling,VB:vacillating–breathing or trembling, PB: parity breaking, x : kayaking). Data is from [134].

for $-\pi/2 < \theta < 0$, it is compressed. In this manner, the membrane alternately stores and releases elastic energy [88]. The resulting shape oscillations feed back on the orientation dynamics and produce oscillations about $\theta \approx 0$. When thermal fluctuations are included, asymmetric shapes can occur during trembling, and occasional tumbling events may be triggered [88]. This sensitivity is often attributed to the proximity of the tank-treading–to–tumbling transition, which is associated with a saddle-node bifurcation [133].

Multiple studies indicate that the trembling region broadens as Ca increases [88, 113, 134]. See also Figure 11 and Figure 12. This is consistent with the notion that the intermittent dynamics stabilizes as the shear rate increases. The oscillation amplitude $\Delta\theta$ generally decreases slightly and then saturates at sufficiently large Ca (typically once $Ca > 10$), because the deformation amplitude, as quantified by D, becomes limited by membrane constraints [15]. As λ increases toward the tumbling transition, the oscillation amplitude grows and the orbit in the D–θ plane expands [201]. The transition to tumbling is marked by the oscillation amplitude reaching $\pm\pi/2$, after which further increases in λ drive the vesicle into the tumbling regime. When a vesicle enters the trembling regime from tank-treading, the oscillations are typically small and the vesicle remains nearly aligned with the flow direction. This limiting case is often termed flow alignment and is commonly treated as a sub-regime of trembling [134].

For interested readers, a first experimental full phase diagram for vesicles in shear flow can be found in [208]. The dynamical modes discussed above are represented in that work using two self-similar variables. As mentioned earlier, however, expressing the phase space solely in terms of two self-similar variables—both of which implicitly incorporate the reduced volume—does not fully capture the independent role of the reduced volume itself. A review of early analytical attempts to describe vesicle dynamics in shear flow can be found in [145]. An early phase diagram obtained from high-fidelity numerical simulations for a reduced volume of $v = 0.95$ is reported in [134]. Experimental confirmation of these numerical findings in the tank-treading regime can be found in [122].

For vesicle configurations arising under equilibrium conditions, the reader is referred to [190]. An early review covering both experimental and numerical results on vesicles and red blood cells in flow is given in [154]. A detailed comparison between early analytical theories [113, 138] and experimental observations is presented in [210]. The work in [201] reports phase diagrams covering all three principal modes of motion down to reduced volumes as low as $v = 0.85$, while [15] presents results for $v = 0.95$ and $v = 0.87$.

Within the trembling region, [15] further distinguishes a dynamical state described as "initially swinging dynamics that relaxes to tank-treading motion along the flow direction," corresponding to the flow-alignment mode introduced in [134]. They also report the complementary case of "initially tumbling motion that relaxes to swinging dynamics," which corresponds to ordinary trembling motion. Such relaxation pathways—toward either flow alignment or trembling—are also discussed as transient behaviors in [134]. For a more recent and comprehensive review of vesicle dynamics in flow, the reader is referred to [193].

With the exception of [88], most numerical studies of vesicle dynamics report phase diagrams at relatively high reduced volumes (i.e., $v \approx 0.9$), where vesicles are nearly spherical. This limitation is partly due to the fact that many analytical treatments rely on expansions in the excess area, which are only accurate when the reduced volume is close to unity. High-fidelity numerical simulations performed at significantly lower reduced volumes (e.g., $v = 0.65$, comparable to that of red blood cells) reveal qualitatively new dynamical modes, including squaring, parity breaking, and S-tumbling [141]. At high reduced volumes, the limited available excess area restricts deformation and therefore reduces the diversity of accessible dynamical states in phase space. See also phase space representation of a vesicle ($v = 0.65$) in Figure 12.

The squaring motion is a distinct morphological transition occurring within the trembling regime at $Ca > 1$ and intermediate-to-high viscosity contrasts. During squaring, the vesicle transiently adopts a square-like shape, and the inclination angle θ exhibits abrupt, discontinuous jumps in time. This behavior is fundamentally different from standard trembling, where θ

oscillates smoothly around zero. The discontinuous jumps occur when a single global maximum develops in the distance between the vesicle membrane and its center of mass. Squaring emerges after the destabilization of tank-treading in favor of trembling and precedes the transition to full tumbling as λ is increased further.

S-tumbling is a distinct subclass of tumbling that occurs at large capillary numbers and high viscosity contrasts. In this regime, vesicles follow a sequence of transitions—from tank-treading to trembling, then squaring, and finally to tumbling—before entering an S-shaped tumbling state. During S-tumbling, the vesicle exhibits a pronounced S-like morphology with a narrow waist at its center, distinguishing it from conventional flipping tumbling motion.

Parity breaking represents a remarkable dynamical state in which the vesicle spontaneously loses centrosymmetry. In this mode, inversion of a vector attached to the membrane does not map onto an equivalent point on the opposite side of the vesicle. This symmetry breaking is particularly striking because it arises in an unbounded linear shear flow, which is itself fully symmetric. Parity breaking occurs at low viscosity contrasts (i.e., $\lambda < 1$) and sufficiently large capillary numbers ($Ca > 6$). A crucial consequence of parity breaking is its ability to induce cross-streamline migration. In Stokes flow, such migration requires a breaking of time-reversal symmetry; among known vesicle deformation modes, parity breaking is unique in enabling this mechanism in unbounded shear flow.

Kayaking, parity breaking, squaring, and S-tumbling are relatively recent dynamical modes first reported in [141] and subsequently analyzed in greater detail in [200]. Figure 11 reveals all mode of motions observed for a vesicle with reduced volume of 0.6. Further systematic investigation is still required, particularly regarding the influence of control parameters (Ca, λ, v) on observable quantities such as θ, deformation D, and vesicle shape. Analytical treatments applicable to vesicles with low reduced volumes can be found in [144].

The dynamics of non-spherical capsules in unbounded shear flow exhibit complex, unsteady behavior, particularly when large shape deformations are involved. Primarily, the motion involves transitions between fluid-like rotation (i.e., tank-treading), as in the case of vesicles, and flipping motion (i.e., tumbling) [13]. In addition, a set of unsteady intermediate modes exists, often collectively referred to as trembling.

For an early review of capsule dynamics and related constitutive equations, interface conditions, and governing equations, the reader is referred to [21]. It should be noted that there are two main categories of constitutive equations: those that preserve the total membrane area (Skalak Model) and those that impose no such constraint(Neo-Hookean Model). These two classes yield qualitatively different dynamics [22].

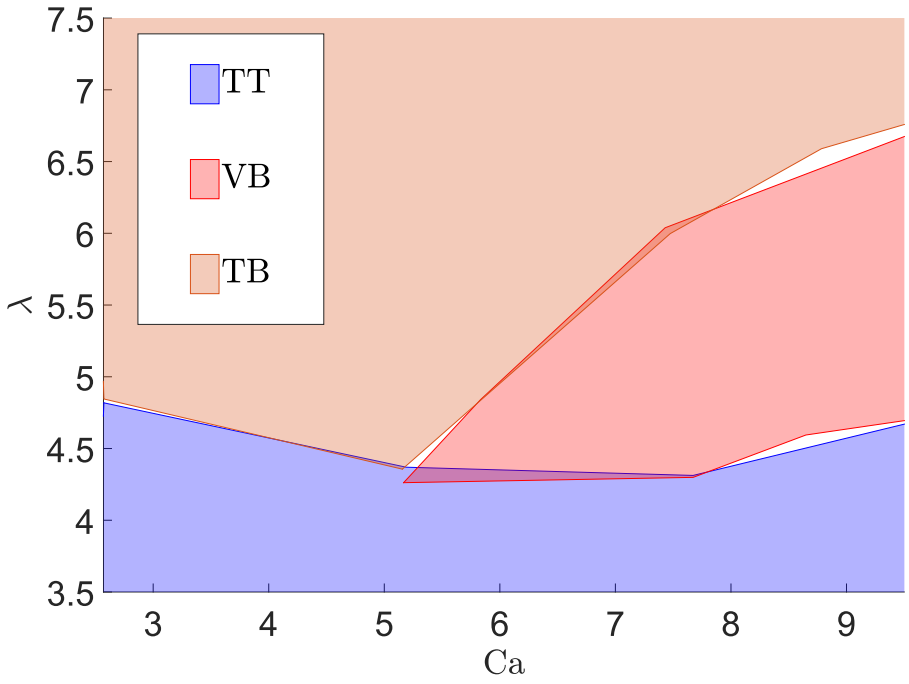

Figure 12: A phase space representation for mode of motions of a vesicle with reduced volume $v = 0.65$. The x-axis is the Ca number and y-axis is the viscosity contrast. (TT:tank–treading,VB:vascillating–breathing/trembling, TB : tumbling. Data is from [200].

The literature confirms that the tank-treading motion of capsules differs fundamentally from that of vesicles. A purely tank-treading vesicle attains a constant inclination angle and a steady shape, corresponding to a fixed point in the D–θ plane. In contrast, the tank-treading motion of capsules resembles trembling: the inclination angle θ oscillates while remaining positive (i.e., $0 < \theta < \pi/2$), unlike vesicle trembling where θ changes sign. These oscillations in θ induce additional shape deformation, causing geometric measures of a tank-treading capsule in unbounded shear flow to oscillate in time. Consequently, the motion traces a closed curve in the D–θ plane [13, 212]. In other words, tank-treading in capsules is intrinsically coupled to oscillations in the inclination angle. Such configuration is indicated in Figure 10(b).

Various naming conventions exist for this motion in the literature, including oscillatory motion or TT/OS. In this thesis, this mode is referred to as either tank-treading with oscillations or swinging. The same terminology is adopted for RBCs.

If a capsule is initially almost spherical, oscillations in the tank-treading regime are typically damped. In this case, both the inclination angle and the deformation parameter attain steady-state values, corresponding to a single point in the D–θ plane [7]. Thus, oscillations in the tank-treading regime arise as a consequence of non-sphericity and shear elasticity. The role of shear elasticity will be discussed further below with the aid of analytical models.

For moderate viscosity contrast λ, the trembling mode typically appears, analogous to vesicle trembling. The inclination angle oscillates periodically, becoming both positive and negative, but the capsule does not undergo a full tumbling motion. These oscillations are usually accompanied by large shape oscillations, which can be quantified by monitoring the deformation parameter D [13]. During trembling, the coupling between shape deformation and orientation is strongest, resulting in the maximum amplitude of deformation. The capsule may momentarily attain a near-circular shape in the shear plane while θ becomes negative, indicating significant compression. This compression reduces the hydrodynamic torque and prevents full tumbling [13, 212].

The amplitudes of tank-treading oscillations, shape oscillations, and inclination-angle oscillations reach their maximum near the boundary between trembling and tumbling. The trembling regime itself can be subdivided, as different transient dynamics may precede the steady state. Typically, either pure trembling or tumbling-to-trembling transitions are observed [13].

For large λ, and across almost the entire range of capillary numbers, capsules tumble. The driving mechanism is similar to that of vesicles: external hydrodynamic forces can no longer sustain tank-treading motion of the membrane, and the capsule undergoes tumbling [13].

The oscillatory behavior observed during tank-treading and trembling can be captured by extending the KS model. The Skotheim–Secomb (SS) model introduces a periodically varying elastic membrane energy into the KS framework, allowing it to predict shear-rate-dependent transitions from tank-treading to tumbling, as well as oscillatory dynamics. The SS theory predicts three regimes based on a dimensionless ratio of shear-elastic resistance to surface stress. Notably, the elastic contribution primarily accounts for shear elasticity and neglects bending energy, which is typically an order of magnitude smaller. Like the KS model, the SS theory assumes a shape-preserving ellipsoid and thus neglects large deformations.

In non-spherical capsules, different material elements of the membrane possess different energy minima depending on their orientation. As a material point—parameterized by a phase angle—moves around the fixed ellipsoidal shape, its associated elastic energy varies periodically [189]. This mechanism is analogous to the shape memory observed in RBCs [72].

Early experimental studies [235] demonstrated that capsules exhibit shear-induced wrinkles, particularly near the equator. During oscillations of θ in unbounded shear flow, the membrane approaches the onset of buckling due to compressive stresses generated by hydrodynamic forces. Because capsules possess finite shear elasticity, wrinkle formation reflects a balance between shear-elastic stresses and bending resistance [194]. An experimental comparison between a

tank-treading vesicle and a non-area-preserving tank-treading capsule can be found in [123]. A recent comprehensive review of capsule dynamics and rheology is provided in [22].

The dynamic behavior of RBCs in unbounded shear flow is even more complex and depends sensitively on both external and internal parameters. The reduced volume of RBCs is fixed at approximately $v = 0.65$, effectively reducing the nominal phase space from (Ca, λ, v) to (Ca, λ). However, additional physiological variability prevents a complete reduction of the phase space. Depending on cell age and physiological condition [124], RBC membrane mechanical properties and internal viscosity may vary. Furthermore, RBCs exhibit shape memory, meaning that membrane material points tend to return to their original positions after deformation [72]. Vesicles, in contrast, lack shear elasticity altogether.

It has also been shown that the stress-free configuration of the RBC membrane influences observable features of its motion [12]. Additionally, RBC geometry—specifically surface area and volume—varies from cell to cell even under physiological conditions [32]. As a result, the dynamical phase space of RBCs in unbounded shear flow is richer than that of either vesicles or capsules.

Tank-treading motion in RBCs was first observed experimentally in [71]. Early interpretations of tank-treading and tumbling relied on the KS model [204], based on Jeffery's solution for rigid ellipsoids in shear flow [103]. Early experimental observations showed qualitative similarities to vesicle dynamics, including steady inclination angle θ and deformation parameter D during tank-treading, and rigid-body-like flipping motion during tumbling [29, 225].

While the KS model provided a valuable initial framework, subsequent experimental and numerical studies revealed several RBC-specific dynamical features that the model could not capture, primarily due to its neglect of membrane elasticity, shape memory, and large deformations.

Experimental observations later demonstrated that under moderate shear stresses, RBCs do not exhibit pure tank-treading. Instead, the inclination angle oscillates while remaining positive (i.e., $0 < \theta < \pi/2$)—a mode known as swinging [1]. The oscillation period of θ is typically half the tank-treading period. Swinging arises directly from the shear elasticity and shape memory of the RBC membrane.

The SS model successfully captures this behavior by introducing a shape-memory energy term into the KS framework [189]. Because RBCs have a non-spherical resting shape, membrane elements undergo periodic elastic energy variations during tank-treading. As membrane elements rotate between the rim and the dimples, elastic energy is alternately stored and re-

leased, generating a periodic perturbation that prevents steady motion.

This mechanism does not operate for spherical capsules, which are centrosymmetric and lack preferred material locations on the membrane. Consequently, spherical capsules reach steady inclination and deformation after transient dynamics [7]. As the reduced volume decreases, non-sphericity increases and shape memory becomes effective. While capsules acquire shear elasticity through cross-linked polymer membranes, RBC shear elasticity originates from the cytoskeleton attached to the inner surface of the lipid bilayer [212]. The shape memory of RBCs was systematically investigated experimentally in [72].

The viscous hydrodynamic forces are controlled by the magnitude of the Ca number. If Ca is large, then viscous forces damp the oscillations in the swinging motion. When Ca is small, the external viscous stress becomes weaker, making it less capable of overcoming the elasticity-induced perturbation. This results in larger amplitude and period of oscillations [1, 212]. At very high shear rates the deformation of the RBC saturates and therefore the change in the deformation parameter and oscillation amplitude (i.e., ΔD and $\Delta\theta$) also approaches zero [17]. Therefore, at high Ca numbers the swinging motion resembles to pure tank-treading.

During swinging motion, the ratio of the period of the tank-treading and the period of oscillation is two. This is due to fact that, tank-treading period is measured over a rotation of 2π whereas the elastic-energy of the RBC due to its symmetry is periodic with π. In other words, after a tank-treading of π the material point reaches a symmetric position where the elastic-energy is released again. Whereas to complete a single tank-treading period a material point has to travel 2π on the membrane [1].

The tank-treading frequency is a non-monotonic function of the capillary number Ca. It attains a maximum at an intermediate value of Ca and then decreases slightly as Ca increases further. This saturation of the tank-treading velocity with increasing Ca is attributed to the inextensibility of the RBC membrane. Once a highly deformed shape is reached, the RBC can no longer deform in response to increasing hydrodynamic forces. This behavior has been demonstrated both numerically [18] and experimentally [73].

At low values of Ca, RBCs begin to exhibit breathing-like dynamics, leading to a sharp decrease in the tank-treading velocity. In addition, internal viscosity resists membrane tank-treading; consequently, a higher internal viscosity results in a lower tank-treading frequency [16].

An early experimental identification of tumbling (also referred to as flipping) was reported in [82]. Early studies treated the tumbling motion of vesicles and RBCs as rigid-body rotation, such that the orientation vector follows a Jeffery orbit. However, it was later demonstrated

experimentally that the flipping motion of RBCs differs from that of a rigid solid object [30]. Specifically, the orientation vector undergoes a transient motion that deviates from the shear plane and ultimately aligns with the vorticity direction. After completing this orbital drift, the RBC rolls like a wheel; this mode of motion is referred to as rolling.

Detailed investigations of red blood cell dynamics under physiologically relevant conditions—such as suspensions in plasma—have emerged only in recent years [62, 65]. At low shear rates, RBCs exhibit flipping, followed by a gradual orbital drift toward rolling as the capillary number increases, similar to behavior observed at low viscosity contrasts λ. However, in physiological media this orbital drift occurs already at significantly lower values of Ca, and the transition to rolling requires markedly lower shear stresses.

The rolling motion remains stable over a broad range of Ca, during which the cell progressively deforms. With further increases in Ca, deformation intensifies until compressive stresses induce a buckling instability, dynamically producing a rolling stomatocyte. Upon cessation of the flow, the discocyte shape is recovered. It is worth noting that discocyte and stomatocyte shapes may coexist at the same shear rate, depending on the mechanical properties of the cell; either morphology may prevail. Further increases in shear rate lead to additional elongation until a critical Ca is reached, beyond which the motion becomes unstable and the cell reorients into a tumbling stomatocyte regime. At even higher Ca, transitions to various multilobed morphologies occur, including trilobed and pyramid- or hexalobe-like shapes [62].

The viscosity contrast λ plays a dominant role in governing RBC dynamical regimes. Low values of λ favor swinging or tank-treading motion, whereas high values promote rolling, stomatocytic shapes, and polylobed morphologies. Numerical studies suggest that this transition occurs near $\lambda \approx 3$, although a comprehensive characterization of this threshold remains incomplete. More generally, the viscosity ratio regulates RBC dynamics by suppressing both deformation and membrane circulation (i.e., tank-treading), while simultaneously shifting shear-controlled transition points. For instance, increasing λ causes the onset of rolling to occur at lower applied shear stresses [65].

As mentioned earlier, the transition from discocyte to stomatocyte is driven by a buckling instability. The compressive and extensional stresses responsible for this transition arise from the elongational component of the shear flow. When a discocyte-shaped RBC is subjected solely to extensional deformation, for example in an optical-tweezer-like setup, the cell retains its symmetry and does not transition toward a stomatocyte morphology. In contrast, when a discocyte RBC is compressed such that its diameter is reduced from approximately $8\,\mu$m to $6.3\,\mu$m, the cell buckles and adopts a stomatocyte geometry [65].Figure 13 shows the full phase space of a RBC in unbounded shear flow.

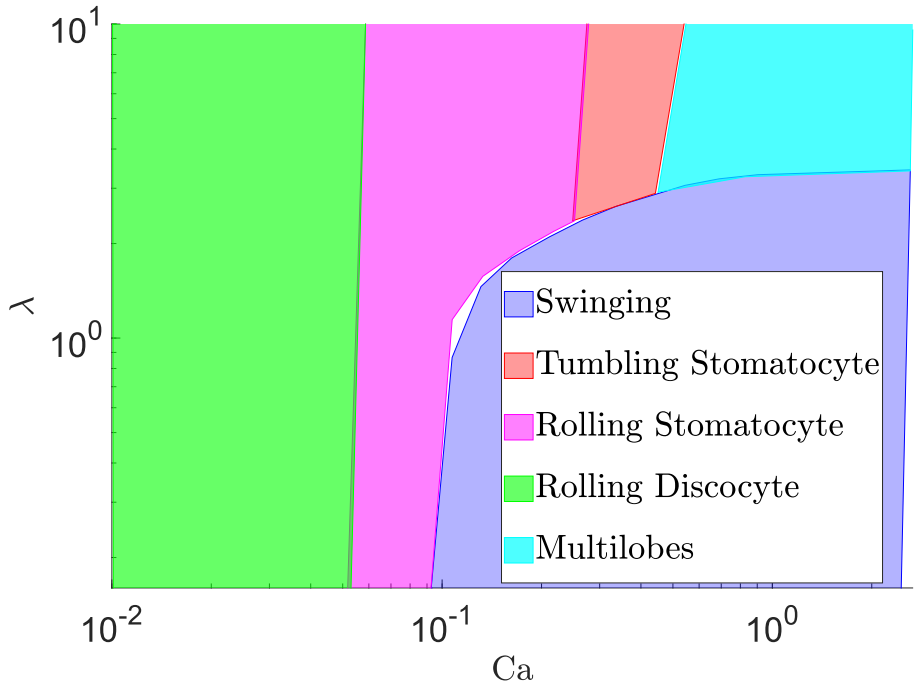

Figure 13: A phase space representation for mode of motions of a vesicle with reduced volume $v = 0.65$. The x-axis is the Ca number and y-axis is the viscosity contrast. Data is from [65]. For the specific three dimensional modes which are not shown in Figure 10, reader is referred to original paper.

2.2.2 Lift Force on Red Blood Cells, Vesicles and Capsules

So far, the different morphologies and dynamical phases of vesicles, capsules, and RBCs in unbounded shear flow have been discussed. This configuration is among the simplest settings in which one can study a deformable entity interacting with a flow. A natural next step is to introduce boundaries by placing one or more walls in the system, thereby making the flow semi-bounded or fully bounded. It is well known that bounding walls alter the characteristics of Stokes flow; for example, they modify the decay of hydrodynamic fields generated by a point force applied near a wall. This adds further complexity, but also brings the model closer to realistic conditions, since blood flow typically occurs in bounded vessels. Wall effects can be neglected when an RBC is sufficiently far from boundaries, for instance when it is located near the centerline of a wide channel. In what follows, the wall-induced motion and the associated lift forces acting on vesicles and RBCs are discussed.

Hydrodynamic lift forces in blood flow and soft-matter flows can arise even in the Stokes limit, where the Reynolds number is vanishingly small. A key feature of this regime is the reversibility of the Stokes equations under time reversal. This symmetry strongly constrains particle dynamics: in the absence of inertia, a neutrally buoyant rigid sphere exhibits no cross-

stream migration, and thus no viscous lift force acts on it. Consequently, the distinction between rigid and deformable particles becomes crucial. Soft biological entities, such as vesicles, can overcome this constraint because they deform under flow stresses. Flow-induced deformation introduces an upstream–downstream (fore–aft) asymmetry, which breaks the relevant symmetry and renders the overall particle–flow system effectively non-reversible. This asymmetry produces a net transverse force that drives non-inertial, viscosity-dominated migration. This phenomenon is broadly known as *viscous lift*, and its specific form depends on the mechanism by which the symmetry breaking is induced [40, 142, 154].

The critical symmetry that must be broken is the upstream–downstream (fore–aft) symmetry. In an unbounded shear flow, the combined configuration (particle plus flow) can retain point symmetry about the particle center, and this symmetry must be lost for a net lift to occur [40]. In bounded systems, the required asymmetry typically arises either from hydrodynamic interaction with the wall or from spatially varying shear in the imposed flow. The resulting transverse force is referred to as the *lift force* and is a direct consequence of this asymmetry. Note that in an unbounded shear flow, deformation alone does not necessarily break fore–aft symmetry; an important exception occurs for vesicles with low reduced volume at sufficiently large Ca, where a symmetry-breaking mode known as *parity breaking* can arise [134].

In such symmetry-breaking situations, the lift force can be obtained by integrating the hydrodynamic stress over the particle membrane. More specifically, the net force originates from an asymmetric pressure field, particularly in the region of the membrane facing the wall. Although the Stokes equations governing the surrounding flow are linear, the coupled problem is a nonlinear free-boundary problem because the particle shape is not known *a priori*; instead, it adapts continuously to hydrodynamic stresses while satisfying internal constraints such as bending elasticity and membrane inextensibility [2].

While viscous lift arises from purely viscous stresses and requires deformability to overcome the reversibility of Stokes flow, lift forces can also be generated by fluid inertia [40]. This inertial mechanism, known as *inertial lift*, which results from inertial corrections to the Stokes equations and becomes relevant at finite Reynolds number. Segré–Silberberg is one example phenomenon for the rigid spheres flowing in a pipe, where inertial effects are present. In this setting, the particles migrates to a certain circular annulus around the pipe center. Unlike viscous lift, the inertial lift can act on rigid spheres [162].

As mentioned earlier, the analytical treatment of a rigid ellipsoid in shear flow dates back to Jeffery [103]. Building on this classical solution, the KS model was developed to describe a tank-treading ellipsoid in shear flow [204]. One of the earliest analytical treatments of lift on a tank-treading ellipsoid near a wall, based on the KS framework, is due to Olla [162]. Olla's

analysis predicts that the lift force decays with wall distance h as $1/h^2$. For vesicles sufficiently far from the wall, both analytical and numerical studies typically recover this far-field scaling. The corresponding lift-induced migration velocity scales as

$$u_{\text{lift}} \sim \dot{\gamma} \frac{R_0^3}{h^2}, \tag{19}$$

where R_0 is an effective vesicle radius, h is the distance between the vesicle center of mass and the wall, and $\dot{\gamma}$ is the shear rate. The first experimental measurements of lift in this regime quantitatively confirmed the above far-field scaling [2].

It is worth noting that, just as the KS model has limitations (e.g., in predicting shear-rate-dependent transitions and other effects), Olla's model can also deviate from numerical results even when the vesicle is not extremely close to the wall [40]. In particular, for vesicles adhering to a wall—where deformations are large—experiments report lift forces that differ by orders of magnitude from Olla's far-field theory [120]. In such near-wall situations, lubrication effects become important, and lubrication-based models are required to rationalize the discrepancy [192]. In the near-wall regime, the lift force typically scales quadratically with the shear rate (i.e., $\sim \dot{\gamma}^2$), and its dependence on wall distance is often steeper than h^{-2}, commonly written as h^{α} with $\alpha < -2$ [2, 40, 196].

The mechanism of migration originates from long-range hydrodynamic interactions between the particle and the wall. A force- and torque-free particle in Stokes flow generates a disturbance field that, in the far field, is dominated by a force dipole represented by the stresslet. For a deformable particle, migration arises from the interaction between this stresslet and its hydrodynamic image in the wall. For a non-deformable sphere, the relevant stresslet contribution vanishes, whereas deformation renders it non-zero and thereby induces a lift velocity [202]. If the wall is located at $z = 0$, an asymptotic estimate for the wall-normal migration velocity reads

$$u_L \sim -\frac{9 S_{zz}}{64\pi\eta\, h^2}, \tag{20}$$

where S_{zz} is the wall-normal component of the stresslet, η is the viscosity, and h is the distance from the vesicle center of mass to the wall. This $1/h^2$ scaling is consistently reported in theoretical [162], numerical [137], and experimental [2, 40] studies for deformable particles sufficiently far from the wall.

For a tank-treading vesicle in shear flow near a wall, the vesicle maintains a well-defined orientation relative to the flow direction, characterized by an inclination angle θ between its longest axis and the flow direction, together with a membrane tank-treading motion [84].

In both experiments and simulations, a common approach is to infer lift by balancing it

against an opposing force that pushes the vesicle toward the wall, such as adhesion or sedimentation. When a vesicle is initially in contact with the wall, increasing the shear rate $\dot{\gamma}$ excites tank-treading, generates lift, and can ultimately detach the vesicle once lift overcomes adhesion or sedimentation. During the unbinding transition, the inclination angle typically increases rapidly. Once the vesicle is sufficiently far from the substrate, the inclination angle approaches a limiting value that is often approximately independent of $\dot{\gamma}$. This behavior is consistent with a torque balance: both the shear-flow torque and the tank-treading-induced torque scale with $\dot{\gamma}$, yielding a shear-rate-independent steady tilt [2, 84].

Near the onset of unbinding, vesicle shapes can be strongly deformed. The wall-induced pressure field generates an additional torque that tends to prevent the inclination angle from reaching its unbounded-flow value, effectively forcing the vesicle to align more parallel to the wall [84]. As the vesicle migrates away from the wall, wall effects on both shape and inclination diminish, and at distances larger than approximately one vesicle radius the vesicle behaves essentially as in an unbounded flow [2, 135].

The limiting inclination angle θ, as well as the transient dynamics leading to it, depends on the reduced volume v. Experimental and numerical results indicate that the lift force can be written in the form $F_L \sim f(1-v)$, where $f(1-v)$ is a monotonically decreasing function of v. Equivalently, decreasing v (i.e., deflating the vesicle) increases lift [2, 137]. This trend reflects the relation between viscous lift and deformability: deflation increases the ability of a vesicle to deform under shear, enhancing the fore–aft asymmetry required for lift and thereby increasing migration velocity. In the limit $v \to 1$, deformability vanishes and the lift force tends to zero.

In the vicinity of a wall, vesicle motion differs from that in unbounded shear flow and typically consists of a combination of sliding and tank-treading along the wall. Early experiments reported that the ratio of tank-treading speed to translational speed is approximately 0.5 [2].

For a vesicle tank-treading near a wall in a semi-bounded shear flow, the lift force decreases significantly as the viscosity contrast λ increases. Increasing internal viscosity generally reduces deformation (for fixed v), thereby reducing the fore–aft asymmetry and consequently decreasing the lift force [84].

In a fully bounded shear flow, multiple stable terminal positions can exist for a vesicle released near one of the walls. Depending on the viscosity contrast λ, the vesicle may migrate toward the channel centerline or reach an off-center equilibrium position. At low viscosity contrasts (i.e., below the transition from tank-treading to tumbling), vesicles typically migrate toward the centerline, largely independent of initial conditions. In contrast, above the critical viscosity contrast where vesicles tumble in unbounded shear flow, two stable configurations

can coexist: a centered terminal state and an off-centered terminal state, depending on initial conditions. The off-centered solution is associated with flow alignment near the wall. The migration scenario is governed by a competition between wall-induced lift and an "anti-lift" associated with flow alignment. In particular, when the inclination angle becomes negative, the wall-induced lift can change sign [152].

Another mechanism that generates lift is the presence of velocity gradients in the imposed flow. In flows with non-uniform shear rate, such as Poiseuille flow, deformable particles undergo non-inertial cross-stream migration even in the absence of wall interactions. This is referred to as *shear-gradient-induced viscous lift*. A key distinction from wall-induced lift is that migration persists without hydrodynamic wall effects; it is a purely bulk mechanism driven by nonlinear shear gradients [137, 142].

In the Stokes-flow regime, this migration results from the combined effects of particle deformability and the curvature of the imposed velocity profile. Because the shear rate varies across the particle size, the hydrodynamic stresses acting on the upstream and downstream portions of the membrane are not identical. This produces an asymmetric deformation pattern along the flow direction and makes a net lift force possible [40, 149]. By contrast, a neutrally buoyant rigid particle does not undergo lateral migration in an unbounded flow solely due to an uneven shear profile in the Stokes limit.

In the small-deformation limit (i.e., weak departures from sphericity), for high reduced volumes (i.e., $v \approx 1$) and unity viscosity contrast (i.e., $\lambda = 1$), one can expand the Stokes equations and boundary conditions in a power series of a small parameter that quantifies the deviation from a sphere. A convenient choice is the excess area, denoted by Γ below. This perturbative framework yields analytical expressions for the lift velocity induced by a wall and by a shear gradient. The resulting asymptotic formulas show good agreement with direct numerical simulations and experiments in the corresponding parameter range [142]:

$$u_{\text{wall}} = \frac{69\,\dot{\gamma}\,R_0^3}{448\,h^2}\sqrt{30\Gamma}\Big[1 - 2.36\Gamma + 19.05\Gamma^2 - 180.2\Gamma^3 + 1754\Gamma^4 - 17021\Gamma^5 + O(\Gamma^6)\Big], \tag{21}$$

$$u_{\text{shear-grad}} = -\frac{\alpha R_0^2}{2}\sqrt{\frac{\Gamma}{30}}\Big[1 - 10.019\Gamma + 104.92\Gamma^2 + O(\Gamma^3)\Big], \tag{22}$$

where Γ is the excess area, h is the distance between the vesicle centroid and the wall, $\dot{\gamma}$ is the local shear rate, and α is the curvature of the Poiseuille profile.

When the flow is confined by walls, both wall-induced lift and shear-gradient-induced lift may act simultaneously, and their interplay can substantially modify migration. In a bounded

Poiseuille flow, this competition leads to a nontrivial migration law: the lift velocity is often found to scale as $u_L \sim \dot{\gamma}(h)/h$, where $\dot{\gamma}(h)$ is the local shear rate and h is measured with respect to the nearest wall. This scaling differs from the far-field expectation in simple shear flow, $u_L \sim \dot{\gamma}/h^2$, and indicates that wall-induced effects can be strongly modulated by flow curvature in confined geometries [137].

As discussed earlier, increasing the viscosity contrast λ can drive a tank-treading vesicle into the tumbling regime. In tumbling, the vesicle flips in a manner close to rigid-body rotation, with relatively small shape deformation. In this regime, the fore–aft symmetry is effectively preserved over a cycle, and the net lift over one full rotation is strongly reduced; even when weak deformations are present, the lateral contributions tend to cancel over a period [137].For a broad overview of lift forces in different configurations, the reader is referred to the recent review [40].

In an unbounded Poiseuille flow, a vesicle released away from the centerline (i.e., away from the point where the shear rate vanishes at the maximum of the parabolic profile) migrates laterally toward the centerline, where the migration velocity eventually vanishes and the vesicle typically adopts a symmetric parachute-like shape. Figure 10(e) shows such a configuration. During its migration, the vesicle may transiently exhibit shapes that do not occur in unbounded shear flow [149]. Migration in this setting is possible because the shear rate varies across the vesicle size; hence, the curvature of the Poiseuille profile plays an essential role. The migration velocity increases with the curvature α of the parabolic profile [149]. In an unbounded Poiseuille flow, the migration speed is controlled primarily by α, rather than by the maximum velocity or the overall width of the profile. Physically, α sets the stress imbalance between the two sides of the vesicle. This behavior contrasts with wall-induced lift, which is a strongly nonlinear function of wall distance (often scaling as $1/h^2$ in the far field). In an unbounded Poiseuille flow, by contrast, the lift generated by the bulk shear gradient can be approximately constant along streamlines until the vesicle approaches the centerline and transitions to a symmetric parachute shape [149].

As the vesicle migrates toward the centerline, its shape typically evolves from an initially ellipsoidal (or otherwise asymmetric) configuration to the final symmetric parachute shape. A commonly observed intermediate state is the *slipper* shape: the vesicle adopts a tilted configuration relative to the flow direction and the membrane tank-treads. Figure 10(f) shows such a configuration. As it approaches the centerline, the shear-rate difference between the "upper" and "lower" sides of the vesicle diminishes, and the vesicle relaxes to a symmetric parachute configuration at the profile maximum [149].

In three-dimensional Poiseuille flow, the range of steady shapes is broader than the slip-

per/parachute dichotomy. Depending on Ca and other control parameters, symmetric shapes such as parachute-, bullet-, or rocket-like morphologies can emerge, while non-symmetric steady states include slipper- and croissant-like shapes. Figure 10(e-g) shows parachute, slipper and bullet shapes. These stationary morphologies and migration scenarios reflect a competition between flow-induced deformation and the elastic bending energy of the membrane. The spontaneous symmetry breaking that leads to off-center non-symmetric shapes arises because the local shear rate varies with distance from the centerline: as the vesicle moves laterally, it continuously adapts its shape to the local shear, which can sustain an asymmetric configuration and thereby a lateral drift [140, 143].

In an unbounded Poiseuille flow, for relatively high reduced volume (i.e., $v = 0.9$) and unit viscosity contrast ($\lambda = 1$), the vesicle dynamics exhibit a well-defined and robust scenario. For sufficiently large capillary numbers (i.e., ($Ca \geq 40$), irrespective of the initial position or shape, the vesicle migrates toward the axis of the Poiseuille flow and eventually adopts an axisymmetric parachute shape. As discussed earlier, the migration velocity induced by shear gradients depends primarily on the curvature of the velocity profile, α. Consequently, during most of its migration, the vesicle experiences an approximately constant lateral lift velocity until it reaches a distance of the order of a few vesicle diameters from the centerline. Throughout this migration phase, the vesicle tank-treads and typically assumes a tilted slipper-like configuration. Upon approaching the vicinity of the flow axis (within a few vesicle radii), the migration velocity smoothly decays to zero, and the vesicle relaxes into a symmetric parachute shape at the centerline [136, 137, 139, 149].

When the capillary number is reduced to an intermediate range (approximately $15 \leq Ca \leq 40$), migration toward the flow axis still occurs; however, the final steady shape at the centerline is no longer a parachute. Instead, the vesicle adopts a croissant-like morphology. This transition reflects the fact that, at lower Ca, hydrodynamic stresses are insufficient to overcome the bending resistance required to sustain a fully axisymmetric parachute shape [143]. Upon further reduction of the capillary number (i.e., $Ca \leq 15$), the croissant shape gives way to a slipper configuration. In this low-Ca regime, the vesicle no longer migrates to the axis of the flow but instead reaches an off-centered equilibrium position. The final lateral position depends sensitively on Ca, and as Ca decreases below unity, the vesicle remains in a slipper state while the distance between its center of mass and the flow axis increases [139].

Under otherwise identical conditions but with increased viscosity contrast (e.g., $\lambda = 5$), the migration scenario changes qualitatively. At sufficiently large capillary numbers (e.g., $Ca \geq 10$), vesicles initially placed far from the centerline may migrate away from the axis rather than toward it. In this regime, the final state becomes a strong function of the initial position and shape. For instance, for $v = 0.9$, $\lambda = 4$, and $Ca = 100$, multiple migration directions and mul-

tiple steady shapes can coexist [143]. This behavior is referred to as *metastability*, indicating the coexistence of distinct stable solutions for identical control parameters but different initial conditions. The viscosity contrast thus introduces additional complexity, leading to inward or outward migration and coexistence regions between parachute and slipper shapes. From a symmetry perspective, the transition from parachute to croissant corresponds to the loss of full axial symmetry; the croissant shape retains only two mirror symmetries. The subsequent transition from croissant to slipper breaks one of these mirror symmetries, leaving a single symmetry plane.

In bounded Poiseuille flow, an additional governing parameter emerges: the confinement ratio, defined as $C_n = R_0/W$ for planar channels and $C_n = R_0/R$ for cylindrical tubes. The metastability and the rich structure of the vesicle dynamical "periodic table" persist under confinement. In this context, transitions between different states occur through successive losses of stability of a given configuration, giving rise to a hierarchy of dynamical modes connected by bifurcations in phase space [131].

Experiments designed to mimic physiological conditions in human venules—where the confinement level, shear rate, and viscosity contrast are representative and $\lambda \approx 1$—show that vesicles with high reduced volume typically adopt a parachute shape and center themselves within the channel. Under the same conditions, but for reduced volumes comparable to that of red blood cells, vesicles preferentially assume either a parachute or a slipper shape depending on the shear rate. At high shear rates, the parachute configuration dominates, whereas at lower shear rates the slipper shape becomes stable. The parachute mode resembles rigid-body-like motion, with little or no tank-treading of the membrane. Nevertheless, due to the three-dimensional structure of the vesicle, a finite lag exists between the local Poiseuille flow velocity and the translational velocity of the vesicle center of mass. By adopting either a slipper or parachute configuration, the vesicle effectively minimizes this lag. The slipper shape is favored at lower reduced volumes and lower Ca because membrane tank-treading enhances internal dissipation, thereby reducing the velocity lag [148].

Finally, bounded Poiseuille flow gives rise to dynamical states that have no counterpart in unbounded geometries. Notably, swirling and snaking motions appear as oscillatory dynamics characterized by limit cycles, distinct from stationary states such as parachute or slipper configurations. Swirling corresponds to a spontaneous transition from straight axial motion to a highly stable, complex trajectory: the vesicle follows a helical path centered around the Poiseuille axis, maintaining a fixed radial distance of its center of mass from the channel center. In this mode, the vesicle adopts a steady deformed shape that both rolls and spins about the flow direction. In contrast, the three-dimensional snaking motion is synchronized with periodic shape deformations of the vesicle. Both swirling and snaking emerge from instabilities in phase space induced by parameter variations and crucially require confinement. These modes are

typically observed at low confinement levels for deflated vesicles (i.e., $C_n < 0.5$ and $v < 0.8$) [150].

Finally, in the context of microfluidic applications, flows in rectangular and square channels are particularly relevant. In experimental settings characterized by high confinement and large reduced volume, vesicles typically assume parachute- or bullet-like shapes. As discussed earlier, these shapes are axisymmetric. The emergence of croissant-like shapes is primarily attributed to asymmetries in the channel cross-section, for instance in rectangular channels. Such geometric asymmetry induces an asymmetric stress distribution on the vesicle membrane, breaking additional symmetries and thereby stabilizing distinct non-axisymmetric shapes [136].

For a comprehensive phase space of vesicle dynamics at unit viscosity contrast and high reduced volume, the reader is referred to [143]. Corresponding phase diagrams for higher viscosity contrast ($\lambda = 5$) and low reduced volume can be found in [131].

The seminal experimental work on red blood cell (RBC) deformation in capillaries is due to Skalak [203], who demonstrated that RBCs flowing in microcapillaries exhibit a wide variety of shapes, including symmetric parachute configurations and asymmetric slipper shapes. Similar to vesicles, slipper-shaped RBCs are typically off-centered. In bounded Poiseuille flow, RBCs display a rich set of dynamical modes, including parachute, slipper, snaking, and tumbling motions. At low flow rates, RBCs may largely preserve their native biconcave (discocyte) shape, particularly during snaking and tumbling. In contrast, other modes involve significant deformation. At sufficiently high shear rates, multilobed morphologies can also emerge, especially during tumbling. Transitions between these shapes and dynamical modes are governed by the interplay between flow strength, confinement, and viscosity contrast.

Recent phase diagrams elucidating the combined effects of flow strength, confinement, and mechanical properties of RBCs can be found in [69]. The specific role of viscosity contrast and the associated phase behavior are discussed in detail in [58].

At high capillary numbers, RBCs, similarly to vesicles, adopt highly deformed and symmetric parachute shapes. As the flow strength decreases, RBCs typically transition from this strongly deformed parachute state toward less deformed and more dynamically active configurations. For example, a reduction in Ca often induces a parachute-to-slipper transition. Further decrease in Ca leads to a loss of stable tank-treading and the onset of tumbling motion. In the slipper state, the membrane tank-treads steadily; however, at sufficiently low flow strengths, tank-treading can no longer be sustained, and the RBC tumbles. Tumbling in bounded Poiseuille flow is particularly relevant for large internal viscosities and strong flow curvature. In such regimes, the vesicle or RBC effectively behaves as if it were placed in an

unbounded shear flow, where the Keller–Skalak (KS) model provides a reasonable description [154]. For RBCs, tumbling is commonly observed in phase spaces corresponding to moderate confinement. At very low capillary numbers, tumbling motion may further evolve into snaking dynamics.

An increase in viscosity contrast λ at fixed Ca generally suppresses membrane tank-treading and promotes a transition from slipper to tumbling motion. It also reduces the region of parameter space in which parachute shapes are stable, since stronger hydrodynamic stresses are required to deform an RBC into a parachute configuration when the internal viscosity is higher. For otherwise identical conditions, larger λ typically corresponds to lower membrane tension.

Strong confinement forces RBCs into a parachute shape through a mechanism similar to that observed for vesicles [136]. The cylindrical channel geometry makes conformity to the wall curvature energetically unfavorable for slipper shapes. At even higher confinement levels, the parachute shape transitions to a bullet shape, in which the rear-end convexity is lost and replaced by concavity. Lowering the confinement effectively increases the curvature of the Poiseuille flow. When the curvature is sufficiently large, the flow locally mimics an unbounded shear flow, and tumbling and slipper modes become relevant in these confinement regimes.

In simple shear flow, an RBC can either tumble or tank-tread, and in both cases its motion relies on the cell maintaining fore–aft symmetry. After a 2π rotation, a tumbling RBC returns to an equivalent configuration, rendering the motion mechanically stable [62]. In Poiseuille flow, however, the velocity profile is curved rather than linear, so different parts of the cell experience different local shear rates. This curvature bends the RBC toward the faster-flowing side, breaking the symmetry required for tumbling. If the cell attempted a full flip, its front part would point upstream, which is hydrodynamically unstable. As a result, regular tumbling is no longer possible. Instead, the cell adopts a compromise state: it migrates slightly off-center, maintains a steady but asymmetric slipper shape, and exhibits membrane rotation even at shear rates or viscosity contrasts for which tank-treading would not occur in simple shear flow [78].

The RBC shapes observed in bounded and unbounded Poiseuille flow form a hierarchy of stable and metastable configurations connected through different types of phase transitions. An energy-based argument, focusing on the minimization of energy expenditure and flow efficiency, has been developed for vesicles [139, 153] and can be extended to RBCs as well. The equilibrium radial position of the RBC centroid correlates strongly with the energy dissipated and stored in the membrane. Each shape corresponds to a distinct level of dissipation and elastic energy storage. The non–tank-treading parachute shape, which allows RBCs to approach the channel axis closely, exhibits the highest energy expenditure due to the membrane load required to maintain this highly deformed and stationary configuration. In contrast, tank-treading shapes

are associated with off-axis migration and display the lowest energy expenditure among the stable shapes. This efficiency arises because the tank-treading configuration has the smallest projected area perpendicular to the flow, thereby minimizing fluid drag and maximizing the flow rate, which is inversely proportional to flow resistance. Consequently, the equilibrium position and shape adopted by an RBC are fundamentally determined by the configuration that minimizes a suitable measure of energy dissipation [215].

Phase spaces for RBC dynamics at different capillary numbers and confinement ratios in bounded Poiseuille flows can be found in [69]. Extensions of these studies that incorporate viscosity contrast are reported in [58]. Phase diagrams relevant to microchannel geometries are presented in [70]. For energy-based arguments and considerations of flow efficiency, the reader is referred to [148, 153, 163]. For studies of migration velocity and lift forces acting on RBCs, see [80, 81].

Having described the motion and dynamics of single cells in both bounded and unbounded canonical flows (shear and Poiseuille), as well as the lift forces induced by shear gradients and confining walls, the discussion now turns to pairwise hydrodynamic interactions between red blood cells and vesicles. These interactions provide the foundation for understanding more complex, crowded configurations that more realistically represent blood flow in vessels.

2.2.3 Pairwise Hydrodynamic Interactions Between Blood Agonists and Shear-Induced Diffusion

In simple shear flow, the interaction between two rigid particles is reversible due to the symmetry of the governing equations. The particles are displaced during the interaction but eventually return to their original trajectories once they are sufficiently far apart. In contrast, interactions between deformable particles are irreversible and lead to a net lateral displacement of their trajectories, which in turn contributes to shear-induced diffusion in the suspension. For vesicles, the lateral displacement Δy decreases monotonically with the initial lateral separation and becomes negligible once the distance exceeds approximately two vesicle radii [209]. This decay can be accurately captured using a simple theoretical model based on the established scaling law for the lateral drift, or lift force, experienced by a vesicle in the vicinity of a wall. The magnitude of Δy depends only weakly on the reduced area Δ, which characterizes vesicle deflation, and on the viscosity contrast λ between the internal and external fluids, provided the vesicles remain in the tank-treading regime. In addition to the shear-gradient direction, vesicles also experience a deflection Δz in the vorticity direction, although this displacement is typically an order of magnitude smaller than Δy. Numerical simulations further reveal a narrow range of initial separations for which a weak hydrodynamic attraction occurs in the vorticity direction [147].

For capsules in simple shear flow, pairwise interactions likewise result in irreversible trajectory shifts, quantified by the displacements Δy in the shear plane and Δz in the vorticity direction. When the initial offset in the vorticity direction is zero (i.e., $\Delta z^0 = 0$), the interaction occurs entirely within the shear plane. During the close-contact stage of the encounter, capsules undergo substantial shape deformation and experience elevated elastic tensions in their membranes. Owing to the rapid elastic relaxation of the membrane, the final cross-stream displacement Δy is smaller than that observed for liquid droplets under comparable conditions. When the capsules are initially separated in the vorticity direction (i.e., $\Delta z^0 \neq 0$), the resulting deflection occurs predominantly along that direction and is characterized by Δz. For sufficiently large initial vorticity offsets, Δz can even become negative, meaning that the capsules are displaced toward closer streamlines after the interaction. This counterintuitive behavior, in contrast to the response of liquid drops, originates from the elastic nature of the capsule membrane [23].

As commonly encountered in blood flow, pairwise interactions between RBCs and platelets in shear flow play a central role in platelet margination. Numerical simulations of isolated RBC–platelet encounters reveal distinct dynamical behaviors that depend on the RBC mode of motion, the initial separation between the particles, and the proximity of a confining wall.

Two qualitatively different interaction scenarios are observed, depending on the initial lateral separation Δy^0 between the centers of mass of the RBC and the platelet. In a crossing event, the platelet approaches the RBC, rolls over its surface, and continues along the same streamline, producing an irreversible trajectory shift. In contrast, in a turning event, the platelet veers away before close contact is established, indicating a longer-range interaction mediated by the closed streamlines generated by the RBC. These two behaviors are separated by a critical initial separation $\Delta^0_{y,\mathrm{crit}}$: crossings occur for $\Delta y^0 > \Delta^0_{y,\mathrm{crit}}$, whereas turnings occur for $\Delta y^0 < \Delta^0_{y,\mathrm{crit}}$ [14, 35].

The value of $\Delta^0_{y,\mathrm{crit}}$ and the nature of the interaction depend strongly on the dynamical state of the RBC. In the tank-treading regime, which occurs at high shear rates and is characterized by a strongly deformed RBC, the critical separation is relatively small, typically $\Delta^0_{y,\mathrm{crit}} \approx 0.6$–$0.7\,\mu$m. In this regime, the probability of turning or crossing is largely insensitive to the initial orientation difference, while remaining strongly dependent on Δy^0 [14].

In the tumbling regime, characteristic of low shear rates where the RBC behaves almost rigidly, the critical separation is significantly larger. Crossing events only occur for $\Delta^0_y \sim 2.0\,\mu$m, implying that turning interactions dominate in this regime. Moreover, tumbling motion induces stronger mixing and greater variability in platelet trajectories: the final platelet displacement

after the interaction becomes highly sensitive to the initial orientation, in contrast to the tank-treading case [14].

In blood flow, the size of an RBC is considerably larger than that of a platelet. Therefore, during interactions between the two, RBCs are only weakly displaced. This effectively leads to the margination of platelets. In interactions between equal-sized rigid and soft particles, the following rule of thumb applies for the displacements occurring after collision: $\Delta_{sr} < \Delta_{ss}$ and $\Delta_{rr} < \Delta_{rs}$, where, for example, the subscript sr denotes a collision between a soft and a rigid particle. This ordering implies that a rigid particle undergoes a larger net lateral deflection than a soft particle during an sr encounter, establishing a fundamental asymmetry between the two species. In a dilute configuration (i.e., when the volume fraction is lower than the physiological hematocrit) in shear flow containing rigid and soft particles, collisions effectively generate clustering of particles in different regions of the slit. Rigid particles marginate toward the wall, whereas soft particles accumulate near the centerline. Including the effect of bounding walls only slightly alters such clustering. Therefore, the dominant mechanism responsible for margination is the enhanced displacement of stiff particles in heterogeneous collisions. At higher volume fractions, which are relevant for microcirculatory blood flow (i.e., where confinement also matches physiological conditions), the contributions of heterogeneous collisions and differential migration become comparable, indicating that both effects play an important role in segregation [89].

In blood flow, interactions between two RBCs are also important. Two interacting RBCs in unbounded shear flow generate irreversible displacements in their trajectories. Up to the semi-dilute limit, where pairwise interactions prevail, the interaction of two RBCs provides fundamental information on shear-induced diffusion, since effects are additive in this regime. The details of shear-induced diffusion will be given in the upcoming sections. However, when two deformable entities of the same size, such as RBCs, encounter each other in unbounded shear flow, they typically follow irreversible trajectories after collision. The displacement occurs both in the shear direction and in the vorticity direction. Typically, the displacement in the shear direction is much larger than that in the vorticity direction [101].

In confined pressure-driven flow (Poiseuille flow), hydrodynamic interactions between deformable particles lead to their attraction and the formation of stable pairs or clusters. This phenomenon is purely hydrodynamic in origin and must be distinguished from rouleaux formation, which is mediated by plasma proteins such as fibrinogen [130, 146]. In a confined flow, two deformable entities may either attract or repel each other: repulsion typically dominates at short interparticle separations, whereas attraction emerges at larger distances. This attraction and repulsion is mediated by formation of voritices between the deformable entities, which is called as bolus. Since fluid flow is at low-Re number regime, these vortices are deterministic.

The corresponding phase diagram exhibits a rich structure, including the coexistence of multiple stationary solutions. For a fixed degree of confinement, at least two stable branches of stationary interdistance may exist, and the branch approached by a given pair depends exclusively on its initial configuration. An unstable branch lies between the two stable ones [130].

The core mechanism dictating the equilibrium interdistance is the flow field perturbation created by the deformable entities. A single vesicle in an unbounded Poiseuille flow creates a flow perturbation characterized by two counter-rotating vortices [146]. Depending on the position of the vortices (i.e., leading- and trailing-edge vortices), a second vesicle will be captured by one of them. In bounded Poiseuille flow, these vortices converge to recirculation zones of fluid located between the cells. At low confinement, this quasi-circular structure of flow is referred to as a bolus [87].

Under weak confinement (for example, a channel width of $W = 20R_\mathrm{v}$), a single, unique stationary interdistance is observed, independent of the initial separation or the initial shape of the interacting particles. In this regime, the equilibrium spacing depends only weakly on the degree of confinement. In contrast, under strong confinement the stationary interdistance increases substantially and shows a pronounced dependence on confinement, ranging from approximately $4R_\mathrm{v}$ up to $32R_\mathrm{v}$. For comparison, the corresponding value in weak confinement is typically on the order of $2.5R_\mathrm{v}$. This behavior indicates an effective screening of hydrodynamic interactions by the walls, which reduces the interaction amplitude between the deformable particles [35].

A notable feature of the resulting phase diagram is its universality: the topology obtained for liquid drops closely matches that for vesicles, both qualitatively and, to a large extent, quantitatively. This similarity suggests that the detailed mechanical properties of the suspended objects—whether vesicles with bending-resistant, inextensible membranes or droplets governed by surface tension—play only a secondary role in the pairing mechanism. Instead, the dominant factor is the generic hydrodynamic interaction arising from particle deformability in confined flows [130].

Pairing and clustering are not restricted to bounded geometries. In unbounded flow, vesicles can also form stable clusters when subjected to a parabolic velocity profile. In this case, clustering is mediated solely by hydrodynamic interactions coupled to deformability. Once the cluster size exceeds a critical threshold N^*, vesicles begin to detach from the leading edge of the cluster through a self-regulated process controlled by the reorganization and merger of internal vortices between the front vesicles [146].

In a flow environment containing multiple deformable entities, hydrodynamic collisions re-

sult in net displacements of vesicles or RBCs. When several such entities are initially placed within a narrow region in a shear flow, this region spreads over time due to hydrodynamic collisions. Because these collisions generate irreversible trajectory shifts, particles deviate from their original streamlines, leading to an effective diffusive transport. In blood flow, shear-induced diffusion is balanced by wall effects and lift forces induced by shear gradients. This balance ultimately determines the thickness of the region depleted of cells near the wall, commonly referred to as the cell-free layer, first observed by Poiseuille in 1835.

For suspensions of rigid, non-Brownian spheres in the dilute and semi-dilute regimes, the shear-induced diffusion coefficient follows the scaling

$$D \sim f\,\dot{\gamma} R^2 \phi,$$

where $\dot{\gamma}$ is the shear rate, ϕ is the volume fraction, and R is the characteristic particle radius. In dilute and semi-dilute blood flow, RBC–RBC collisions under shear follow a similar scaling, with ϕ corresponding to the hematocrit. Physically, the factor $\dot{\gamma}\phi$ represents the frequency of pairwise interactions, multiplied by a characteristic spatial scale R^2. Higher shear rates increase the frequency of encounters, while higher concentrations increase the number of available collision partners. This scaling applies to athermal, non-Brownian particles with large Péclet numbers, for which Brownian motion is negligible, and at low Reynolds numbers, where inertial effects can be ignored. The formulation fundamentally assumes that interactions are pairwise and is therefore valid for moderate hematocrit levels (typically $Ht < 30\%$).

Experimentally, in plane Poiseuille flow and for the first time at mid-range concentrations ($\phi < 16\%$), which are relevant to microcirculation under moderate shear rates, the prefactor f was measured to be 1.7 ± 0.1 in the shear direction and 0.07 ± 0.001 in the vorticity direction [90]. This pronounced anisotropy reflects the directional nature of hydrodynamic interactions under shear. More recent simulations performed under pure shear at 15% hematocrit indicate that f depends strongly on the capillary number and is significantly influenced by the mode of motion of RBCs in crowded environments. In the low-Ca regime ($0.01 < Ca < 0.15$), where tumbling dominates, f increases to values in the range 0.25–0.3. As transient modes emerge at intermediate shear rates ($0.2 < Ca < 0.25$), f decreases and exhibits a dip to approximately 0.2–0.25. Upon further increasing the shear rate ($0.4 < Ca < 0.5$), f rises again as tank-treading becomes the dominant mode of motion. The prefactor f is also sensitive to material properties and viscosity contrast: stiffened or hardened RBCs, whether due to increased membrane rigidity or elevated internal viscosity, typically exhibit lower shear-induced diffusion coefficients [180].

Most of the aforementioned studies either consider unbounded domains or terminate their

analysis before wall effects become significant. However, when rigid spheres are placed between bounding walls and subjected to shear flow, the dynamics are strongly altered by confinement. In confined shear flow, hydrodynamic interactions between neighboring particles can reverse their relative motion and prevent direct collisions. This behavior has been observed in platelet–RBC interactions and discussed earlier. For particles of equal size, such as two RBCs, interactions may lead to a reversal of relative motion that effectively avoids collision. In a collective setting, this mechanism suppresses shear-induced diffusion and can drive rigid spheres in confined shear flow to organize into layers. The reversal of relative motion limits large collisional displacements, thereby reducing the effective diffusivity near the wall. The underlying physical mechanism is the reflection of the collision-induced perturbation flow by the wall, which modifies the hydrodynamic interaction between particles [247].

If blood flow takes place in a bounded environment, hydrodynamic layering becomes relevant. In particular, near the vessel walls, RBCs tend to swap their trajectories during encounters and form quasi-ordered layers, which effectively reduces shear-induced diffusion in these regions. This process inherently generates a gradient of shear-induced diffusivity in the wall-normal direction, with markedly lower values close to the wall [199]. Layering effects are not confined to the near-wall region; they also manifest in the bulk flow, leading to a reorganization of the microstructural arrangement of cells and introducing an additional characteristic time scale. This time scale is distinct from, and typically longer than, the one associated with the formation of the cell-free layer (CFL) [61].

With shear-induced diffusion accounted for, all principal hydrodynamic mechanisms governing the formation of the cell-free layer are in place. In summary, deformable entities in bounded flows experience lift forces arising from wall proximity and shear gradients, counteracted by shear-induced diffusion. The balance among these competing effects gives rise to a stable CFL adjacent to the wall. Depending on the shear rate, mechanical properties of the cells, degree of confinement, and viscosity contrast, these deformable entities adopt specific morphologies and execute distinct modes of motion.

There are additional factors relevant to the hydrodynamics of blood flow that fall outside the scope of this thesis but are important in physiological contexts. The walls of human blood vessels are coated with a layer of macromolecules attached to the surface of endothelial cells, commonly referred to as the glycocalyx. Although its thickness is variable, it is often assumed to be on the order of $1\,\mu$m. From a hydrodynamic perspective, this layer behaves like a porous gel that resists flow. Mechanical stresses transmitted through the glycocalyx play a crucial role in mechanotransduction pathways, whereby mechanical forces are converted into biochemical signals within endothelial cells [188]. Red blood cells themselves are also estimated to be covered by a much thinner glycocalyx layer, with a thickness of approximately 6 nm [76].

The vessel wall, together with the glycocalyx layer, effectively repels cells from the wall, generating a size-exclusion effect due to the finite dimensions of blood constituents. This size-exclusion mechanism differs between plane Poiseuille flow and tube flow geometries and contributes to variations in the CFL thickness observed under different flow conditions [61, 188].

In vivo experimental measurements typically report a CFL thickness in the range of 1–1.8 μm for vessel diameters between 10 and 40 μm at a physiological hematocrit of approximately 45% [61, 205]. Several parameters influence the CFL thickness, including the hematocrit level, the capillary number, and the vessel diameter.

2.3 Physical Background : Methods and Models

2.3.1 Fluid Mechanics and Fluid Model

In this thesis, the fluid phase is modeled using an angular-momentum–conserving smoothed dissipative particle dynamics (SDPD) method. Fluid–structure interactions are treated separately using the dissipative particle dynamics (DPD) framework. In this section, the essential features of these methods are summarized and the governing equations of fluid mechanics relevant to blood flow is introduced.

Blood is a complex fluid whose rheological properties cannot, in general, be described by a constant viscosity. Instead, the effective viscosity depends on hydrodynamic variables and, under certain conditions, on the deformation and flow history. At sufficiently small length scales, blood must be modeled by explicitly resolving its constituents, most notably red blood cells (RBCs), and the assumption of a homogeneous continuum fluid breaks down. At these scales, the dynamics of blood consist of the motion of the outer fluid (blood plasma), the inner fluid (the hemoglobin solution enclosed by the RBC membrane), and the deformation and motion of the membrane itself. The membrane responds to mechanical constraints and forces exerted by both the inner and outer fluids. The constitutive modeling of membrane mechanics and associated constraints is discussed in the next section.

Both the inner and outer fluids are governed by the Navier–Stokes equations, which express conservation of linear momentum (Newton's second law) together with mass conservation. Here the derivation of mass conservation is briefly intorduced. Let m denote the total mass of a material volume V. Mass conservation implies

$$\dot{m} = 0, \tag{23}$$

$$\frac{d}{dt}\int_V \rho \, dV = 0, \tag{24}$$

where ρ is the mass density. Transforming the integral to the reference configuration V_0 using the Jacobian determinant J, we obtain

$$\int_{V_0} \frac{d}{dt} (\rho J) \, dV_0 = 0, \tag{25}$$

$$\int_{V_0} \left(\dot{\rho} J + \rho \dot{J} \right) \, dV_0 = 0. \tag{26}$$

Using the identity $\dot{J} = J \nabla \cdot \mathbf{v}$ and transforming back to the current configuration yields

$$\int_V \dot{\rho} \, dV + \int_V \rho \nabla \cdot \mathbf{v} \, dV = 0, \tag{27}$$

$$\int_V (\dot{\rho} + \rho \nabla \cdot \mathbf{v}) \, dV = 0. \tag{28}$$

Since the material volume V is arbitrary, the local form of mass conservation follows as

$$\frac{\partial \rho}{\partial t} + \nabla \cdot (\rho \mathbf{v}) = 0. \tag{29}$$

Equation (23) expresses conservation of mass in its most compact form. Equation (24) represents the same statement applied to a material control volume. Equations (25)–(28) illustrate the application of the Reynolds transport theorem, which allows the time derivative to be moved inside the integral and subsequently transformed back to the current configuration. To this end, the current volume is mapped to the reference configuration, introducing the Jacobian determinant J of the deformation gradient. The time derivative is then applied using the product rule. The time derivative of the Jacobian satisfies the identity $\dot{J} = J \nabla \cdot \mathbf{v}$. In Equation (27), the integrals are transformed back to the current configuration. Equation (28) represents the integral form of mass conservation, where $\dot{\rho}$ denotes the material (substantial) derivative of the density. Finally, Equation (29) gives the local, differential form of mass conservation, obtained from Equation (28) by application of the localization theorem.

To derive the momentum equation, conservation of linear momentum is required. It may be written as

$$\dot{\mathbf{P}} = \mathbf{F}, \tag{30}$$

$$\frac{d}{dt} \int_V \rho \mathbf{v} \, dV = \int_A \mathbf{t} \, dA + \int_V \rho \mathbf{b} \, dV, \tag{31}$$

where $\mathbf{P}$ denotes the total linear momentum of the material volume V, $\mathbf{t}$ is the traction acting on the boundary A, and $\mathbf{b}$ is the body force per unit mass. Using Cauchy's stress theorem, the traction vector is related to the Cauchy stress tensor $\boldsymbol{\sigma}$ as $\mathbf{t} = \boldsymbol{\sigma} \cdot \mathbf{n}$, yielding

$$\frac{d}{dt} \int_V \rho \mathbf{v} \, dV = \int_A \boldsymbol{\sigma} \cdot \mathbf{n} \, dA + \int_V \rho \mathbf{b} \, dV. \tag{32}$$

Application of the divergence theorem converts the surface integral into a volume integral,

$$\frac{d}{dt}\int_V \rho\mathbf{v}\,dV = \int_V \nabla\cdot\boldsymbol{\sigma}\,dV + \int_V \rho\mathbf{b}\,dV. \tag{33}$$

Employing the Reynolds transport theorem to evaluate the time derivative of the momentum integral leads to

$$\int_V \rho\dot{\mathbf{v}}\,dV = \int_V \nabla\cdot\boldsymbol{\sigma}\,dV + \int_V \rho\mathbf{b}\,dV. \tag{34}$$

Rearranging terms gives the integral form of the linear momentum balance,

$$\int_V (\rho\dot{\mathbf{v}} - \nabla\cdot\boldsymbol{\sigma} - \rho\mathbf{b})\,dV = 0. \tag{35}$$

Since the material volume V is arbitrary, application of the localization theorem yields the local form of the momentum balance,

$$\rho\frac{D\mathbf{v}}{Dt} = \nabla\cdot\boldsymbol{\sigma} + \rho\mathbf{b}, \tag{36}$$

which is commonly referred to as Cauchy's equation of motion.

To obtain the Navier–Stokes equations, a constitutive relation relating the stress tensor to the rate of deformation must be specified. For a Newtonian fluid, theoretical and experimental evidence leads to

$$\boldsymbol{\sigma} = -p\mathbf{I} + \eta\left(\nabla\mathbf{v} + (\nabla\mathbf{v})^T\right), \tag{37}$$

where p is the hydrodynamic pressure and η is the dynamic viscosity. For an incompressible fluid, the governing equations for the fluid motion simulated in this thesis reduce to

$$\rho\left(\frac{\partial\mathbf{v}}{\partial t} + \mathbf{v}\cdot\nabla\mathbf{v}\right) = -\nabla p + \eta\nabla^2\mathbf{v} + \rho\mathbf{b}, \tag{38}$$

$$\nabla\cdot\mathbf{v} = 0. \tag{39}$$

Equations (38)–(39) govern the motion of the fluid under the assumption of incompressibility, such that the density ρ remains constant throughout the flow. It is important to emphasize that Equation (38) does not reduce to the Stokes equations, since the convective term $\mathbf{v}\cdot\nabla\mathbf{v}$ is retained and inertial effects may therefore be present. Although the Reynolds number in all simulations presented in this thesis is small ($\mathrm{Re}\approx 1$), the full Navier–Stokes equations are solved throughout.

At the cellular scale, the suspending fluid may be accurately modeled as a Newtonian fluid. Non-Newtonian rheological behavior of blood then emerges from the collective dynamics and deformation of red blood cells interacting with the plasma, rather than from a non-Newtonian

constitutive law at the fluid level. Consequently, the viscosity η appearing in Equation (38) is taken to be constant and independent of the local hydrodynamic state.

Finally the conservation of angular momentum is introduced. Rather than introducing an independent field equation, angular momentum balance imposes a constraint on the Cauchy stress tensor appearing in the linear momentum balance. The angular momentum balance may be written as

$$\dot{\mathbf{L}} = \boldsymbol{\tau}, \tag{40}$$

where $\mathbf{L}$ denotes the total angular momentum of a material volume and $\boldsymbol{\tau}$ the total torque acting on it. In the absence of body couples, application of the angular momentum balance together with the linear momentum balance leads to the condition

$$\boldsymbol{\sigma} = \boldsymbol{\sigma}^T, \tag{41}$$

i.e. the Cauchy stress tensor must be symmetric. A detailed derivation can be found in standard continuum mechanics texts and is omitted here for brevity. This result ensures that the linear momentum balance is compatible with angular momentum conservation. Notably, the constitutive relation for a Newtonian fluid automatically satisfies this symmetry requirement. The implications of angular momentum conservation for the numerical methods employed to solve Equations (39) and (38) are discussed in detail in the subsequent sections of this chapter.

A variety of numerical methods exist to solve the Navier–Stokes equations. Traditional continuum-based approaches, such as finite-volume or finite-element methods, rely on a spatial discretization of the computational domain using a mesh. While highly successful for many applications, such methods become challenging for particulate flows involving large deformations and continuous rearrangements of suspended objects, as frequent remeshing is required. Blood flow, by its nature, is a particulate flow problem in which cells move, deform, and interact dynamically with the surrounding fluid. Although extensive literature exists on continuum approaches to particulate flows, the need for repeated remeshing motivates the use of mesh-free methods in the present work.

A class of numerical methods, named as immersed boundary methods, solves the fluid flow in an Eulerian grid, and deformable entities are treated as collection of Lagrangian particles. The Lagrangian particles are used to discretize the membrane. The Lagrangian points appears as body force in the Eulerian fluid flow solver, thereby fluid and membrane is coupled.

In this thesis, a particle-based method, smoothed dissipative particle dynamics (SDPD), is employed to solve the fluid equations. Fluid–structure interactions are modeled using dissipa-

tive particle dynamics (DPD). Since SDPD is formulated as an extension of DPD, it is natural to proceed with DPD. DPD is first intorduced in [94].

2.3.2 Dissipative Particle Dynamics (DPD)

Both DPD and SDPD represent the fluid as a collection of N interacting point particles. In DPD, particles interact via a conservative force that controls the equation of state and generates local structure characterized by a radial distribution function, a dissipative force that gives rise to viscous behavior, and a random force that accounts for thermal fluctuations. The dissipative and random forces are constructed to satisfy a fluctuation–dissipation balance, such that the system is thermostatted at a prescribed temperature. The temperature is extracted from the average kinetic energy in accordance with equilibrium statistical mechanics. The total force acting on particle i is therefore given by

$$\mathbf{f}_i^{\mathrm{tot}} = \sum_j \left(\mathbf{F}_{ij}^{\mathrm{C}} + \mathbf{F}_{ij}^{\mathrm{D}} + \mathbf{F}_{ij}^{\mathrm{R}} \right), \tag{42}$$

where the superscripts C, D, and R denote the conservative, dissipative, and random contributions, respectively.

The summation in Equation (42) is restricted to particles within a finite cutoff radius r_C, beyond which the DPD interaction forces vanish. As a result, all interactions are local. Moreover, all DPD forces are pairwise additive and act along the line connecting particle pairs, i.e. in the direction of the relative position vector $\mathbf{r}_{ij}$. Consequently, the forces satisfy Newton's third law exactly, ensuring strict conservation of linear momentum. Since the forces are central, angular momentum is also conserved strictly.

The conservative force between a pair of particles is typically chosen as

$$\mathbf{F}_{ij}^{\mathrm{C}}(r) = a \left(1 - \frac{r}{r_C} \right) \mathbf{e}_{ij}, \qquad r \leq r_C, \tag{43}$$

where $\mathbf{F}_{ij}^{\mathrm{C}}$ denotes the conservative DPD force, a is the interaction strength, $r = |\mathbf{r}_{ij}|$, and $\mathbf{e}_{ij} = \mathbf{r}_{ij}/r_{ij}$ is the unit vector pointing from particle j to particle i. The conservative force controls the local structure of the fluid by inducing a nontrivial radial distribution function. In the absence of conservative interactions, the radial distribution function is uniform.

In addition, the conservative force gives rise to an effective equation of state for the thermodynamic pressure and determines the speed of sound of the DPD fluid. For sufficiently large

number densities ($\rho > 2$), these quantities may be approximated as

$$p = \rho k_B T + \alpha a \rho^2, \tag{44}$$

$$c^2 = k_B T + 2\alpha a \rho, \tag{45}$$

where p is the pressure, T is the temperature, k_B is the Boltzmann constant, and α is a fitting parameter ($\alpha = 0.101 \pm 0.001$ for $\rho > 2$). Details can be found in [236]. Both the pressure and the speed of sound are key parameters in characterizing the effective compressibility of the fluid. A sufficiently large pressure is required to approximate incompressible flow, consistent with the constraint $\nabla \cdot \mathbf{v} = 0$ in Equation (39). The speed of sound determines the rate at which pressure disturbances propagate through the fluid. For incompressible flow, the Mach number $\mathrm{Ma} = v/c$ must remain small, typically $\mathrm{Ma} \leq 0.3$, so that characteristic flow velocities are much smaller than the speed of sound.

Both the pressure and the speed of sound are controlled by the interaction parameter a. This coupling constitutes a limitation of standard DPD, as modifying a simultaneously alters multiple physical properties of the fluid. In particular, achieving a sufficiently incompressible fluid requires choosing a large value of a, which may lead to freezing or ordering artifacts. In practice, such artifacts can be mitigated by increasing the temperature, at the expense of requiring a smaller time step for numerical stability [236].

The dissipative force is given by

$$\mathbf{F}_{ij}^{\mathrm{D}} = -\gamma\, w^{\mathrm{D}}(r)\, (\mathbf{v}_{ij} \cdot \mathbf{e}_{ij})\, \mathbf{e}_{ij}, \tag{46}$$

where γ is the dissipative force coefficient, $\mathbf{v}_{ij} = \mathbf{v}_i - \mathbf{v}_j$ is the relative velocity, and $w^{\mathrm{D}}(r)$ is a distance-dependent weight function. This force dissipates kinetic energy associated with relative particle motion and thereby gives rise to viscous behavior at the continuum level. The viscosity of the DPD fluid depends on the strength of the dissipative interactions, and changing γ while keeping other parameters fixed modifies the effective fluid properties. An approximate expression for the dynamic viscosity is

$$\eta = \frac{2\pi\gamma\rho^2}{15} \int_0^\infty r^4 w^{\mathrm{D}}(r)\, dr, \tag{47}$$

which is valid for sufficiently large densities ($\rho > 2$). Again the details might be found in [236].

Thermal fluctuations are incorporated through a random force,

$$\mathbf{F}_{ij}^{\mathrm{R}} = \sigma\, w^{\mathrm{R}}(r)\, \xi_{ij}\, \delta t^{-1/2}\, \mathbf{e}_{ij}, \tag{48}$$

where σ is the noise amplitude, $w^{\mathrm{R}}(r)$ is the random-force weight function, δt is the integra-

tion time step, and ξ_{ij} is a Gaussian random variable with zero mean and unit variance. The symmetry condition $\xi_{ij} = \xi_{ji}$ ensures exact conservation of linear momentum. Together, the random and dissipative forces satisfy a fluctuation–dissipation balance, maintaining the system at the prescribed temperature.

The random and dissipative forces act together to maintain the system in thermal equilibrium at a prescribed temperature. The random force may be interpreted as a stochastic heat bath that injects energy into the system by inducing random velocity fluctuations, while the dissipative force removes excess kinetic energy through velocity-dependent friction. To ensure that these two mechanisms balance exactly, the fluctuation–dissipation theorem must be satisfied. Consequently, the strengths of the random and dissipative forces, as well as the functional forms of their weighting functions, cannot be chosen independently.

For standard DPD, the required relations are

$$w^{\mathrm{D}}(r) = \left[w^{\mathrm{R}}(r)\right]^2, \tag{49}$$

$$\sigma = \sqrt{2k_B T\gamma}, \tag{50}$$

which guarantee that the system samples the canonical ensemble at temperature T. A derivation of the fluctuation–dissipation relations (Eqs. (49)–(50)) is provided in Appendix A. Although the functional form of the weighting functions is not unique, a commonly adopted choice is

$$w^{\mathrm{D}}(r) = \left(1 - \frac{r}{r_C}\right)^k, \qquad r \le r_C, \tag{51}$$

where k is an exponent that controls the spatial distribution and strength of the dissipative interactions within the cutoff radius.

In combination with the random and dissipative forces, several dynamical properties of the DPD fluid can be estimated analytically. In particular, the self-diffusion coefficient and the Schmidt number, which measures the relative importance of momentum transport compared to mass diffusion, are given by

$$D = \frac{45k_B T}{2\pi\gamma\rho r_C^3}, \tag{52}$$

$$\mathrm{Sc} = \frac{1}{2} + \frac{(2\pi\rho\gamma r_C^4)^2}{70875k_B T}, \tag{53}$$

valid for sufficiently large densities [236]. Once again, the intrinsic limitation of standard DPD becomes apparent: the fluid properties depend explicitly on the model parameters and there are no closed form formulas (i.e, except the approximations given above) to determine transport coefficients.

For typical liquids, the Schmidt number is of order 10^3, whereas standard DPD fluids usually exhibit much smaller values, indicating that mass diffusion dominates over momentum transport. One practical approach to enhance momentum advection is to choose the exponent k of the dissipative weighting function in the range $0 < k < 1$, which increases the effective Schmidt number.

2.3.3 Smoothed Dissipative Particle Dynamics (SDPD)

Smoothed dissipative particle dynamics (SDPD) combines concepts from smoothed particle hydrodynamics (SPH) and DPD. The method solves the Navier–Stokes equations directly in a Lagrangian framework while incorporating thermal fluctuations through DPD-inspired stochastic forces. As a result, an SDPD fluid obeys the Navier–Stokes equations at the continuum level and simultaneously possesses a well-defined finite temperature [47].

The foundation of the SPH discretization lies in the representation of a scalar field using the Dirac delta distribution. For a function $f(\mathbf{x})$,

$$f(\mathbf{x}_0) = \int_V f(\mathbf{x})\delta(\mathbf{x} - \mathbf{x}_0)\, dV, \tag{54}$$

$$f(\mathbf{x}_0) \approx \int_V f(\mathbf{x})W(\mathbf{x}, \mathbf{x}_0, r_h)\, dV, \tag{55}$$

where the Dirac delta distribution is approximated by a smooth kernel function W. The parameter r_h denotes the smoothing length, and the kernel is constructed such that $\lim_{r_h \to 0} W(\mathbf{x}, \mathbf{x}_0, r_h) = \delta(\mathbf{x} - \mathbf{x}_0)$.

The integral approximation in Equation (55) is further discretized by replacing the continuum with a finite set of particles. Each equality introduces a controlled approximation error, yielding

$$f(\mathbf{x}_0) = \int_V f(\mathbf{x})W(\mathbf{x}, \mathbf{x}_0, r_h)\, dV \approx \sum_j f(\mathbf{x}_j)W(\mathbf{x}_j, \mathbf{x}_0, r_h)\frac{m_j}{\rho(\mathbf{x}_j)}, \tag{56}$$

where the summation is restricted to particles within the kernel support and $dV = m_j/\rho(\mathbf{x}_j)$ has been used. As an example, the density at the location $\mathbf{x}_0$ is approximated as

$$\rho(\mathbf{x}_0) = \sum_j m_j W(\mathbf{x}_j, \mathbf{x}_0, r_h). \tag{57}$$

A variety of kernel functions $W(\mathbf{x}, \mathbf{x}_0)$ may be employed within the SPH framework. In this

thesis, the Lucy kernel and its derivative are used,

$$W(\mathbf{x}, \mathbf{x}_0) = W_{ij} = \frac{105}{16\pi r_C^3}\left(1 + 3\frac{r}{r_C}\right)\left(1 - \frac{r}{r_C}\right)^3, \tag{58}$$

$$F(\mathbf{x}, \mathbf{x}_0) = F_{ij} = \frac{315}{4\pi r_C^5}\left(1 - \frac{r}{r_C}\right)^2, \tag{59}$$

where $r = |\mathbf{r}_{ij}|$ and r_C denotes the cutoff radius for SDPD interactions. The kernel function satisfies the normalization condition $\int_V W(\mathbf{x}, \mathbf{x}_0)\, dV = 1$, ensuring zeroth-order consistency.

Direct discretization of Equations (38)–(39) is not straightforward, as these equations are written in an Eulerian frame, whereas SDPD is a particle-based method formulated in a Lagrangian framework. The governing equations must therefore be expressed in material form prior to discretization. Retaining transient and compressible contributions, the Lagrangian form of the Navier–Stokes equations reads

$$\rho\frac{d\mathbf{v}}{dt} = -\nabla p + \eta\nabla^2\mathbf{v} + \left(\frac{\eta}{3} + \xi\right)\nabla\nabla\cdot\mathbf{v} + \rho\mathbf{b}, \tag{60}$$

$$\frac{d\rho}{dt} + \rho\nabla\cdot\mathbf{v} = 0, \tag{61}$$

where ξ denotes the bulk viscosity.

Several points require justification. First, unsteady term (i.e., $d\mathbf{v}/dt$) is retained because the resulting discretized equations integrate naturally into molecular-dynamics–style time-stepping schemes. In contrast, a steady formulation would lead to a system of elliptic equations requiring fundamentally different numerical treatment. Second, even for flows at low and moderate Reynolds numbers, transient relaxation is essential because the initial particle distribution does not, in general, correspond to the equilibrium radial distribution function associated with the chosen model parameters. A finite relaxation time is therefore required before the system reaches a physically meaningful hydrodynamic state.

Furthermore, inclusion of compressible contributions through the bulk viscosity term suppresses spurious force fluctuations arising from large local density gradients, which are particularly pronounced during early stages of the simulation. For these reasons, the Lagrangian system (Eqs. (60)–(61)) is more suitable for SDPD discretization than the strictly incompressible Eulerian formulation (Eqs. (38)–(39)).

A further limitation arises when the above equations are discretized using standard SPH-type approximations. In general, the resulting interaction forces are not strictly parallel to the interparticle vector $\mathbf{r}_{ij}$. As a consequence, linear momentum is conserved exactly, but angular

momentum is only weakly conserved. The importance of exact angular momentum conservation has been demonstrated in the context of vesicle and capsule dynamics, particularly for systems involving fluids of different viscosities separated by deformable interfaces [66]. At the discrete particle level, the angular momentum balance (Eqs. (40)–(41)) is therefore not satisfied exactly, although it may be recovered approximately in the continuum limit.

To address this issue, an angular-momentum–conserving formulation of SDPD is employed in this thesis. The approach is inspired by the theory of micropolar fluids, in which the angular momentum balance introduces additional rotational degrees of freedom and associated body torques. In addition to the continuity equation, the modified Navier–Stokes equation reads

$$\rho\frac{d\mathbf{v}}{dt} = -\nabla p + (\eta+\eta_R)\nabla^2\mathbf{v} + \left(\frac{\eta}{3}+\xi-\eta_R\right)\nabla\nabla\cdot\mathbf{v} + 2\eta_R\nabla\times\boldsymbol{\omega}, \tag{62}$$

where $\boldsymbol{\omega}$ is the local angular velocity field and η_R denotes the rotational viscosity.

Discretization of Equation (62) requires assigning both mass and moment of inertia to each particle. Using a particle-based discretization analogous to DPD, the resulting deterministic interaction forces can be written as

$$\mathbf{F}_{ij}^{\mathrm{C}} = \left(\frac{p_i}{\rho_i^2}+\frac{p_j}{\rho_j^2}\right)F_{ij}\,\mathbf{r}_{ij}, \tag{63}$$

$$\mathbf{F}_{ij}^{\mathrm{D}} = -\left(\frac{5\eta}{3}+3\eta_R-\xi\right)\frac{F_{ij}}{\rho_i\rho_j}\mathbf{v}_{ij} - 5\left(\frac{\eta}{3}+\xi-\eta_R\right)\frac{F_{ij}}{\rho_i\rho_j}\mathbf{e}_{ij}\left(\mathbf{e}_{ij}\cdot\mathbf{v}_{ij}\right), \tag{64}$$

$$\mathbf{F}_{ij}^{\mathrm{R}} = -2\eta_R\frac{F_{ij}}{\rho_i\rho_j}\mathbf{r}_{ij}\times\left(\boldsymbol{\omega}_i+\boldsymbol{\omega}_j\right). \tag{65}$$

Here, $\mathbf{F}_{ij}^{\mathrm{C}}$ controls the density field through the pressure, $\mathbf{F}_{ij}^{\mathrm{D}}$ introduces viscous dissipation associated with shear, bulk, and rotational viscosities, and $\mathbf{F}_{ij}^{\mathrm{R}}$ arises from the angular-momentum–conserving coupling between translational and rotational degrees of freedom. This last term, absent in standard DPD, allows for exchange of angular momentum between neighboring particles and ensures exact conservation of total angular momentum at the discrete level. A detailed derivation of the above expressions is provided in Appendix B. Further details about the method can be found in [48, 51, 66]

The above set of equations is not yet closed, as no governing relation for the pressure has been specified. In this thesis, the pressure is determined through an equation of state of the form

$$p = p_0\left(\frac{\rho}{\rho_0}\right)^{\alpha} + b, \tag{66}$$

which is known to yield robust results in particle-based simulations of liquid water. Here, p denotes the instantaneous pressure as a function of the instantaneous density ρ, ρ_0 is the ref-

erence (target) density, and p_0, α, and b are model parameters. In the present simulations, the SDPD density is identified with the particle number density. While alternative choices for mass density and number density are possible, such distinctions may lead to numerical instabilities, particularly for large values of α, which strongly penalize density fluctuations. The offset b provides a uniform background pressure and ensures a finite pressure even when $\rho = \rho_0$.

Equations (63)–(65) may be interpreted as smoothed particle hydrodynamics (SPH) equations augmented to enforce angular momentum conservation. In addition to deterministic forces, SDPD requires stochastic forces to thermalize the fluid. The random forces cannot be chosen arbitrarily; instead, they must satisfy a detailed balance condition with the dissipative forces to ensure convergence to thermal equilibrium at a prescribed temperature. A detailed derivation of fluctuation–dissipation relation of angular momentum conserving SDPD is given in Appendix C.

The derivation of the appropriate stochastic forcing relies on rewriting the equations of motion as a system of stochastic differential equations and constructing the corresponding Fokker–Planck equation governing the probability density of the particle degrees of freedom. Requiring that the stationary solution of the Fokker–Planck equation corresponds to the Boltzmann distribution uniquely constrains the form and strength of the random forces.

Motivated by this framework, a generic tensorial representation of the pairwise interaction operator is introduced,

$$\mathbf{T}_{ij} = A(r)\mathbf{I} + B(r)\,\mathbf{e}_{ij} \otimes \mathbf{e}_{ij}, \tag{67}$$

where indices i, j label particle identities, $\mathbf{I}$ is the identity tensor, and $\mathbf{e}_{ij} = \mathbf{r}_{ij}/r_{ij}$ is the unit vector connecting particles i and j. Using this notation, the dissipative and rotational forces can be written as

$$\mathbf{F}^{\mathrm{D}}_{ij} = -\mathbf{T}_{ij} \cdot \mathbf{v}_{ij}, \tag{68}$$

$$\mathbf{F}^{\mathrm{R}}_{ij} = -\mathbf{T}_{ij} \cdot \left(\frac{\mathbf{r}_{ij}}{2} \times (\boldsymbol{\omega}_i + \boldsymbol{\omega}_j) \right), \tag{69}$$

which implies the following expressions for the coefficients $A(r)$ and $B(r)$,

$$A(r) = 4\left(\frac{5\eta}{3} - \xi \right) \frac{F_{ij}}{\rho_i \rho_j}, \tag{70}$$

$$B(r) = 10\left(\xi - \frac{2\eta}{3} \right) \frac{F_{ij}}{\rho_i \rho_j}, \tag{71}$$

provided that the rotational viscosity satisfies $\eta_R = \frac{5\eta}{3} - \xi$.

A stochastic force consistent with detailed balance is then postulated in the form

$$\tilde{\mathbf{F}}_{ij}\,dt = \sqrt{2k_BT}\left(\tilde{A}(r)\,d\mathbf{W}^S_{ij} + \frac{\tilde{B}(r)}{3}\,\mathrm{tr}[d\mathbf{W}_{ij}]\,\mathbf{I} + \tilde{C}(r)\,d\mathbf{W}^A_{ij}\right)\cdot\mathbf{e}_{ij}, \tag{72}$$

where $d\mathbf{W}_{ij}$ is a second-order tensor composed of independent Wiener increments. A scalar Wiener increment satisfies $dW^2 = dt$ and $dW^{2+N} = 0$ for any positive integer N. The symmetric and antisymmetric parts of the tensor are defined as

$$d\mathbf{W}^S_{ij} = \tfrac{1}{2}(d\mathbf{W}_{ij} + d\mathbf{W}^T_{ij}), \qquad d\mathbf{W}^A_{ij} = \tfrac{1}{2}(d\mathbf{W}_{ij} - d\mathbf{W}^T_{ij}).$$

Requiring detailed balance between deterministic and stochastic contributions yields the relations

$$A(r) = \tfrac{1}{2}\left(\tilde{A}(r)^2 + \tilde{C}(r)^2\right), \tag{73}$$

$$B(r) = \tfrac{1}{2}\left(\tilde{A}(r)^2 - \tilde{C}(r)^2\right) + \tfrac{1}{3}\left(\tilde{B}(r)^2 - \tilde{A}(r)^2\right). \tag{74}$$

For simplicity, choosing $\tilde{C}(r) = 0$ leads to

$$\tilde{A}(r_{ij}) = \left[2\left(\frac{20\eta}{3} - 4\xi_b\right)\frac{F_{ij}}{r^2_{ij}}\right]^{1/2}, \tag{75}$$

$$\tilde{B}(r_{ij}) = \left[2\left(\frac{17\xi_b - 40\eta}{3}\right)\frac{F_{ij}}{r^2_{ij}}\right]^{1/2}. \tag{76}$$

The SDPD interaction forces may then be written as

$$\mathbf{F}^{\mathrm{C}}_{ij} = \left(\frac{p_i}{\rho_i^2} + \frac{p_j}{\rho_j^2}\right)F_{ij}\,\mathbf{r}_{ij}, \tag{77}$$

$$\mathbf{F}^{\mathrm{D}}_{ij} = -\frac{\gamma^a_{ij}}{3}\left(\mathbf{v}_{ij} + \mathbf{e}_{ij}(\mathbf{e}_{ij}\cdot\mathbf{v}_{ij})\right) - 2\gamma^b_{ij}\mathbf{e}_{ij}(\mathbf{e}_{ij}\cdot\mathbf{v}_{ij}), \tag{78}$$

$$\mathbf{F}^{\mathrm{R}}_{ij} = -\gamma^a_{ij}\frac{\mathbf{r}_{ij}}{2}\times(\boldsymbol{\omega}_i + \boldsymbol{\omega}_j), \tag{79}$$

$$\tilde{\mathbf{F}}_{ij} = \left(\sigma^a_{ij}\,d\mathbf{W}^S_{ij} + \sigma^b_{ij}\,\frac{1}{3}\,\mathrm{tr}[d\mathbf{W}_{ij}]\,\mathbf{I}\right)\cdot\mathbf{e}_{ij}\,\frac{1}{dt}. \tag{80}$$

Here, $\mathbf{F}^{\mathrm{C}}_{ij}$, $\mathbf{F}^{\mathrm{D}}_{ij}$, and $\mathbf{F}^{\mathrm{R}}_{ij}$ denote conservative, dissipative, and rotational deterministic forces, respectively, while $\tilde{\mathbf{F}}_{ij}$ represents the stochastic contribution. The associated coefficients are

given by

$$\gamma_{ij}^{a} = \left(\frac{20\eta}{3} - 4\xi_b\right)\frac{F_{ij}}{\rho_i\rho_j}, \tag{81}$$

$$\gamma_{ij}^{b} = \left(\frac{17\xi_b - 40\eta}{3}\right)\frac{F_{ij}}{\rho_i\rho_j}, \tag{82}$$

$$\sigma_{ij}^{a,b} = 2\sqrt{k_B T\,\gamma_{ij}^{a,b}}, \tag{83}$$

subject to the constraint

$$\frac{2\eta}{3} \leq \xi \leq \frac{5\eta}{3}, \tag{84}$$

which guarantees positivity of the friction coefficients. For the particular choice $\xi = \frac{20\eta}{21}$, the coefficients simplify to

$$\gamma_{ij} = \frac{20\eta}{7}\frac{F_{ij}}{\rho_i\rho_j}, \tag{85}$$

$$\sigma_{ij}^{a} = \sigma_{ij}^{b} = 2\sqrt{2k_B T\,\gamma_{ij}}. \tag{86}$$

This final set of equations defines an SDPD fluid that obeys the Navier–Stokes equations in the continuum limit while exactly conserving angular momentum at the discrete level.

For the further details of the classical SDPD as a numerical method reader is referred to Ref [47]. Here, only the relevant part of this reference is discussed.

Although DPD is comparatively straightforward to implement and (for central pairwise forces) conserves angular momentum, it suffers from well-known limitations. SDPD alleviates several of these drawbacks by discretizing the governing continuum equations of fluid motion more directly. A central advantage of SDPD is that fluid transport coefficients can be prescribed at the level of the discretized equations. In particular, one may specify a target shear viscosity that is reproduced to good accuracy by construction. This degree of control is generally not available in standard DPD, where the effective viscosity emerges from the parametrization of the pairwise forces and depends on the details of the discretization.

A related issue is the dependence of transport properties on resolution. In DPD, the effective material response varies with the particle number density: changing the number density while keeping other parameters fixed effectively changes the fluid. In contrast, in SDPD the number density primarily sets the numerical resolution with which hydrodynamic gradients are represented. Once the constitutive parameters of the continuum model (e.g. shear viscosity, bulk viscosity, equation of state) are fixed, the target transport coefficients are fixed as well, and the particle density mainly controls the question of how accurately the fields are discretized.

Within the SPH/SDPD paradigm, two dominant sources of numerical error arise: (i) the kernel (or smoothing) error associated with replacing the Dirac delta distribution by a finite-width kernel, and (ii) the quadrature (particle discretization) error associated with approximating an integral by a finite sum. A commonly quoted scaling for the total error reads

$$\text{err} = \mathcal{O}\Big[\Big(\frac{r_C}{R}\Big)^n\Big] + \mathcal{O}\Big[\Big(\frac{\Delta}{r_C}\Big)^m\Big], \tag{87}$$

where r_C is the interaction cutoff (kernel support radius), R is a characteristic macroscopic length scale of the domain, and Δ is the characteristic interparticle spacing. The first term reflects kernel consistency (error due to finite smoothing), whereas the second reflects quadrature accuracy. For the Lucy kernel, the kernel-consistency order is typically $n = 2$. When thermal motion is present, particle configurations remain well mixed, which substantially reduces quadrature errors; in SDPD one often observes an effective quadrature convergence exponent of approximately $m \approx 4$.

To achieve small quadrature errors in practice, SDPD generally requires a larger neighbor count than standard DPD. In this thesis, a typical choice corresponds to a number density of order $\rho \approx 5$, which yields roughly $\mathcal{O}(10^2)$ neighbors within the kernel support in three dimensions (the exact count depends on r_C and the kernel). In contrast, standard DPD simulations often use neighbor counts of order $\mathcal{O}(10^1)$–$\mathcal{O}(10^2)$ while still producing qualitatively meaningful results. This improved accuracy comes at increased computational cost: SDPD force evaluations are more involved than DPD and are typically more expensive per interaction.

Another key practical advantage of SDPD is its improved control of compressibility. In standard DPD, the commonly used linear conservative force results in a relatively soft equation of state, which may be insufficient to suppress density fluctuations in the presence of strong hydrodynamic gradients. By contrast, the equation of state used here (Eq. (66)) can be made stiff by choosing a sufficiently large exponent α, such that deviations of ρ from ρ_0 are strongly penalized through large pressure forces in Eq. (63). This introduces numerical stiffness and may require a smaller time step, but it enables density fluctuations to be kept small when the time integration is stable.

These considerations are particularly relevant for blood flow, which is intrinsically particulate and exhibits secondary effects on top of the base hydrodynamic response. One important example is collision-driven migration (margination), which emerges from hydrodynamic interactions and leads to intermittent, localized stress and pressure fluctuations. If compressibility is not controlled sufficiently, such fluctuations can translate into spurious density variations. Moreover, the focus of this thesis is aggregate formation driven by hemostatic reactions, leading to thrombi or hemostatic plugs that substantially modify the effective flow geometry. These

evolving obstacles can generate steep pressure gradients, further amplifying the need for robust control of density fluctuations. In such situations, the standard DPD conservative interaction may be insufficiently stiff, whereas the SDPD formulation employed here provides a more reliable approximation of incompressible flow while simultaneously allowing prescription of viscosity and other transport properties and maintaining thermalization via the SDPD thermostat. For these reasons, SDPD is used to discretize the fluid equations, whereas DPD is employed for fluid–structure coupling due to its simplicity and widespread use in modeling momentum exchange between deformable/rigid bodies and the surrounding fluid.

A final modeling note concerns the distinction between the cytosol (interior fluid) of red blood cells and the surrounding plasma. In this thesis, the inner and outer fluids are not distinguished, i.e. the cytosol viscosity is taken equal to the plasma viscosity. Differences between inner and outer viscosities are known to affect single-cell dynamics of capsules, vesicles, and droplets under flow, and RBCs are no exception. However, it has been reported in the literature that, for many bulk flow observables of interest in blood suspensions, assuming equal viscosities has only a minor quantitative effect, although subtle differences can arise in specific dynamical regimes at the single-cell level.

Distinguishing inner and outer fluids would require an additional algorithm to prevent unphysical mixing across the membrane (e.g. a bounce-back or related interface treatment), which significantly increases computational cost. The simulations performed here are already computationally demanding, as they target laboratory-scale setups and in vitro–motivated conditions (e.g. elevated platelet and von Willebrand factor concentrations). Given the expected modest impact of inner/outer viscosity contrast on the primary questions addressed in this thesis, and the substantial additional computational burden, the inner and outer fluids are treated as identical throughout.

2.3.4 Mechanics of Membranes and Membrane Model

After discretizing the governing equations of fluid motion and specifying an appropriate description of fluid–structure interactions, it is essential to model the mechanical behavior of blood constituents. For clarity, the mechanics of membrane-enclosed blood agonists (e.g. red blood cells and platelets) and the mechanics of polymeric components will be treated in separate chapters. In the present section, we introduce the mathematical framework underlying the membrane mechanics of blood agonists.

As discussed earlier, red blood cells (RBCs) are enclosed by a lipid bilayer membrane that is mechanically coupled to an underlying spectrin cytoskeleton. The spectrin network provides in-plane shear elasticity, while the lipid bilayer enforces near incompressibility of the membrane area and contributes bending resistance. The RBC cytosol is a Newtonian fluid whose viscosity

exceeds that of blood plasma under physiological conditions and provides effective volume conservation of the cell. Accordingly, a mechanically consistent model of the RBC membrane must incorporate the following features:

- shear elasticity,
- bending resistance,
- area incompressibility,
- volume incompressibility.

These properties are represented through four distinct energetic contributions,

$$U_{\text{tot}} = U_{\text{in-plane}} + U_{\text{bending}} + U_{\text{area}} + U_{\text{volume}}. \tag{88}$$

Blood cells are deformable entities whose shape dynamics strongly couple to the surrounding flow field. While RBC deformations are moderate in large arteries and venules, they become pronounced in capillaries and microvessels. Many characteristic properties of blood, including its apparent viscosity, emerge only when this fluid–structure interaction problem is resolved consistently. For example, increased membrane stiffness reduces cell deformation and leads to a lower apparent viscosity of the suspension. Consequently, a membrane model capable of capturing the mechanical features listed above is required to obtain physically meaningful simulation results.

In this thesis, a mesoscopic membrane model originally introduced in Ref. [213, 214] and further developed in Ref. [52, 54, 107] is employed. The model captures both static and dynamic mechanical responses of the membrane across small and large deformation regimes.

A central modeling assumption is the two-dimensional representation of the membrane. The physical thickness of the RBC membrane is of order nanometers, which is several orders of magnitude smaller than the characteristic cell diameter ($\sim 8\,\mu$m). Under this scale separation, variations of stress across the membrane thickness can be neglected, and the membrane may be treated as an effectively two-dimensional elastic surface.

In addition, membrane viscosity is neglected in the present model, although the underlying framework allows its inclusion. As discussed in the previous chapter, viscosity contrast between inner and outer fluids plays a more prominent role in RBC dynamics. Given its comparatively minor influence and the additional computational cost associated with modeling membrane viscosity, it is neglected here.

At the core of the membrane description lies a mesoscopic modeling approach. Rather than resolving individual molecules or atoms constituting the membrane—which would be computationally prohibitive at the scales considered here—the membrane is represented using effective interaction potentials. Pure continuum membrane models, while less expensive than molecular simulations, typically require spatial discretization and solution of nonlinear systems of equations, which are less compatible with particle-based Lagrangian simulation frameworks. In contrast, mesoscopic approaches represent membrane mechanics through a small number of two-, three-, and four-body potentials that integrate naturally into molecular-dynamics–style solvers at substantially reduced computational cost. For the purposes of this thesis, mesoscopic and continuum approaches provide comparable accuracy in the relevant deformation regimes.

The chosen model reproduces a linear force–displacement relation at small deformations and a nonlinear response at larger deformations, consistent with experimental observations of RBC mechanics.

Shear elasticity of the RBC membrane originates from the spectrin cytoskeleton coupled to the lipid bilayer. Under shear, the membrane resists deformation, in contrast to pure lipid vesicles or liquid droplets. In the present approach, the membrane surface is discretized into Lagrangian nodes connected through a triangulated mesh. Triangles are required to define three- and four-body interaction potentials that enforce area and volume conservation and generate bending resistance.

Two modeling choices arise at this stage: the discretization of the surface mesh and the constitutive form of the in-plane elastic interactions. Surface meshes may be unstructured, as generated by standard meshing algorithms, or structured, such as transfinite meshes that produce regular triangulations (e.g. cross, cross-center, or hexagonal arrangements). For the in-plane elasticity, a natural initial choice is a harmonic spring model acting along mesh edges.

For a regular hexagonal triangulation with harmonic springs, the effective elastic properties of the membrane can be derived analytically in the small-deformation limit. In this case, the Young's modulus Y, Poisson's ratio ν, and area dilation modulus K are given by

$$Y = \frac{2}{\sqrt{3}}k, \qquad \nu = \frac{1}{3}, \qquad K = \frac{\sqrt{3}}{2}k,$$

where k is the spring constant [100]. However, this simple choice suffers from notable limitations. In particular, harmonic spring networks fail to reproduce the correct nonlinear mechanical response at large deformations. Moreover, when combined with strict area conservation, such models may exhibit strain-softening behavior and numerical stiffness, which can compromise stability in large-deformation simulations.

A more accurate representation capable of capturing the nonlinear elasticity of the cell membrane is provided by the worm-like chain (WLC) model, which is commonly used to describe the nonlinear mechanical response of polymeric filaments such as spectrin.
Upon discretizing the membrane surface into N_v vertices, one obtains $N_e = 3(N_v - 2)$ edges, each of which is modeled as a WLC spring. The corresponding elastic energy is given by

$$U_{\mathrm{WLC}} = \sum_j \left[\frac{k_B T \, l_m \left(3x_j^2 - 2x_j^3\right)}{4p\,(1 - x_j)} \right], \tag{89}$$

where l_j is the length of edge j, l_m is the maximum extensible length of the spring, $x_j = l_j/l_m$, p is the persistence length, and $k_B T$ denotes the thermal energy. The summation runs over all membrane edges. The corresponding force acting along edge j reads

$$\mathbf{f}^j_{\mathrm{WLC}} = -\frac{k_B T}{p} \left[\frac{1}{4(1 - x_j)^2} - \frac{1}{4} + x_j \right] \mathbf{e}_{ij}, \tag{90}$$

where $\mathbf{e}_{ij}$ is the unit vector along the edge.

The WLC force is purely attractive at small extensions and diverges as $x_j \to 1$. In isolation, this would cause all membrane nodes to collapse to a single point in the absence of additional constraints, leading to numerical instabilities. To prevent this unphysical behavior, a short-range repulsive potential is introduced. A commonly used choice is a power-law potential of the form

$$U_{\mathrm{POW}} = \sum_j \frac{-k_p}{1 - \alpha} \, l_j^{1-\alpha}, \tag{91}$$

with the associated force

$$\mathbf{f}^j_{\mathrm{POW}} = \frac{k_p}{l_j^{\alpha}} \mathbf{e}_{ij}, \tag{92}$$

where $\alpha \neq 1$ is a positive exponent and k_p is the repulsive coefficient. The summation again runs over all edges.

Following the analysis in Ref. [213, 214], the effective shear modulus of the membrane in the small-deformation limit is given by

$$\mu_0 = \frac{\sqrt{3} k_B T}{4 p l_m x_0} \left(\frac{x_0}{2(1 - x_0)^3} - \frac{1}{4(1 - x_0)^2} + \frac{1}{4} \right) + \frac{3\sqrt{3} k_p}{4 l_0^3}, \tag{93}$$

where $x_0 = l_0/l_m$ and l_0 denotes the equilibrium edge length.

Area incompressibility of the membrane is enforced using harmonic three-body potentials,

$$U_{\text{area}} = k_a \frac{(A - A_0)^2}{2A_0} + \sum_j k_d \frac{(A_j - A_j^0)^2}{2A_j^0}, \tag{94}$$

where A_0 is the reference total membrane area, A is the instantaneous total area, A_j^0 and A_j are the reference and instantaneous areas of triangle j, respectively, and k_a and k_d denote the global and local area penalty coefficients.

Volume incompressibility is enforced via a global harmonic constraint,

$$U_{\text{volume}} = k_v \frac{(V - V_0)^2}{2V_0}, \tag{95}$$

where V is the instantaneous cell volume, V_0 is the reference volume, and k_v is the volume penalty coefficient.

Bending resistance between adjacent triangles is modeled using a dihedral-angle potential,

$$U_{\text{bending}} = k_b \sum_j \left[1 - \cos(\theta_j - \theta_0)\right], \tag{96}$$

where θ_j is the instantaneous dihedral angle between the normals of two adjacent triangles, θ_0 is the equilibrium angle, and k_b is the bending stiffness. Derivations of the nodal forces corresponding to Eqs. (89)–(96) are provided in Appendix D.

The membrane described by the above potentials is characterized by the area compression modulus K, bending rigidity κ, and Young's modulus Y, which are related to the model parameters as

$$K = 2\mu_0 + k_a + k_d, \tag{97}$$

$$Y = \frac{4K\mu_0}{K + \mu_0}, \tag{98}$$

$$\kappa = \frac{\sqrt{3}}{2} k_b. \tag{99}$$

These relations enable a direct mapping between simulation parameters and target mechanical properties of the red blood cell membrane. Specific parameter values used in the simulations are provided in the corresponding chapters. Owing to its general formulation, the same membrane model is also employed to describe platelet membranes, with appropriate choices of the elastic parameters to reflect their differing mechanical rigidity.

2.3.5 von Willebrand Factor and Polymer Model

The biological role of von Willebrand factor (vWF) and its importance in hemostasis and thrombosis were discussed in the previous chapter. Here, we describe the modeling methodology adopted in this thesis. From a mechanical perspective, vWF may be modeled as a polymer chain whose effective interactions are designed to reproduce the following key properties:

- excluded-volume interactions between monomers,
- finite-extensible, nonlinear bonds connecting adjacent monomers,
- attractive–repulsive interactions between nonbonded monomers.

The first property is generic to polymer models and is required to prevent unphysical overlap or collapse of monomers, whether they belong to the same polymer or to different polymers within the simulation domain. The defining mechanical feature of vWF is its ability to undergo a shear-induced coil–stretch transition: the polymer extends under sufficiently strong hydrodynamic forces and collapses back into a globular conformation when these forces are removed. This behavior is captured by introducing attractive interactions between monomers, combined with excluded-volume repulsion.

In the present model, both excluded-volume and attractive interactions are described using a Lennard–Jones (LJ) potential of the form

$$U_{\mathrm{LJ}} = \sum_j 4\epsilon \left[\left(\frac{\sigma}{r_j} \right)^{12} - \left(\frac{\sigma}{r_j} \right)^{6} \right], \tag{100}$$

where the summation runs over all relevant monomer pairs. The attraction is only applied to the monomers of the same vWF. The cutoff radius is chosen to exceed the purely repulsive regime of the Lennard–Jones potential, thereby allowing for an attractive interaction that stabilizes the compact conformation of vWF under low-stress conditions. The specific parameter values used in the simulations are provided in the corresponding chapters. The force derived from the Lennard–Jones potential is standard and is therefore not reproduced here.

Finite extensibility, nonlinear elasticity at large deformations, and a linear response at small deformations are introduced through finitely extensible nonlinear elastic (FENE) bonds between adjacent monomers. The corresponding potential is given by

$$U_{\mathrm{FENE}} = \sum_j -\frac{k_{\mathrm{FENE}} r_{\max}^2}{2} \ln \left[1 - \left(\frac{r}{r_{\max}} \right)^2 \right], \tag{101}$$

where the summation runs over all bonds within a single polymer chain, k_{FENE} is the bond stiffness, and $r_{\max}$ is the maximum allowable bond extension. Together, the Lennard–Jones and

FENE potentials generate a polymer that adopts a globular conformation in the absence of external forcing and transitions to an extended state when hydrodynamic stresses are sufficiently large to overcome the cohesive energy barrier. This behavior closely reflects the mechanical response of vWF under flow.

As discussed previously, stretching of vWF exposes binding sites along the polymer backbone, enabling interactions relevant to hemostasis and thrombosis. The activation of these binding sites is modeled separately from the polymer mechanics. Following the approach introduced in Ref. [98, 169], a monomer becomes active—i.e. capable of forming adhesive bonds governed by specified bond kinetics—when certain geometric criteria are satisfied. Two conditions are imposed:

- an angular criterion, requiring the angle formed by consecutive bonds to exceed a prescribed threshold,
- a distance criterion, requiring the separation between neighboring monomers to exceed a prescribed value.

More precisely, monomer i is considered activated when

$$\theta_{ijk} > \theta_0,$$
$$r_{ij} > \delta,$$

where θ_{ijk} denotes the angle formed by monomers (i, j) and (j, k), and r_{ij} is the distance between monomers i and j. The threshold values θ_0 and δ are specified in the subsequent chapters, along with the kinetic rules governing bond formation once activation has occurred.

2.3.6 Adhesive Bonds and Bond Kinetics

The biological basis of hemostasis and thrombosis lies in the formation of adhesive bonds between different agents in blood. In hemostatic and thrombotic settings, platelets and von Willebrand factor (vWF) form bonds with each other, and both can also bind to a hemostatic surface representing exposed subendothelial material. Such a surface contains immobilized ligands, including collagen, fibronectin, and surface-anchored vWF, which are mechanically and functionally distinct from soluble vWF in the bloodstream.

In the present model, adhesive interactions between platelets, vWF, and the hemostatic surface are described using effective chemical bond kinetics. Although the molecular details of these bonds are complex and remain an active area of research, a coarse-grained kinetic description is sufficient to capture the essential dynamics of bond formation and rupture at the

mesoscopic level. The binding process is modeled as a reversible two-state reaction,

$$\text{Unbound} \underset{k_{\text{off}}}{\overset{k_{\text{on}}}{\rightleftharpoons}} \text{Bound}.$$

Here, k_{on} denotes the bond formation (on) rate, and k_{off} denotes the bond dissociation (off) rate.

The on-rate k_{on} is assumed to be constant, reflecting the fact that it primarily depends on environmental conditions such as temperature, pressure, and pH, as well as on ligand–receptor proximity, all of which are treated as fixed in the present simulations. In contrast, the off-rate k_{off} depends strongly on the mechanical loading of the bond, which is governed by the separation distance between binding partners and the resulting tensile force.

In this thesis, three types of force-dependent bond behavior are considered: slip bonds, catch bonds, and catch–slip bonds. These bond types play a critical role in determining the stability and growth dynamics of hemostatic and thrombotic aggregates. A general expression for the force-dependent off-rate is written as

$$k_{\text{off}} = k_c^0 \exp\left[\frac{\phi_1(r)}{k_B T}\right] + k_s^0 \exp\left[\frac{\phi_2(r)}{k_B T}\right], \tag{102}$$

which represents a catch–slip bond model. Here, r denotes the instantaneous bond length, which serves as a proxy for the tensile force acting on the bond. The coefficients k_c^0 and k_s^0 set the characteristic dissociation rates of the catch and slip components, respectively.

The function $\phi_1(r)$ enhances the catch-bond character, such that the bond lifetime increases with increasing tensile force over a certain range, whereas $\phi_2(r)$ induces slip-bond behavior, in which the bond lifetime decreases as the force increases. By appropriate choices of the parameters and functional forms, pure slip bonds, pure catch bonds, or combined catch–slip bonds can be realized. In this thesis, all three bond types are employed, depending on the specific interaction being modeled. The numerical values of the kinetic parameters are provided in the corresponding chapters.

2.3.7 Integration

The equation of motion of each particle is governed by Newton's second law and results in a coupled system of first-order ordinary differential equations for the particle position $\mathbf{r}$ and velocity $\mathbf{v}$ in both DPD and SDPD methods. For the angular-momentum–conserving SDPD formulation, an additional first-order ordinary differential equation governs the angular velocity $\boldsymbol{\omega}$. The equations of motion for position, velocity, and angular velocity are given by

Eqs. (103)–(105):

$$\frac{d\mathbf{r}_i}{dt} = \mathbf{v}_i, \tag{103}$$

$$\frac{d\mathbf{v}_i}{dt} = \sum_j \frac{1}{m_i}\mathbf{F}_{ij} = \mathbf{f}_i, \tag{104}$$

$$\frac{d\boldsymbol{\omega}_i}{dt} = \sum_j \frac{1}{I_i}\boldsymbol{\tau}_{ij} = \boldsymbol{\tau}_i. \tag{105}$$

Here, $\mathbf{F}_{ij}$ denotes the force exerted on particle i by particle j, m_i and I_i are the mass and moment of inertia of particle i, and

$$\boldsymbol{\tau}_{ij} = \frac{1}{2}\,\mathbf{r}_{ij} \times \mathbf{F}_{ij}$$

is the torque arising from pairwise interactions. The summations run over neighboring particles j interacting with particle i.

The forces $\mathbf{F}_{ij}$ arise from a variety of interactions obeying Newton's third law, including two-body interparticle forces (DPD and SDPD fluid forces, bonded membrane forces, adhesive bonds), three-body interactions (e.g. area or volume constraints), and four-body interactions (e.g. dihedral bending forces). External body forces, such as those used to drive the flow, are added explicitly to the right-hand side of Eq. (104). The corresponding torques generated by these interactions contribute to the right-hand side of Eq. (105).

The coupled system of Eqs. (103)–(105) is integrated in time using the velocity–Verlet algorithm, which is symplectic and conserves energy in the absence of dissipative and stochastic forces. For the translational degrees of freedom, the discretized scheme reads

$$\begin{aligned}
\mathbf{v}_i\big(t + \tfrac{1}{2}\Delta t\big) &= \mathbf{v}_i(t) + \tfrac{1}{2}\,\dot{\mathbf{v}}_i(t)\,\Delta t,\\
\mathbf{r}_i(t + \Delta t) &= \mathbf{r}_i(t) + \mathbf{v}_i\big(t + \tfrac{1}{2}\Delta t\big)\,\Delta t,\\
\dot{\mathbf{v}}_i(t + \Delta t) &= \boldsymbol{\Phi}\big(\mathbf{r}_i(t + \Delta t), \mathbf{v}_i(t + \tfrac{1}{2}\Delta t)\big)\,,\\
\mathbf{v}_i(t + \Delta t) &= \mathbf{v}_i\big(t + \tfrac{1}{2}\Delta t\big) + \tfrac{1}{2}\,\dot{\mathbf{v}}_i(t + \Delta t)\,\Delta t,
\end{aligned}$$

where the function $\boldsymbol{\Phi}$ represents the total acceleration resulting from all deterministic and stochastic forces evaluated at the updated particle positions. The angular velocity $\boldsymbol{\omega}_i$ is integrated using an analogous velocity–Verlet scheme.

2.3.8 Boundary conditions and fluid–structure interaction

All simulations presented in this thesis involve bounded flows and therefore require explicit modeling of confining walls. The walls are represented by layers of frozen particles that inter-

act with the fluid through the same SDPD force fields. In this sense, the wall and fluid are composed of the same material, but the wall particles are held fixed in space to impose a no-slip boundary condition. The wall thickness is taken to be equal to the SDPD cutoff radius. A schematic illustration is shown in Figure. 14(a).

To enforce the no-penetration condition, a bounce-back reflection method is employed at the wall surface. Upon collision with the wall, the normal component of a particle's velocity is reversed, ensuring that particles do not cross the boundary (Fig. 14(a)). While alternative reflection schemes exist (e.g. Maxwellian or bounce-forward reflections), the bounce-back method is known to provide a robust approximation of no-slip conditions in particle-based simulations.

However, the combination of frozen wall particles and bounce-back reflections is generally insufficient to completely eliminate slip, and residual slip velocities may persist in the near-wall region. This behavior can be understood by analogy with reverse-Poiseuille flow in a fully periodic domain. In such a setup, the periodic simulation box is divided into two equal regions, and fluid particles are driven by applying external forces of equal magnitude but opposite direction in the respective regions. This configuration generates two Poiseuille velocity profiles with opposing flow directions, while particles located near the periodic interfaces remain nearly stationary. In the presence of a frozen wall, one side of this opposing momentum flux is missing, which results in a finite slip velocity at the wall.

To compensate for this effect, an adaptive shear force is applied to fluid particles within a distance δ from the wall. The additional force is directed tangentially to the wall and is given by

$$f = C(t)\left(1 - \frac{x}{\delta}\right)^4, \tag{106}$$

where x denotes the normal distance from the wall and $C(t)$ is a time-dependent coefficient chosen to suppress the residual slip velocity. This procedure ensures an effective no-slip boundary condition over the near-wall region.

Here, x denotes the normal distance from the wall and δ is the cutoff distance of the adaptive shear force. The coefficient C is a time-dependent control parameter updated according to

$$C(t + \Delta t) = C(t) + \alpha\, \Delta v,$$

where α is the controller gain and Δv is the difference between the desired velocity (zero, corresponding to no slip) and the measured tangential velocity at the wall. This procedure corresponds to a proportional feedback controller that applies a force (i.e. acts on the acceleration) to regulate the velocity field. After a sufficient number of iterations, the coefficient C converges to a steady-state value and the update procedure is terminated (see Fig. 14(a.ii)).

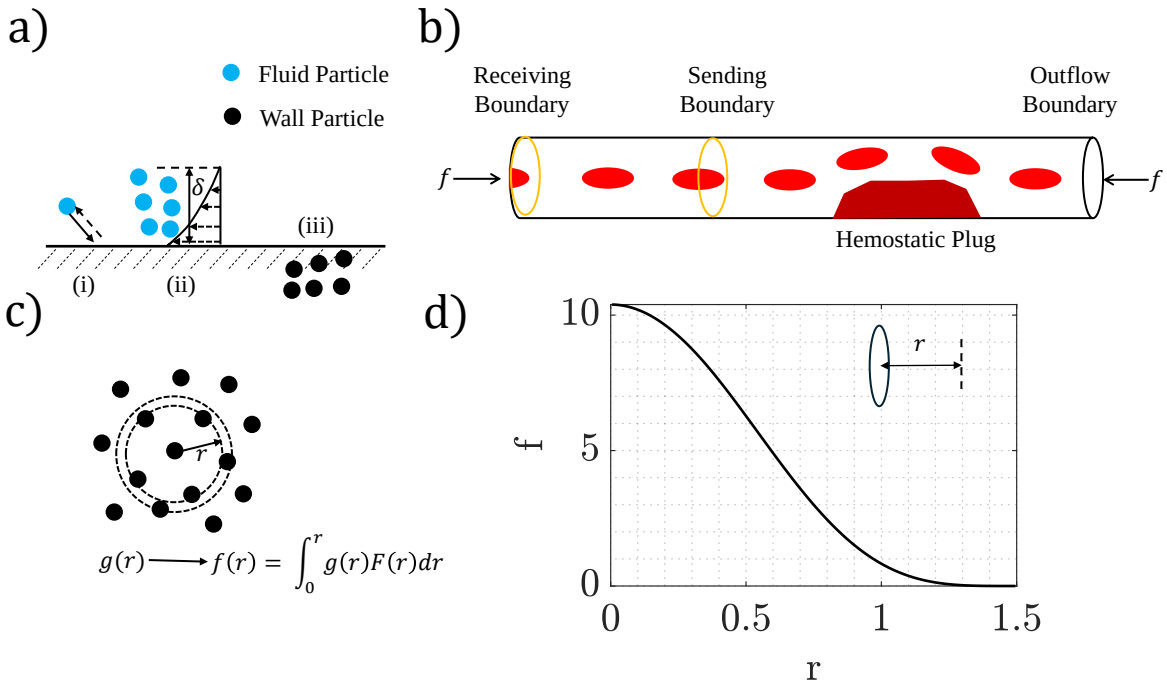

Figure 14: Overview of the boundary conditions and numerical tools used to maintain mechanical and thermal equilibrium at the domain boundaries. (a) Interaction between fluid particles and a static wall. (a.i) Bounce-back reflection boundary condition: upon collision with the wall, the particle velocity is reversed to prevent penetration. (a.ii) Adaptive shear force given by Eq. 106, applied within a distance δ from the wall (the cutoff length of the adaptive force), to suppress residual slip and more accurately enforce the no-slip boundary condition. (a.iii) Frozen wall particles used to ensure hydrodynamic and thermal equilibrium at the boundary; wall particles (black) and fluid particles (blue) interact via identical SDPD force fields. (b) Schematic of the inflow/outflow boundary conditions. Three boundary surfaces are introduced: particles crossing the outflow boundary are removed from the domain, while particles crossing the sending boundary are replicated and reintroduced at the receiving boundary. This procedure ensures a constant material flux through the domain, even as particles are consumed by hemostatic plug formation. (c) Construction of the inflow/outflow force: the local radial distribution function (i.e. the atomistic structure of the fluid) generates an effective force field, which is applied at the inflow and outflow boundaries shown in panel (b). (d) Example of an inflow/outflow force profile as a function of the distance measured normal to the inflow and outflow boundaries.

For simulations of reversible and irreversible aggregate formation, periodic boundary conditions are employed. In contrast, hemostasis simulations require a non-periodic inflow/outflow boundary condition in order to maintain a constant material flux through the simulation domain. In these simulations, hemostatic plug formation acts as a sink that continuously consumes material. Periodic boundary conditions, which fix the total number of particles, are therefore unsuitable. To obtain physically meaningful results, inflow/outflow boundaries are introduced to replenish material as it is consumed.

A schematic of the inflow/outflow boundary condition is shown in Figure 14(b). Three surfaces are defined within the simulation domain. One surface is located at the outlet and removes particles that cross it. Two additional surfaces are placed upstream: the receiving boundary, located at the entrance of the simulation domain, and the sending boundary, placed sufficiently far upstream. When particles cross the sending boundary, copies of these particles are created at the receiving boundary with identical positions (modulo a translation), velocities, and particle types. The region between the receiving and sending boundaries constitutes an inlet section that effectively operates under periodic boundary conditions and supplies material to the main simulation domain.

The inlet section must be sufficiently long to allow hydrodynamic and microstructural properties of the suspension to develop correctly, such as the formation of the cell-free layer and the spatial distribution of red blood cells, platelets, and other hemostatic agents. If this section is too short, material is injected with improper statistical properties. Previous studies have shown, for example, that correlations in the thickness of the cell-free layer persist over length scales of approximately $27\,\mu$m for a hematocrit of 45% and a vessel diameter of $40\,\mu$m. Accordingly, an inlet length of at least $27\,\mu$m is required to ensure a physically consistent material feed.

Under periodic boundary conditions, particles near a boundary interact with periodic images of particles on the opposite side of the domain, ensuring equilibrium force balance and correct thermodynamic behavior. This mechanism is absent at inflow and outflow boundaries, which are not periodic. To compensate for the missing interactions, an additional force field derived from the SDPD pressure contribution is applied to particles near the inflow and outflow boundaries. This force is indicated by $\mathbf{f}$ in Fig. 14(b).

In an equilibrated SDPD fluid, particles adopt a characteristic spatial distribution described by the radial distribution function. From this distribution, an effective force field can be constructed and applied at the inflow and outflow boundaries (Figure 14(c)). A representative example of the resulting force profile, as a function of the distance r normal to the boundary, is shown in Figure 14(d). This procedure mimics the presence of ghost fluid particles outside the computational domain and maintains hydrodynamic and thermal equilibrium near the bound-

aries.

Accurate modeling of fluid–structure interaction is essential for describing the motion of blood agonists. In this thesis, fluid–structure coupling is implemented via DPD interactions between fluid particles and membrane or polymer particles. Consider a thought experiment in which membrane particles are distributed uniformly over a planar surface and subjected to a shear flow with shear rate $\dot{\gamma}$. This flow induces a hydrodynamic shear stress and a corresponding drag force on the membrane, which in the continuum description is given by

$$f_{\text{drag}} = \int_A \eta\,\dot{\gamma}\,dA, \tag{107}$$

where η is the fluid viscosity and A is the membrane area.

At the mesoscopic level, this drag must be reproduced by the DPD viscous interaction between fluid and membrane particles. Equating the continuum and mesoscopic descriptions yields

$$\int_A \eta\,\dot{\gamma}\,dA = \int_A \gamma\,w(r)\,\mathbf{v}_{ij}\,dA, \tag{108}$$

$$\int_A \eta\,\dot{\gamma}\,dA = \int_A \gamma\,w(r)\,\dot{\gamma}z\,dA, \tag{109}$$

where γ is the strength of the DPD dissipative interaction to be determined, $w(r)$ is the DPD weight function, and z denotes the normal distance from the membrane surface.

Although the macroscopic flow around a blood agonist is generally not a simple shear flow, a linear shear approximation is valid in the immediate vicinity of the fluid–structure interface when examined at sufficiently small length scales. Taking the integral in Eq. (109) over a hemispherical interaction volume and neglecting conservative DPD interactions between fluid and membrane particles (i.e. assuming a uniform radial distribution function $g(r) = 1$), one obtains

$$\gamma = \frac{4\eta A}{\pi\rho n_V Q}, \tag{110}$$

$$Q = 6\delta^4 \frac{\Gamma(k+1)}{\Gamma(k+5)}, \tag{111}$$

where ρ is the fluid number density, δ is the DPD cutoff distance, k is the exponent of the dissipative weight function, Γ denotes the Gamma function, A is the surface area of the blood agonist, and n_V is the surface number density of membrane particles. This calibration yields excellent agreement with continuum expectations, as demonstrated in previous studies.

3 Outline

Chapter 4 investigates the formation and dynamics of platelet–von Willebrand factor aggregates in blood flow, with a focus on the distinction between reversible and irreversible aggregation mechanisms. Using particle-based simulations that explicitly resolve red blood cells, platelets, and vWF polymers, this chapter examines how hydrodynamic interactions, margination, and force-dependent adhesive bond kinetics jointly govern aggregate growth, migration, and stability. Particular emphasis is placed on the role of bond lifetime in controlling whether aggregates remain intact or dissociate upon migrating toward the channel center, where the shear rate is lowest. By systematically comparing different bond models, including catch-slip and slip-only kinetics, Chapter 4 identifies the physical conditions under which stable or transient aggregates emerge in flowing blood.

Chapter 5 builds on the insights obtained in Chapter 4 and presents an in silico model of primary hemostasis at a site of vascular injury. The simulations capture the accumulation of platelets and vWF at a damaged vessel wall and follow the time-dependent formation, growth, and remodeling of a hemostatic plug under physiologically relevant flow conditions. This chapter analyzes clot geometry, internal structure, and mechanical stability, and characterizes distinct phases of clot evolution, including growth, deformation, and embolization events. By resolving the interactions between blood flow, red blood cells, platelets, and vWF at the microscale, Chapter 5 provides a mechanistic description of how hydrodynamic forces and adhesive interactions regulate clot formation and stability during primary hemostasis.

For the sake of clarity, each chapter is divided into problem description, simulation parameters and model, results, discussion and conclusion. Note that, the models and the methods for the upcoming two chapters significantly overlap. Therefore, in Chapter 4 the models are explained in detail by making necessary references to the Chapter 1. In Chapter 5, only model parameters are given and the reader is referred to either Chapter 4 or Chapter 1.

4 Reversible - Irreversible Aggregates in Blood Flow

4.1 Problem Description

The process of hemostasis or blood clotting is essential to stop bleeding in case of a vessel injury in order to maintain vascular integrity [155, 232]. Even though blood platelets are one of the major players in the hemostatic process, their adhesion to an injury site becomes unreliable at high shear rates (larger than about $600-900\ \mathrm{s}^{-1}$) [102, 182], which are often encountered within the microvasculature [115, 167]. Under high-shear-rate conditions, a long multimeric protein von Willebrand factor (VWF) plays a vital role, facilitating platelet capture and activation at the injury site [126, 172, 181]. Malfunctions of VWF proteins often lead to either prolonged bleeding or undesired thrombotic events, some of which are described by different types of von Willebrand disease [178, 186].

VWF proteins are long concatemers of dimeric units, with a total length reaching tens of micrometers [41, 75, 207]. Each VWF dimer contains an adhesive domain that is able to bind platelet receptors, or collagen exposed at the site of endothelial injury. Despite this capability for adhesion, VWF retains a globular form under static conditions due to self-attractive interactions, such that its adhesive sites are shielded and remain inactive [206, 226]. In fact, VWF is a shear sensitive molecule, because it stretches only at high enough shear rates ($\geq 2000\ s^{-1}$), which has been shown in microfluidic experiments [185] and by numerical simulations [9, 10, 95]. More importantly, VWF stretching is directly associated with the activation of VWF for adhesion, as the adhesive domains become accessible in the stretched state [77, 96, 185, 207]. The strong correlation between VWF stretching and its activation for adhesion has been demonstrated directly for a single VWF attached to a surface [77] and indirectly through the formation of surface-bound VWF-platelet aggregates [36, 96, 185]. In the latter, VWF-platelet aggregates at a surface form only at high enough shear rates, which are sufficient to stretch VWF molecules.

The formation of VWF-platelet aggregates at a surface has been studied in *in vitro* experiments [36, 96, 185] to better understand the role of VWF in primary hemostasis. Despite the fact that such aggregates form primarily at high shear rates, their aggregation is reversible upon flow cessation or substantial reduction [36, 176, 183]. A simulation of VWFs with colloids mimicking platelets in shear flow, but in absence of red blood cells (RBCs) [36], has also confirmed shear-induced aggregation, which is reversible under flow cessation. The aggregation process critically depends on the strength of binding interactions between activated VWF molecules and colloids. In fact, atomic force microscopy experiments on the interaction of a single VWF adhesive domain with platelet receptors [110] have shown that such a bond has a non-monotonic lifetime as a function of the applied force. After an initial decrease of the bond lifetime with increasing force, the lifetime jumps up by nearly two orders of magnitude, making the bond long-lived at higher applied forces. This behavior is characteristic for a so-called catch

bond (i.e., bond lifetime increases with increasing applied force), which has also been observed in other interactions in biological systems [219, 221]. Interactions between VWF and platelet can be affected by mutations [177, 242], making it interesting to investigate distinct interaction scenarios for the formation of VWF-platelet aggregates.

Even though there are multiple sources of VWF during hemostasis, blood plasma contains a certain amount of soluble VWFs [41, 171]. This amount is generally sufficient to initiate wall-bound VWF networks or VWF-platelet aggregates, if VWF can adhere to the surface [20, 36, 176]. This raises an interesting question whether dynamic VWF-platelet aggregates can spontaneously form in the microvasculature without any vessel damage (i.e., without a substrate for aggregate formation), since flow stresses in the microcirculation (at least in its arteriolar part) should be sufficient for VWF stretching with a consequent activation for adhesion. A further important aspect is whether such VWF-platelet aggregates would be long-lived or reversible.

We employ mesoscopic hydrodynamic simulations to demonstrate a surprising behavior of VWF-platelet aggregates in microvascular blood flow. The blood model rests on a particle-based hydrodynamics method, smoothed dissipative particle dynamics (SDPD) [45, 157] and mechanistic models of red blood cells (RBCs), platelets and VWFs. At the initial stage of blood flow in a microchannel, platelets and VWF chains migrate (or marginate) into a near wall layer free of RBCs (called RBC free layer or RBC-FL), such that their concentration is substantially enhanced near the wall [170]. The margination phenomenon in microvessels has also been observed for leukocytes and drug delivery particles [59, 83, 156, 170]. Since VWFs are primarily stretched near the walls, they bind flowing platelets, leading to a growth of VWF-platelet aggregates. When such aggregates become large enough, they migrate away from the walls into the bulk of blood flow due to hydrodynamic lift forces [3, 33, 197], where the flow stresses are significantly smaller than those near the walls. As a result, VWF- platelet aggregates dissociate near the channel center into single platelets and deactivated VWFs. Then, this process repeats itself, following the described steps, which include margination of platelets and VWFs, VWF stretching near the walls, the formation of VWF-platelet aggregates, with a consecutive migration away from the wall and dissociation. Thus, our simulations predict dynamic formation and dissociation of reversible VWF-platelet aggregates in microvascular flow. Furthermore, changes in VWF-platelet interactions, such as their catch- or slip-bond natures, can lead to the formation of irreversible aggregates, which possibly represent different types of pathological conditions related to VWF dysfunction or mutation.

4.2 Simulation Setup and Model Parameters

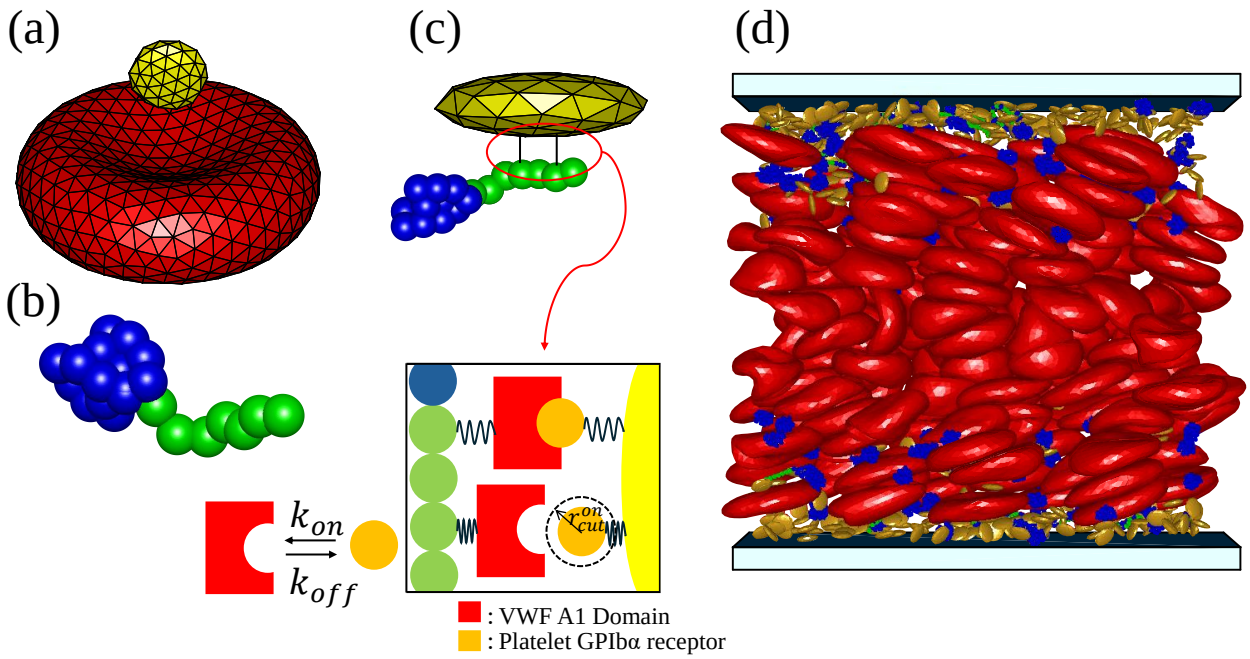

Figure 15: Illustration of the employed models and simulation setup. (a) Membrane model of a RBC (red) and a platelet (yellow), whose surfaces are represented by a triangulated bead-spring network. The model incorporates shear and bending elasticity, and the conservation of surface area and cell volume. (b) Polymer model of VWF whose globular part remains inactive (i.e., nonadhesive), while the stretched portion (green) is activated for adhesion. (c) Adhesive bonds between activated monomers of VWF and platelet vertices, whose dynamics follows the prescribed on- and off-rates. (d) The simulation domain of size $80\mu m \times 40\mu m \times 30\mu m$ with 360 RBCs, 768 platelets, and 384 VWFs. The snapshot shows that the majority of platelets and VWFs marginate into a near wall layer, where some VWFs are stretched by fluid stresses and become activated (marked by green), enabling their adhesion to platelets and leading to the formation of aggregates.

Simulations of the dynamic formation of VWF-platelet aggregates in blood flow require models of blood cells (i.e., RBCs, platelets) and VWF molecules as well as a model to describe the dynamics of the suspending fluid (blood plasma). Figure 15 illustrates these models and shows a snapshot of the simulation domain, whose detailed description is given in Section 2.3.1.

Fluid flow is modeled by the smoothed dissipative particle dynamics (SDPD) method [45, 157], a mesoscopic hydrodynamics technique. SDPD is derived through a Lagrangian discretization of the Navier-Stokes equation with a consistent representation of thermal fluctuations [231]. The detailed description of the fluid model is given in Section 2.3.1.

No-slip boundary conditions (BCs) at the channel walls are implemented by freezing a number of wall particles within a layer of thickness r_c, whose structural properties (e.g., radial

	RBC		Platelet	
Parameters	Scaled units	Physical units	Scaled units	Physical units
N_v	500		60	
A		132.83×10^{-12} m^2	$0.162 D_r^2$	6.85×10^{-12} m^2
V	$0.336\ D_r^3$	92.4×10^{-18} m^3	$0.0041\ D_r^3$	1.127×10^{-18} m^3
μ	$4.77 \times 10^4\ k_BT/D_r^2$	4.83×10^{-6} N/m	$4.77 \times 10^5\ k_BT/D_r^2$	4.83×10^{-5} N/m
κ	$70\ k_BT$	3×10^{-19} J	$700\ k_BT$	3×10^{-18} J
k_d	$4.23 \times 10^4\ k_BT/D_r^2$	4.28×10^{-6} N/m	$4.23 \times 10^5\ k_BT/D_r^2$	4.28×10^{-5} N/m
k_a	$2.07 \times 10^6\ k_BT/D_r^2$	2.1×10^{-4} N/m	$3.81 \times 10^6\ k_BT/D_r^2$	3.86×10^{-4} N/m
k_v	$1.37 \times 10^7\ k_BT/D_r^3$	213.28 N/m^2	$2.75 \times 10^7\ k_BT/D_r^3$	428.11 N/m^2

Table 1: Parameters of RBCs and platelets in units of the effective RBC diameter $D_r = \sqrt{A_r/\pi}$ and the thermal energy k_BT ($T = 310$ K), and the corresponding values in physical units. N_v is the number of membrane vertices, A is the membrane area, V is the volume, μ is the membrane shear modulus, κ is the membrane bending rigidity, and k_d, k_a, and k_v are the local area, global area, and volume constraint coefficients, respectively. In all simulations, we have chosen $A_r = 132.83$ and $k_BT = 0.1$, which implies that $D_r = 6.5$.

distribution function) are the same as those of SDPD fluid. To prevent penetration of the walls by fluid particles, bounce-back reflections at the fluid-solid interface are implemented. Furthermore, an adaptive shear force is applied to SDPD fluid particles within a near-wall layer of thickness r_c [60, 114], since the dissipative interaction between fluid and wall particles may not be sufficient to strictly impose no-slip BCs. Blood cells and VWF molecules are coupled to the SDPD fluid through the dissipative interactions [53], which is similar to viscous coupling in the immersed boundary method [6]. Relevant information can be found in Section 2.3.8.

Both RBCs and platelets are modeled by a triangulated network of N_v particles (with coordinates $\{\mathbf{x}_i\}_{i=1...N_v}$) interconnected by bonds, which represents the cell surface [53, 55, 161], see Fig. 15(a). The potential energy of the network is defined as

$$U(\{\mathbf{x}_i\}) = U_s + U_b + U_a + U_v, \tag{112}$$

where U_s is the bond potential, U_b is the bending energy, and U_a and U_v correspond to area and volume conservation constraints, respectively. U_s represents the membrane stretching elasticity. The curvature energy U_b supplies bending resistance of the membrane, while the area U_a and volume U_v conservation constraints mimic the area incompressibility of the membrane and incompressibility of a cytosol, respectively. For further details, we refer the reader to Refs. [53, 55]. Detailed information can be found in Section 2.3.4.

Elastic properties of both RBCs and platelets are characterized by the membrane shear modulus μ and the bending rigidity κ. Table 1 presents RBC and platelet characteristics in both simulation and physical units. The spontaneous curvature for RBCs is set to zero.

Platelets assume an oblate shape with a diameter of 2 µm and an aspect ratio of 0.3. Platelets are set to be about ten times stiffer (both μ and κ) than RBCs, in order to make platelets nearly non-deformable. To keep a characteristic oblate shape, local spontaneous curvature at the surface of platelets has been set to the curvature of the original oblate shape.

VWF is a self-attractive shear-activated protein, such that it remains non-adhesive in a globular form at low fluid stresses or in the absence of flow, but it becomes adhesive upon stretching at high enough shear stresses [77, 171, 185]. In our simulations, VWF is represented by a self-avoiding bead-spring model of N_m monomers ($N_m = 30$) [see Fig. 15(b)] with attractive interactions between monomers [8–10] connected by finite extensible nonlinear elastic (FENE) springs to form a linear polymer chain, with bond potential

$$U_{\mathrm{FENE}}(r) = -\frac{k_{\mathrm{s}}}{2} r_{\mathrm{max}}^2 \ln\left(1 - \left(\frac{r}{r_{\mathrm{max}}}\right)^2\right), \tag{113}$$

where k_{s} is the spring stiffness, $r_{\mathrm{max}} = 2\sigma$ is the maximum spring extension ($\sigma = 0.077 D_r$ is the bead diameter), and r is the distance between two consecutive monomers. k_{s} is set to $25000 k_{\mathrm{B}}T/\sigma^2$ in all simulations, making the connecting springs nearly inextensible. Self-avoidance and self-attraction within the polymer are implemented by the 12-6 Lennard-Jones (LJ) potential

$$U_{\mathrm{LJ}}(r) = 4\epsilon\left[\left(\frac{\sigma}{r}\right)^{12} - \left(\frac{\sigma}{r}\right)^{6}\right], \tag{114}$$

where $\epsilon = 16 k_{\mathrm{B}}T$ controls the attraction strength. The LJ interaction for monomers within the same VWF is cut beyond $r_{LJ} = 2.5\sigma$. VWF chains are coupled to the SDPD fluid by a frictional force [99, 175]. Details of the model can be found in Section 2.3.5

This VWF model keeps a globular configuration at low shear rates and stretches out at large enough shear rates ($\leq 2000\ s^{-}1$) [9, 10, 95, 99], similarly to the observed behavior of VWF in shear flow [77, 171, 185]. In the stretched state, VWF becomes adhesive, such that it can bind to platelet receptors. The activation of adhesion depends on the local stretching of VWF model in flow [99], which is described by two geometrical criteria. The first criterion concerns the local angle $\theta_{i-1,i,i+1}$ between two consecutive bonds linking neighboring monomers $i-1$, i, and $i+1$, and is expressed as $\theta_{i-1,i,i+1} \geq \theta_{\mathrm{thres}}$ for $2 < i < N_m - 1$, with a threshold angle θ_{thres} that defines the degree of local stretching of VWF. This condition is always assumed to be satisfied for the first and the last bead in the VWF. The second condition monitors the presence of non-bonded neighboring monomers N_{neigh} within the polymer as $N_{neigh} = 0$ for $r_{ij} \leq R_{\mathrm{thres}}$, $j \neq i, i \pm 1$, prohibiting the activation of monomers within a globule configuration. Here, R_{thres} is a threshold radius. In all simulations, $\theta_{\mathrm{thres}} = 150^{\mathrm{o}}$ and $R_{\mathrm{thres}} = 1.2\sigma$ are employed. The sensitivity of VWF activation to the choice of θ_{thres} and R_{thres} has been investigated in Ref. [95]. An inactive monomer is activated whenever both conditions are satisfied. Consistently, any activated VWF

monomer is deactivated whenever one or the both criteria are no longer met.

For molecular interactions, the probability of bond rupture usually increases with increasing applied forces. This type of behavior is well described by a slip-bond model, which assumes a positive correlation between the rupture probability and the applied force. A high rupture probability implies a short lifetime of the bond, such that the lifetime of a slip bond decreases with increasing applied force. However, experiments [42, 111, 220] have demonstrated that the lifetime of certain ligand-receptor interactions may increase as the applied force is elevated, at least for some intermediate range of force magnitudes. In this case, the bond is referred to as a catch bond [42]. Clearly, any physical bond will eventually rupture at large enough forces. Therefore, the catch behavior of a real bond should rather be considered as a dual catch-slip behavior, where the lifetime first increases (i.e., catch behavior) and then decreases (i.e., slip behavior) with increasing applied force. Even though the catch-slip behavior has been found for a few ligand-receptor pairs [111, 220], the existence of this type of bonds is well accepted in the context of biological systems [220]. Importantly, adhesion of VWF to platelet GPIbα receptor exhibits the catch-slip behavior [43, 110, 242].

Adhesive interactions between activated VWF monomers and platelet vertices are implemented through the formation of bonds with predefined association, k_{on}, and dissociation, k_{off}, rates [see Fig. 15(c)]. Formed bonds are modeled by the harmonic potential $U_b = k_b(r - r_0)^2$, where k_b is the bond strength and r_0 is its equilibrium length. Probabilities for bond formation P_{on} and dissociation P_{off} are determined by the rate equations [25]

$$\frac{\mathrm{d}P_{\mathrm{on}}}{\mathrm{d}t} = -k_{\mathrm{on}}P_{\mathrm{on}}, \text{ for } r \leq r_{\mathrm{cut}}^{\mathrm{on}}, \tag{115}$$

$$\frac{\mathrm{d}P_{\mathrm{off}}}{\mathrm{d}t} = -k_{\mathrm{off}}P_{\mathrm{off}}, \text{ for } r \leq r_{\mathrm{cut}}^{\mathrm{off}}, \tag{116}$$

where $r_{\mathrm{cut}}^{\mathrm{on}}$ and $r_{\mathrm{cut}}^{\mathrm{off}}$ are the cutoff ranges for bond association and dissociation, respectively. Note that $P_{\mathrm{on}} = 0$ for $r > r_{\mathrm{cut}}^{\mathrm{on}}$ and $P_{\mathrm{off}} = 1$ for $r > r_{\mathrm{cut}}^{\mathrm{off}}$. In simulations, we assume k_{on} to be constant, while k_{off} follows the aforementioned catch-slip behavior. This is described by the two-pathway model [165], which assumes two force-dependent barriers for bond dissociation,

$$k_{\mathrm{off}}(r) = k_{\mathrm{c}}^0 \exp\left(\frac{\lambda_c(r - x_{\mathrm{eq}})\delta_{\mathrm{c}}}{k_{\mathrm{B}}T}\right) + k_{\mathrm{s}}^0 \exp\left(\frac{\lambda_s(r - x_{\mathrm{eq}})\delta_{\mathrm{s}}}{k_{\mathrm{B}}T}\right), \tag{117}$$

where the first term represents a catch-bond dissociation rate, while the second term corresponds to a slip-bond rate. Here, k_{c}^0 and k_{s}^0 are the catch and slip equilibrium off-rates. λ_c and λ_s represent the strengths of the catch and slip contributions, respectively, and $\delta_{\mathrm{c}} = x_{\mathrm{c}} - x_{\mathrm{eq}}$ and $\delta_{\mathrm{s}} = x_{\mathrm{s}} - x_{\mathrm{eq}}$, where x_{c}, x_{s}, and x_{eq} are the catch, slip, and equilibrium characteristic lengths, respectively. Note that the condition $x_{\mathrm{c}} < x_{\mathrm{eq}} < x_{\mathrm{s}}$ should be satisfied, so that the

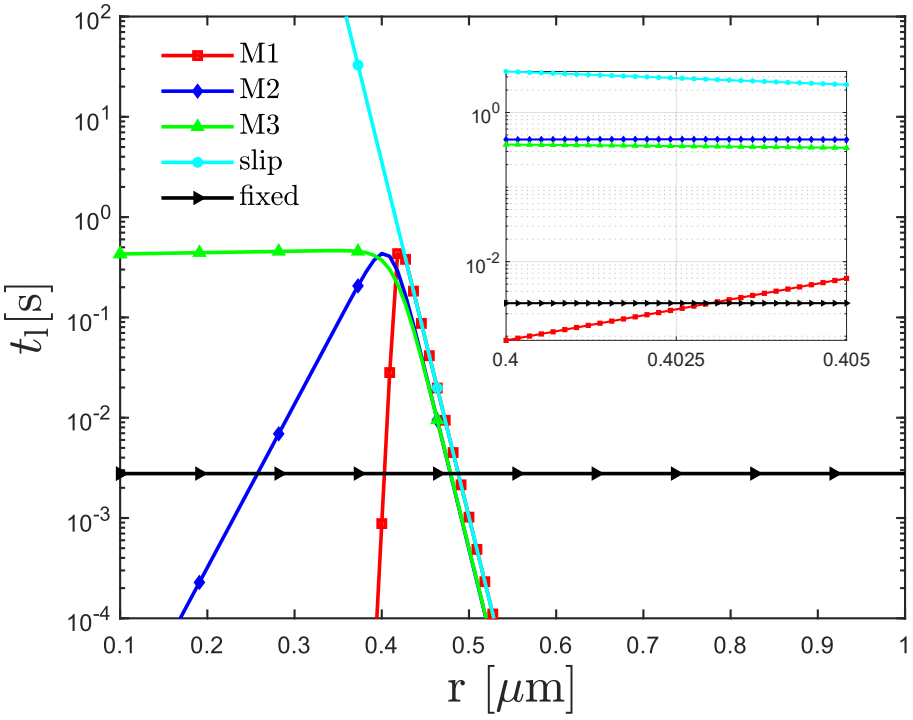

Figure 16: Comparison of lifetimes $t_l = 1/k_{\text{off}}$ for different bond types (see Table 2) as a function of bond length r. The inset shows the behavior of same curves near the average bond length.

bond type	k_c^0	x_c	x_{eq}	k_s^0	x_s
catch-slip M1	$5.76 \times 10^{-1}/\tau$	$0.0385 D_r$	$0.062 D_r$	$5.76 \times 10^{-4}/\tau$	$0.067 D_r$
catch-slip M2	$1.73 \times 10^{-2}/\tau$	$0.0517 D_r$	$0.054 D_r$	$1.73 \times 10^{-5}/\tau$	$0.059 D_r$
catch-slip M3	$3.46 \times 10^{-3}/\tau$	$0.05098 D_r$	$0.051 D_r$	$3.46 \times 10^{-6}/\tau$	$0.056 D_r$
slip	0	$0.062 D_r$	$0.062 D_r$	$5.76 \times 10^{-4}/\tau$	$0.067 D_r$
fixed	$5.77 \times 10^{-1}/\tau$	$0.062 D_r$	$0.062 D_r$	0	$0.062 D_r$

Table 2: VWF-platelet interaction parameters for different bond types. In all cases, $\lambda_c = \lambda_s = 1.06 \times 10^5 k_{\text{B}} T / D_r^2$.

catch part dominates for $r < x_{\text{eq}}$, while the slip part dominates for $r > x_{\text{eq}}$. Further details can be found in Section 2.3.6

Blood flow is simulated within a rectangular box of dimension $L_x \times L_y \times L_z = 80\mu m \times 40\mu m \times 30\mu m$ with 360 RBCs, 768 platelets, and 384 VWFs. Periodic BCs are assumed in x and z directions, while wall boundaries with no-slip BCs are set in y direction. The volume fraction of RBCs (or hematocrit) is approximately 42%, and platelets and VWFs account for about 1.7% and 0.8% by volume, respectively. Note that the simulated volume fractions of VWFs and platelets are higher than under physiological conditions, in order to allow the formation of large enough aggregates with a limited number of platelets and VWFs within the simulation domain. The suspending fluid is modeled by 4.8×10^5 SDPD particles, correspond-

ing to the number density of $n = 16.875/r_c^3$ with $r_c = 0.23D_r$. The SDPD fluid parameters are $p_0 = b = 33750k_BT/r_c^3$, $\rho_0 = mn$ with the particle mass m ($m = 1$ in simulations), and $\gamma = 7$. Fluid viscosity is set to $\eta = 100$, which defines a time scale $\tau = \eta D_r/\mu_r$. For the blood plasma viscosity of $\eta = 1.2 \times 10^{-3}\ Pa \cdot s$, this yields $\tau \approx 0.0016$ s. The flow is driven by a pressure gradient of $\Delta P/L_x = fn = 81k_BT/r_c^4$, corresponding to a force f applied to each SDPD fluid particle in the flow direction along the x axis.

Excluded-volume interactions between RBCs, platelets, and VWFs are implemented through the repulsive part of the LJ potential in Eq. (114). For all repulsive interactions, $\epsilon = 16k_BT$ and $r_{LJ} = 2^{1/6}\sigma$. However, $\sigma = 0.077D_r$ for VWF-VWF interactions, $\sigma = 0.062D_r$ for RBC-VWF and platelet-VWF repulsion, and $\sigma = 0.046D_r$ for RBC-RBC, platelet-platelet, and RBC-platelet interactions, due to slight differences in the discretization resolution of various suspended components.

In the model, platelet vertices represent receptors, and activated VWF monomers represent ligands. Each adhesive site on VWF or platelet can accommodate only a single bond. Figure 16 shows the lifetime $t_l = 1/k_{\text{off}}$ of different bond types as a function of the bond length r. The parameters of different bond types are given in Table 2. Note that these parameters represent effective bonds and do not correspond to molecular bond properties, because the minimally resolved length scale in our model is significantly above the molecular level. The bond parameters have been calibrated in separate shear flow simulations without RBCs, where the formation of stable VWF-platelet aggregates was targeted at high shear rates, with their consecutive dissociation at low shear rates. Furthermore, for all bond types, $k_{\text{b}} = 8.45 \times 10^6 k_{\text{B}}T/D_r^2$, $r_0 = 0.062D_r$, $k_{\text{on}} = 5760/\tau$, $r_{\text{cut}}^{\text{on}} = 0.068D_r$, and $r_{\text{cut}}^{\text{off}} = 0.23D_r$. The bond parameters are calibrated for the catch-slip model M1 to properly reproduce reversible aggregation of VWFs and platelets. The other two catch-slip models (M2 and M3) represent intermediate lifetimes between the catch-slip model M1 and the slip bond model.

4.3 Results

The formation of VWF-platelet aggregates in flow relies on two basic requirements. First, flow stresses need to be large enough to stretch VWF globules, and therefore, activate VWFs for adhesion. Second, bonds formed between activated VWFs and platelets have to be durable enough to maintain the stability of the formed aggregates. This means that their lifetime has to be long enough to prevent a quick breakage of bonds within the aggregate. Figure 17(a) schematically illustrates bond lifetimes for different models as a function of shear rate $\dot{\gamma}$ (or stress), which is expected to determine local bond extension (compare Fig. 16). The shaded area in Fig. 17(a) denoted as 'aggregation' corresponds to $\dot{\gamma} \leq \dot{\gamma}_c$ and $t_l \leq t_l^*$, where $\dot{\gamma}_c$ repre-

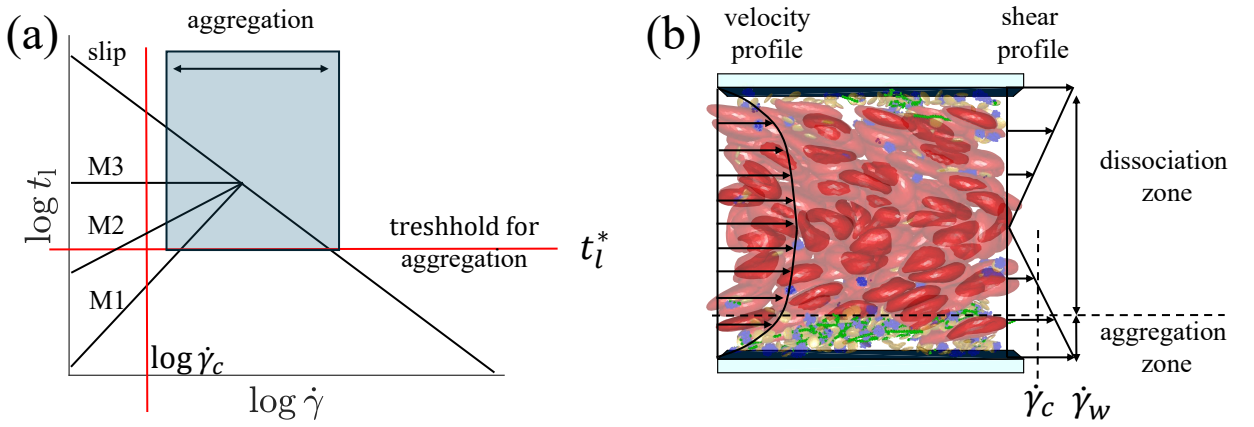

Figure 17: A schematic of the conditions for the formation of VWF-platelet aggregates. (a) Qualitative dependence of VWF-platelet aggregate formation as a function of shear rate and the lifetime of bonds between VWFs and platelets. Lifetime for several bond scenarios, including catch and slip bonds, is shown. $\dot{\gamma}_c$ denotes a critical shear rate for VWF stretching and activation, while t_l^* represents a critical lifetime of bonds that is long enough to maintain stable aggregates. Thus, VWF-platelet aggregates form under the conditions of $\dot{\gamma} \leq \dot{\gamma}_c$ and $t_l \leq t_l^*$. (b) A snapshot of modeled blood flow with a potential aggregation zone in the vicinity of the walls. Near the center of the channel, no aggregates can form and existing VWF-platelet aggregates would dissociate, which is marked by the dissociation zone. In the snapshot, RBCs are plotted in red and platelets in yellow. VWFs are shown by blue (inactive) and green (active) monomers.

sents a critical shear rate for VWF stretching and activation, and t_l^* denotes a critical lifetime of bonds that is long enough to ensure stable aggregates. Thus, in this area, both conditions are satisfied and the formation of stable VWF-platelet aggregates can take place.

The VWF model from Refs. [95, 99] shows a shear-dependent stretching of VWF at $\dot{\gamma}_c \approx 2000\ s^{-1}$, in agreement with experimental observations [77, 171, 185]. Furthermore, the parameters of the catch-slip model M1 in Table 2 are calibrated in simulations of pure shear flow using a suspension of only platelets and VWFs, such that stable VWF-platelet aggregates form for $\dot{\gamma} \leq \dot{\gamma}_c$. Using the catch-slip model M1, we have also verified that VWF-platelet aggregates dissolve when the shear rate is reduced below $\dot{\gamma}_c$, which is consistent with the reversible aggregation of platelets and VWFs observed in experiments [36, 43, 77]. The dissociation of aggregates at $\dot{\gamma} < \dot{\gamma}_c$ is primarily due to a significant reduction in bond lifetime in comparison to $\dot{\gamma} > \dot{\gamma}_c$, see the catch-slip model M1 in Fig. 17(a). In contrast, the slip-bond case in Fig. 17(a) results in the formation of irreversible VWF-platelet aggregates, since the dissociation of aggregates at $\dot{\gamma} < \dot{\gamma}_c$ is limited by long lifetimes. Theoretically, VWF-platelet aggregates based on the slip-bond model would also eventually dissolve at $\dot{\gamma} < \dot{\gamma}_c$, however, their disaggregation time is several orders of magnitude longer than that for the case of catch-slip M1 bonds. Thus, the dissociation of aggregates for the slip-bond case does not occur during typical simulation times, and this type of aggregates is considered to be irreversible.

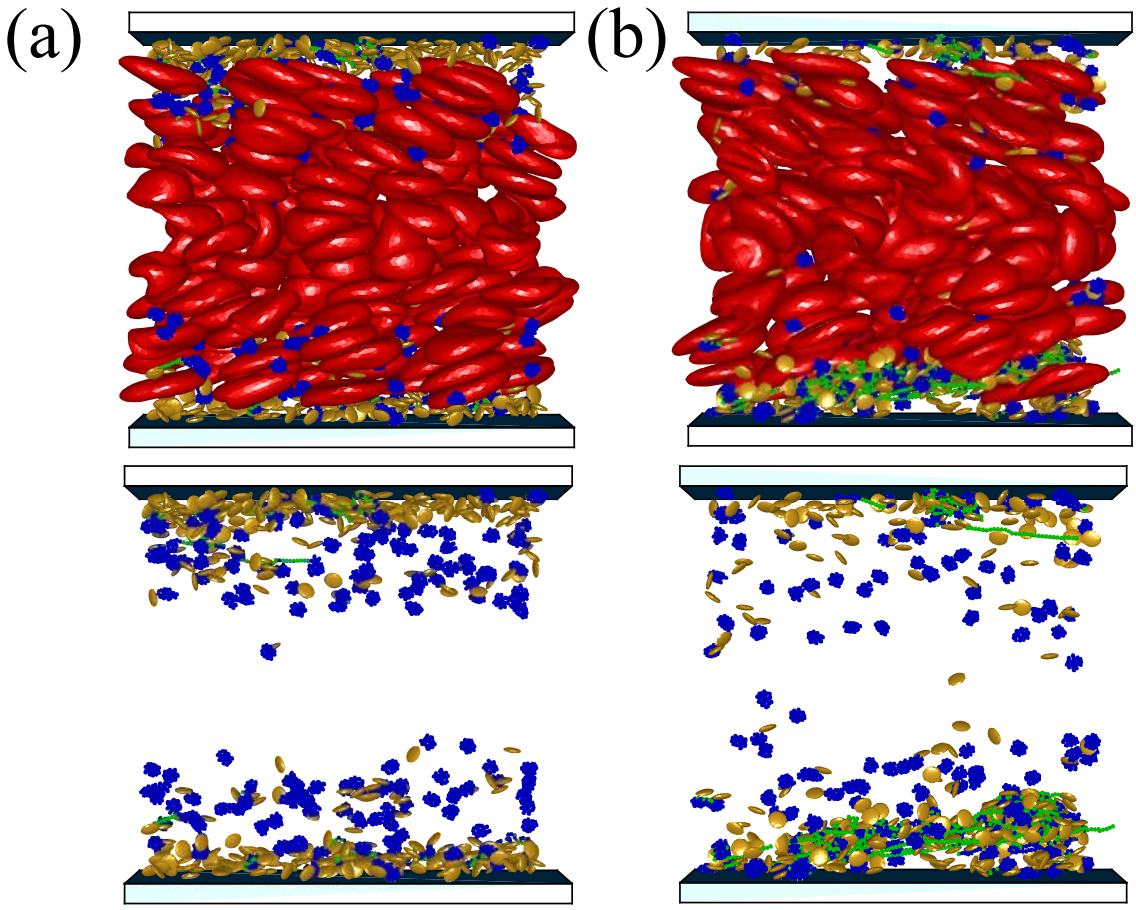

Figure 18: (a) Margination of platelets and VWFs into the RBC-FL leads to their localization near the walls. (b) Formation of VWF-platelet aggregates near the walls after the stretching and activation of marginated VWFs. In the snapshots, RBCs are plotted in red and platelets in yellow. VWFs are shown by blue (inactive) and green (active) monomers. The bottom row shows the corresponding snapshots with only platelets and VWFs present.

Following the two conditions for the formation of VWF-platelet aggregates, blood flow in a channel (or a vessel) can be divided in two zones depending on the local shear rate, which is schematically shown in Fig. 17(b). The region near the walls with $\dot{\gamma} > \dot{\gamma}_c$ is called an aggregation zone, where the formation of aggregates is possible. The region around the center of the channel is referred to as a dissociation zone, where formed VWF-platelet aggregates are expected to break apart (at least for the case of catch-slip model M1). Note that the formation of new aggregates is not possible in the dissociation zone due to small local shear stresses, which does not facilitate the activation of VWFs. Clearly, when blood flow in a vessel is weak enough, the aggregation zone may completely disappear due to small local shear rates near the walls, leading to no aggregate formation under such flow conditions.

4.3.1 Reversible aggregate formation in blood flow

We first focus on the case of normal functioning of VWF, which is mimicked by the catch-slip model M1. At the start of the simulation, all VWFs have a globular form (i.e., non-adhesive), and are uniformly distributed within the simulation domain together with platelets and RBCs, without any overlaps and any bonded structures. As the driving force is applied to initiate blood flow, RBCs migrate toward the channel center, while platelets and VWF globules slowly migrate (or marginate) toward the channel walls, see Fig. 18(a). As a result, the concentration of platelets and VWFs in the RBC-free layer (RBC-FL) increases many folds, providing favorable conditions for the formation of VWF-platelet aggregates.

In addition to the increased concentration of platelets and VWFs near the walls due to margination, the shear rate close to the walls is the largest in blood flow. In our simulations, the wall shear rate is $\dot{\gamma}_w = fnL_y/(2\eta) \approx 1152\ s^{-1}$. Note that it is smaller than $\dot{\gamma}_c \approx 2000\ s^{-1}$ predicted for VWF stretching in pure shear flow. In blood flow within the RBC-FL, VWF stretches and becomes activated at much lower shear rates, due to its quasi-confinement between the wall and flowing RBCs [170]. As a result, marginated VWFs quickly stretch within the RBC-FL and start binding nearby platelets, resulting in the formation of VWF-platelet aggregates [see Fig. 18(b)]. These aggregates grow in size by binding other activated VWFs and platelets or through the coalescence of two or more smaller aggregates.

As the aggregates grow in size within the RBC-FL, they acquire a significant lift force due to hydrodynamic interactions with the wall [3, 33, 197], and start migrating away from the wall. The migration away from the wall occurs roughly when the aggregate size exceeds the thickness of the RBC-FL. As VWF-platelet aggregates move toward the channel center, they experience a significant reduction in flow stresses, which results in their dissociation into separate unbound platelets and VWFs, as shown in Fig. 19(a). This behavior is consistent with the proposition of aggregation and dissociation zones illustrated in Fig. 17(b), depending on the lateral position of VWF-platelet aggregates in the channel. Interestingly, the described process repeats after the dissociation of aggregates. Freed platelets and VWFs marginate into the RBC-FL again, and participate in the formation of new aggregates near the walls. As a result, bond interactions described by the catch-slip model M1 lead to the formation of reversible aggregates with a continuous interchange between aggregation and dissociation, as a function of the lateral position within the channel.

4.3.2 Irreversible aggregates in blood flow

As we mentioned before, the slip bond model is expected to result in the formation of stable irreversible aggregates. At the start of the simulation, the behavior of the slip bond model

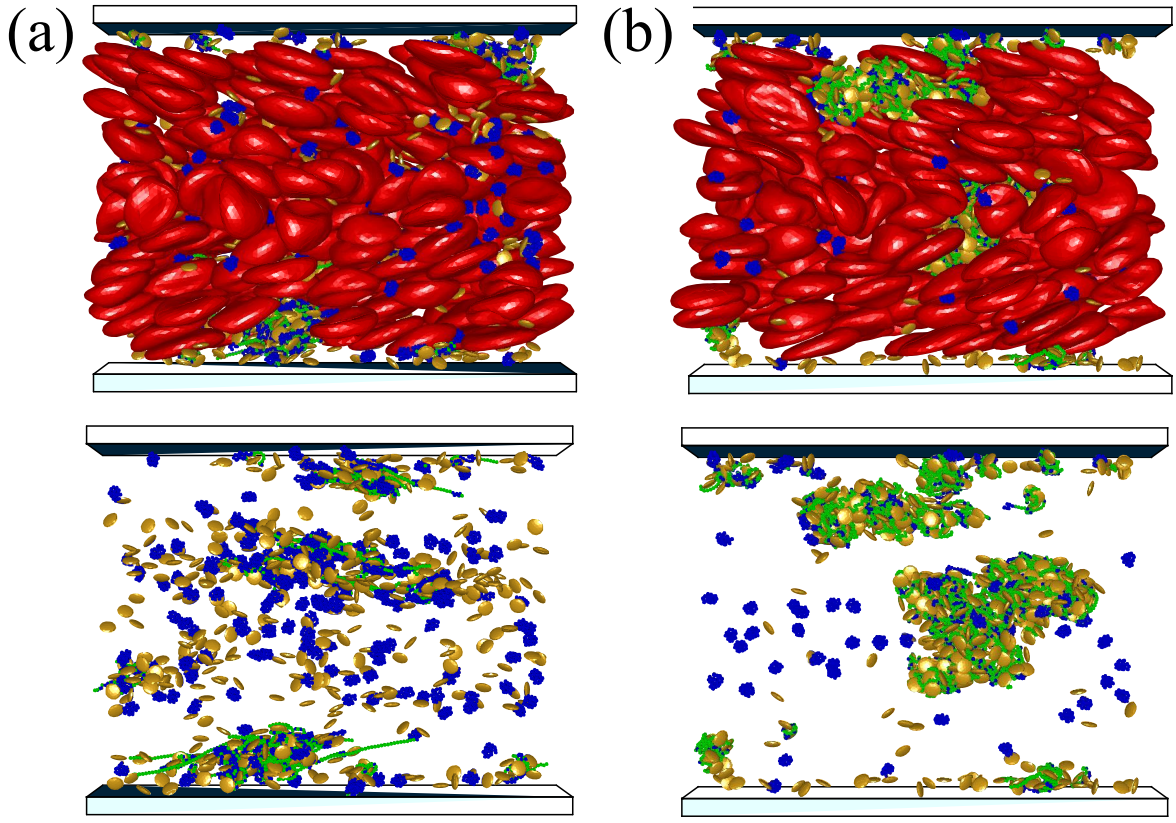

Figure 19: VWF-platelet aggregates in blood flow. (a) Dissociation of aggregates for the case of catch-slip model M1, as they migrate away from the walls and enter the dissociation zone with $\dot{\gamma} < \dot{\gamma}_c$. In this case, reversible aggregation of platelets and VWFs is observed. (b) The slip bond model leads to the formation of irreversible VWF-platelet aggregates. They migrate toward the channel center and show no significant dissociation during the simulation time. The bottom row shows the corresponding snapshots with only platelets and VWFs present.

is similar to that with the catch-slip model M1 described in Section 4.3.1. Free platelets and VWFs first marginate into the RBC-FL, where VWFs stretch and become activated, followed by the formation of VWF-platelet aggregates. When the aggregates are large enough, they migrate toward the channel center, where no significant dissociation is observed, as shown in Fig. 19(b). In fact, these aggregates eventually reach the channel center, where the shear stresses are quite small, but do not exhibit any dissociation for the rest of the simulation. The formation of new aggregates near the walls also stops, because the numbers of platelets and VWFs are fixed in the simulation, and most of them are already part of the existing irreversible aggregates.

4.3.3 Dynamic characteristics of different aggregate types

To quantify the behavior of VWF-platelet aggregates for different bond models, we analyse the size of aggregates (i.e., the total number of VWFs and platelets), their lateral position within

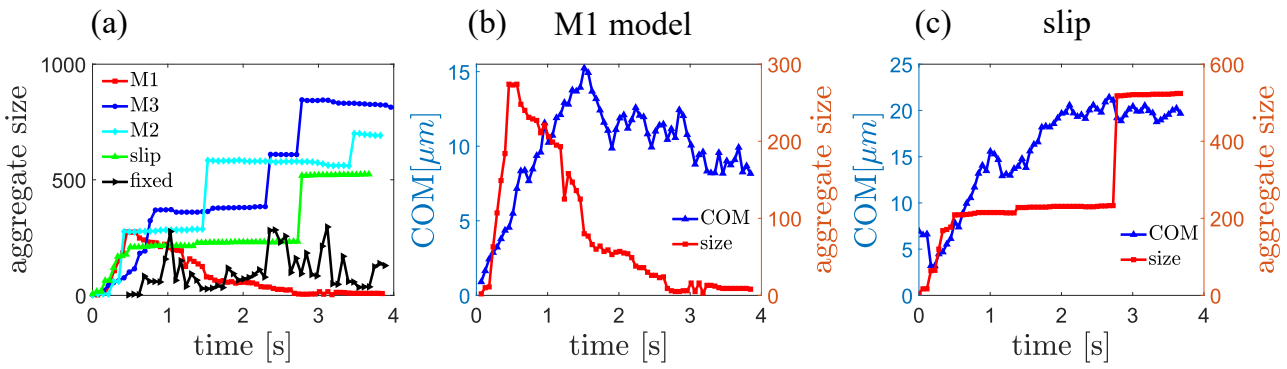

Figure 20: Size of aggregates and their position in the channel as a function of time. (a) Aggregate size (or the total number of platelets and VWFs forming it) for different bond models, including catch-slip models M1 (red squares), M2, (blue circles), and M3 (cyan diamonds), the slip model (green triangles), and the model with a fixed off rate (black triangles). (b) Aggregate size and the distance of its center-of-mass (COM) to the wall for catch-slip model M1. (c) Aggregate size and the distance of its COM to the wall for the slip model.

the channel and their asphericity, stretching of VWFs, and the average lifetime of bonds within the aggregates. Figure 20(a) presents aggregate sizes as a function of time for different bond models (see Fig. 16 and Table 2). Note that initial conditions are the same in all simulations, so that the processes of margination and aggregate formation near the wall at short times are similar for all cases [see Fig. 20(a)], except for the model with a fixed off-rate. It is apparent that the chosen fixed value of k_{off} is too large to sustain large aggregates consisting of more than about 200 platelets and VWFs. Another striking difference is that the aggregate size for the catch-slip model M1 starts to decay after the initial growth, while for the M2, M3, and slip models, the size monotonically increases. The onset of the decay for the M1 model coincides with aggregate migration away from the wall and entering the flow dissociation zone, as can be seen from the center-of-mass (COM) position of the aggregate with respect to the wall in Fig. 20(b). After the migration toward the channel center, the aggregate fully dissociates. The time of aggregate dissociation corresponds to several seconds, as can be seen from the decay of aggregate size. In contrast, the size of aggregates with slip bonds increases monotonically, even after the aggregate left the wall, see Fig. 20(c). This quantitatively confirms the irreversibility of aggregates with slip bonds, at least over the time scale of our simulations. The sudden jumps in aggregate size in Fig. 20(c) correspond to merging of two separate aggregates as they spontaneously encounter each other in flow. A very similar behavior is also observed for the catch-slip models M2 and M3 [see Fig. 20(a)], such that the formed aggregates are nearly irreversible on the time scale of simulations.

Differences in aggregate formation and dissociation described above are due to distinct bond lifetimes (or off-rates), which also depend on the length of bonds or stresses applied to them. Figure 21 shows the average lifetime of bonds within aggregates for the catch-slip model M1 and the slip model as a function of time. The average lifetime of catch-slip bonds in Fig. 21(a) is

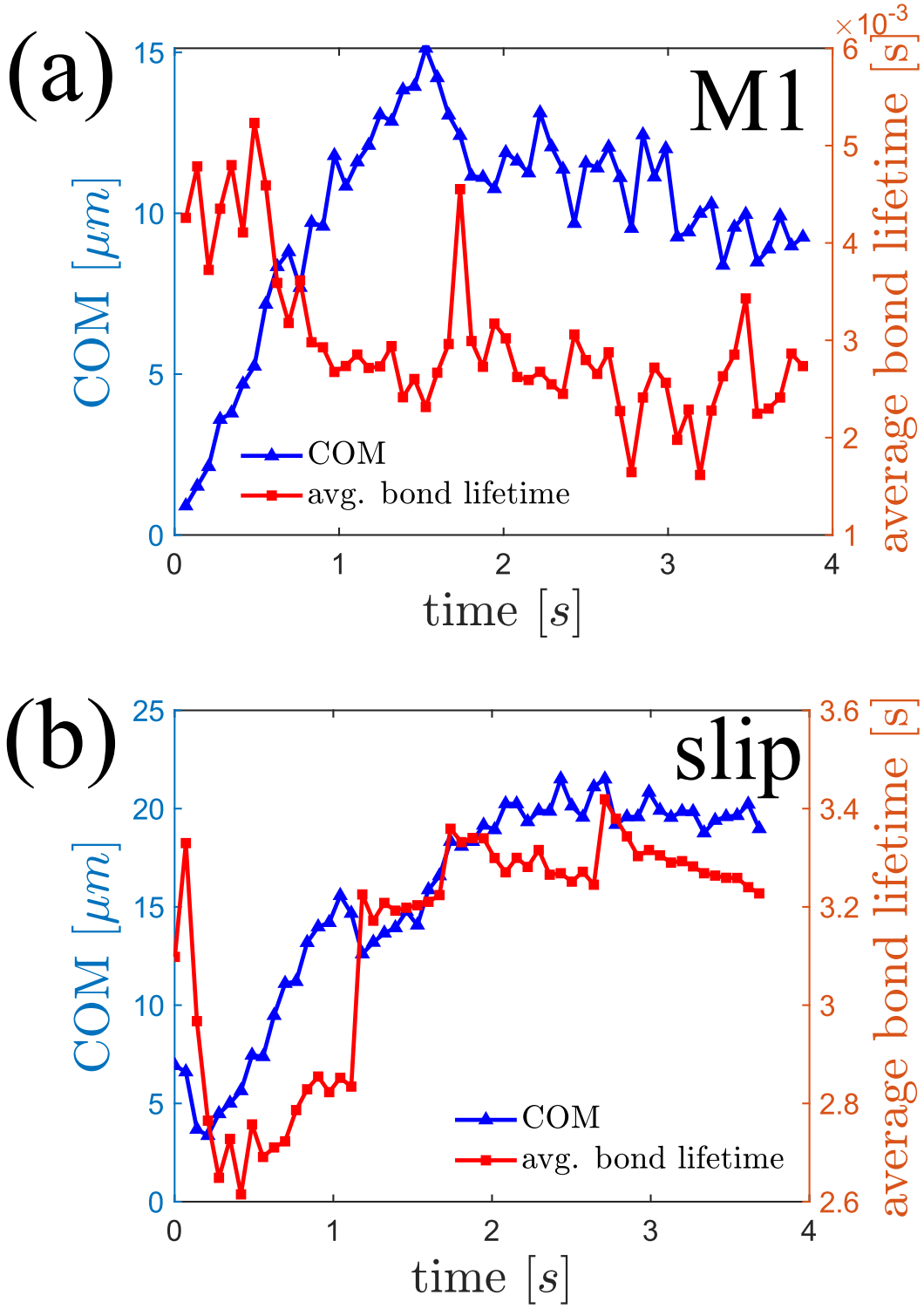

Figure 21: Average bond lifetime and the center-of-mass (COM) position of aggregate with respect to the wall as a function of time for (a) catch-slip model M1 and (b) slip model.

about three orders of magnitude smaller than that for slip bonds in Fig. 21(b). For comparison, the average lifetime of catch-slip bonds is also about three orders of magnitude smaller than the dissociation time of several seconds for the whole aggregate [see Fig. 20(b)]. For reversible aggregation, it is intuitive that the average bond lifetime should be significantly smaller than the aggregate dissociation time, because many bonds need to be broken during dissociation, and new bonds can also be formed. Furthermore, as aggregates migrate away from the wall, the average lifetime of catch-slip bonds decreases, since flow stresses in the middle of the channel are smaller than at the wall. In contrast, the average lifetime of slip bonds increases as the aggregates migrate toward the channel center. Thus, the magnitude of bond lifetime and its dependence on applied stresses are crucial for the reversibility of VWF-platelet aggregation. Another important aspect for the reversibility of aggregation is the deactivation of VWF monomers. Within the near-wall region, even if a bond between a platelet and VWF monomer is broken, the VWF chain remains stretched and activated, so that the free binding site quickly forms a new bond. In contrast, within the dissociation zone, a freed monomer of VWF can get deactivated due to local chain collapse at low shear stresses. As a result, the dependencies of both bond lifetime and monomer activation/deactivation on local flow stresses determine whether VWF-platelet aggregates are reversible or not.

Another interesting property is the deformability of formed VWF-platelet aggregates in flow. Figure 22 shows the asphericity of aggregates for the catch-slip model M1 and slip model as a function of time. Asphericity is computed as $\alpha = [(\lambda_1-\lambda_2)^2+(\lambda_2-\lambda_3)^2+(\lambda_3-\lambda_1)^2]/(2R_g^4)$, where λ_1, λ_2, and λ_3 are the eigenvalues of the gyration tensor based on all particles within the aggregate and $R_g^2 = \lambda_1 + \lambda_2 + \lambda_3$. The asphericity characterizes the deviation from spherical symmetry, such that it should be close to zero for a spherical aggregate, and to unity for a stretched configuration. For the catch-slip model M1 in Fig. 22(a), the asphericity first rapidly increases, as the aggregate grows, and then fluctuates around a value of $\alpha \simeq 0.5 - 0.6$, which indicates that the aggregate is rather soft and subject to significant stretching in flow. The fluctuations in α are due to local shear flow that periodically stretches and compresses the aggregate. For the slip model in Fig. 22(b), the asphericity is on average smaller than for the catch-slip model M1 and also has smaller fluctuations. This indicates that the aggregate for the slip model has a more spherical shape and is less deformable, which is expected due to persistent integrity of the irreversible aggregate.

Finally, Fig. 23 presents end-to-end distance distributions for both free VWFs and those within aggregates to characterize and compare VWF stretching under different conditions. Intuitively, the distributions of end-to-end distances for free VWFs (i.e., when they are not a part of any aggregate) are very similar for the catch-slip model M1 and the slip model, since blood flow conditions and the associated shear stresses are the same. However, VWFs within aggregates are much more stretched than freely flowing VWFs, as they frequently connect several

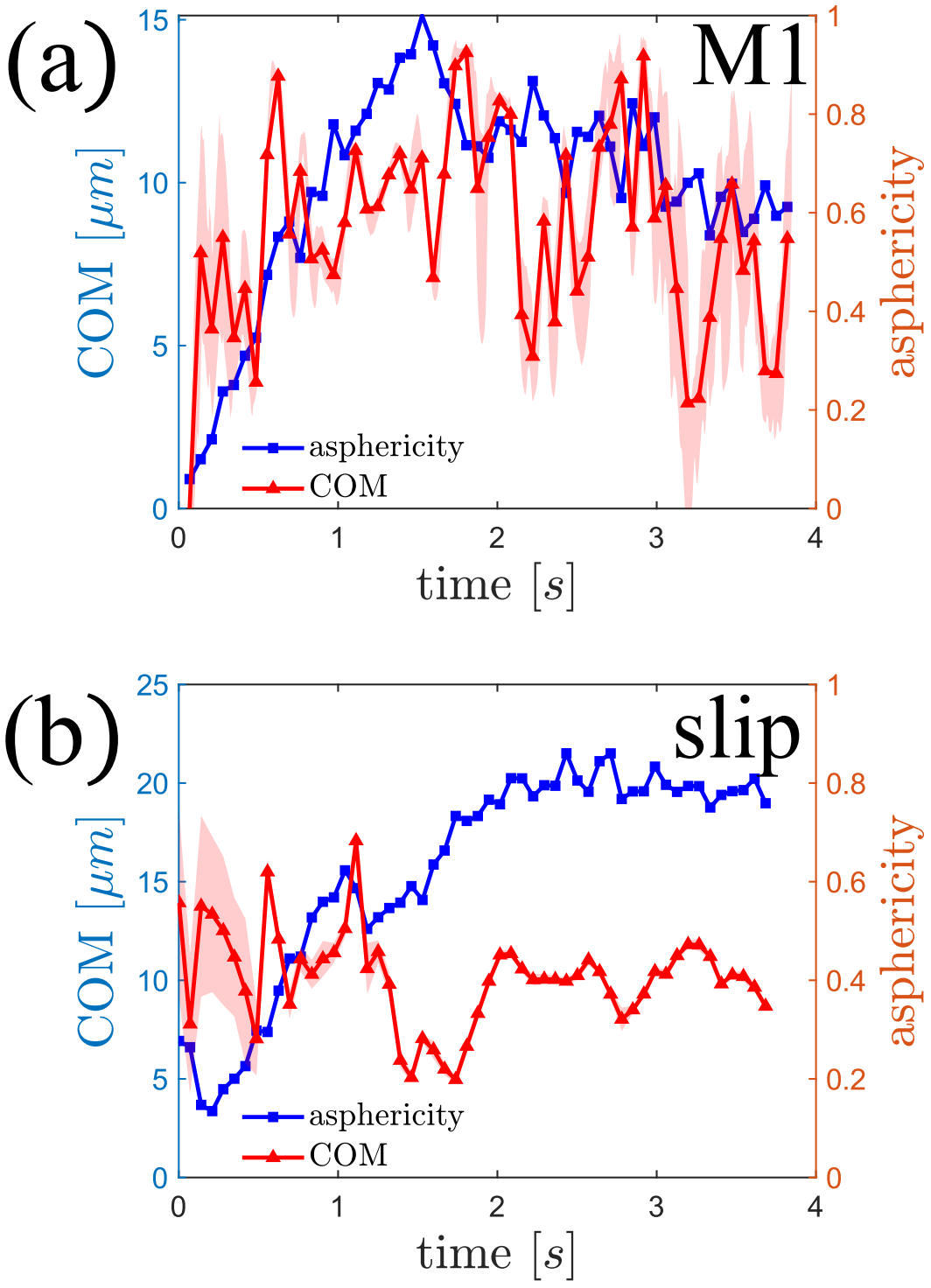

Figure 22: Asphericity and the position of aggregate center-of-mass (COM) with respect to the wall as a function of time for (a) catch-slip model M1 and (b) slip model. The shaded areas represent local standard deviation.

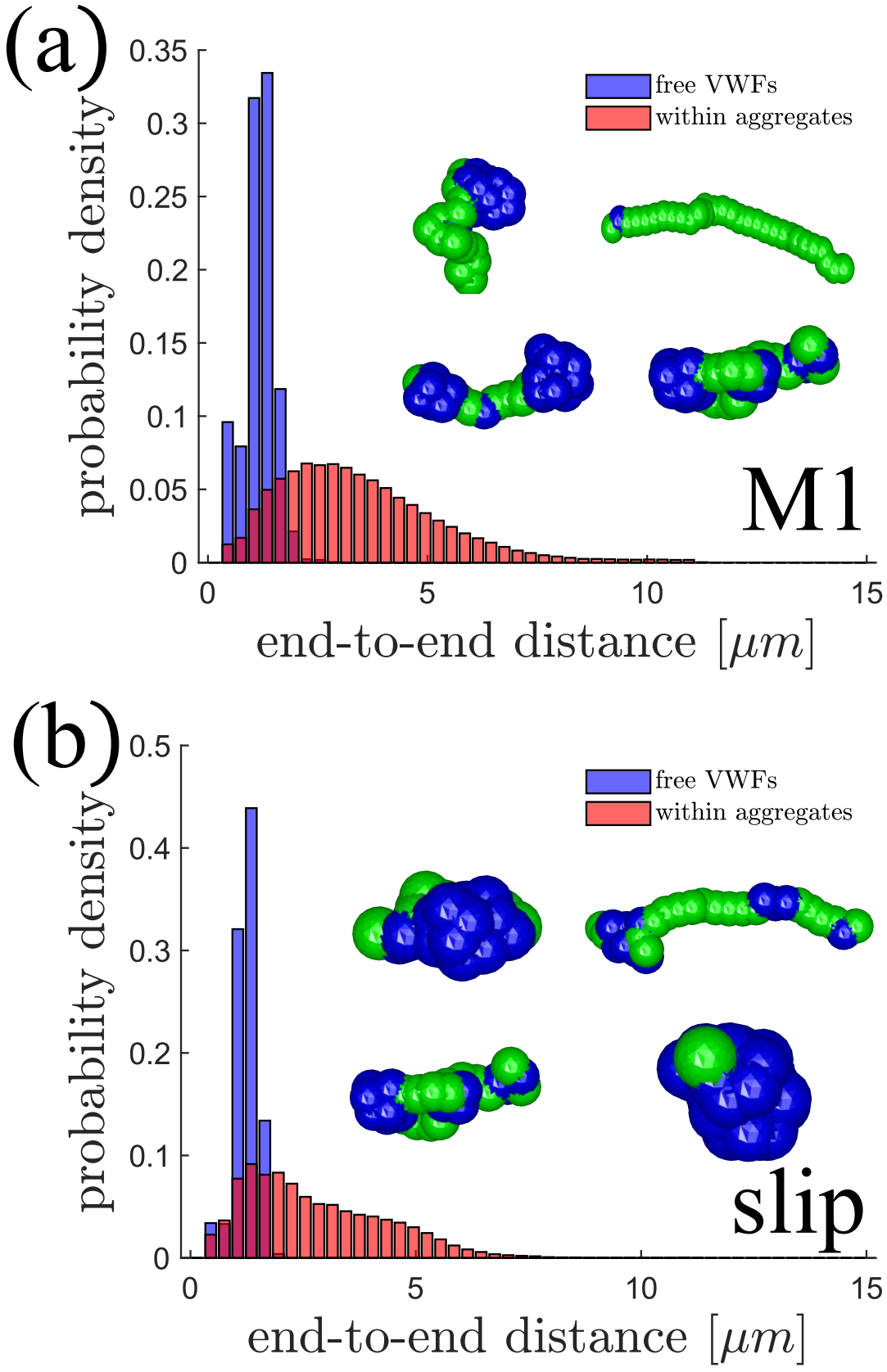

Figure 23: End-to-end distance distributions for both soluble VWFs and those within aggregates for (a) catch-slip model M1 and (b) slip model. Insets show a few exemplary configurations of VWF within aggregates. Activated monomers are green, while inactive monomers are blue.

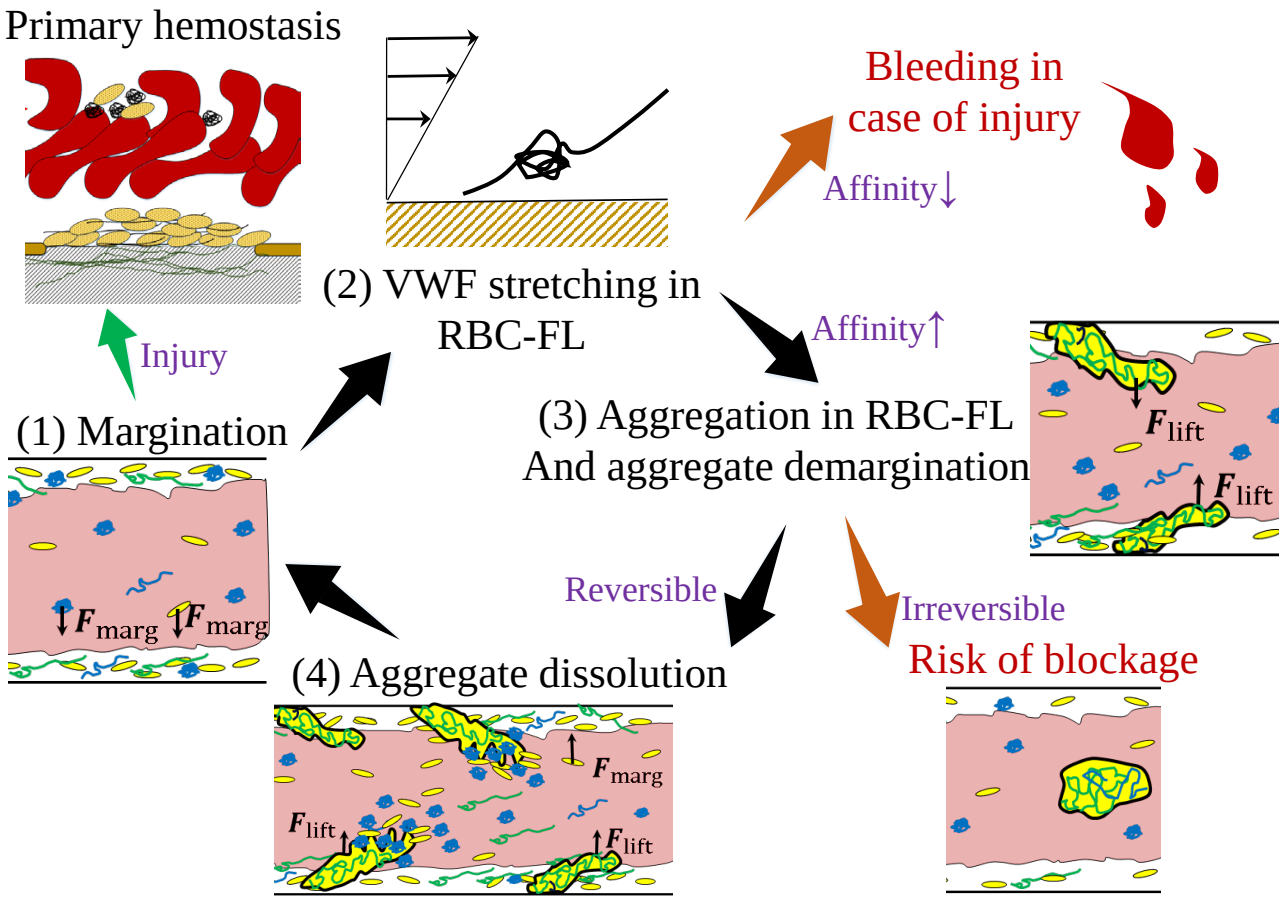

Figure 24: A comprehensive summary of platelet-VWF aggregation in blood flow. The aggregate formation process includes several stages, including (1) margination of platelets and VWF molecules, (2) VWF stretching in the RBC-FL, (3) aggregate growth within the RBC-FL, and (4) the migration away from the wall with a consecutive disaggregation under physiological conditions or possible retention of the aggregate in a pathological scenario. Note that this process is expected to be continuously repeated within the microvasculature.

platelets together. The typical VWF conformations in aggregates [see insets in Fig. 23] show moderate stretching and binding to only a few platelets. The distribution in Fig. 23(a) for VWFs within aggregates indicates that they are more stretched than those for the slip model in Fig. 23(b). This is due to the reversibility of aggregates in case of the catch-slip model M1, so that when the aggregates dissociate, they become more deformable, which results in additional stretching of VWF polymers.

4.4 Discussion

We have studied the behavior of VWF-platelet aggregates in blood flow. A comprehensive overview of the deduced mechanisms is shown in Fig. 24. To initiate aggregation, VWF molecules must be stretched by flow stresses, and come into contact with flowing platelets. The stretching of VWF takes place primarily near the wall, where the shear stresses are largest

[170]. Through the margination of VWFs and platelets into the RBC-FL, their concentration in the near wall layer might be substantially increased, which favors the formation of VWF-platelet aggregates as long as the activation of VWF can occur. As a result, VWF-platelet aggregates grow within the RBC-FL until they are large enough to be forced back into the bulk of blood flow. In the bulk, reversible aggregates may fall apart due reduced flow stresses, while in the case of irreversible aggregation, they may retain their content for a long time. This process is expected to continuously repeat with a periodic formation and dissociation of small VWF-platelet aggregates.

Under normal conditions, our model predicts the dissociation of aggregates when they are away from the walls, and therefore, are subject to reduced flow stresses. This is qualitatively consistent with the dissociation of wall-bound aggregates in the experiments [36, 43, 77], whenever the flow is significantly reduced or stopped. To verify that a reduction of flow stresses is the primary mechanism for disaggregation, we have also simulated blood under Couette flow, where the lower wall in our setup is kept stationary and the upper wall is moved with a prescribed velocity. The aggregation process for the Couette flow conditions initially resembles that for the pressure-driven Poiseuille flow. VWFs and platelets first marginate into the RBC-FL, where the formation of aggregates is observed. However, after the migration of large enough aggregates away from the wall, they show no disaggregation even for the case of catch-slip M1 bonds, since no reduction in flow stresses occurs in the bulk. Thus, the simulations confirm that a significant reduction in applied stresses is necessary for disaggregation.

There can be numerous deviations from the described process under some pathological conditions, with both reduced and enhanced aggregate formation. For instance, in vessels with low flow rates (e.g., venular flow), the shear stresses near vessel walls might be not sufficient for VWF stretching and activation, resulting in reduced formation of aggregates. Furthermore, when interactions between VWFs and platelets are too weak to sustain large enough aggregates under local flow conditions, the formation of aggregates can be significantly limited. In this case, small floppy aggregates can still form, but they are generally very short lived. This can occur in certain types of von Willebrand disease (VWD) [177, 207] due to malfunctioning of VWF proteins. Moreover, reliable formation of VWF-platelet aggregates requires the presence of long enough VWF molecules, since short VWF chains do not stretch significantly at physiological shear rates and thus cannot result in proper aggregate formation.

On the other hand, the formation of VWF-platelet aggregates can also be significantly enhanced. For example, when VWF molecules are stretched and activated at lower shear stresses than those for normal VWF functioning, the formation of aggregates should also become possible at reduced flow rates. Furthermore, if the lifetime of bonds between VWFs and platelets is substantially increased, the dissociation of aggregates can also become significantly slower.

This has been illustrated in our simulations by the catch-slip models M2 and M3, where the formed aggregates did not dissociate over the whole time of simulations. Theoretically, such VWF-platelet aggregates are still reversible, but the disaggregation is expected to occur over much longer time scales. These simulations can mimic a variety of pathological conditions under which the aggregation is significantly enhanced, leading to an increased risk of vessel blockages [186].

It is worthwhile to compare the main conclusions of our study with a previous simulation study [36] without RBCs, where platelets were modeled as spherical colloids. The presence of RBCs is essential for the margination of platelets and VWFs in the RBC-FL, which implies much higher wall-shear rates for a fixed flow rate, locally higher concentrations of VWFs and platelets near the wall, and thereby strongly enhanced aggregate formation. Furthermore, the presence of RBCs implies a blunt flow profile in the channel center, which favors aggregate dissociation. At low hematocrits, the margination of platelets and VWFs is significantly diminished, so that aggregate formation near a wall is expected to be strongly reduced. On the other hand, the size of aggregates near a wall (if they can form) may become a bit larger, since the thickness of the RBC-FL is larger at lower hematocrits. In summary, the presence of RBCs is essential and affects the hemostasis process both qualitatively and quantitatively.

It is also important to discuss possible limitations of the simulation model. Note that we study channel flow with concentrations of VWFs and platelets which are larger than under physiological conditions. The main reason for this choice is to accelerate the formation of VWF-platelet aggregates, making our simulations feasible. Since margination and stretching of individual VWFs should be nearly independent of their concentration, as this is not a cooperative process, the formation of VWF-platelet aggregates near the wall should be qualitatively similar for the case of reduced concentration of platelets and VWF, but slower due to a lower collision rate. Note that growing VWF-platelet aggregates remain stable at high shear rates near the wall, which is well supported by the simulations of linear Couette flow, suggesting that the aggregates can grow up to sizes required for leaving the RBC-FL. As a result, lower concentrations of VWFs and platelets are expected to slow down the formation of aggregates, but the described process of reversible aggregation should remain qualitatively unaffected. Furthermore, VWF-platelet aggregation can be significantly affected by various regulatory processes present in blood. For instance, VWF length is regulated by the protease ADAMTS13, which is able to cleave VWF molecules when the cleavage sites are accessible (normally when VWF is stretched) [206, 207]. We did not consider possible cleavage of VWF, and the effect of reduced chain lengths, which are expected to reduce the tendency of aggregate formation. Clearly, the blood-flow geometry considered in simulations is relatively simple, in comparison to complex network-like structures in the microvasculature. Despite this simplification, our simulations qualitatively predict reversible aggregation in blood flow, though the aggregation process can

be quantitatively different for a variety of geometries and flow conditions within the microvasculature. Finally, we did not consider the adhesion of aggregates at vessel walls, which would be expected at sites of injured endothelium. In such cases, we expect a stronger stretching of wall-bound VWFs, leading to efficient aggregate formation at the wall. Wall-bound aggregates should not spontaneously dissociate, as they are constantly subjected to large flow stresses near the wall.

4.5 Conclusion

Our simulations suggest the continuous formation and dissociation of small VWF-platelet aggregates within the microcirculation. This process has not been observed directly in experiments, though the formation of stationary wall-bound reversible aggregates was demonstrated in several experimental studies [36, 43, 77]. It is clearly difficult to follow and observe unbound dynamic aggregates for a longer time, as they are quickly advected by the flow. It should be easier to observe already formed aggregates downstream, for which relatively long microchannels used in *in vitro* experiments are required to allow for aggregate formation. For the proof of concept, an elevated concentration of platelets and VWF would be advantageous to significantly accelerate the formation of VWF-platelet aggregates. Furthermore, microchannels employed in experiments should be small enough (presumably smaller than about $40 - 50\ \mu m$ in diameter) to avoid the obstruction of optical observation of aggregates by the presence of a large number of RBCs. In addition, flow rates in small channels are lower than in large channels, which can simplify reliable monitoring of VWF-platelet aggregates. *In vivo* observation of dynamic VWF-platelet aggregates is likely even more challenging than their monitoring in *in vitro* experiments.

Even less clear is whether the reversible formation and dissolution of such aggregates has some biological function or not. Undoubtedly, hemostasis is a finely-tuned process that has to function for a wide range of local vascular geometries and flow conditions, since seemingly small changes in the hemostatic process can cause bleeding or undesirable thrombotic events. A possible function of reversible aggregation is the neutralization of aggregates which have spontaneously formed or detached from an existing stationary aggregate, thus preventing possible occlusion of microvessels – while at the same time recycling the components for further use. The formation of VWF-platelet aggregates may also affect the distribution of platelets and VWFs in the microvasculature, since the aggregates contain significant amounts of these two components. We hope that our simulation predictions will motivate further experimental studies in this area of research.

5 Primary Hemostasis in Silico

5.1 Problem Description

Hemostasis, or blood clotting, is the physiological response of the body to vascular injury. It involves a tightly regulated sequence of steps that lead to the formation of a blood clot to stop bleeding. The first phase of this response (*i.e.*, primary hemostais) refers to the adhesion and aggregation of blood platelets at the site of vascular injury [155, 232]. Under low shear rates, platelet attachment is primarily mediated by integrin receptors. However, at shear rates exceeding approximately 600–900 s^{-1} [102, 182] — relevant for microvascular flows[115, 167] — integrin-mediated adhesion becomes unreliable. In such cases, a large multimeric protein called von Willebrand factor (vWF) plays a key role, mediating platelet capture at the injury site [126, 172, 181, 238].

vWF molecules, composed of dimeric subunits and reaching lengths of several tens of micrometers, are found both freely circulating in plasma and anchored to subendothelial tissue [41, 75, 207]. Under static conditions, vWF assumes a compact, globular conformation due to self-attractive interactions between its subunits, which shield its adhesive domains and prevent platelet binding [206, 226]. However, when exposed to elevated shear rates (i.e., $\geq 2000\ s^{-1}$), as demonstrated in both experiments [77, 185] and simulations [9, 10, 95], vWF unfolds, exposing its adhesive sites. Single-molecule experiments have shown that upon stretching, these adhesive domains become accessible, enabling vWF to bind platelets and facilitate aggregation when tethered to a surface[77]. Moreover, experiments at high-shear environments show reversible platelet-vWF aggregates can form both on surfaces and in soluble form [36, 96, 184, 185]. These reversible aggregates constitute the main building block of the primary hemostasis.

Platelets, or thrombocytes, are small, disc-shaped cell fragments found in the blood that plays a central role in hemostasis. Unlike red blood cells (RBCs), platelets are anucleate and they originate from large bone marrow cells called megakaryocytes, which release platelets into the bloodstream [128]. Once activated by signals from damaged blood vessels, platelets adhere to exposed collagen or von Willebrand factor at the injury site, undergo a shape change, and release chemical signals that recruit and activate additional platelets [31, 183]. This leads to the formation of a platelet plug. Platelets also provide a surface for the coagulation cascade, which stabilizes the plug with a fibrin mesh [106].

Following vascular injury, the immediate physiological response involves rapid platelet adhesion and aggregation at the injury site, followed by platelet activation and the formation of fibrin bridges to stabilize the clot. This adhesion mechanism is mediated by vWF at high-shear rates. Platelet adhesion and aggregation typically occur within 1–5 seconds, whereas activation and stabilization can take minutes [109, 228]. Due to these differing time scales, various model-

ing approaches have been proposed to address different phases of the process [91, 159]. Recent modeling studies have focused on the clot stabilization [27, 93, 216, 218] and material transport [19, 216, 217, 245] within the formed clot. These studies assume a predefined shape of the blood clot either obtained from an experiment or calculating the material transport using PDEs omitting the existence of the RBCs. Experimental studies address the pathological conditions of occlusive thrombosis at extreme shear-rates ($> 10000\text{s}^{-1}$) [108, 109, 117, 118, 229, 237, 246], a regime where the clot formation known as shear-induced platelet aggregation (SIPA). In this setting clot formation is followed by vessel occlusion or thromboembolism and the targeted time scales for analysis is beyond the time scale of primary hemostais. Omitting the presence of vWF and assuming already formed clot, several studies address the capture of platelets and RBCs in the microvasculature [243, 244]. However, under elevated shear rates presence of soluble vWF is a must for clot growth [184].

Dysfunction in the hemostatic process can lead to life-threatening bleeding disorders and may arise from multiple causes. In high-shear environments, disorders related to primary hemostasis include von Willebrand disease, which is caused by vWF deficiency or dysfunction [97], and its platelet-side counterpart, the Bernard-Soulier syndrome, which involves defects in the GPIb receptor complex [119]. Moreover, recent studies have shown that COVID-19 can trigger thrombo-inflammation via exposition of anchored vWF to the vessel, leading to hypercoagulation, thromboembolism, and stroke [37]. Addressing the early phase of blood clot formation is therefore crucial for understanding and treating such conditions.

In this work, we investigate clot formation following vascular injury using a direct numerical simulation involving red blood cells (RBCs), platelets, and vWF in a high-shear microchannel environment under physiological shear rates [179]. We model the mechanosensitive behavior of vWF, which can bind to both platelets and a hemostatic surface representing the site of injury. The simulations employ non-periodic boundary conditions to allow continuous material transport thereby mimicking realistic blood flow during hemostasis. We analyze the dynamics of clot growth and thromboembolization, and demonstrate that hemodynamic conditions alone can impose an upper limit on clot size. In the following, the terms “low-shear”, "mid-shear" and “high-shear” simulations correspond to shear rates of $1152\,s^{-1}$, $1728\,s^{-1}$ and $2304\,s^{-1}$, respectively. Note that even the $1152\ s^{-1}$ case falls within the elevated-shear regime.

5.2 Simulation Setup and Model Parameters

Simulations of primary hemostasis requires models of blood agonists (*i.e.*, RBCs, platelets), vWF molecules, non-periodic boundary conditions and adhesive bonds. Figure 25 illustrates these models and shows a snapshot from a simulation, and problem setup whose detailed de-

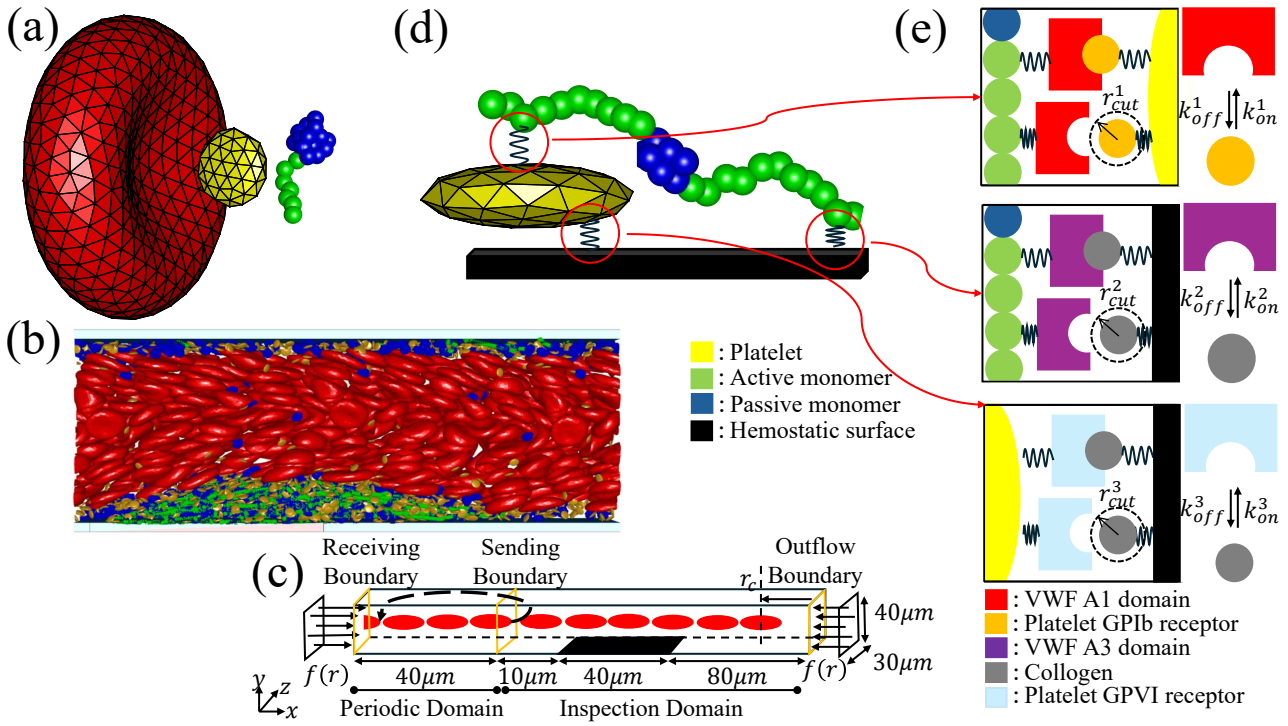

Figure 25: Illustration of the employed models and simulation setup.(a) Membrane model of the RBC (red), membrane model for platelet (yellow), shear-activated vWF model (green for activated monomers and blue for inactivated monomers). (b) A snapshot illustrating the growing clot. Same color code in panel (a) applies here. (c) A schematic of the simulation domain of size $170\mu m \times 40\mu m \times 30\mu m$. The domain is divided into an inspection domain and periodic domain. Periodic domain is bounded with receiving and sending boundaries whereas the inspection domain is bounded with outflow boundary. An SDPD pressure force, using the radial distribution function of a stagnant fluid, is applied to fluid particles within the SDPD interaction cutoff radius at the outflow and receiving boundaries to ensure continuity and force balance across the boundaries.(d) A representation of various bonding scenarios. (e) A schematic representation of various associating and disassociating bonds.

scription is provided below.

Fluid flow is simulated using an angular momentum conserving smoothed dissipative particle dynamics approach. The details of the method were given in Section 2.3.1 and Section 4. In the vicinity of the walls, to ensure no-slip boundary condition, we employed an adaptive shear force and frozen particles. Details can be found in Section 2.3.8 and Section 4.

Interactions between the fluid and suspended biological components — such as blood cells and von Willebrand factor (vWF) molecules — are captured by a dissipative coupling, which ensures momentum exchange and mimics viscous drag. More information about FSI interactions can be found in Section 2.3.8

Traditional periodic boundary conditions used in particle-based simulations can lead to ma-

	RBC		Platelet	
Parameters	Scaled units	Physical units	Scaled units	Physical units
N_v	500		60	
A		132.83×10^{-12} m^2	$0.162 D_r^2$	6.85×10^{-12} m^2
V	$0.336\ D_r^3$	92.4×10^{-18} m^3	$0.0041\ D_r^3$	1.127×10^{-18} m^3
μ	$4.77 \times 10^4\ k_BT/D_r^2$	4.83×10^{-6} N/m	$4.77 \times 10^5\ k_BT/D_r^2$	4.83×10^{-5} N/m
κ	$70\ k_BT$	3×10^{-19} J	$700\ k_BT$	3×10^{-18} J
k_d	$4.23 \times 10^4\ k_BT/D_r^2$	4.28×10^{-6} N/m	$4.23 \times 10^5\ k_BT/D_r^2$	4.28×10^{-5} N/m
k_a	$2.07 \times 10^6\ k_BT/D_r^2$	2.1×10^{-4} N/m	$3.81 \times 10^6\ k_BT/D_r^2$	3.86×10^{-4} N/m
k_v	$1.37 \times 10^7\ k_BT/D_r^3$	213.28 N/m^2	$2.75 \times 10^7\ k_BT/D_r^3$	428.11 N/m^2

Table 3: Parameters for RBCs and platelets are reported in dimensionless form using the effective RBC diameter $D_r = \sqrt{A_r/\pi}$ and the thermal energy scale k_BT at $T = 310, \mathrm{K}$, together with their corresponding physical values. Here, N_v denotes the number of membrane vertices, A the membrane surface area, V the enclosed volume, μ the membrane shear modulus, and κ the bending rigidity. The parameters k_d, k_a, and k_v represent the coefficients enforcing local area, global area, and volume constraints, respectively. Throughout all simulations, we set $A_r = 132.83$ and $k_BT = 0.1$, and and effective diameter of $D_r = 6.5$.

terial depletion when there is a sink present within the simulation domain. In our case, the vascular injury acts as an active sink, continuously extracting hemostatic material by capturing it from the free flow. As the simulation progresses, to prevent such depletion, we implement non-periodic boundary conditions at the inflow and outflow ends of the channel, as illustrated in Fig. 25(c).

In this setup, the simulation domain is divided into two subdomains using virtual surfaces. The sending boundary tracks the position and velocity of particles as they pass through and transmits this information to a receiving boundary, which then generates an identical copy of each corresponding particle (see Fig. 25(c)). The region between the sending and receiving boundaries effectively conserves mass, behaving as if it were a periodic domain. The sending boundary then injects the original copy into the inspection domain, where the hemostatic reaction occurs.

The inspection domain is bounded at the downstream by an outflow boundary, where particles, which are not captured by the vascular injury are removed from the system. To maintain continuity of mass and force balance across the boundaries, a SDPD pressure-force is applied to the fluid next to outflow and receiving boundary within a cut-off radii . This force is calculated based on the radial distribution function of the fluid particles sampled from bulk substance at rest.

Both red blood cells (RBCs) and platelets are represented as deformable particles, with a membrane enclosing a fluid volume. The RBC and platelet model has been discussed in Sec-

tion 2.3.4 and further details were given in Section 4. A more detailed formulation of these energy terms for the red blood cells can be found in Refs. [53, 55]. For the sake of clarity, parameters used for RBCs and platelets are re-summarized in Table 3, given in both simulation and physical units.

vWF model can be found in Chapter 2.3.5 and furhter details were given in Chapter 4. We use the same model parameters as in Chapter 4. For the sake of clarity, the parameters used for Equation 113 are as follows: $r_{\max} = 2\sigma$, $\sigma = 0.077 D_r$, $k_{\mathrm{s}} = 25000 k_{\mathrm{B}}T/\sigma^2$. k_BT is given in Table 3.

Excluded volume interactions and attraction between the monomers of same vWF molecule were imposed by Equation 114. The model parameters for vWF molecule are: $\epsilon = 16 k_{\mathrm{B}}T$, $r_{LJ} = 2.5\sigma$,where σ is given in the above paragraph.

The activation of the vWF monomers upon stretching is governed by two conditions which require extension and certain particle density in the vicinity of the monomer. These conditions were introduced in Section 2.3.5 and the corresponding parameters were given in Section 4.

A difference with Section 4; the number of adhesive bond types are more in this section. As we have hemostatic surface, the interactions between platelets-hemostatic surface and vWFs-hemostatic surface must be modeled. Attachment of platelets to vWF is modeled with the catch-slip mechanism as described in Chapter 4. For the sake of clarity, we explain the extended model and introduce the model parameters.

A pathway for platelet recruitment from the blood is the direct binding by collagen exposed from the damaged endothelial surface. This interaction however, mediates the platelet capture at moderate to low shear rates and its effect in high-shear environments is small. Therefore we model platelet-collagen interactions via a slip bond model, with a lower bond lifetime compared to vWF-platelet interactions. The interaction of vWF with a hemostatic surface can take place through various pathways. Soluble vWF can attach to collagen and other surface ligands on the exposed endothelial surface. We describe the adhesive interaction between vWF and a hemostatic surface with a catch-slip bond model, but keep bond lifetime highest among the other interactions in order to maintain a strong adhesion of vWF to the surface.

Adhesive interactions between activated vWF monomers, platelet membrane vertices and hemostatic surface are modeled via the formation of reversible bonds, characterized by predefined association and dissociation rates, denoted by $k^{\mathrm{i}}_{\mathrm{on}}$ and $k^{\mathrm{i}}_{\mathrm{off}}$, respectively [see Fig. 25(e)], where i from 1 to 3 denotes vWF-platelet, vWF-ligand and ligand-platelet interactions, respectively. Once a bond is established, it is represented by a harmonic potential of the form

bond type	k_{c}^0	x_c	x_{eq}	k_{s}^0	x_s	$r_{\mathrm{cut}}^{\mathrm{on}}$	$r_{\mathrm{cut}}^{\mathrm{off}}$
vWF − PLA	$5.75 \times 10^{-1}/\tau$	$0.0385D_r$	$0.0615D_r$	$5.75 \times 10^{-4}/\tau$	$0.0662D_r$	$0.067D_r$	$0.23D_r$
vWF − LIG	$5.75 \times 10^{-3}/\tau$	$0.0307D_r$	$0.0384D_r$	$5.75 \times 10^{-4}/\tau$	$0.0415D_r$	$0.046D_r$	$0.23D_r$
PLA − LIG	0	0	$0.023D_r$	$1.44/\tau$	$0.037D_r$	$0.0308D_r$	$0.23D_r$

Table 4: Kinetic, geometric, and cutoff parameters for different bond types. In all cases, $\lambda_c = \lambda_s = 1.06 \times 10^5\, k_{\mathrm{B}}T/D_r^2$ and $k_{\mathrm{on}} = 5.73 \times 10^3/\tau$.

bond type	k_{b}	r_0
vWF − PLA	$8.45 \times 10^6\, k_{\mathrm{B}}T/D_r^2$	$0.0615D_r$
vWF − LIG	$8.45 \times 10^6\, k_{\mathrm{B}}T/D_r^2$	$0.0384D_r$
PLA − LIG	$2.11 \times 10^6\, k_{\mathrm{B}}T/D_r^2$	$0.023D_r$

Table 5: Elastic bond parameters.

$U_b = k_b^{\mathrm{i}}(r - r_0^{\mathrm{i}})^2$, where k_b^{i} is the bond stiffness of the corresponding adhesive interaction, and r_0^{i} is the equilibrium bond length. The probabilities of bond formation ($P_{\mathrm{on}}^{\mathrm{i}}$) and rupture ($P_{\mathrm{off}}^{\mathrm{i}}$) are governed by kinetic expressions derived from Bell's model [25], which relate these probabilities to the local mechanical environment and force-dependent dynamics of the bond,

$$\frac{\mathrm{d}P_{\mathrm{on}}^i}{\mathrm{d}t} = -k_{\mathrm{on}}^i P_{\mathrm{on}}^i, \quad \text{for } r \le r_{\mathrm{cut}}^{\mathrm{on,i}}, \tag{118}$$

$$\frac{\mathrm{d}P_{\mathrm{off}}^{\mathrm{i}}}{\mathrm{d}t} = -k_{\mathrm{off}}^{\mathrm{i}} P_{\mathrm{off}}^{\mathrm{i}}, \quad \text{for } r \le r_{\mathrm{cut}}^{\mathrm{off,i}}, \tag{119}$$

where $r_{\mathrm{cut}}^{\mathrm{on,i}}$ and $r_{\mathrm{cut}}^{\mathrm{off,i}}$ are the cutoff ranges for bond association and dissociation, respectively. Note that $P_{\mathrm{on}}^{\mathrm{i}} = 0$ for $r > r_{\mathrm{cut}}^{\mathrm{on,i}}$ and $P_{\mathrm{off}}^{\mathrm{i}} = 1$ for $r > r_{\mathrm{cut}}^{\mathrm{off,i}}$. In simulations, we assume $k_{\mathrm{on}}^{\mathrm{i}}$ to be constant, while $k_{\mathrm{off}}^{\mathrm{i}}$ follows the aforementioned catch-slip or slip behavior. This is described by the two-pathway model [165], which assumes two force-dependent barriers for bond dissociation,

$$k_{\mathrm{off}}^{\mathrm{i}} = k_{\mathrm{c}}^0 \exp\left(\frac{\lambda_c(r - x_{\mathrm{eq}})\delta_{\mathrm{c}}}{k_{\mathrm{B}}T}\right) + k_{\mathrm{s}}^0 \exp\left(\frac{\lambda_s(r - x_{\mathrm{eq}})\delta_{\mathrm{s}}}{k_{\mathrm{B}}T}\right), \tag{120}$$

where the first term represents a catch-bond dissociation rate, while the second term corresponds to a slip-bond rate. Here, k_{c}^0 and k_{s}^0 are the catch and slip equilibrium off-rates. λ_c and λ_s represent the strengths of the catch and slip parts, and $\delta_{\mathrm{c}} = x_{\mathrm{c}} - x_{\mathrm{eq}}$ and $\delta_{\mathrm{s}} = x_{\mathrm{s}} - x_{\mathrm{eq}}$, where x_{c}, x_{s}, and x_{eq} are the catch, slip, and equilibrium characteristic lengths. Note that the condition $x_{\mathrm{c}} < x_{\mathrm{eq}} < x_{\mathrm{s}}$ should be satisfied, so that the catch part dominates for $r < x_{\mathrm{eq}}$, while the slip part dominates for $r > x_{\mathrm{eq}}$.

Blood flow is simulated within a domain of $L_x \times L_y \times L_z = 170\mu m \times 40\mu m \times 30\mu m$, with 180 RBCs, 384 platelets, and 192 vWFs in the periodic domain enclosed by the sending and receiving boundaries. The subdomain between these two boundaries has a size of $L_x \times L_y \times L_z = 40\mu m \times 40\mu m \times 30\mu m$, and is long enough in the flow(x)-direction so that any

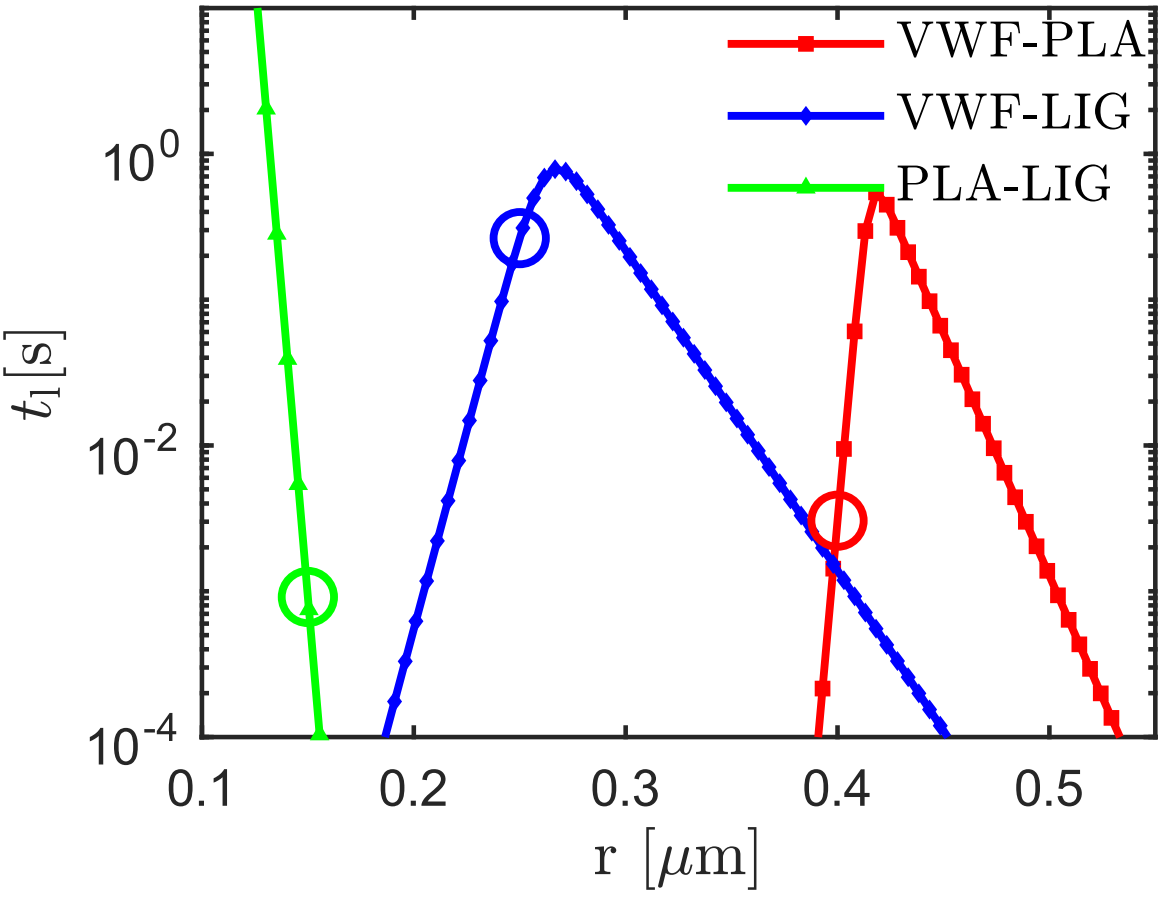

Figure 26: Comparison of lifetimes $t_l = 1/k_{\text{off}}$ for different bond types (see Table 4 and Table 5) as a function of bond length r. The centers of circles on each curve shows the equilibrium bond length of the adhesive interaction represented by a harmonic spring.

correlation in the 3D-structural composition of RBCs decays to zero for the given channel height (*i.e.* L_y) and percentage hematocrit [56]. Periodic subdomain strictly conserves the number of particles, but the number of blood agonists can vary in the inspection domain due to arrest of hemostatic material to the wound. The simulation domain is bounded by no-slip walls in the y direction, has periodic boundary conditions in the z direction, and non-periodic boundary conditions in the x direction (as described above) which keeps volume fractions of RBCs (hematocrit) at approximately 42%, of platelets at 1.7%, and of vWF at 0.8% in the periodic domain (see Fig. 25(c)). Note that the simulated volume fractions of vWFs and platelets are higher than under physiological conditions, in order to reduce the time scale of hemostatic plug formation to a reasonable computation time. The suspending fluid contains 10.2×10^5 SDPD particles, corresponding to the number density of $n = 16.875/r_c^3$ with $r_c = 0.23D_r$. The SDPD fluid parameters are $p_0 = b = 33750k_BT/r_c^3$, $\rho_0 = mn$ with particle mass m ($m = 1$ in simulations), and $\gamma = 7$. Fluid viscosity is set to $\eta = 100$, which defines a time scale $\tau = \eta D_r/\mu_r$. $\tau \approx 0.0016$ s for the blood plasma viscosity of $\eta = 1.2 \times 10^{-3}\ Pa \cdot s$. The flow is driven by a pressure gradient of $\Delta P/L_x = fn = ck_BT/r_c^4$, where f is the force applied to each SDPD fluid particle and c takes the values of $81, 121.5$ and 162 for low-, mid- and high-shear rate simulations, respectively.

Excluded-volume interactions between RBCs, platelets, and vWFs are implemented through the repulsive part of the LJ potential in Eq. (114). The interaction parameters as same as Section 4. For the sake of clarity, all repulsive interaction pairs, $\epsilon = 16k_{\mathrm{B}}T$ and $r_{LJ} = 2^{1/6}\sigma$, $\sigma = 0.077D_r$ for vWF-vWF interactions, $\sigma = 0.062D_r$ for RBC-vWF and platelet-vWF repulsion, and $\sigma = 0.046D_r$ for RBC-RBC, platelet-platelet, and RBC-platelet interactions, were used.

In the simulations, platelet vertices, activated vWF monomers, and point particles representing the wound—located on the lower wall—can form adhesive bonds (see Fig. 15(d)). Adhesive bonds are permitted only between platelet–vWF, platelet–wound, and vWF–wound pairs. The stationary point cloud, representing the hemostatic interaction zones on the lower wall, forms a two-dimensional lattice characterized by the lattice spacings $\Delta x = 0.25\,\mu$m and $\Delta z = 0.25\,\mu$m, corresponding to a surface number density of 16.23 particles/μm^2. The overall hemostatic surface patch on the lower wall has dimensions $L_x \times L_z = 40\,\mu\mathrm{m} \times 30\,\mu\mathrm{m}$ (see Fig. 25(c)).

The parameters for the various bond types are given in Table 4 and Table 5. The corresponding lifetime $t_l = 1/k_{\mathrm{off}}^{\mathrm{i}}$ as a function of the bond length r are displayed in Fig. 26 . The value for the on rate $k_{\mathrm{on}} = 5.73 \times 10^3/\tau$ is constant and same for all bond types. The given set of on- and off-rates can produce reversible aggregation of the hemostatic plug which refers to the dissolution of the clot upon cessation of fluid flow.

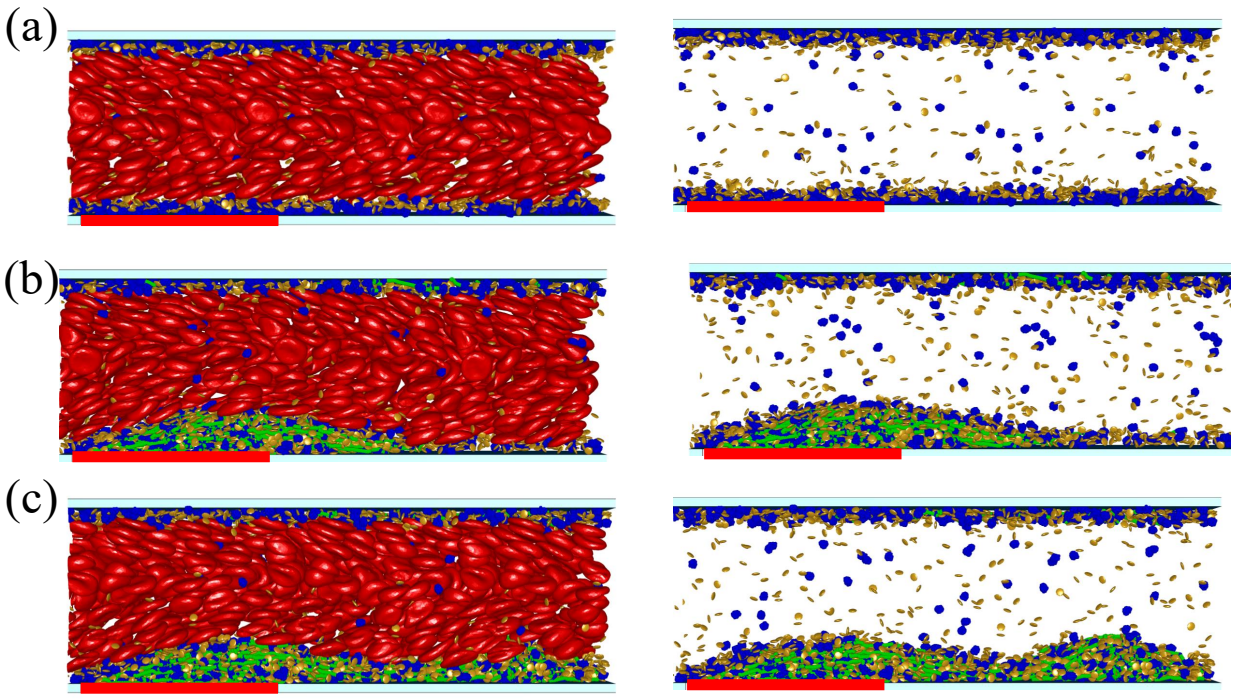

Figure 27: (a) After marginating into cell-free layer, platelets and vWFs form a zone near the wall ready to form blood clot indicated by a red bar in all figures. This snapshot shows the initial condition of low-shear simulation. (b) As time progresses, attached hemostatic material accumulates on the wound, to stop bleeding. (c) Excess hemostatic material is pushed away from the wound region due to hydrodynamic interactions.

5.3 Results

5.3.1 vWF-platelet aggregation and clot formation

The formation of a platelet plug upon vascular injury at elevated shear rates requires flow stresses to be large enough to stretch vWF and activate it for forming adhesive bonds with platelets.

We simulated three different scenarios to analyze the effect of flow rate on clot formation. In the low-, mid-, and high-shears rate simulations, the wall shear rates are $\dot{\gamma}_w = fnL_y/(2\eta) \approx 1152\ \mathrm{s}^{-1}$, $\dot{\gamma}_w = 1728\ \mathrm{s}^{-1}$, and $\dot{\gamma}_w = 2304\mathrm{s}^{-1}$, respectively. These rates are relevant for the circulation in arterioles and small arteries[179]). In principle, the low- and mid-shear rate scenarios have average shear rates below the critical shear rate $\dot{\gamma}_c \approx 2000\ \mathrm{s}^{-1}$ for soluble vWF to extend [77, 171, 185]. However, margination of platelets and quasi-confinement effects induced by flowing RBCs on vWFs effectively reduce this critical shear threshold [170]. In all our simulations, vWF stretches and exposes its adhesive domains, initiating clot formation.

Figure 27 shows representative simulation snapshots for various stages of the clot-formation process. The left column includes all blood components, such as RBCs and hemostatic material,

while the right column displays only the hemostatic material. At the start of the simulation, when the driving force is just switched on to initiate blood flow, all vWFs have a globular form (*i.e.*, they are non-adhesive), and are homogeneously distributed within the simulation domain together with platelets and RBCs, without any bonded structures. RBCs migrate in flow toward the channel center, while platelets and vWF globules slowly migrate toward the channel walls.

The displacement of the hemostatic material in the vicinity of the walls is called margination, which has also been observed for leukocytes and drug delivery particles in blood flow [59, 83, 156, 170].

This margination of platelets and vWFs is facilitated by the hydrodynmic lift force of the deformable RBCs with the channel walls [3, 33, 127], effectively pushing the other blood components (*i.e.*, platelets, vWFs) into a RBC-free layer (RBC-FL) near the wall. As a result, the concentration of platelets and vWFs in the RBC-FL strongly increases, providing favorable conditions for the formation of a blood clot. We do not allow formation of any bonded structures during the formation of the RBC-FL. Figure 27(a) shows the condition where margination is complete and the hemostatic material trapped inside RBC-FL. A typical hemostatic reaction initiates at different locations of the injury site, depending on the availability of hemostatic material. These small "islands" of attached material then grow into three-dimensional structures and eventually merge at different timescales, depending on the flow rate. Figure 27(b) shows a snapshot when these small islands have merged into one intact, connected blood clot.

Once the clot reaches a certain size, it occludes certain part of the channel and experiences increased drag forces due to hydrodynamic stresses. These stresses impose an upper limit on the clot size. Further growth causes a structural instability, leading to thromboembolization. Figure 27(c) displays a typical conformation at the onset of embolization. Shortly after this snapshot, a portion of the clot detaches from the main clot and enters the circulation.

We have analyzed clot formation under different shear rates. Specifically we focused on geometric properties, dynamics of the clot, bond formation characteristics and various time scales occurring in hemostatic process.

5.3.2 Clot geometry – surface coverage, clot thickness, and thrombotic events

The purpose of the hemostatic process is the cessation of the blood flow upon vascular injury. This is executed with several consecutive steps first of which being the platelet plug formation on the wound. The relevant parameter of this very first step to measure surface coverage of the clot due to attachment of platelets to the wound as a function of time.

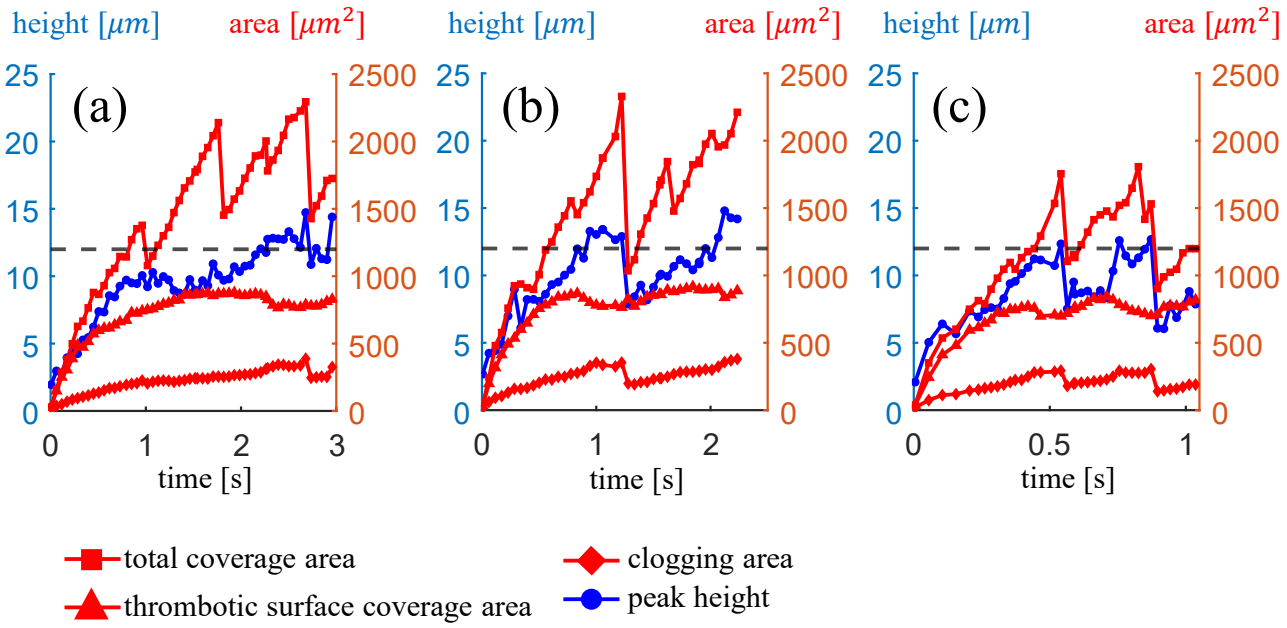

Figure 28: Time-dependent total coverage, thrombotic coverage, clogging surface area and peak height of the platelet-vWF plug, for (a) low-shear-rate, (b) mid-shear-rate and (c) high-shear-rate blood flows. The corresponding surface coverage areas are obtained by projecting the individual platelets into the flow direction (clogging area), on the wound (thrombotic surface coverage) and on the lower wall (total coverage area). The peak height corresponds to the maximum instantaneous y-coordinate of the platelets. The dashed line displays the total area of the wound, corresponding to $1200\mu m^2$.

Figure 28(a-c) shows the different surface-coverage measures of the platelet plug for low-, mid- and high-shear-rate simulations, respectively.Here, total coverage area is computed, projecting the platelets onto lower wall, thrombotic surface coverage area is calculated by computing the overlap between the total coverage area and the wound, and the clogging area is calculated projecting the platelets into flow direction. In all cases, a typical time scale τ_e for the thrombotic surface coverage can be identified, since both quantities approach saturation exponentially [*i.e.*, $a\,(1-\exp\,(-t/\tau_e))$]. The corresponding time required to attain 95% of the steady-state value is chosen as the steady-state time (*i.e.*, τ_{ss}).These two measures of the typical time scale should display essentially the same dependence of shear rate and other parameters.

The steady-state time for the low-, medium- and high-shear-rate cases are $\tau_{ss} = 1.18$s, $\tau_{ss} = 0.79$s, and $\tau_{ss} = 0.41$s, where thrombotic surface coverage reach $833.4\mu m^2$, $859.6\mu m^2$, and $774.1\mu m^2$, respectively.Note that the total surface area of the wound is $1200\mu m^2$, highlighted in Fig. 28(a-c); in all simulations, the formed clot was not able to cover the whole surface area of the wound. The steady-state times τ_{ss} display an inversely proportional relation with the wall-shear rate (*i.e*, $\tau_{ss} \approx 1.3 \times 10^3/\dot{\gamma}_w$).The steady-state thrombotic surface coverage values for all simulations reaches approximately the same value.

Unlike thrombotic surface coverage, total surface coverage (*i.e.*, the whole area after projection of platelets on xz plane) is interrupted by the consecutive embolization (*i.e.*, detachment) events. The mechanism of the emobolization is explained below. We could not analyze the time between two consecutive embolizations due to limited time range of the simulations. The detachments from the platelet plugs can also be traced from the Fig. 29(a-c) by tracking the hemostatic material counts. When an embolization event happens, the fragment detaching from the clot does not overlap with the wound. This can be seen from Fig. 28(a-c), as the drops in the total surface coverage do not effect the thrombotic surface coverage. That implies that once the platelet plug is formed on the wound, the clotting process is ready to proceed with secondary hemostasis without any interruption from the embolizations.

Fig. 28(a-c) also show the clogging area (*i.e.*, the area of the clot obtained by projecting the individual platelets into flow direction) and the peak height (*i.e.*, maximum y-coordinate of all platelets) of the clot. The drag force experienced by the clot is proportional to the clogging area or equivalently to the peak height. The hydrodynamic stresses on the clot increase as the channel increasingly occludes. Beyond some critical value, the drag force becomes strong enough to scavenge excess clotting material from the hemostatic plug thereby limiting further growth of the clot. It is also notable that, for the low-shear rate simulation, peak height remains almost constant after the steady-state has been reached, even though there are repeated detachments from the clot. This is relevant to the embolization mechanism that will be explained below. For the mid- and high-shear-rate simulations the peak height value is subjected to sudden drops as detachments take place. The maximum peak heights for the low-, mid- and high-shear-rate simulations are $14.72\mu m$, $14.79\mu m$ and $12.67\mu m$, respectively. The corresponding clogging areas are $388\mu m^2$, $379\mu m^2$ and $305\mu m^2$, respectively.

From the simulation results for the peak heights, clogging areas, thrombotic and total surface coverage areas, we conclude that all clots subjected to different shear-rates approximately reach the same geometric measures, but at different timescales. Due to high shear rate and hence the high drag force, the highest shear-rate clot remains slightly smaller than the clots at lower shear rates. We will describe and discuss other geometric measures for the low-shear-rate simulation in subsequent sections, which are also found to display a similar behavior for the mid- and high-shear-rate cases.

An important result of our simulations is the emergence of an upper limit to the size of the blood clot. Although our model includes only hydrodynamics, bond formation, and the mechanics of blood agonists, it consistently yields a clot that does not occlude the entire channel. This suggests that invoking additional mechanisms such as advection–diffusion or chemical reactions that govern, for example fibrin bond formation between platelets, is not necessary to

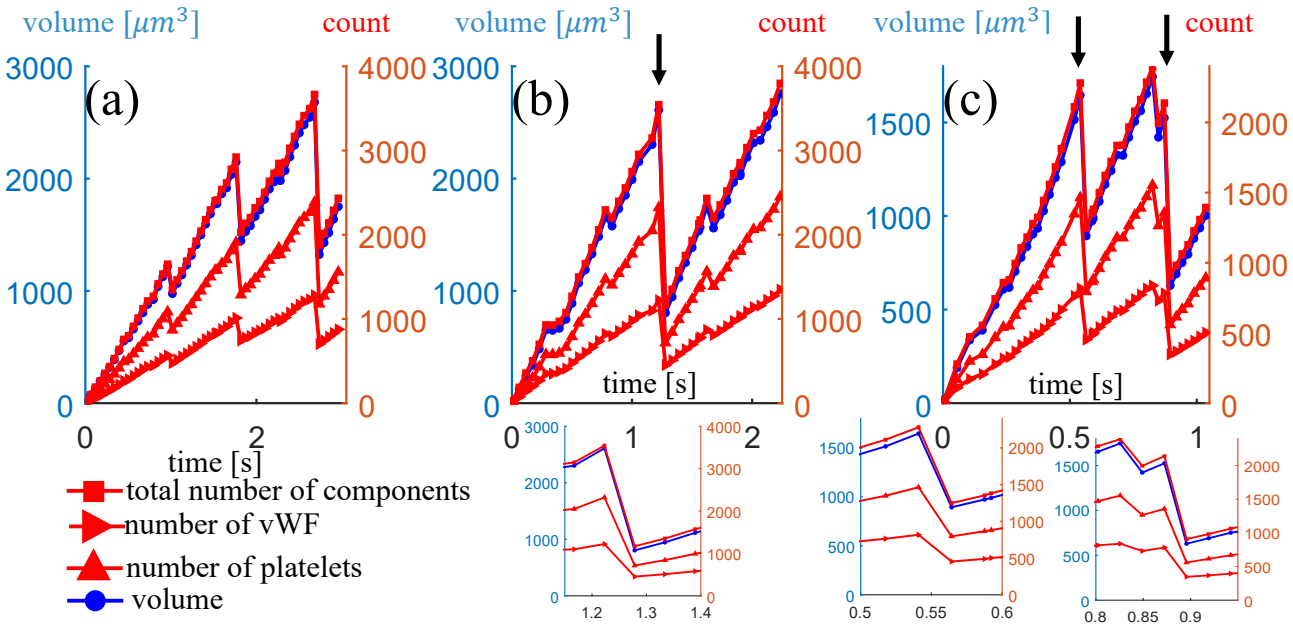

Figure 29: Time-dependent measure of number of platelets, vWFs, total number of components, and total volume of the platelet-vWF plug, for (a) low-shear-rate, (b) mid-shear-rate and (c) high-shear-rate flow. The volume is calculated using the total sum of individual platelet volumes, number of componenets corresponds the total count of vWF and platelets. Black arrows indicate embolization events. For clarity, zoomed-in views of the same data, highlighting the onset and aftermath of embolizations during the mid- and high-shear simulations, are shown below the corresponding panels.

achieve a finite clot size. By applying a constant force to all fluid particles, we actually mimic the pressure-relief conditions in experiments, where flow is driven by a pressure pump, and clogging is possible since the pressure pump reliefs the applied pressure gradient as channel occludes. In contrast, in experiments with a syringe pump, due to the constant flow rate clogging of a channel is not possible [38].

5.3.3 Clot structure – vWF and platelet content, and embolization events

Fig. 29(a-c) shows the counts of platelets and vWFs in the hemostatic clot, and the total volume of the platelets for low-, mid- and high-shear-rate simulations, respectively. The embolization events can be easily traced by observing the sudden drops in the time dependence of these equantities. For all simulations, the ratio of the vWF and platelet counts within the clot is almost constant, and equals about 0.55 (*i.e.* about two platelets per vWF). Even when an embolization takes place this ratio does not change. This implies that the clot is homogenous in terms of platelet and vWF counts. The ratio matches the number fraction in the periodic domain (*i.e.*, 192 and 384 for vWF and platelets, respectively). We also measured the rate of material deposition by tracking the time derivative of the total number of components (*i.e*, sum of platelets and vWFs) attaching to the clot, which yield deposition rates of $1907, 3192$

and 4293 components s^{-1} for the three experiments. These values are proportional to the wall shear rate with the scaling ($\dot{N} \approx 1.79\dot{\gamma}_{\text{wall}}$).Note that even if there are jumps in the curves in Fig. 29(a-c), after the detachment the clot continues to grow with approximately the same rate. The mechanism of embolization is illustrated in Fig. 30 for the low-shear-rate clot, using a slice parallel to the xy-plane that cuts the simulation domain exactly in half along the z-axis (perpendicular to the flow x direction). The mechanism is identical for the clots for high- and mid-shear-rate flows, and is therefore depicted only for the low-shear-rate case. Fig. 30 displays the platelets attached to the clot, together with the velocity field sampled using only the hemostatic material, as well as the distribution of the local extensions of the platelet–vWF bonds.

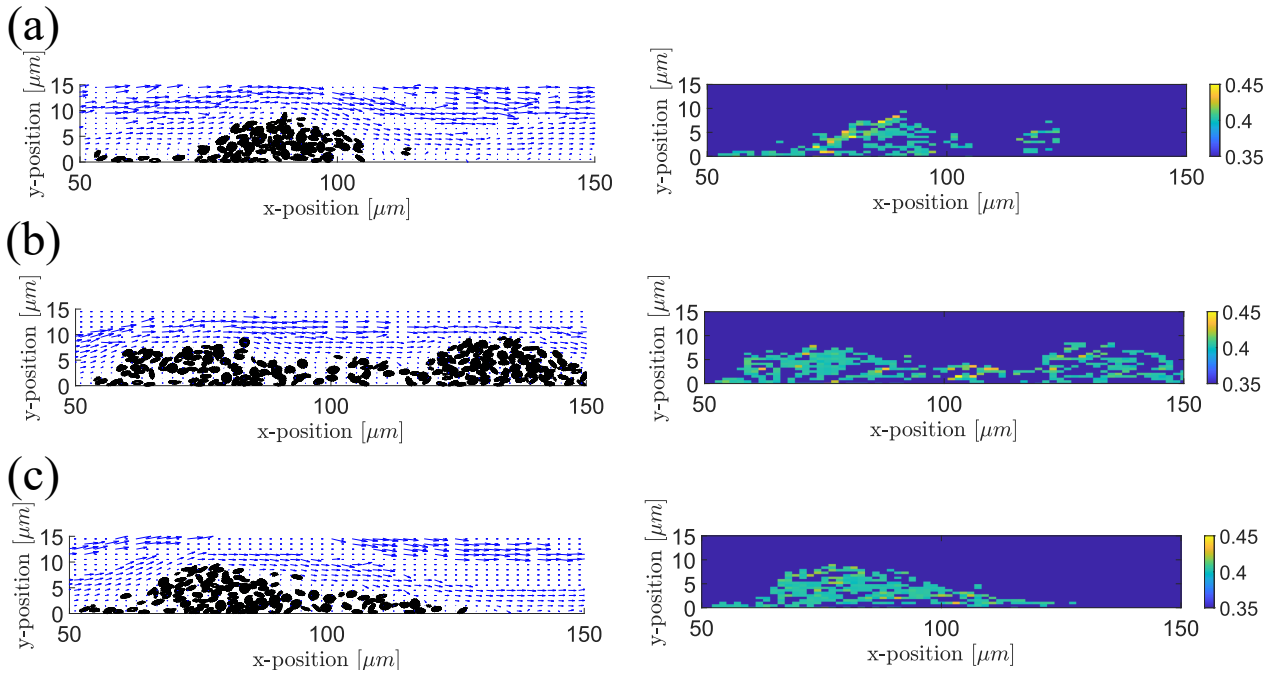

Figure 30: Structure of the clot during embolization events, illustrated by the conformation in a two-dimensional (xy-plane) slice at the middle ($z = 15\mu m$) of the vWF-platelet clot at various time steps. (a) Early phase (*form*) of platelet-vWF plug formation. The flowing platelets and vWFs are captured by the thrombotic surface and form a growing plug placed on the top of the wound. (b) Intermediate phase (*push*) with displacement of platelets due to hydrodynamic forces, downstream from the vascular injury. The two islands are still connected via vWF-platelet chains. (c) Late phase (*break*) of platelet-vWF plug. The second island at the down stream is now detached from the clot. At later times, this configuration evolves to configuration as in (a).
Left column: Conformation of platelets attached to the clot, and fluid velocity field during cyclic *form-break-push* behaviour. *Right column:* Heat-map of the extension of the vWF-platelet bonds. The wound lies between $50\mu m - 90\mu m$. Blue arrows indicate the velocity field sampled using the hemostatic material (*i.e.,* vWFs and platelets). Highest extension vWF-platelet bonds occurs in (a) at the leading edge of the clot, in (b) between the vWF-platelet bonds between two islands.

As described above, the clot formation initiates at different locations on the wound depending upon the physical conditions surrounding the wound. As these small islands grow, they merge into a one large intact blood clot, reaching a certain peak height, as shown in Fig. 28(a-c). This process is displayed in Fig. 30(a). At this phase the clot is located exactly on the top of the wound and highest force is applied to the bonds between vWF-platelet pairs located on the leading edge of the clot (see Fig. 30(a)). As the clot grows, the drag force due to fluid flow increases and the whole clot is slowly pushed downstream. Simultaneously, new material is transported by the fluid flow to the hemostatic zone and partially added to the existing clot. At this stage, some portion of the clot is on the top of the wound, whereas the other part is floating downstream near the lower wall of the channel. This is displayed on Fig. 30(b). The part located on the wound, which is also anchored to the hemostatic surface via ligand-platelet and ligand-vWF bonds, can resist the extra drag force generated by the partial occlusion of the channel, but the floating part slowly detaches from the main body of the clot by forming a neck between the anchored and floating parts. At this stage, the largest stretch of the platelet-vWF pairs is located in the neck (see right column of Fig. 30(b)). Any additional force on the clot implies the detachment of the fragment floating near the lower channel wall, resulting in embolization, asdisplayed in Fig. 30(c). This cycle of clot formation, growth, and embolization continues for both the low-, mid-, and high-shear-rate cases as long as as there is additional hemostatic material available through flow-assisted transport through the channel.

An important result of our simulations is the identification of mode of detachment of fragments from the clot. This *form-push-break* process is the embolization pathway for high shear hemostasis. In all our simulations, detachment of clot fragment from the zone of vascular injury was minimal. The main contribution of embolization comes from the floating part of the clot.

5.3.4 Clot formation – internal bond structure and forces

Within the clot there are different adhesive bonds that sustain structural forces and attain a certain bond lifetime. This is shown in Figure. 31(a-c) for the low-shear clot. We do not report the results of mid- and high-shear-rate simulations, because the behavior is similar to low-shear-rate case. Since the wound has a finite size, there is a limited number of available ligands (*i.e.*, total of 19476 ligands) to form bonds. As simulation progresses, these ligands are quickly occupied by the vWF and platelets. The ratio of number of vWF-ligand and platelet-ligand bonds is constant throughout the simulation and equals 0.75. Only 18 % of the ligands are filled within the $\tau_{ss} \approx 1.18$s. Beyond this moment, the number of bonded ligands increases linearly in time (see Fig. 31(a)).

The majority of bonds is between vWFs and platelets, and their number is proportional to the clot size (*i.e*, total number of components in the clot.). For a clot after τ_{ss}, 50% of the

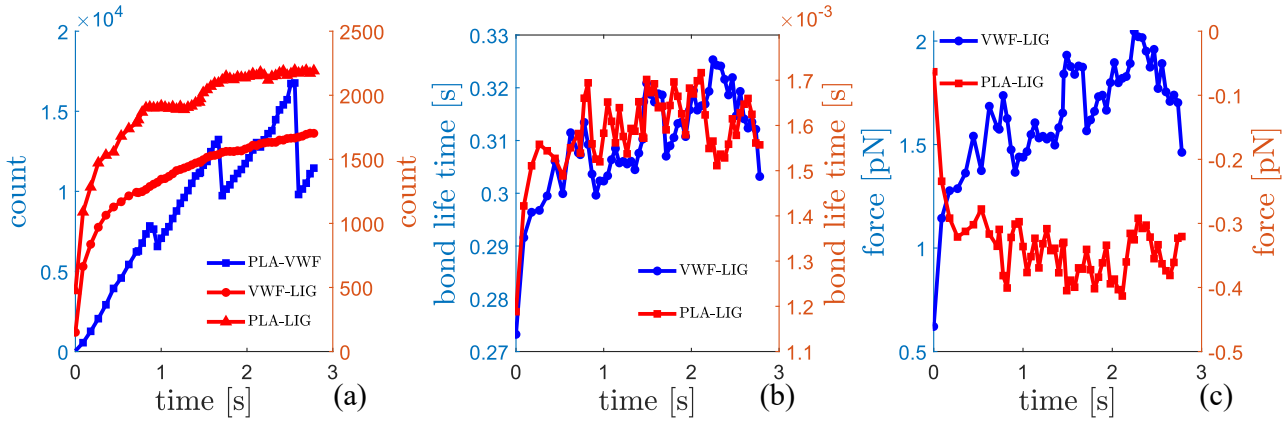

Figure 31: Bond properties for the low-shear rate clot. (a) Shows the number of bond counts as a function of time between different pairs. (b) Ensemble average of bond lifetimes corresponding different pairs. (c) Ensemble average of the forces between vWF-ligand and platelet-ligand pairs as a function of time.

monomers of the attached vWFs are activated, with a majority of them (*i.e.*, $\approx 90\%$) occupied with either ligand-vWF or platelet-vWF bonds. As noted earlier, when embolization occurs, the fragment detaches from the trailing edge of the clot, not from the anchored zone. Therefore the number of ligand bonds are not affected, whereas the number of vWF-platelet bonds are subject to sudden jumps. Figure. 31(a) shows the corresponding bond counts between platelet-vWF, vWF-ligand and platelets-ligand pairs in low-shear clot.

Once the clot has formed, it is anchored to the wound either by ligand-vWF or ligand-platelet bonds. Each bond is loaded depending on the hydrodynamic drag force applied to the blood clot. Figure 31(c) shows the force carried by the each bond averaged over the all pair of bonds at a particular time step. Interestingly, the platelet-ligand bonds are compressed on an average , whereas vWF-ligand bonds are stretched. Of course, both tensile and compressive forces appear throughout the simulation on both bond types at various levels. The force carried by the platelets on average almost vanishes; thus, the resistance of the clot against hydrodynamic forces is carried predominantly by the bonds of ligand-vWF pairs.

Figure 31(b) shows the respective bond lifetimes of different types of adhesive bonds. The force carried by the bond is directly related to the corresponding bond lifetime. The platelet-ligand interactions during primary hemostatsis for high-shear-rate environments are almost negligible. Even though the average bond lifetime of the platelet-ligand interactions are increasing with time, the bond lifetime is short, of the order of $10^{-3}s$. When compared with the lifetime of vWF-ligand bonds, this is three orders of magnitude smaller. The monotonic temporal increase can be attributed to compressive load on the slip bonds, which is reflected in an increase in bond lifetime (see Figure 16).

Similar arguments apply to the adhesive bonds in vWF-ligand pairs. Since the loads are

tensile on an average, the stretch of the vWF-ligand bonds increases over time, which makes them the main load carrier against hydrodynamic stresses. This is reflected in a monotonic temporal increase of bond lifetime. The order of magnitude of this bond lifetime is $10^{-1}s$.

Figure 32(a) shows the probability distribution of bond formation between vWF monomers and their binding partners (*i.e.*, either platelets or ligands) along the vWF contour. The data is displayed for low-shear-rate clot. A single vWF chain attaches to the hemostatic surface mainly at the leading and trailing edges of the polymer chain. On average, vWF molecules assume a snake-like shape, where intermediate parts of the chain form loops separated by occasional attachments. vWF-platelet interactions are similar to vWF-ligand interactions, but intermediate monomers have a higher probability to form adhesive bonds. Two cases are illustrated schematically at the inset of Fig. 32(a). The average force distribution along vWF chains is shown in Fig. 32(b). Soluble chains exhibit an almost uniform tension profile.In contrast, when a vWF chain is adsorbed onto the hemostatic surface (*i.e.*, anchored) or forms a bond with a platelet (*i.e.*, structural), the average tension increases, and the tension is large at the front (adsorbed) end, and decreases along the contour, resembling the tension distribution of a polymer attached to a surface and subjected to a uniform external load along its monomers (so that all forces sum up at the front end, but the drag force of only a few monomers remains at the trailing end). This ideal tension distribution is affected by adhesive bond formation in the middle and end of the chain, which implies a reduced tension near the trailing end.

Furthermore, the clot is a three-dimensional elastic body, anchored to the wall. This implies that the external flow is screened, and flow forces are weak inside the clot, while the main drag forces occur at the free surface of the clot. Thus, the highest forces, corresponding to vWF–ligand interactions, can be expected at the wall, the smallest forces near the top surface

5.3.5 Instantaneous Clot Geometry and Shape

We measured the aspect ratios, which are obtained by comparing the length scales ℓ_x and ℓ_y of the clot. The length of the clot in flow direction, ℓ_x, can become as large as twice the length of the vascular injury, about $100\mu m$. The dimension ℓ_y is the peak height, and is also displayed in Fig. 28(a-c) for the low-shear-rate clot. Since the clot is subject to embolization, ℓ_y and ℓ_x experience sudden jumps, and also the aspect ratio experiences the same jumps. Despite these events, the aspect ratio remains nearly constant between two jumps, which implies that clot rupture reduces the size significantly, but the remaining clot quickly recovers its previous size and shape. The ratio remains $\ell_y/\ell_x = 0.12 \pm 0.01$ once the τ_{ss} is reached.

Figure 32(c) shows the Fourier spectrum of the projection of edge contour $x(z)$ of the clot in the xz plane. The inset of the same panel displays the corresponding averaged boundary

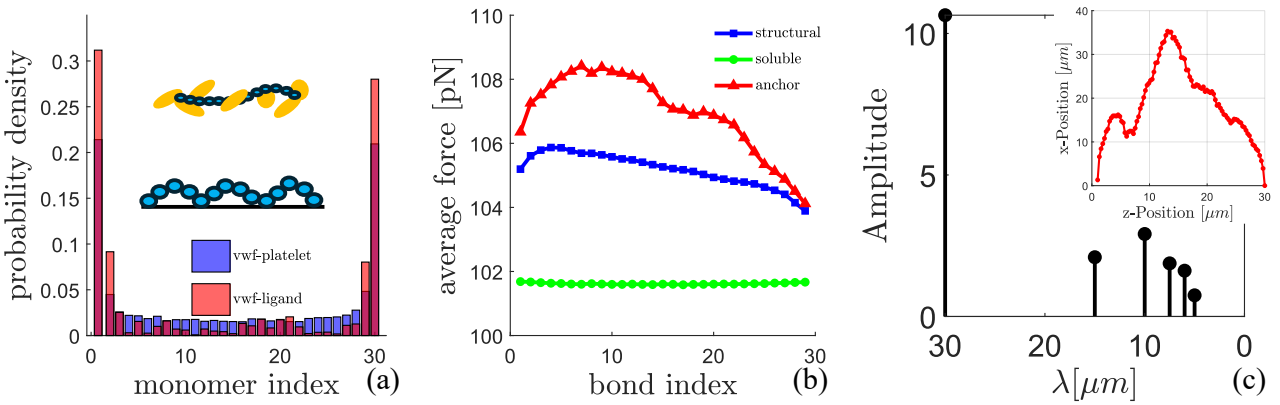

Figure 32: (a) Probability of bond formation between vWF chains' active monomers and platelets or ligands. (b) Ensemble-averaged force derived from potentials given in Equation (113 - 114) between the neighboring monomers of different type of vWF chains. Structural vWFs are part of the clot without forming adhesive bonds with ligands. Anchor vWFs have at least one monomer attached to the wound surface. Soluble vWFs do not participate in any adhesive interactions. (c) Fourier spectral analysis of the clot edge profile, with the first six modes shown. The inset displays the xz projection of the ensemble-averaged clot edge

curve after τ_{ss} for the low-shear simulation between two events. The average curve is calculated in shifted 'normalized' coordinates, such that the value at $x = 0$ always corresponds to the trailing edge of the clot. This normalization does not affect the shape analysis, as only the shape of the edge is relevant. The Fourier representation of the contour is given by

$$x(z) = h_0 + \sum_{j=1}^{M} A_j \cos(2\pi\kappa_j z) \tag{121}$$

where h_0 denotes the mean x distance of the interface from the wound front end, the amplitudes A_j characterize the shape of the clot edge, and the spatial frequencies are defined by $\kappa_j = 1/\lambda_j = j/(N\Delta z)$. The rapid drop in amplitude with decreasing λ_j implies that small-wavelength modes are not significant, so that the contour is smooth and dominated by one or two mesoscopic length scales — consistent with the "tongue-like" elongation shown in the inset of Fig. 32(c). This specific "tongue-like" shape appears due to material flow. As clot grows, the material on the top of the clot is dragged by hydrodynamic forces to the trailing edge.

5.4 Discussion

We have investigated the dynamics of formation of a platelet clot at a vascular injury in blood flow for physiologically relevant shear rates. For all considered shear rates, clot formation begins with the attachment of vWF chains and platelets at various locations on the wound surface, creating small, discrete islands. These islands gradually merged into a single, continuous blood clot that covers a large part of the wound and, in all cases, extends beyond the hemostatic

surface. Even though the structural properties (*e.g*, total number of components, bond counts, surface coverage areas) of the clots are similar, the dynamics are strong function of the shear rate. As the clot grows with time and partially occludes the channel, the resulting increase in hydrodynamic forces pushes portions of the clot beyond the wound site, leading to the detachment of fragments of the clot. This process continues cyclically as long as the supply and transport of hemostatic material are maintained.

The behavior of clot formation for the range of applied wall shear rates is as follows. The steady-state time τ_{ss} is inversely proportional to wall shear-rate $\dot{\gamma}_{\text{wall}}$ of the flow, and scales as $\tau_{ss} = 1.3 \times 10^3/\dot{\gamma}_{\text{wall}}$. The thrombotic surface coverage areas at a time τ_{ss} after flow initiation reaches approximately same values for all shear rates, and fluctuates within the range of $58 - 76\%$ of the total wound area. This area measure is not affected by the emobilizations from the clot, *i.e.*, as soon as a steady-state value is reached, the primary hemostasis is essentially completed, and the system is ready to proceed with the secondary hemostasis without interruption. The material deposition rate is proportional to applied force with a scaling of $\dot{N} \approx 1.79\dot{\gamma}_{\text{wall}}$.The composition of the clot is homogeneous and keeps about the same vWF to platelet number ratio(*i.e.*, 0.55) as in periodic subdomain.

It is important to note that, even though the thrombotic surface coverage is free of disruptions, under arterial flow conditions with whole blood, embolization occurs through a three-step process: clot formation – flow-induced push to downstream side – rupture and embolization. Due to limited simulation time of our simulations, an quantitative estimate of the average embolization time was not possible. However, the observed mechanism of primary hemostatis suggest that the transition to secondary hemostasis is initiating in the vicinity of the wound. Fibrin bridges could form gradually from platelets at the vascular surface to the platelets at the upper portion of the clot, thus stabilizing the clot from bottom to top, until the clot solidifies and embolization is prevented.

Previous stability studies of blood clots formed under arterial flow have typically assumed a predefined clot shape based on experimental observations and distinguished between weak and strong platelet–platelet bonds. In these studies, embolization most often occurs at the free surface of the clot, where the local shear rate is highest [27, 224]. In our simulations without platelet activation, the clot is continuously displaced out of the wound while maintaining a finite amount of hemostatic material at the wound site. We therefore predict that secondary hemostasis initiates within this retained material, which is not subjected to material scavenging. Once the material adjacent to the wound solidifies, subsequently deposited material accumulates on this solidified scaffold and undergoes secondary hemostasis. In this manner, the clot grows and solidifies progressively in a layer-by-layer fashion.

An important results of our simulations is the finite size of the clot. We model clot formation in the presence of RBCs, platelets, and vWF, but in the absence of soluble fibrinogen, using a hemostatic surface that allows vWF and platelets to attach (i.e., collagen-coated without tissue factor); also, our model does not include any chemical reactions that produce additional fibrinogen at arterial shear rates. Under these conditions, we observe no channel occlusion, unlike recent experiments [34]. A key difference is the presence of RBCs in our simulations, which exert additional drag on the clot and contribute to its scavenging. Under whole-blood arterial-flow conditions with diluted tissue factor and blocked fibrin polymerization, clots embolize and the probability of occlusion is low [38], consistent with our findings.

To characterize the micro-environment of the clot, we also measured the average minimum distance between platelets inside the clot. Recent simulations and experiments [222, 239] indicate that after the formation of platelet plug, platelets form fibrin bridges and these bridges contract to decrease the porosity of the environment. In this micro-environment, the material transport favors diffusion over advection, so that the chemicals released to initiate/propagate secondary hemostasis are not scavenged by the fluid flow. Our simulations does not include platelet activation and the formation of fibrinogen bridges. For three-experiments, we conducted this measurement, as soon as the peak-height of the clot reaches $12\mu m$ for all shear-rates. Next to wall, all averaged values are nearly same and corresponds to minimum inter-platelet distance of approximately $0.18\mu m$. This minimum value then linearly rises for up-to $0.21\mu m$ until the distance to wall becomes $10\mu m$. In the outermost $2\mu m$-thick layer, this distance rises exponentially to $0.35\mu m$. These results support the concept of distinct core and shell regions, where the core's shielding effect can favor diffusion dependant material transport and thereby facilitate secondary hemostasis. No net dependence of the minimum inter-platelet distance on the shear-rate is observed. The lowest distance is about to be $0.17\mu m$ next to the wall for mid-shear rate, whereas for high-shear-rate simulation this distance is $0.19\mu m$ next to the wall.

5.5 Conclusion

In conclusion, this work presents a direct numerical framework for investigating the long-time dynamics of primary hemostasis under physiologically relevant flow conditions. By explicitly resolving red blood cells, platelets, and shear-activated von Willebrand factor, the model captures the mechanically driven processes that govern platelet adhesion, aggregation, and material transport during the early stages of clot formation. The simulations highlight the crucial role of hydrodynamic interactions and shear-dependent mechanisms in regulating clot growth, stability, and embolization over time scales that are difficult to access experimentally. Building on this foundation, it would be particularly interesting to extend the present model to incorporate fibrin generation and polymerization, thereby enabling a unified in silico description of the

transition from primary to secondary hemostasis and the subsequent mechanical stabilization of the clot.

6 Conclusion

In this thesis, we have employed direct numerical simulations to investigate key mechanistic aspects of blood-mediated aggregation and hemostatic processes under flow. The work is organized into two main chapters. In the first chapter, we study the formation of reversible and irreversible aggregates, focusing on the interplay between hydrodynamic interactions and adhesive binding kinetics. The second chapter is devoted to an in silico investigation of primary hemostasis, where clot formation at a vascular injury site is explicitly modeled. In both chapters, red blood cells, platelets, and shear-activated von Willebrand factor (vWF) are resolved explicitly, and adhesive interactions between blood agonists are described through physically motivated bond models. To enable sustained clot growth and material exchange in the hemostasis simulations, non-periodic inflow and outflow boundary conditions are implemented in the second chapter, allowing the system to evolve under physiologically relevant flow conditions.

The first chapter addresses a dynamical regime that is experimentally challenging to access, namely the formation and evolution of small, freely advected aggregates in blood flow. The simulations identify minimal physical conditions required for the emergence of irreversible aggregates under physiological shear conditions. In particular, the results demonstrate that the transition between reversible and irreversible aggregation is governed primarily by the nature of the adhesive interactions between vWF and platelets. Catch–slip bond kinetics lead predominantly to reversible aggregate formation, whereas alternative bond types give rise to irreversible aggregates. This behavior arises from a balance between shear-induced diffusion, wall-induced lift forces, and shear-gradient-induced lift forces, which together determine the spatial position of an aggregate within the flow and, consequently, the hydrodynamic shear it experiences. Depending on the bond type, different shear environments result in distinct bond extensions, which in turn control bond lifetimes and ultimately determine whether an aggregate remains reversible or evolves into an irreversible state.

In the second chapter, we address a regime that is particularly challenging to capture in silico, namely primary hemostasis under high-shear conditions, where the large multimeric protein von Willebrand factor (vWF) plays a central role. Modeling this process requires the implementation of non-periodic inflow and outflow boundary conditions to sustain clot growth and material transport, a feature that is often neglected in large-scale simulations. Moreover, this high-shear stage of primary hemostasis has been largely omitted in many experimental studies due to technical limitations. In this chapter, we perform direct numerical simulations that explicitly resolve red blood cells, shear-activated vWF, and platelets, together with adhesive interactions between these blood agonists, and analyze the influence of shear rate on the dynamics and morphology of clot formation in a microchannel. The primary objective is to identify how shear rate controls key clot properties, including geometry and size. In addition,

the simulations reveal a distinct pathway for embolization in high-shear primary hemostasis, characterized by a *form–push–break* sequence. Based on these observations, we further speculate on possible connections between the mechanically driven processes of primary hemostasis and the subsequent onset of secondary hemostasis.

Overall, this thesis demonstrates the potential of direct numerical, cell-resolved simulations to elucidate mechanistic aspects of blood aggregation and primary hemostasis that are difficult to access experimentally. By systematically linking hydrodynamic forces, shear-dependent molecular interactions, and collective cell dynamics, the present work provides a unified physical picture of reversible and irreversible aggregation as well as high-shear clot formation and embolization. The results highlight the importance of long-time simulations and realistic boundary conditions for capturing the sustained evolution of hemostatic processes under flow. Beyond the specific findings presented here, the developed framework establishes a flexible foundation for future extensions, including the incorporation of biochemical pathways such as fibrin generation and polymerization, thereby enabling a more comprehensive in silico description of the transition from primary to secondary hemostasis.

7 Future Work

Several important extensions of the present work can be envisioned for both chapters of this thesis. First, the inclusion of more complex and physiologically realistic vessel geometries is essential. Blood flow in vivo rarely occurs in idealized, undisturbed channels; instead, vascular networks exhibit geometric irregularities, bifurcations, and curved segments, while vessel walls are coated with a glycocalyx layer that modifies near-wall hydrodynamics and cell adhesion. At lower shear rates, red blood cell (RBC) rouleaux formation, becomes prevalent and can significantly alter the rheological properties of blood. In addition, although physiologically relevant high shear rates were considered in both chapters, the present model employs a minimal criterion for vWF activation. A more refined description incorporating force-dependent vWF activation would provide a more realistic representation of vWF mechanochemistry [26]. Furthermore, pathological conditions can give rise to shear rates exceeding 10^4 s^{-1}, where inertial effects and shear-induced platelet aggregation become relevant; these regimes are particularly important for extending the high-shear hemostasis simulations presented in the second chapter.

For the first chapter, the spectrum of adhesive interactions was limited to a small number of bond types. Expanding this range would allow a more systematic exploration of the boundary between reversible and irreversible aggregation. Since the freely advected aggregates studied in this chapter are difficult to observe experimentally, targeted experimental validation will be necessary to assess the relevance of the predicted aggregation pathways. Moreover, the volume fraction of hemostatic material was chosen to be at least an order of magnitude larger than physiological values in order to access relevant time scales within feasible simulation times. This choice may influence the aggregation dynamics and associated time scales, which are expected to increase under physiological concentrations. Such effects become particularly important in complex geometries, where vessel bifurcations can disrupt the flow field and alter the balance of shear-induced diffusion, wall-induced lift, and shear-gradient-induced lift forces that govern aggregate positioning.

In the second chapter, the wound size was kept constant, whereas in reality clot growth and stability depend sensitively on the extent of vascular injury. Larger wounds may promote excessive clot growth and ultimately lead to channel occlusion. In addition, the simulations were performed under pressure-relief conditions, which are physiologically relevant, while many laboratory experiments impose a constant flow-rate condition. Systematically comparing these two driving conditions would provide valuable insight into how boundary constraints influence clot formation dynamics. Furthermore, platelet activation was not included in the present model. Once primary hemostasis is complete, platelet activation and subsequent fibrin formation lead to the development of strong and weak bonds within the clot [28], which are expected to significantly affect clot stability and thromboembolization dynamics. Finally, due

to computational time constraints, the simulations did not allow for a quantitative analysis of embolization time scales. Extending the simulations to longer durations will be crucial for characterizing embolization statistics and assessing long-term clot stability under high-shear conditions.

A Appendix A

Derivation of fluctuation-dissipation theorem for DPD is rigorous and hence will be given here in this appendix. This heuristic introduction will be the foundation of the derivation of the fluctuation-dissipation relation for angular momentum conserving SDPD. Same methodology will be followed for both paradigms. The methods employed in [49] is elaborated here. One begins expressing the stochastic differential equations of the DPD which are the governing equations of the primary variables position and velocity. Note that a DPD particle is under the effect of three forces; a conservative force, a dissipative force and a random force. Conservative and dissipative forces are deterministic and depends upon the position and/or momenta of the particle whereas the random force is purely stochastic. A relation between the strength of the dissipative force and random force will be required in order to obtain a thermodynamically consistent system. Otherwise the system's dynamics will be either killed by the dissipative forces or dynamics diverges due to random forces. This can be understood from an energy argument as follows; the dissipative force must cancel the exact amount of the energy supplied from the heath bath whereby attending an equilibrium.

One begins with the stochastic differential equations of the DPD system composed of N interacting particles which reads;

$$d\mathbf{r} = \frac{\mathbf{p}}{m}dt \tag{A.1}$$

$$d\mathbf{v} = (\mathbf{F}^C + \mathbf{F}^D)dt + d\tilde{\mathbf{v}} \tag{A.2}$$

where $\mathbf{F}^C, \mathbf{F}^D$ are the conservative and dissipative acceleration (not force, see the definition below) vectors on the particles and $d\tilde{\mathbf{v}}$ is the stochastic contribution to the velocity due to random force. Here $d\mathbf{r} = [d\mathbf{r}_1; ...; d\mathbf{r}_N]$ and $d\mathbf{v} = [d\mathbf{v}_1; ...; d\mathbf{v}_N]$ are column vectors bookkeeping the changes in the velocity and position for particles $1...N$. Same applies for the $\mathbf{F}^C$,$\mathbf{F}^D$ and $d\tilde{\mathbf{v}}$ Therefore, $d\mathbf{r}_i = \frac{\mathbf{p}_i}{m}dt$ and $d\mathbf{v}_i = 1/m(\mathbf{F}_i^C + \mathbf{F}_i^D)dt + d\tilde{\mathbf{v}}_i$ are the governing equations of particle i. $\mathbf{F}_i^C, \mathbf{F}_i^D$ are conservative and dissipative forces given by the Equations (46,43). The dissipative and conservative forces are deterministic. In principle $d\tilde{\mathbf{v}}_i$ occurs due to random forces and has a specific representation but will be kept like as it is for the time being. The only assumption required (according to Ito interpretation of random forces) is $d\tilde{\mathbf{v}}$ is of the infinitesimal order of $1/2$ of dt i.e. $O(d\tilde{\mathbf{v}}) \approx dt^{1/2}$. If one recast the set of equations into a single equation format, it reads;

$$d\mathbf{x} = \mathbf{a}dt + d\tilde{\mathbf{x}},$$

$$d\mathbf{x} = \begin{bmatrix} d\mathbf{r} \\ d\mathbf{v} \end{bmatrix}, \quad \mathbf{a} = \begin{bmatrix} \frac{\mathbf{p}}{m} \\ \mathbf{F}^C + \mathbf{F}^D \end{bmatrix}, \quad d\tilde{\mathbf{x}} = \begin{bmatrix} \mathbf{0} \\ d\tilde{\mathbf{v}} \end{bmatrix}$$

In order to obtain the corresponding Fokker-Planck equation relevant to the above governing

equations, one seeks for the change in an arbitrary random function $\phi = \phi(\mathbf{x})$ which is a function of $\mathbf{x}$ and $d\mathbf{x}$,that are given above. The change is denoted by $d\phi = \phi(\mathbf{x} + d\mathbf{x}) - \phi(\mathbf{x})$ and expressed as up to second order Taylor expansion of the following form;

$$d\phi = \nabla\phi \cdot d\mathbf{x} + \frac{1}{2} d\mathbf{x} \cdot \nabla\nabla\phi d\mathbf{x} = \nabla\phi \cdot d\mathbf{x} + \frac{1}{2}\nabla\nabla\phi : (d\mathbf{x} \otimes d\mathbf{x}) \tag{A.3}$$

Here the outer product or tensor product represented by $\otimes$ symbol. $d\mathbf{x} \otimes d\mathbf{x} = d\mathbf{x}d\mathbf{x}^T$ in the language of linear algebra. Operator : is the double contraction which conducts the following operation between two second order tensors $\mathbf{A} : \mathbf{B} = A_{ij}B_{ij}$. Throughout the whole appendix, Einstein summation convention is used, meaning that repeating indices mean sum. Therefore $A_{ij}B_{ij} = \sum_i \sum_j A_{ij}B_{ij}$. Furthermore, the derivative index appears at last. That means, for example $\nabla\mathbf{A} = \frac{\partial A_{ij}}{\partial x_k}(\mathbf{e}_i \otimes \mathbf{e}_j \otimes \mathbf{e}_k)$. $\nabla\nabla\phi = \frac{\partial^2\phi}{\partial x_i \partial x_j}\mathbf{e}_i \otimes \mathbf{e}_j$ is the Hessian of the function ϕ which is double contracted with $d\mathbf{x} \otimes d\mathbf{x} = (\mathbf{a}dt + d\tilde{\mathbf{x}}) \otimes (\mathbf{a}dt + d\tilde{\mathbf{x}})$. The only surviving term from this outer product is $d\tilde{\mathbf{x}} \otimes d\tilde{\mathbf{x}}$ because if one assumes the Ito rules, $dt^{1+N} = 0$ for $(N > 0)$ and recalling $O(d\tilde{\mathbf{v}}) \approx dt^{1/2}$. Rewriting the equation and taking the expected values of both sides and dividing by dt one gets;

$$\begin{aligned} d\phi &= \nabla\phi \cdot \mathbf{a}\, dt + \nabla\phi \cdot d\tilde{\mathbf{x}} + \frac{1}{2}\nabla\nabla\phi : [\mathbf{a} \otimes d\tilde{\mathbf{x}}\, dt + d\tilde{\mathbf{x}} \otimes \mathbf{a}\, dt] + \frac{1}{2}\nabla\nabla\phi : (d\tilde{\mathbf{x}} \otimes d\tilde{\mathbf{x}}) \\ &\Rightarrow \frac{\langle d\phi \rangle}{dt} = \langle \nabla\phi \cdot \mathbf{a} \rangle + \left\langle \frac{1}{2}\nabla\nabla\phi : (d\tilde{\mathbf{x}} \otimes d\tilde{\mathbf{x}}) \right\rangle \frac{1}{dt}. \end{aligned} \tag{A.4}$$

where by definition $\langle d\tilde{\mathbf{x}} \rangle = 0$. Note also that $\langle \cdot \rangle = \int_V (\cdot) p dV$ where p is the probability distribution governing the stochastic variable $\mathbf{x}$ and therefore;

$$\frac{\langle d\phi \rangle}{dt} = \frac{d\langle \phi \rangle}{dt} = \int_V \phi \frac{\partial p}{\partial t} dV = \int_V (\nabla\phi \cdot \mathbf{a}) p dV + \frac{1}{2dt}\int_V (\nabla\nabla\phi : (d\tilde{\mathbf{x}} \otimes d\tilde{\mathbf{x}})) p dV \tag{A.5}$$

condensing $\mathbf{D} = \frac{d\tilde{\mathbf{x}} \otimes d\tilde{\mathbf{x}}}{dt}$ and integration by parts yields;

$$\begin{aligned} \int_V \nabla\phi \cdot \mathbf{a} p dV &= \int_V \nabla \cdot (\phi p \mathbf{a}) dV - \int_V \phi \nabla \cdot (\mathbf{a}p) dV \\ &= -\int_V \phi \nabla \cdot (\mathbf{a}p)\, dV \end{aligned} \tag{A.6}$$

$$\begin{aligned} \int_V (\nabla\nabla\phi : \mathbf{D}) p dV &= \int_V \nabla \cdot (\mathbf{D}\nabla\phi p)\, dV - \int_V \nabla \cdot \left(\mathbf{D}^T p\right) \cdot \nabla\phi dV \\ &= \int_V \nabla \cdot (\mathbf{D}\nabla\phi p)\, dV - \int_V \nabla \cdot (\phi \nabla \cdot (\mathbf{D}^T p)) dV + \int_V \phi \nabla \cdot \nabla \cdot (\mathbf{D}p)\, dV \\ &= \int_V \phi \nabla \cdot \nabla \cdot (\mathbf{D}p)\, dV \end{aligned} \tag{A.7}$$

where $\int_V \nabla \cdot (.) dV = \int_A (.) \cdot \mathbf{n} dA$ due to divergence theorem, $p(\mathbf{x}) = 0$ as $|\mathbf{x}| \to \infty$ means the probability p vanishes at the boundary together with its flux (i.e., $\mathbf{J} \cdot \mathbf{n} \to 0$, where

$\mathbf{J} = \mathbf{a}p - \nabla \cdot \left(\mathbf{D}^T p\right)$). Combining;

$$\int_V \phi \frac{\partial p}{\partial t} dV = -\int_V \phi \nabla \cdot (\mathbf{a}p) dV + \int_V \phi \nabla \cdot \nabla \cdot (\mathbf{D}p) dV \tag{A.8}$$

$$0 = \int_V \phi \left(-\frac{\partial p}{\partial t} - \nabla \cdot (\mathbf{a}p) + \frac{1}{2} \nabla \cdot \nabla \cdot (\mathbf{D}p) \right) dV \tag{A.9}$$

$$\frac{\partial p}{\partial t} = -\nabla \cdot (\mathbf{a}p) + \frac{1}{2} \nabla \cdot \nabla \cdot (\mathbf{D}p) \tag{A.10}$$

Where at final step one applies the localization theorem and gets transient Fokker-Planck equation where it can be further simplified by;

$$\nabla \cdot \nabla \cdot (\mathbf{D}p) = (\mathbf{D} : \nabla \nabla p + 2 (\nabla \cdot \mathbf{D}) \cdot \nabla p + \nabla \cdot \nabla \cdot \mathbf{D}\, p) \tag{A.11}$$

and noting that $d\tilde{\mathbf{v}}$ is a function of position not momenta (see below for the definiton);

$$\begin{aligned} \nabla \cdot \mathbf{D} &= \nabla \cdot \left(\frac{1}{dt} d\tilde{\mathbf{x}} \otimes d\tilde{\mathbf{x}} \right) \\ &= \nabla \cdot \begin{bmatrix} \mathbf{D}_{rr} & \mathbf{D}_{rp} \\ \mathbf{D}_{pr} & \mathbf{D}_{pp} \end{bmatrix} \\ &= \nabla \cdot \left(\frac{1}{dt} \begin{bmatrix} \mathbf{0} & \mathbf{0} \\ \mathbf{0} & d\tilde{\mathbf{v}} \otimes d\tilde{\mathbf{v}} \end{bmatrix} \right) \\ &= \mathbf{0} \end{aligned} \tag{A.12}$$

one gets the simplified Fokker-Planck equation;

$$\frac{\partial p}{\partial t} = -\nabla \cdot (\mathbf{a}p) + \frac{1}{2} \mathbf{D} : \nabla \nabla p \tag{A.13}$$

Recalling $d\tilde{\mathbf{v}} = [d\tilde{\mathbf{v}}_1; ...; d\tilde{\mathbf{v}}_N]$, $d\tilde{\mathbf{v}}_i = \sum_j d\tilde{\mathbf{v}}_{ij}$ and $d\tilde{\mathbf{v}}_{ij}$ is from Equation 48 $\mathbf{D}_{pp}$ yields;

$$\mathbf{D}_{pp} = \frac{1}{dt} \begin{bmatrix} d\tilde{\mathbf{v}}_1 \otimes d\tilde{\mathbf{v}}_1 & d\tilde{\mathbf{v}}_1 \otimes d\tilde{\mathbf{v}}_2 & \cdots & d\tilde{\mathbf{v}}_1 \otimes d\tilde{\mathbf{v}}_N \\ \vdots & \vdots & \ddots & \vdots \\ d\tilde{\mathbf{v}}_N \otimes d\tilde{\mathbf{v}}_1 & d\tilde{\mathbf{v}}_N \otimes d\tilde{\mathbf{v}}_2 & \cdots & d\tilde{\mathbf{v}}_N \otimes d\tilde{\mathbf{v}}_N \end{bmatrix} \tag{A.14}$$

Here a closer look of diagonal and off-diagonal terms reveals the following;

$$d\tilde{\mathbf{v}}_1 \otimes d\tilde{\mathbf{v}}_1 = (d\tilde{\mathbf{v}}_{11} + d\tilde{\mathbf{v}}_{12} + \cdots + d\tilde{\mathbf{v}}_{1N}) \otimes (d\tilde{\mathbf{v}}_{11} + d\tilde{\mathbf{v}}_{12} + \cdots + d\tilde{\mathbf{v}}_{1N}) \tag{A.15}$$

$$= d\tilde{\mathbf{v}}_{11} \otimes d\tilde{\mathbf{v}}_{11} + d\tilde{\mathbf{v}}_{12} \otimes d\tilde{\mathbf{v}}_{12} + \cdots + d\tilde{\mathbf{v}}_{1N} \otimes d\tilde{\mathbf{v}}_{1N} + \text{cross terms} \tag{A.16}$$

Here one recalls the following $d\tilde{\mathbf{v}}_{ij} = \sigma w(r_{ij}) dW_{ij} \mathbf{e}_{ij}$ which is the definition of the random force where dW_{ij} is the Wiener increment. Also $\mathbf{e}_{ii} = \mathbf{0}$ (no sum). Therefore, example three terms

from the above tensorial muliplication;

$$d\tilde{\mathbf{v}}_{11} \otimes d\tilde{\mathbf{v}}_{11} = \mathbf{0} \tag{A.17}$$

$$d\tilde{\mathbf{v}}_{12} \otimes d\tilde{\mathbf{v}}_{12} = \sigma^2 w_R(r_{12})^2 dW_{12} dW_{12} \mathbf{e}_{12} \otimes \mathbf{e}_{12} \tag{A.18}$$

$$d\tilde{\mathbf{v}}_{12} \otimes d\tilde{\mathbf{v}}_{13} = \sigma^2 w_R(r_{12}) w_R(r_{13}) dW_{12} dW_{13} \mathbf{e}_{12} \otimes \mathbf{e}_{13} \quad \text{cross term)} \tag{A.19}$$

Wiener increment satisfies the following Ito interpretation;

$$dW_{ij} dW_{i'j'} = \left(\delta_{ii'}\delta_{jj'} + \delta_{ij'}\delta_{ji'}\right) dt \tag{A.20}$$

where δ_{ij} is the Kronecker delta. This equation means the independent Wiener increments are only correlated with itself (e.g. $dW_{12}dW_{12} = dt \quad dW_{12}dW_{13} = 0$). Therefore all cross-terms are zeroed out. Also, for example following is satisfied;

$$d\tilde{\mathbf{v}}_1 \otimes d\tilde{\mathbf{v}}_2 = (d\tilde{\mathbf{v}}_{11} + d\tilde{\mathbf{v}}_{12} + \cdots + d\tilde{\mathbf{v}}_{1N}) \otimes (d\tilde{\mathbf{v}}_{21} + d\tilde{\mathbf{v}}_{22} + \cdots + d\tilde{\mathbf{v}}_{2N}) \tag{A.21}$$

$$= d\tilde{\mathbf{v}}_{12} \otimes d\tilde{\mathbf{v}}_{21} + \text{other terms} \tag{A.22}$$

$$= \sigma^2 w_R(r_{12}) w_R(r_{21}) dW_{12} dW_{21} \mathbf{e}_{12} \otimes \mathbf{e}_{21} \tag{A.23}$$

$$= -\sigma^2 w_R(r_{12})^2 dt \mathbf{e}_{12} \otimes \mathbf{e}_{12} \tag{A.24}$$

and all other terms are zero where one uses $\mathbf{e}_{ij} = -\mathbf{e}_{ji}$. Then the matrix $\mathbf{D_{pp}}$ reads;

$$\mathbf{D}_{pp} = \frac{1}{dt} \begin{bmatrix} \sum_j d\tilde{\mathbf{v}}_{1j} \otimes d\tilde{\mathbf{v}}_{1j} & d\tilde{\mathbf{v}}_{12} \otimes d\tilde{\mathbf{v}}_{21} & d\tilde{\mathbf{v}}_{13} \otimes d\tilde{\mathbf{v}}_{31} & \cdots & d\tilde{\mathbf{v}}_{1N} \otimes d\tilde{\mathbf{v}}_{N1} \\ d\tilde{\mathbf{v}}_{21} \otimes d\tilde{\mathbf{v}}_{12} & \sum_j d\tilde{\mathbf{v}}_{2j} \otimes d\tilde{\mathbf{v}}_{2j} & \cdots & \cdots & d\tilde{\mathbf{v}}_{2N} \otimes d\tilde{\mathbf{v}}_{N2} \\ \vdots & \vdots & \ddots & \vdots & \vdots \\ d\tilde{\mathbf{v}}_{N1} \otimes d\tilde{\mathbf{v}}_{1N} & d\tilde{\mathbf{v}}_{N2} \otimes d\tilde{\mathbf{v}}_{2N} & \cdots & \cdots & \sum_j d\tilde{\mathbf{v}}_{Nj} \otimes d\tilde{\mathbf{v}}_{Nj} \end{bmatrix} \tag{A.25}$$

also;

$$\nabla \cdot (\mathbf{a}p) = \nabla p \cdot \mathbf{a} + p \nabla \cdot \mathbf{a} \tag{A.26}$$

$$\tag{A.27}$$

the dift term reads;

$$\mathbf{a} = \begin{bmatrix} \frac{\mathbf{p}}{m} \\ \mathbf{F}^C + \mathbf{F}^D \end{bmatrix} \tag{A.28}$$

$$\nabla \cdot (\mathbf{a}p) = \nabla_{\mathbf{r}} p \cdot \frac{\mathbf{p}}{m} + \nabla_{\mathbf{p}} p \cdot \left(\mathbf{F}^C + \mathbf{F}^D\right) + p \nabla_{\mathbf{r}} \cdot \frac{\mathbf{p}}{m} + p \nabla_{\mathbf{p}} \cdot \left(\mathbf{F}^C + \mathbf{F}^D\right) \tag{A.29}$$

Here $\mathbf{F}^C$ is a function of position then the equation above simplifies to.

$$\nabla \cdot (\mathbf{a}p) = \frac{\mathbf{p}}{m} \cdot \nabla_{\mathbf{r}} p + \mathbf{F}^C \cdot \nabla_{\mathbf{p}} p + \nabla_{\mathbf{p}} p \cdot \mathbf{F}^D + p \nabla_{\mathbf{p}} \cdot \mathbf{F}^D \tag{A.30}$$

$$= L^C [p] + \nabla_{\mathbf{p}} p \cdot \mathbf{F}^D + p \nabla_{\mathbf{p}} \cdot \mathbf{F}^D \tag{A.31}$$

$$= L^C [p] + \nabla_{\mathbf{p}} \cdot \left(p \mathbf{F}^D \right) \tag{A.32}$$

where $L^C [p] = \frac{\mathbf{p}}{m} \cdot \nabla_{\mathbf{r}} p + \mathbf{F}^C \cdot \nabla_{\mathbf{p}} p$ is the Liouville operator of the Hamiltonian system governed by conservative forces. Therefore the Fokker-Planck equation reads;

$$\frac{\partial p}{\partial t} = -L^C [p] - \nabla_{\mathbf{p}} \cdot \left(p \mathbf{F}^D \right) + \frac{1}{2} \mathbf{D} : \nabla \nabla p \tag{A.33}$$

One seeks for a solution of the equilibrium and therefore transient terms vanish. Furthermore the equilibrium solution is the Boltzmann distribution of the form $p_{eq} = \frac{1}{Z} \exp(-\beta H)$ where H is the Hamiltonian of the system given by the summation of the kinetic and potential energy and β is the inverse energy. The selection of Boltzmann distribution as equilibrium solution is not random rather it means that at steady-state the system attains an equilibrium where equipartition theorem is satisfied. $L^C [p_{eq}] = 0$ by definition. Furthermore, the double contraction with Hessian can be written like this $\mathbf{D} : \nabla \nabla p = \sum_i D_{ii} \frac{\partial^2 p}{\partial x_i^2} + \sum_{i,j \neq i} D_{ij} \frac{\partial p}{\partial x_i \partial x_j}$ here only $\mathbf{D}_{pp}$ block matters since the rest is zero and recall $\mathbf{D}_{ii} = \sum_j \sigma^2 w_R^2(r_{ij}) dt \mathbf{e}_{ij} \otimes \mathbf{e}_{ij}$ (no sum) and $\mathbf{D}_{ij} = -\sigma^2 w_R(r_{ij})^2 dt \mathbf{e}_{ij} \otimes \mathbf{e}_{ij}$. One also notes $\frac{\partial p_{eq}}{\partial \mathbf{p}_i} = -\frac{-\beta}{m} \mathbf{p}_i p_{eq} = -\beta \mathbf{v}_i p_{eq}$.Then the steady Fokker-Planck equation in indical form reads;

$$\begin{aligned} 0 = & \sum_i \sum_{j \neq i} \frac{\partial}{\partial \mathbf{p}_i} \left(\gamma \left(\mathbf{e}_{ij} \otimes \mathbf{e}_{ij} \right) \mathbf{v}_{ij} \, w_D(r_{ij}) \, p_{eq} \right) \\ & + \frac{1}{2} \sum_i \sum_{j \neq i} \left(\sigma^2 w_R(r_{ij})^2 \left(\mathbf{e}_{ij} \otimes \mathbf{e}_{ij} \right) \frac{\partial^2 p_{eq}}{\partial \mathbf{p}_i^2} - \sigma^2 w_R(r_{ij})^2 \left(\mathbf{e}_{ij} \otimes \mathbf{e}_{ij} \right) \frac{\partial^2 p_{eq}}{\partial \mathbf{p}_i \partial \mathbf{p}_j} \right) \end{aligned}$$

$$0 = \frac{\partial}{\partial \mathbf{p}_i} \sum_i \sum_{j \neq i} \left[\gamma \left(\mathbf{e}_{ij} \otimes \mathbf{e}_{ij} \right) \mathbf{v}_{ij} w_D(r_{ij}) p_{eq} + \frac{\sigma^2 w_R(r_{ij})^2}{2} \left(\mathbf{e}_{ij} \otimes \mathbf{e}_{ij} \right) \left(-\frac{\beta}{m} \mathbf{p}_i p_{eq} + \frac{\beta}{m} \mathbf{p}_j p_{eq} \right) \right]$$

$$0 = \gamma w_D(r_{ij}) \left(\mathbf{e}_{ij} \otimes \mathbf{e}_{ij} \right) \mathbf{v}_{ij} p_{eq} - \frac{\sigma^2 w_R(r_{ij})^2 \beta}{2} \left(\mathbf{e}_{ij} \otimes \mathbf{e}_{ij} \right) \mathbf{v}_{ij} p_{eq}$$

$$0 = \left(\gamma w_D(r_{ij}) - \frac{\sigma^2 w_R(r_{ij}) \beta}{2} \right) \left(\mathbf{e}_{ij} \otimes \mathbf{e}_{ij} \right) \mathbf{v}_{ij} p_{eq} \tag{A.34}$$

which then yields two constraints

$$w_D(r) = [w_R(r)]^2 \tag{A.35}$$

$$\sigma = \sqrt{2 k_B T \gamma} \tag{A.36}$$

B Appendix B

There are some conventions, that are used in this appendix relevant to tensor algebra. They are explained in Appendix A. The discretization of the Navier-Stokes equation in SPH formalism is a rigorous task therefore the details will be given in this appendix. Reader can also refer to [48] for the results. Here the intermediate steps are elaborated. For the sake of clarity some information in the main text will be repeated here. Derivation of the correct coefficients and correct forms of the operators appearing in the Navier-Stokes equations with spin is essential in order to get physically meaningful results.One requires some fundamental definitions before the derivations. Recall the governing equations of the fluid flow in Lagrangian form;

$$\rho\frac{d\mathbf{v}}{dt} = -\nabla p + (\eta+\eta_R)\nabla^2\mathbf{v} + \left(\frac{\eta}{3}+\xi-\eta_R\right)\nabla\nabla\cdot\mathbf{v} + 2\eta_R\nabla\times\omega \tag{B.1}$$

$$\frac{d\rho}{dt}+\rho\nabla\cdot\mathbf{v} = 0 \tag{B.2}$$

One considers the following exact representation and its approximation to discretize a field;

$$f(\mathbf{x}_0) = \int_V f(\mathbf{x})\delta(\mathbf{x}-\mathbf{x}_0)dV \tag{B.3}$$

$$f(\mathbf{x}_0) \approx \int_V f(\mathbf{x})W(\mathbf{x},\mathbf{x}_0,r_C)dV \tag{B.4}$$

where the integral is further discretized for a Lagrangian fluid particle with mass m and density ρ.

$$f(\mathbf{x}_0) = \int_V f(\mathbf{x})W(\mathbf{x},\mathbf{x}_0,r_C)dV = \sum_j f(\mathbf{x}_j)W(\mathbf{x}_j,\mathbf{x}_0,r_C)\frac{m(\mathbf{x}_j)}{\rho(\mathbf{x}_j)} \tag{B.5}$$

For the sake of brevity third argument standing for cutoff radii is dropped. Here;

$$W(\mathbf{x},\mathbf{x}_0) = W_{ij} = \frac{105}{16\pi r_C^3}\left(1+3\frac{r}{r_C}\right)\left(1-\frac{r}{r_C}\right)^3, \tag{B.6}$$

$$F(\mathbf{x},\mathbf{x}_0) = F_{ij} = \frac{315}{4\pi r_C^5}\left(1-\frac{r}{r_C}\right)^2. \tag{B.7}$$

where

$$\nabla W(\mathbf{x},\mathbf{x}_0) = \mathbf{r}F(\mathbf{x},\mathbf{x}_0) \tag{B.8}$$

where $\mathbf{r} = \mathbf{x}_0 - \mathbf{x}$ and the derivatives are with respect to $\mathbf{x}$. Following are also required;

$$\int_V W(\mathbf{x},\mathbf{x}_0,r_C)dV = 1 \tag{B.9}$$

$$\lim_{r_C\to 0} W(\mathbf{x},\mathbf{x}_0,r_C) = \delta(\mathbf{x},\mathbf{x}_0) \tag{B.10}$$

In following, particle coordinates are indexed as subscripts (i.e, $\mathbf{x}_j$) is the coordinate vector

of the jth particle not the jth component of vector $\mathbf{x}$. If a property of particle is to be measured with position vector $\mathbf{x}_j$ as $\phi(\mathbf{x}_j)$, then the shorthand notation of this is $\phi(\mathbf{x}_j) = \phi_i$. Therefore, $\mathbf{v}(\mathbf{x}_j) = \mathbf{v}_j$ where $\mathbf{v}_j$ is not the jth component of vector $\mathbf{v}$. That is denoted as $v_j = \mathbf{v}_j \cdot \mathbf{e}_j$.

There are couple of operators to approximate in the modified Navier-Stokes equation, which can be divided into two categories. First being the operators where the first derivative appears and operators where the second derivative appears. ∇p,$\nabla \cdot \mathbf{v}$,$\nabla \times \omega$ belong the first class whereas $\nabla^2 \mathbf{v}$ and $\nabla \nabla \cdot \mathbf{v}$ belong to the second class. It is convenient to start with the first derivatives. Following identity plays a crucial role in deriving the discrete forms of the first class.

$$
\begin{aligned}
\nabla(\phi W) &= \nabla\phi W + \phi \nabla W \\
\int_V \nabla(\phi W) dV &= \int_V \nabla\phi W dV + \int_V \phi \nabla W dV \\
\int_A (\phi W)\mathbf{n} dA &= \nabla\phi(\mathbf{x}_0) + \int_V \phi \nabla W dV \\
0 &= \nabla\phi(\mathbf{x}_0) + \int_V \phi \nabla W dV \\
\nabla\phi(\mathbf{x}_i) &= -\int_V \phi \nabla W dV \\
\nabla\phi(\mathbf{x}_i) &= -\sum_j \phi(\mathbf{x}_j) \nabla W(\mathbf{x}_i, \mathbf{x}_j) \frac{m(\mathbf{x}_j)}{\rho(\mathbf{x}_j)} \\
\nabla\phi\left(\mathbf{x}_i\right) &= -\sum_j \phi(\mathbf{x}_j) \frac{m(\mathbf{x}_j)}{\rho(\mathbf{x}_j)} F\left(\mathbf{x}_i, \mathbf{x}_j\right) \mathbf{r}_{ij} \\
\nabla\phi_i &= -\sum_j \phi_j \frac{m_j}{\rho_j} F_{ij} \mathbf{r}_{ij}
\end{aligned}
\tag{B.11}
$$

This expression is not convenient when $\phi(\mathbf{x}) = c$ it returns non-zero results. Therefore following identity is highlighted using the above derived result However Equation (B.11) will be used to

get Equation (B.13).;

$$\nabla\left(\frac{\phi}{\rho}\right) = \frac{\nabla\phi\rho - \phi\nabla\rho}{\rho^2} \tag{B.12}$$

$$\nabla\phi = \rho\nabla\left(\frac{\phi}{\rho}\right) + \frac{\phi\nabla\rho}{\rho}$$

$$\nabla\phi_i = -\rho_i \sum_j \frac{\phi_j}{\rho_j} F_{ij}\mathbf{r}_{ij}\frac{m_j}{\rho_j} - \frac{\phi_i}{\rho_i}\sum_j \rho_j F_{ij}\mathbf{r}_{ij}\frac{m_j}{\rho_j} \tag{B.13}$$

$$\nabla\phi_i = -\rho_i \sum_j \left[\frac{\phi_j}{\rho_j} + \rho_j\frac{\phi_i}{\rho_i^2}\right] F_{ij}\mathbf{r}_{ij}\frac{m_j}{\rho_j}$$

$$\nabla\phi_i = -\rho_i \sum_j m_j F_{ij}\mathbf{r}_{ij}\left[\frac{\phi_i}{\rho_i^2} + \frac{\phi_j}{\rho_j^2}\right]$$

$$-\frac{\nabla p_i}{\rho_i} = \sum_j m_j\left(\frac{p_i}{\rho_i^2} + \frac{p_j}{\rho_j^2}\right) F_{ij}\mathbf{r}_{ij} \tag{B.14}$$

Equation (B.14) corresponds the discretized form of the pressure term appearing in Equation (B.1).Similarly following the same paradigm divergence is approximated as;

$$\nabla\cdot(\mathbf{v}W) = \nabla\cdot\mathbf{v}W + \mathbf{v}\cdot\nabla W$$

$$\int_V \nabla\cdot(\mathbf{v}W)\,dV = \int_V \nabla\cdot\mathbf{v}W dV + \int_V \mathbf{v}\cdot\nabla W dV$$

$$0 = \int_V \nabla\cdot\mathbf{v}W dV + \int_V \mathbf{v}\cdot\nabla W dV$$

$$\nabla\cdot\mathbf{v}(\mathbf{x}_i) = -\int_V \mathbf{v}\nabla W dV$$

$$\nabla\cdot\mathbf{v}(\mathbf{x}_i) = -\sum_j \mathbf{v}_j(\mathbf{x}_j)\nabla W(\mathbf{x}_i,\mathbf{x}_j)\frac{m(\mathbf{x}_j)}{\rho(\mathbf{x}_j)}$$

$$\nabla\cdot\mathbf{v}_i = -\sum_j \mathbf{v}_j\frac{m_j}{\rho_j}F_{ij}\mathbf{r}_{ij}$$

$$\nabla\cdot(\mathbf{v}\rho) - \mathbf{v}\nabla\rho = \nabla\cdot\mathbf{v}\rho$$

$$\nabla\cdot\mathbf{v} = \frac{\nabla\cdot(\mathbf{v}\rho) - \mathbf{v}\nabla\rho}{\rho}$$

$$\nabla\cdot\mathbf{v}_i = -\frac{1}{\rho_i}\sum_j \mathbf{v}_j\rho_j F_{ij}\mathbf{r}_{ij}\frac{m_j}{\rho_j} + \frac{\mathbf{v}_i}{\rho_i}\sum_j \rho_j F_{ij}\mathbf{r}_{ij}\frac{m_j}{\rho_j}$$

$$-\rho_i\nabla\cdot\mathbf{v}_i = \sum_j \left[\mathbf{v}_j - \mathbf{v}_i\right]\rho_j F_{ij}\mathbf{r}_{ij}\frac{m_j}{\rho_j}$$

$$\left.\frac{d\rho}{dt}\right|_i = -\sum_j \left[\mathbf{v}_i - \mathbf{v}_j\right] F_{ij}\mathbf{r}_{ij}m_j \tag{B.15}$$

Equation (B.15) is the discretized form of Equation (B.2). In order to calculate $\nabla\times\mathbf{v}$ one has to recall Equation (B.12) and instead of ρ another function λ is introduced. Using the same

procedure and picking $\lambda = 1$ at the final step yields a new description to the $\nabla\phi$ which reads;

$$\nabla\phi = \lambda\nabla\left(\frac{\phi}{\lambda}\right) + \frac{\phi\nabla\lambda}{\lambda} \tag{B.16}$$

$$\nabla\phi_i = -\sum_j \frac{m_j}{\rho_j}\left(\phi_i + \phi_j\right)\nabla W \tag{B.17}$$

Here the following identity will be utilized. $\nabla \times \mathbf{v} = \frac{\partial v_j}{\partial x_i}\varepsilon_{ijk}\mathbf{e}_k$ which is the definition of the curl. Furthermore;

$$\begin{aligned}
\nabla \times \mathbf{v} &= -\nabla\mathbf{v} : \varepsilon_{ijk}\left(\mathbf{e}_i \otimes \mathbf{e}_j \otimes \mathbf{e}_k\right) \\
\nabla \times \mathbf{v} &= \sum_j \frac{m_j}{\rho_j}\left(\mathbf{v}_i + \mathbf{v}_j\right) \times \nabla W_{ij} \\
\nabla \times \mathbf{v} &= \rho_i \sum_j \frac{m_j}{\rho_i\rho_j}\left(\mathbf{v}_i + \mathbf{v}_j\right) \times \nabla W_{ij}
\end{aligned} \tag{B.18}$$

Then the rotational term in the Equation (B.1) reads;

$$\begin{aligned}
2\eta_R\,\nabla \times \boldsymbol{\omega}_i &= 2\eta_R \sum_j \frac{F_{ij}}{\rho_i\rho_j}\left(\left(\boldsymbol{\omega}_i + \boldsymbol{\omega}_j\right) \times \mathbf{r}_{ij}\right) \\
&= -2\eta_R \sum_j \frac{F_{ij}}{\rho_i\rho_j}\left(\mathbf{r}_{ij} \times \left(\boldsymbol{\omega}_i + \boldsymbol{\omega}_j\right)\right)
\end{aligned} \tag{B.19}$$

The above derivations complete the operators which only have first derivatives of the field variables. For higher order derivatives following is used for field variable ϕ;

$$\begin{aligned}
\phi(\mathbf{x}) &= \phi(\mathbf{x}_0) + \nabla\phi(\mathbf{x}_0)\cdot(\mathbf{x} - \mathbf{x}_0) + \frac{1}{2}\nabla\nabla\phi(\mathbf{x}_0) : \left((\mathbf{x} - \mathbf{x}_0) \otimes (\mathbf{x} - \mathbf{x}_0)\right) \\
\phi(\mathbf{x}) - \phi(\mathbf{x}_0) &= \nabla\phi(\mathbf{x}_0)\cdot(\mathbf{x} - \mathbf{x}_0) + \frac{1}{2}\nabla\nabla\phi(\mathbf{x}_0) : \left((\mathbf{x} - \mathbf{x}_0) \otimes (\mathbf{x} - \mathbf{x}_0)\right)
\end{aligned}$$

multiplying both sides with $F(r)\frac{\mathbf{r}\otimes\mathbf{r}}{r^2}$ where $\mathbf{r} = \mathbf{x}_0 - \mathbf{x}$ yields;

$$\begin{aligned}
\left(\phi(\mathbf{x}) - \phi(\mathbf{x}_0)\right)F(r)\frac{\mathbf{r}\otimes\mathbf{r}}{r^2} &= \left(-\nabla\phi(\mathbf{x}_0)\cdot\mathbf{r}F(r)\frac{\mathbf{r}\otimes\mathbf{r}}{r^2} + \frac{1}{2}\nabla\nabla\phi(\mathbf{x}_0) : F(r)\left(\mathbf{r}\otimes\mathbf{r}\right)\frac{\mathbf{r}\otimes\mathbf{r}}{r^2}\right) \\
\int_V \left(\phi(\mathbf{x}) - \phi(\mathbf{x}_0)\right)F(r)\frac{\mathbf{r}\otimes\mathbf{r}}{r^2}dV &= \int_V \left(-\nabla\phi(\mathbf{x}_0)\cdot\mathbf{r}F(r)\frac{\mathbf{r}\otimes\mathbf{r}}{r^2} + \frac{1}{2}\nabla\nabla\phi(\mathbf{x}_0) : \left(\mathbf{r}\otimes\mathbf{r}\right)F(r)\frac{\mathbf{r}\otimes\mathbf{r}}{r^2}\right)dV \\
\int_V \left(\phi(\mathbf{x}) - \phi(\mathbf{x}_0)\right)F(r)\frac{\mathbf{r}\otimes\mathbf{r}}{r^2}dV &= \int_V \left(-\nabla\phi(\mathbf{x}_0)F(r)\frac{\mathbf{r}\otimes\mathbf{r}\otimes\mathbf{r}}{r^2} + \frac{1}{2}\nabla\nabla\phi(\mathbf{x}_0) : F(r)\frac{\mathbf{r}\otimes\mathbf{r}\otimes\mathbf{r}\otimes\mathbf{r}\otimes\mathbf{r}}{r^2}\right)dV
\end{aligned} \tag{B.20}$$

Following also holds;

$$\int_V \lambda(r)\frac{\mathbf{r}\otimes\mathbf{r}\otimes\mathbf{r}}{r^2} = 0 \quad \text{(Due to anisotropy for any } \lambda(r))$$

$$\int_V \left(\frac{1}{2}\nabla\nabla\phi(\mathbf{x}_0) : F(r)\frac{\mathbf{r}\otimes\mathbf{r}\otimes\mathbf{r}\otimes\mathbf{r}\otimes\mathbf{r}}{r^2}\right) dV = \frac{1}{2}\nabla\nabla\phi(\mathbf{x}_0) : \int_V F(r)\frac{\mathbf{r}\otimes\mathbf{r}\otimes\mathbf{r}\otimes\mathbf{r}\otimes\mathbf{r}}{r^2} dV$$

The integral over a sphere of a second order tensor formed by distance vectors yields an identity tensor of the following form;

$$\int_V \lambda(r)\frac{\mathbf{r}\otimes\mathbf{r}}{r^2} = c\mathbf{I} = c\delta_{ij}\left(\mathbf{e}_i\otimes\mathbf{e}_j\right)$$

similarly fourth order distance tensor yields a fourth order identity tensor of the following form where $\lambda_{1,2}$ to be determined;

$$\int_V F(r)\,\frac{\mathbf{r}\otimes\mathbf{r}\otimes\mathbf{r}\otimes\mathbf{r}}{r^2}\,dV = \left(\lambda_1\,\delta_{ij}\,\delta_{mn} + \lambda_2\left(\delta_{im}\,\delta_{jn} + \delta_{in}\,\delta_{jm}\right)\right)\left(\mathbf{e}_i\otimes\mathbf{e}_j\otimes\mathbf{e}_m\otimes\mathbf{e}_n\right)$$

Contracting different indices yields two equations for two unknowns;

$$\begin{aligned}\int_V F(r)\,\frac{r_i r_j r_m r_n}{r^2}\,\delta_{ij}\,\delta_{mn}\,dV &= \int_V F(r)\,\frac{r_i r_i r_m r_m}{r^2}\,dV \\ &= \int_V F(r)\,\frac{r^2 r^2}{r^2}\,dV \\ &= \int_V F(r)\,r^2\,dV \\ &= 9\lambda_1 + 6\lambda_2\end{aligned} \tag{B.21}$$

Where above contraction turns i to j and m to n. Also Kronocker delta satisfies the following properties $\delta_{ii} = 3$ and $\delta_{ij}\delta_{ij} = \delta_{ii} = 3$. Similarly applying the the contraction of i to m and j to n gives the second equation.

$$\int_V F(r)r^2 dV = 3\lambda_1 + 12\lambda_2 \tag{B.22}$$

and noting that $\int_V F(r)r^2 dV = 3$, $\lambda_1 = \lambda_2 = \frac{1}{5}$. Therefore;

$$\int_V F(r)\,\frac{\mathbf{r}\otimes\mathbf{r}\otimes\mathbf{r}\otimes\mathbf{r}}{r^2}\,dV = \left(\frac{1}{5}\,\delta_{ij}\,\delta_{mn} + \frac{1}{5}\left(\delta_{im}\,\delta_{jn} + \delta_{in}\,\delta_{jm}\right)\right)\left(\mathbf{e}_i\otimes\mathbf{e}_j\otimes\mathbf{e}_m\otimes\mathbf{e}_n\right) \tag{B.23}$$

$$\frac{1}{2}\nabla\nabla\phi : \left(\frac{1}{5}\,\delta_{ij}\,\delta_{mn} + \frac{1}{5}\left(\delta_{im}\,\delta_{jn} + \delta_{in}\,\delta_{jm}\right)\right)(\mathbf{e}_i \otimes \mathbf{e}_j \otimes \mathbf{e}_m \otimes \mathbf{e}_n) = \frac{1}{10}\,\frac{\partial^2\phi}{\partial x_i \partial x_j}\,\delta_{ij}\,\delta_{mn} + \frac{1}{10}\left(\frac{\partial^2\phi}{\partial x_i \partial x_j}\,\delta_{im}\,\delta_{jn} + \frac{\partial^2\phi}{\partial x_i \partial x_j}\,\delta_{in}\,\delta_{jm}\right)(\mathbf{e}_m \otimes \mathbf{e}_n)$$
$$= \left(\frac{1}{10}\frac{\partial^2\phi}{\partial x_i^2}\delta_{mn} + \frac{2}{10}\frac{\partial^2\phi}{\partial x_i \partial x_j}\right)(\mathbf{e}_m \otimes \mathbf{e}_n)$$
$$= \frac{1}{10}\nabla^2\phi\mathbf{I} + \frac{2}{10}\nabla\nabla\phi \tag{B.24}$$

Therefore;

$$\int_V \left(\phi(\mathbf{x}) - \phi(\mathbf{x}_0)\right) F(r)\frac{\mathbf{r}\otimes\mathbf{r}}{r^2}dV = \frac{1}{10}\nabla^2\phi\mathbf{I} + \frac{2}{10}\nabla\nabla\phi \tag{B.25}$$

Taking the trace of both sides yields;

$$\int_V \left(\phi(\mathbf{x}) - \phi(\mathbf{x}_0)\right) F(r)dV = \frac{5}{10}\nabla^2\phi \tag{B.26}$$
$$2\int_V \left(\phi(\mathbf{x}) - \phi(\mathbf{x}_0)\right) F(r)dV = \nabla^2\phi \tag{B.27}$$

Plugging in Equation (B.27) into Equation (B.25) gives;

$$\int_V \left(\phi(\mathbf{x}) - \phi(\mathbf{x}_0)\right) F(r)\frac{\mathbf{r}\otimes\mathbf{r}}{r^2}dV = \frac{1}{5}\int_V \left(\phi(\mathbf{x}) - \phi(\mathbf{x}_0)\right) F(r)\mathbf{I}dV + \frac{1}{5}\nabla\nabla\phi$$
$$\nabla\nabla\phi = \int_V \left(\phi(\mathbf{x}) - \phi(\mathbf{x}_0)\right) F(r)\left[5\frac{\mathbf{r}\otimes\mathbf{r}}{r^2} - \mathbf{I}\right]dV \tag{B.28}$$

Therefore;

$$\nabla^2\mathbf{v} = -2\sum_j \frac{F_{ij}m_j}{\rho_j}\mathbf{v}_{ij} \tag{B.29}$$
$$\nabla\nabla\cdot\mathbf{v} = -\sum_j \frac{F_{ij}m_j}{\rho_j}\left(5\left(\mathbf{e}_{ij}\otimes\mathbf{e}_{ij}\right) - \mathbf{I}\right)\mathbf{v}_{ij}$$
$$= -\sum_j \frac{F_{ij}m_j}{\rho_j}\left(5\left(\mathbf{e}_{ij}\cdot\mathbf{v}_{ij}\right)\mathbf{e}_{ij} - \mathbf{v}_{ij}\right) \tag{B.30}$$

Now using the derived operators above the deterministic forces are;

$$\mathbf{F}_{ij}^C = m_i m_j\left(\frac{p_i}{\rho_i^2} + \frac{p_j}{\rho_j^2}\right)F_{ij}\mathbf{r}_{ij} \tag{B.31}$$
$$\mathbf{F}_{ij}^D = -m_i m_j\left(\frac{5\eta}{3} + 3\eta_r - \xi\right)\frac{F_{ij}}{\rho_i\rho_j}\mathbf{v}_{ij} - 5m_i m_j\left(\frac{\eta}{3} + \xi - \eta_r\right)\frac{F_{ij}}{\rho_i\rho_j}\mathbf{e}_{ij}\left(\mathbf{e}_{ij}\cdot\mathbf{v}_{ij}\right) \tag{B.32}$$
$$\mathbf{F}_{ij}^R = -2m_i m_j\eta_R\frac{F_{ij}}{\rho_i\rho_j}\mathbf{r}_{ij}\times\left(\omega_i + \omega_j\right) \tag{B.33}$$

C Appendix C

There are some conventions, that are used in this appendix relevant to tensor algebra. They are explained in Appendix A. In the Appendix B the deterministic forces of for the Navier-Stokes equation with spin are derived. Only with the deterministic forces the method can be called as angular momentum conserving SPH. However, many physical systems require the modeling of stochastic forces arising from the random collisions of the molecules to the body of interest. Therefore a random force must be included to mimic the thermal bath. As discussed in the Appendix A a balance between the deterministic forces and the random forces must be set in order to obtain correct thermodynamic behaviour of the system. Since the derivation is rigorous the details will be given in this appendix. Same paradigm will be followed as in Appendix A. The results of [46] is obtained in this appendix and combined with the methodology of [66]. A generic approach requires the following. One has a system of particles. These particles interact each other between conservative, dissipative, rotational and stochastic forces which alters the linear velocity. On the top of that one there are torque interactions arising from the dissipative, rotational forces and stochastic forces. The conservative force strictly conserves the angular momentum hence no moment is created due to conservative force. The SDE, that governs the motion can be recast into the following form;

$$d\mathbf{x} = \mathbf{a}dt + d\tilde{\mathbf{x}} \tag{C.1}$$

$$\tag{C.2}$$

here;

$$d\mathbf{x} = \begin{bmatrix} d\mathbf{r} \\ d\mathbf{v} \\ d\boldsymbol{\omega} \end{bmatrix} = \begin{bmatrix} \mathbf{v} \\ \mathbf{F}^C + \mathbf{F}^D + \mathbf{F}^R \\ \mathbf{T}^D + \mathbf{T}^R \end{bmatrix} dt + \begin{bmatrix} \mathbf{0} \\ d\tilde{\mathbf{v}} \\ d\tilde{\boldsymbol{\omega}} \end{bmatrix}, \tag{C.3}$$

where $d\mathbf{r}, d\mathbf{v}, d\omega$ are the changes is position, linear velocity and angular velocity respectively. $\mathbf{a}$ is the drift vector and contains $\mathbf{v}, \mathbf{F}^C, \mathbf{F}^D, \mathbf{F}^R$, linear velocity, conservative, dissipative and rotational accelerations (not forces, see below for the definitions of the forces), $\mathbf{T}^D, \mathbf{T}^R$ are the rotational accelerations (not torques, see below for the definitions of the forces) due to viscous forces and rotational forces. $d\tilde{\mathbf{v}}, d\tilde{\omega}$ are the stochastic contributions due to thermal bath. For the time being they will be kept as it is actual expressions for them will be given later.The explicit form of the SDE for the sake of clarity is given below for particle i.

$$d\mathbf{r}_i = \mathbf{v}_i \, dt \tag{C.4}$$

$$d\mathbf{v}_i = \frac{1}{m} \sum_j \left[\mathbf{F}_{ij}^C + \mathbf{F}_{ij}^D + \mathbf{F}_{ij}^R \right] dt + \sum_j d\tilde{\mathbf{v}}_{ij} \tag{C.5}$$

$$d\boldsymbol{\omega}_i = -\frac{1}{I}\sum_j \frac{\mathbf{r}_{ij}}{2} \times \left[\mathbf{F}_{ij}^D + \mathbf{F}_{ij}^R\right] dt - \frac{m}{I}\sum_j \frac{\mathbf{r}_{ij}}{2} \times d\tilde{\mathbf{v}}_{ij} \tag{C.6}$$

Here $\mathbf{F}^D$,$\mathbf{F}^R$ and $\mathbf{F}^C$ are assumed to be of the form;

$$\mathbf{F}_{ij}^D = -\gamma m\, \mathbf{M}^D(\mathbf{r}_{ij})\, \mathbf{v}_{ij} \tag{C.7}$$

$$\mathbf{F}_{ij}^R = -\gamma m\, \mathbf{M}^R(\mathbf{r}_{ij}) \left(\frac{\mathbf{r}_{ij}}{2} \times (\boldsymbol{\omega}_i + \boldsymbol{\omega}_j)\right) \tag{C.8}$$

$$\mathbf{F}_{ij}^C = -\nabla U\,(r) \tag{C.9}$$

where

$$\mathbf{M}^D = A(r_{ij})\mathbf{I} + B(r_{ij})\mathbf{e}_{ij} \otimes \mathbf{e}_{ij} \tag{C.10}$$

$$\mathbf{M}^R = C(r_{ij})\mathbf{I} + D(r_{ij})\mathbf{e}_{ij} \otimes \mathbf{e}_{ij} \tag{C.11}$$

$$\tag{C.12}$$

The form of $d\tilde{\mathbf{v}}_{ij}$ will be introduced later on.

Similar to Appendix A for example $d\mathbf{r} = [d\mathbf{r}_1; d\mathbf{r}_2; ...; d\mathbf{r}_N]$ it the column vector bookkeeping the change in positions of the particles. Here the I and m are the moment of inertia and mass of the particles. The summations and co-factors are embedded inside the grand variables. Such as $-\frac{1}{I}\sum_j \frac{r_{ij}}{2} \times \mathbf{F}_{ij}^D$ is inside the grand variable $\mathbf{T}^D = [\mathbf{T}_1^D; ...; \mathbf{T}_i^D; ...; \mathbf{T}_N^D]$. If the steps in Appendix A is followed (Equation (A.3) - A.13) the transient Fokker-Planck equation reads;

$$\frac{\partial p}{\partial t} = -\nabla \cdot (\mathbf{a}p) + \frac{1}{2}\mathbf{D} : \nabla\nabla p \tag{C.13}$$

This time $\mathbf{D}$ is;

$$\mathbf{D} = \frac{1}{dt} d\tilde{\mathbf{x}} \otimes d\tilde{\mathbf{x}} = \frac{1}{dt} \begin{bmatrix} \mathbf{0} & \mathbf{0} & \mathbf{0} \\ \mathbf{0} & d\tilde{\mathbf{v}} \otimes d\tilde{\mathbf{v}} & d\tilde{\mathbf{v}} \otimes d\tilde{\boldsymbol{\omega}} \\ \mathbf{0} & d\tilde{\boldsymbol{\omega}} \otimes d\tilde{\mathbf{v}} & d\tilde{\boldsymbol{\omega}} \otimes d\tilde{\boldsymbol{\omega}} \end{bmatrix}. \tag{C.14}$$

and again $\nabla \cdot \mathbf{D} = 0$. Following inter particle noise term is postulated $d\tilde{\mathbf{v}}_{ij}$

$$d\tilde{\mathbf{v}}_{ij} = \sigma \left[\tilde{A}(r)(d\mathbf{W}_{ij})^\dagger + \tilde{B}(r)\frac{1}{D} tr\left[d\mathbf{W}_{ij}\right]\mathbf{I} + \tilde{C} d\mathbf{W}_{ij}^A\right] \mathbf{e}_{ij} \tag{C.15}$$

where $d\mathbf{W}_{ij}$ tensor of independent Wiener increments between particle i and j. It is a second order 3 by 3 tensor. $d\mathbf{W}_{ij}^\dagger$ is the deviatoric part of symmetric $d\mathbf{W}_{ij}$ whereas $d\mathbf{W}_{ij}^A$ is the

skew-symmetric part of the same matrix give as follows;

$$d\mathbf{W}_{ij}^{S} = \frac{1}{2}\left(d\mathbf{W}_{ij} + d\mathbf{W}_{ij}^{T}\right) \tag{C.16}$$

$$d\mathbf{W}_{ij}^{\dagger} = d\mathbf{W}_{ij}^{S} - \frac{1}{D} tr[d\mathbf{W}_{ij}^{S}]\mathbf{I} \tag{C.17}$$

$$d\mathbf{W}_{ij}^{A} = \frac{1}{2}\left(d\mathbf{W}_{ij} - d\mathbf{W}_{ij}^{T}\right) \tag{C.18}$$

where $d\mathbf{W}^{T}$ is the transpose of the same matrix. In principle $d\mathbf{W}$ is a fourth order tensor which have 4 independent indices and hence $d\mathbf{W} \otimes d\mathbf{W}$ is a 8th order tensor. The actual representation of $d\mathbf{W}$ is unknown but its correlation with another Wiener increment tensor in the system is symmetric under particle interchange and ensures the momentum conservation obeying the Ito interpretation as being infinitesimal order of $1/2$ in dt.

$$d\mathbf{W} \otimes d\mathbf{W} = dW_{ii'}^{\mu\mu'} dW_{jj'}^{\nu\nu'} \left(\mathbf{e}_i \otimes \mathbf{e}_{i'} \otimes \mathbf{e}_j \otimes \mathbf{e}_{j'} \otimes \mathbf{e}_\mu \otimes \mathbf{e}_{\mu'} \otimes \mathbf{e}_\nu \otimes \mathbf{e}_{\nu'}\right) \tag{C.19}$$

$$dW_{ii'}^{\mu\mu'} dW_{jj'}^{\nu\nu'} = \left[\delta_{ij}\delta_{i'j'} + \delta_{ij'}\delta_{ji'}\right] \delta_{\mu\nu}\delta_{\mu'\nu'}\, dt \tag{C.20}$$

Here the indices i, i', j, j' run over the particles indices whereas ν, ν', μ, μ' run over the spatial dimensions. For example $d\mathbf{W}_{12}$ is a second order tensor of three by three. dW_{12}^{xy} is the xy component of the same tensor. Another example, $d\mathbf{W}_{12} \otimes d\mathbf{W}_{35} = \mathbf{0}$. Here $i = 1, i' = 2, j = 3, j' = 5$ and all Kronocker deltas which has the indices running over the particle markers are zeroed out. Since the spatial dimensions are not indicated the second part of the expression still remains (i.e., the part in front of dt). This also means $d\mathbf{W}_{12}$ has no correlation with $d\mathbf{W}_{35}$. If one picks $d\mathbf{W}_{12} \otimes d\mathbf{W}_{21}$ or $d\mathbf{W}_{12} \otimes d\mathbf{W}_{12}$ the calculation yields a fourth order tensor with a coefficient of dt. A closer look for example to term $d\tilde{\mathbf{v}}_1 \otimes d\tilde{\mathbf{v}}_1$ reveals;

$$\begin{aligned} d\tilde{\mathbf{v}}_1 \otimes d\tilde{\mathbf{v}}_1 &= (d\tilde{\mathbf{v}}_{11} + d\tilde{\mathbf{v}}_{12} + \cdots + d\tilde{\mathbf{v}}_{1N}) \otimes (d\tilde{\mathbf{v}}_{11} + d\tilde{\mathbf{v}}_{12} + \cdots + d\tilde{\mathbf{v}}_{1N}) \\ &= d\tilde{\mathbf{v}}_{11} \otimes d\tilde{\mathbf{v}}_{11} + d\tilde{\mathbf{v}}_{12} \otimes d\tilde{\mathbf{v}}_{12} + \cdots d\tilde{\mathbf{v}}_{1N} \otimes d\tilde{\mathbf{v}}_{1N} + \text{cross terms} \end{aligned} \tag{C.21}$$

where for example;

$$\begin{aligned} d\tilde{\mathbf{v}}_{12} \otimes d\tilde{\mathbf{v}}_{12} = \sigma^2 &\left[\tilde{A}(r_{12})(d\mathbf{W}_{12})^{\dagger} + \tilde{B}(r_{12})\frac{1}{D} tr\left[d\mathbf{W}_{12}\right]\mathbf{I} + \tilde{C}(r_{12}) d\mathbf{W}_{12}^{A}\right] \mathbf{e}_{12} \\ \otimes &\left[\tilde{A}(r_{12})(d\mathbf{W}_{12})^{\dagger} + \tilde{B}(r_{12})\frac{1}{D} tr\left[d\mathbf{W}_{12}\right]\mathbf{I} + \tilde{C}(r_{12}) d\mathbf{W}_{12}^{A}\right] \mathbf{e}_{12} \end{aligned} \tag{C.22}$$

Using the following identity $(\mathbf{Au}) \otimes (\mathbf{Bu}) = \mathbf{u} \cdot \left(\mathbf{A}^T \otimes \mathbf{B}\right) \cdot \mathbf{u}$

$$
\begin{aligned}
d\tilde{\mathbf{v}}_{12} \otimes d\tilde{\mathbf{v}}_{12} = \sigma^2\, \mathbf{e}_{12} \cdot \Bigg[& \left(\tilde{A}(r_{12})\, (d\mathbf{W}_{12})^\dagger + \tilde{B}(r_{12})\, \frac{1}{D}\, \mathrm{tr}(d\mathbf{W}_{12})\, \mathbf{I} + \tilde{C}(r_{12})\, d\mathbf{W}_{12}^A \right)^T \\
& \otimes \left(\tilde{A}(r_{12})\, (d\mathbf{W}_{12})^\dagger + \tilde{B}(r_{12})\, \frac{1}{D}\, \mathrm{tr}(d\mathbf{W}_{12})\, \mathbf{I} + \tilde{C}(r_{12})\, d\mathbf{W}_{12}^A \right) \Bigg] \cdot \mathbf{e}_{12} \qquad \text{(C.23)} \\
= \sigma^2\, \mathbf{e}_{12} \cdot \Bigg[& \left(\tilde{A}(r_{12})\, (d\mathbf{W}_{12})^\dagger + \tilde{B}(r_{12})\, \frac{1}{D}\, \mathrm{tr}(d\mathbf{W}_{12})\, \mathbf{I} - \tilde{C}(r_{12})\, d\mathbf{W}_{12}^A \right) \\
& \otimes \left(\tilde{A}(r_{12})\, (d\mathbf{W}_{12})^\dagger + \tilde{B}(r_{12})\, \frac{1}{D}\, \mathrm{tr}(d\mathbf{W}_{12})\, \mathbf{I} + \tilde{C}(r_{12})\, d\mathbf{W}_{12}^A \right) \Bigg] \cdot \mathbf{e}_{12} \\
= \sigma^2\, \mathbf{e}_{12} \cdot \Big[& \tilde{A}^2\, (d\mathbf{W}_{12})^\dagger \otimes (d\mathbf{W}_{12})^\dagger + \tilde{B}^2\, \frac{1}{D^2}\, \mathrm{tr}(d\mathbf{W}_{12})^2\, \mathbf{I} \otimes \mathbf{I} \\
& - \tilde{C}^2\, d\mathbf{W}_{12}^A \otimes d\mathbf{W}_{12}^A + (\text{cross terms}) \Big] \cdot \mathbf{e}_{12}
\end{aligned}
$$

Note also $(d\mathbf{W}_{ij}^\dagger)^T = d\mathbf{W}_{ij}^\dagger$ and $(d\mathbf{W}_{ij}^A)^T = -d\mathbf{W}_{ij}^A$. This equation can be generalized for the particle i and j simply by changing 1 to i and 2 to j. Further investigation of the outer products needs to be done.

$$
\mathrm{tr}\left(d\mathbf{W} \otimes d\mathbf{W}\right) = \mathrm{tr}\left(dW_{ii'}^{\mu\mu'} dW_{jj'}^{\nu\nu'}\right) = dW_{ii'}^{\mu\mu} dW_{jj'}^{\nu\nu} = \left[\delta_{ij}\delta_{i'j'} + \delta_{ij'}\delta_{ji'}\right] D dt \qquad \text{(C.24)}
$$

$$
d\mathbf{W}^A \otimes d\mathbf{W}^A = \frac{1}{4}\left(d\mathbf{W} - d\mathbf{W}^T\right) \otimes \left(d\mathbf{W} - d\mathbf{W}^T\right)
$$

where,

$$
\begin{aligned}
d\mathbf{W} \otimes d\mathbf{W} &= dW_{ii'}^{\mu\mu'}\, dW_{jj'}^{\nu\nu'} \\
d\mathbf{W} \otimes d\mathbf{W}^T &= dW_{ii'}^{\mu\mu'}\, dW_{jj'}^{\nu'\nu} \\
d\mathbf{W}^T \otimes d\mathbf{W} &= dW_{ii'}^{\mu'\mu}\, dW_{jj'}^{\nu\nu'} \\
d\mathbf{W}^T \otimes d\mathbf{W}^T &= dW_{ii'}^{\mu'\mu}\, dW_{jj'}^{\nu'\nu}
\end{aligned} \qquad \text{(C.25)}
$$

therefore;

$$
\begin{aligned}
d\mathbf{W}^A \otimes d\mathbf{W}^A &= \frac{1}{4}\left[\delta_{ij}\delta_{j'i'} + \delta_{ij'}\delta_{ji'}\right]\left(\delta_{\mu\nu}\delta_{\mu'\nu'} - \delta_{\mu\nu'}\delta_{\mu'\nu} - \delta_{\mu\mu'}\delta_{\nu\nu'} + \delta_{\mu\nu}\delta_{\mu'\nu'}\right) dt \\
&= \frac{1}{2}\left[\delta_{ij}\delta_{j'i'} + \delta_{ij'}\delta_{ji'}\right]\left(\delta_{\mu\nu}\delta_{\mu'\nu'} - \delta_{\mu\nu'}\delta_{\mu'\nu}\right) dt
\end{aligned} \qquad \text{(C.26)}
$$

In the equations above the tensor notation is omitted but if there is an indical notation it must

have multiplied with necessary tensor operators $\mathbf{e}_i \otimes \mathbf{e}_j$...

$$d\mathbf{W}^{\dagger} \otimes d\mathbf{W}^{\dagger} = \left(d\mathbf{W}_{ij}^{S} - \frac{1}{D} tr[d\mathbf{W}_{ij}^{S}]\mathbf{I} \right) \otimes \left(d\mathbf{W}_{ij}^{S} - \frac{1}{D} tr[d\mathbf{W}_{ij}^{S}]\mathbf{I} \right) \tag{C.27}$$
$$= [\delta_{ij}\delta_{j'i'} + \delta_{ij'}\delta_{ji'}] \left[\frac{1}{2} \left(\delta_{\mu\nu}\delta_{\mu'\nu'} + \delta_{\mu\nu'}\delta_{\mu'\nu} \right) - \frac{1}{D}\delta_{\mu\mu'}\delta_{\nu\nu'} \right] dt$$

Here the details are skipped because they are lengthy but the logic is the same. Further it can be easily showed the cross terms are zero therefore;

$$d\tilde{\mathbf{v}}_{12} \otimes d\tilde{\mathbf{v}}_{12} = \sigma^2 \, \mathbf{e}_{12} \cdot \left[\tilde{A}^2 \, (d\mathbf{W}_{12})^{\dagger} \otimes (d\mathbf{W}_{12})^{\dagger} + \tilde{B}^2 \, \frac{1}{D^2} \, \mathrm{tr}(d\mathbf{W}_{12})^2 \, \mathbf{I} \otimes \mathbf{I} - \tilde{C}^2 \, d\mathbf{W}_{12}^{A} \otimes d\mathbf{W}_{12}^{A} \right] \cdot \mathbf{e}_{12} \tag{C.28}$$

In order to further simplify the calculation, let;

$$\boldsymbol{\Sigma}_1 = \delta_{\mu\nu}\delta_{\mu'\nu'} \, (\mathbf{e}_{\mu} \otimes \mathbf{e}_{\mu'} \otimes \mathbf{e}_{\nu} \otimes \mathbf{e}_{\nu'}) \Rightarrow \mathbf{u}\cdot\boldsymbol{\Sigma}_1\cdot\mathbf{u} = u_{\mu}\delta_{\mu\nu}\delta_{\mu'\nu'}u_{\nu'}(\mathbf{e}_{\mu'}\otimes\mathbf{e}_{\nu}) = u_{\nu}u_{\mu'}(\mathbf{e}_{\mu'}\otimes\mathbf{e}_{\nu}) = \mathbf{u}\otimes\mathbf{u} \tag{C.29}$$

$$\boldsymbol{\Sigma}_2 = \delta_{\mu\nu'}\delta_{\mu'\nu} \, (\mathbf{e}_{\mu} \otimes \mathbf{e}_{\mu'} \otimes \mathbf{e}_{\nu} \otimes \mathbf{e}_{\nu'}) \Rightarrow \mathbf{u}\cdot\boldsymbol{\Sigma}_2\cdot\mathbf{u} = u_{\mu}\delta_{\mu\nu'}\delta_{\mu'\nu}u_{\nu'}(\mathbf{e}_{\mu'}\otimes\mathbf{e}_{\nu}) = u_{\nu'}u_{\nu'}\delta_{\mu'\nu}(\mathbf{e}_{\mu'}\otimes\mathbf{e}_{\nu}) = (\mathbf{u}\cdot\mathbf{u})\mathbf{I} \tag{C.30}$$

$$\boldsymbol{\Sigma}_3 = \delta_{\mu\mu'}\delta_{\nu\nu'} \, (\mathbf{e}_{\mu} \otimes \mathbf{e}_{\mu'} \otimes \mathbf{e}_{\nu} \otimes \mathbf{e}_{\nu'}) \Rightarrow \mathbf{u}\cdot\boldsymbol{\Sigma}_3\cdot\mathbf{u} = u_{\mu}\delta_{\mu\mu'}\delta_{\nu\nu'}u_{\nu'}(\mathbf{e}_{\mu'}\otimes\mathbf{e}_{\nu}) = u_{\mu'}u_{v}(\mathbf{e}_{\mu'}\otimes\mathbf{e}_{\nu}) = \mathbf{u}\otimes\mathbf{u} \tag{C.31}$$

If $\boldsymbol{\Pi} = [\delta_{ij}\delta_{j'i'} + \delta_{ij'}\delta_{ji'}] \, dt$ then i = 1, i' = 2, j = 2 and j' =2 corresponds to $\boldsymbol{\Pi} = dt$;

$$\mathbf{e}_{12} \cdot d\mathbf{W}_{12}^{\dagger} \otimes d\mathbf{W}_{12}^{\dagger} \cdot \mathbf{e}_{12} = dt \left(\frac{1}{2} \left(\mathbf{e}_{12} \otimes \mathbf{e}_{12} + (\mathbf{e}_{12} \cdot \mathbf{e}_{12})\mathbf{I} \right) - \frac{1}{D} \mathbf{e}_{12} \otimes \mathbf{e}_{12} \right) \tag{C.32}$$

$$\mathbf{e}_{12} \cdot d\mathbf{W}_{12}^{A} \otimes d\mathbf{W}_{12}^{A} \cdot \mathbf{e}_{12} = dt \left(\frac{1}{2} \left(\mathbf{e}_{12} \otimes \mathbf{e}_{12} - (\mathbf{e}_{12} \cdot \mathbf{e}_{12})\mathbf{I} \right) \right) \tag{C.33}$$

$$\mathbf{e}_{12} \cdot \mathrm{tr}[d\mathbf{W}_{12}]^2 \, (\mathbf{I} \otimes \mathbf{I}) \cdot \mathbf{e}_{12} = D dt \mathbf{e}_{12} \otimes \mathbf{e}_{12} \tag{C.34}$$

$$d\tilde{\mathbf{v}}_{12} \otimes d\tilde{\mathbf{v}}_{12} = \sigma^2 \left(\frac{1}{2} \left(\tilde{A}^2 + \tilde{C}^2 \right) \mathbf{I} + \left(\left(\frac{1}{2} - \frac{1}{D} \right) \tilde{A}^2 + \frac{1}{D} \tilde{B}^2 - \frac{1}{2} \tilde{C}^2 \right) (\mathbf{e}_{12} \otimes \mathbf{e}_{12}) \right) \tag{C.35}$$

Generalizing;

$$d\tilde{\mathbf{v}}_{ij} \otimes d\tilde{\mathbf{v}}_{ij} = \sigma^2 \left(\frac{1}{2} \left(\tilde{A}^2 + \tilde{C}^2 \right) \mathbf{I} + \left(\left(\frac{1}{2} - \frac{1}{D} \right) \tilde{A}^2 + \frac{1}{D} \tilde{B}^2 - \frac{1}{2} \tilde{C}^2 \right) (\mathbf{e}_{ij} \otimes \mathbf{e}_{ij}) \right) \tag{C.36}$$

$$d\tilde{\mathbf{v}}_{ij} \otimes d\tilde{\mathbf{v}}_{ij} = \sigma^2 T_{ij} (\mathbf{e}_{ij} \otimes \mathbf{e}_{ij}) \tag{C.37}$$

Now for the sake of clarity;

$$\mathbf{D} = \begin{bmatrix} \mathbf{D}_{rr} & \mathbf{D}_{rv} & \mathbf{D}_{r\omega} \\ \mathbf{D}_{vr} & \mathbf{D}_{vv} & \mathbf{D}_{v\omega} \\ \mathbf{D}_{\omega r} & \mathbf{D}_{\omega v} & \mathbf{D}_{\omega\omega} \end{bmatrix} \tag{C.38}$$

$$\mathbf{D} = \frac{1}{dt} d\tilde{\mathbf{x}} \otimes d\tilde{\mathbf{x}} = \frac{1}{dt} \begin{bmatrix} \mathbf{0} & \mathbf{0} & \mathbf{0} \\ \mathbf{0} & d\tilde{\mathbf{v}} \otimes d\tilde{\mathbf{v}} & d\tilde{\mathbf{v}} \otimes d\tilde{\boldsymbol{\omega}} \\ \mathbf{0} & d\tilde{\boldsymbol{\omega}} \otimes d\tilde{\mathbf{v}} & d\tilde{\boldsymbol{\omega}} \otimes d\tilde{\boldsymbol{\omega}} \end{bmatrix}. \tag{C.39}$$

and for example

$$\mathbf{D}_{vv} = \frac{1}{dt} \begin{bmatrix} \sum_j d\tilde{\mathbf{v}}_{1j} \otimes d\tilde{\mathbf{v}}_{1j} & d\tilde{\mathbf{v}}_{12} \otimes d\tilde{\mathbf{v}}_{21} & d\tilde{\mathbf{v}}_{13} \otimes d\tilde{\mathbf{v}}_{31} & \cdots & d\tilde{\mathbf{v}}_{1N} \otimes d\tilde{\mathbf{v}}_{N1} \\ d\tilde{\mathbf{v}}_{21} \otimes d\tilde{\mathbf{v}}_{12} & \sum_j d\tilde{\mathbf{v}}_{2j} \otimes d\tilde{\mathbf{v}}_{2j} & \cdots & \cdots & d\tilde{\mathbf{v}}_{2N} \otimes d\tilde{\mathbf{v}}_{N2} \\ \vdots & \vdots & \ddots & \vdots & \vdots \\ d\tilde{\mathbf{v}}_{N1} \otimes d\tilde{\mathbf{v}}_{1N} & d\tilde{\mathbf{v}}_{N2} \otimes d\tilde{\mathbf{v}}_{2N} & \cdots & \cdots & \sum_j d\tilde{\mathbf{v}}_{Nj} \otimes d\tilde{\mathbf{v}}_{Nj} \end{bmatrix} \tag{C.40}$$

In case of confusion reader is referred to Appendix A same methodology has been followed there. Therefore

$$\nabla\nabla p : \mathbf{D} = \nabla_{\mathbf{v}}\nabla_{\mathbf{v}} p : \mathbf{D}_{vv} + \nabla_{\mathbf{v}}\nabla_{\omega} p : \mathbf{D}_{v\omega} + \nabla_{\omega}\nabla_{\mathbf{v}} p : \mathbf{D}_{\omega v} + \nabla_{\omega}\nabla_{\omega} p : \mathbf{D}_{\omega\omega} \tag{C.41}$$

also

$$\nabla\cdot(\mathbf{a}p) = \nabla\cdot \begin{bmatrix} \mathbf{v}\, p \\ \left(\mathbf{F}^C + \mathbf{F}^D + \mathbf{F}^R\right) p \\ \left(\mathbf{T}^D + \mathbf{T}^R\right) p \end{bmatrix} = \nabla_{\mathbf{r}}\cdot(\mathbf{v}p) + \nabla_{\mathbf{v}}\cdot\left(\mathbf{F}^C p\right) + \nabla_{\mathbf{v}}\cdot\left(\left(\mathbf{F}^D + \mathbf{F}^R\right) p\right) + \nabla_{\omega}\cdot\left(\left(\mathbf{T}^D + \mathbf{T}^R\right) p\right) \tag{C.42}$$

$$\nabla \cdot (\mathbf{a}p) = L^C[p] + \nabla_{\mathbf{v}} \cdot \left(\left(\mathbf{F}^D + \mathbf{F}^R\right) p\right) + \nabla_{\omega} \cdot \left(\left(\mathbf{T}^D + \mathbf{T}^R\right) p\right) \tag{C.43}$$

$L^C[p]$ is the Liouville operator of the Hamiltonian system under the effect of conservative forces.

$$d\tilde{\omega}_{ij} = -\frac{m}{I} \sum_j \frac{\mathbf{r}_{ij}}{2} \times d\tilde{\mathbf{v}}_{ij} \tag{C.44}$$

and

$$\frac{\partial p}{\partial t} = -\nabla \cdot (\mathbf{a}p) + \frac{1}{2}\mathbf{D} : \nabla\nabla p \tag{C.45}$$

$$\begin{aligned} \frac{\partial p}{\partial t} = &-L^C[p] - \nabla_{\mathbf{v}} \cdot \left(\left(\mathbf{F}^D + \mathbf{F}^R\right) p\right) - \nabla_{\omega} \cdot \left(\left(\mathbf{T}^D + \mathbf{T}^R\right) p\right) \\ &+ \frac{1}{2}\left(\nabla_{\mathbf{v}}\nabla_{\mathbf{v}} p : \mathbf{D}_{vv} + \nabla_{\mathbf{v}}\nabla_{\omega} p : \mathbf{D}_{v\omega} + \nabla_{\omega}\nabla_{\mathbf{v}} p : \mathbf{D}_{\omega v} + \nabla_{\omega}\nabla_{\omega} p : \mathbf{D}_{\omega\omega}\right) \end{aligned} \tag{C.46}$$

where for example

$$\mathbf{D}_{vv} = \begin{bmatrix} (d\tilde{\mathbf{v}}_{11} \otimes d\tilde{\mathbf{v}}_{11} + d\tilde{\mathbf{v}}_{12} \otimes d\tilde{\mathbf{v}}_{12} + d\tilde{\mathbf{v}}_{13} \otimes d\tilde{\mathbf{v}}_{13} + \cdots) & d\tilde{\mathbf{v}}_{12} \otimes d\tilde{\mathbf{v}}_{21} & d\tilde{\mathbf{v}}_{13} \otimes d\tilde{\mathbf{v}}_{31} & \cdots \\ \vdots & \ddots & \vdots & \\ \vdots & \cdots & \ddots & \end{bmatrix} \tag{C.47}$$

$$\nabla_{\mathbf{v}} \nabla_{\mathbf{v}} p = \begin{bmatrix} \frac{\partial^2 p}{\partial \mathbf{v}_1^2} & \frac{\partial^2 p}{\partial \mathbf{v}_1 \partial \mathbf{v}_2} & \frac{\partial^2 p}{\partial \mathbf{v}_1 \partial \mathbf{v}_3} & \cdots \\ \vdots & \ddots & \vdots & \\ \vdots & \cdots & \ddots & \end{bmatrix} \tag{C.48}$$

Therefore the first row of the contraction operation $\mathbf{D}_{vv} : \nabla_{\mathbf{v}} \nabla_{\mathbf{v}} p$ yields;

$$\begin{aligned} \mathbf{D}_{vv} : \nabla_{\mathbf{v}} \nabla_{\mathbf{v}} p = & \left(d\tilde{\mathbf{v}}_{12} \otimes d\tilde{\mathbf{v}}_{12} : \frac{\partial^2 p}{\partial^2 \mathbf{v}_1} - d\tilde{\mathbf{v}}_{12} \otimes d\tilde{\mathbf{v}}_{12} : \frac{\partial^2 p}{\partial \mathbf{v}_1 \partial \mathbf{v}_2} \right) \\ & + \left(d\tilde{\mathbf{v}}_{13} \otimes d\tilde{\mathbf{v}}_{13} : \frac{\partial^2 p}{\partial^2 \mathbf{v}_1} - d\tilde{\mathbf{v}}_{13} \otimes d\tilde{\mathbf{v}}_{13} : \frac{\partial^2 p}{\partial \mathbf{v}_1 \partial \mathbf{v}_3} \right) + \cdots \end{aligned} \tag{C.49}$$

where $d\tilde{\mathbf{v}}_{11} \otimes d\tilde{\mathbf{v}}_{11} = 0$ since $\mathbf{e}_{ii} = \mathbf{0}$ (no sum) and $d\tilde{\mathbf{v}}_{ij} = -d\tilde{\mathbf{v}}_{ji}$. The first term in the parenthesis

$$\begin{aligned} d\tilde{\mathbf{v}}_{12} \otimes d\tilde{\mathbf{v}}_{12} : \frac{\partial^2 p}{\partial^2 \mathbf{v}_1} - d\tilde{\mathbf{v}}_{12} \otimes d\tilde{\mathbf{v}}_{12} : \frac{\partial^2 p}{\partial \mathbf{v}_1 \partial \mathbf{v}_2} &= d\tilde{\mathbf{v}}_{12} \otimes d\tilde{\mathbf{v}}_{12} : \left(\frac{\partial^2 p}{\partial^2 \mathbf{v}_1} - \frac{\partial^2 p}{\partial \mathbf{v}_1 \partial \mathbf{v}_2} \right) \\ &= d\tilde{\mathbf{v}}_{12} \otimes d\tilde{\mathbf{v}}_{12} : \frac{\partial}{\partial \mathbf{v}_1} \left(\frac{\partial p}{\partial \mathbf{v}_1} - \frac{\partial p}{\partial \mathbf{v}_2} \right) \end{aligned} \tag{C.50}$$

Using the following identity $\nabla \cdot (\mathbf{A}\mathbf{u}) = \nabla \cdot \mathbf{A}^T \mathbf{u} + \mathbf{A}^T : \nabla \mathbf{u}$ where $\mathbf{A} = d\tilde{\mathbf{v}}_{12} \otimes d\tilde{\mathbf{v}}_{12}$ and $\mathbf{A} = \mathbf{A}^T$ and $\mathbf{u} = \frac{\partial p}{\partial \mathbf{v}_1} - \frac{\partial p}{\partial \mathbf{v}_2}$.

$$d\tilde{\mathbf{v}}_{12} \otimes d\tilde{\mathbf{v}}_{12} : \frac{\partial}{\partial \mathbf{v}_1} \left(\frac{\partial p}{\partial \mathbf{v}_1} - \frac{\partial p}{\partial \mathbf{v}_2} \right) = \frac{\partial}{\partial \mathbf{v}_1} \cdot \left[\sigma^2 \mathbf{T}_{ij} \left[\frac{\partial p}{\partial \mathbf{v}_1} - \frac{\partial p}{\partial \mathbf{v}_2} \right] \right] \tag{C.51}$$

Then one gets;

$$\frac{1}{2} \mathbf{D}_{vv} : \nabla_{\mathbf{v}} \nabla_{\mathbf{v}} p = \frac{\sigma^2}{2} \sum_{i,j} \frac{\partial}{\partial \mathbf{v}_i} \cdot \left(\mathbf{T}_{ij} \left[\frac{\partial p}{\partial \mathbf{v}_i} - \frac{\partial p}{\partial \mathbf{v}_j} \right] \right) \tag{C.52}$$

Similarly;

$$\mathbf{D}_{v\omega} = \begin{bmatrix} (d\tilde{\mathbf{v}}_{11} \otimes d\tilde{\omega}_{11} + d\tilde{\mathbf{v}}_{12} \otimes d\tilde{\omega}_{12} + d\tilde{\mathbf{v}}_{13} \otimes d\tilde{\omega}_{13} + \cdots) & d\tilde{\mathbf{v}}_{12} \otimes d\tilde{\omega}_{21} & d\tilde{\mathbf{v}}_{13} \otimes d\tilde{\omega}_{31} & \cdots \\ \vdots & \ddots & \vdots & \\ \vdots & \cdots & \ddots & \end{bmatrix} \tag{C.53}$$

$$\mathbf{D}_{v\omega} : \nabla_{\mathbf{v}} \nabla_{\omega} p = \left(d\tilde{\mathbf{v}}_{12} \otimes d\tilde{\omega}_{12} \frac{\partial^2 p}{\partial \mathbf{v}_1 \partial \omega_1} + d\tilde{\mathbf{v}}_{12} \otimes d\tilde{\omega}_{12} \frac{\partial^2 p}{\partial \mathbf{v}_1 \partial \omega_2} \right) + \cdots \tag{C.54}$$

Note this time $d\tilde{\omega}_{12} = d\tilde{\omega}_{21}$. Using the same methodology one gets

$$d\tilde{\mathbf{v}}_{12} \otimes d\tilde{\omega}_{12} : \frac{\partial}{\partial \mathbf{v}_1}\left(\frac{\partial p}{\partial \mathbf{v}_1} + \frac{\partial p}{\partial \omega_2}\right) = \frac{\partial}{\partial \mathbf{v}_1} \cdot \left[d\tilde{\mathbf{v}}_{12} \otimes d\tilde{\omega}_{12}\left[\frac{\partial p}{\partial \omega_1} + \frac{\partial p}{\partial \omega_2}\right]\right] \tag{C.55}$$
$$= \frac{\partial}{\partial \mathbf{v}_1} \cdot \left[\left(d\tilde{\mathbf{v}}_{12} \otimes \left(\frac{\mathbf{r}_{12}}{2} \times d\tilde{\mathbf{v}}_{12}\right)\right)\left[\frac{\partial p}{\partial \omega_1} + \frac{\partial p}{\partial \omega_2}\right]\right]$$

Now this time $\mathbf{w} \otimes (\mathbf{u} \times \mathbf{w})\mathbf{c} = [\mathbf{c} \cdot (\mathbf{u} \times \mathbf{w})]\,\mathbf{w} = [\mathbf{w} \cdot (\mathbf{c} \times \mathbf{u})]\,\mathbf{w} = (\mathbf{w} \otimes \mathbf{w})(\mathbf{c} \times \mathbf{u})$. Therefore;

$$\frac{\partial}{\partial \mathbf{v}_1} \cdot \left[\left(d\tilde{\mathbf{v}}_{12} \otimes \left(\frac{\mathbf{r}_{12}}{2} \times d\tilde{\mathbf{v}}_{12}\right)\right)\left[\frac{\partial p}{\partial \omega_1} + \frac{\partial p}{\partial \omega_2}\right]\right] = \frac{\partial}{\partial \mathbf{v}_1} \cdot \left[\sigma^2 \mathbf{T}\left(\frac{\mathbf{r}_{12}}{2} \times \left[\frac{\partial p}{\partial \omega_1} + \frac{\partial p}{\partial \omega_2}\right]\right)\right] \tag{C.56}$$

Therefore

$$\frac{1}{2}\mathbf{D}_{v\omega} : \nabla_{\mathbf{v}}\nabla_{\omega} p = \frac{\sigma^2}{2}\sum_{i,j} \frac{\partial}{\partial \mathbf{v}_i} \cdot \left(\mathbf{T}_{ij}\left(\frac{\mathbf{r}_{ij}}{2} \times \left(\frac{\partial p}{\partial \omega_i} + \frac{\partial p}{\omega_j}\right)\right)\right) \tag{C.57}$$

Similarly using $(\mathbf{u} \times \mathbf{w}) \otimes \mathbf{w} = -\mathbf{u} \times (\mathbf{w} \otimes \mathbf{w})$;

$$\frac{1}{2}\mathbf{D}_{\omega v} : \nabla_{\omega}\nabla_{\mathbf{v}} p = -\frac{\sigma^2}{2}\sum_{ij} \frac{\partial}{\partial \boldsymbol{\omega}_i} \cdot \left(\frac{\mathbf{r}_{ij}}{2} \times \mathbf{T}_{ij} \cdot \left[\frac{\partial p}{\partial \mathbf{v}_i} - \frac{\partial p}{\partial \mathbf{v}_j}\right]\right) \tag{C.58}$$

For the fourth item $(\mathbf{u} \times \mathbf{w}) \otimes (\mathbf{w} \times \mathbf{u}) = -\mathbf{u} \times (\mathbf{w} \otimes \mathbf{w}) \times \mathbf{u}$ is utilized.

$$\frac{1}{2}\mathbf{D}_{\omega\omega} : \nabla_{\omega}\nabla_{\omega} p = -\frac{\sigma^2}{2}\sum_{ij} \frac{\partial}{\partial \boldsymbol{\omega}_i} \cdot \left(\frac{\mathbf{r}_{ij}}{2} \times \mathbf{T}_{ij} \cdot \left[\frac{\mathbf{r}_{ij}}{2} \times \left(\frac{\partial p}{\partial \boldsymbol{\omega}_i} + \frac{\partial p}{\partial \boldsymbol{\omega}_j}\right)\right]\right) \tag{C.59}$$

Now returning back to the original definitions of the forces. Following operators are defined together with the standard Lioville operator L^C.

$$L^D = \sum_{i,j\neq i} \frac{\partial}{\partial \mathbf{v}_i} \cdot \left[\mathbf{L}_{ij}^T + \mathbf{L}_{ij}^R\right] \tag{C.60}$$

$$L^R = -\frac{m}{I}\sum_{i,j\neq i} \frac{\partial}{\partial \boldsymbol{\omega}_i} \cdot \left(\frac{\mathbf{r}_{ij}}{2} \times \left[\mathbf{L}_{ij}^T + \mathbf{L}_{ij}^R\right]\right) \tag{C.61}$$

where

$$\mathbf{L}_{ij}^T = -\frac{1}{m}\mathbf{F}_{ij}^D + \frac{\sigma^2}{2}\,\mathbf{T}_{ij} \cdot \left[\frac{\partial}{\partial \mathbf{v}_i} - \frac{\partial}{\partial \mathbf{v}_j}\right] \tag{C.62}$$

$$\mathbf{L}_{ij}^R = -\frac{1}{m}\mathbf{F}_{ij}^R + \frac{m\sigma^2}{2I}\,\mathbf{T}_{ij} \cdot \left(\frac{\mathbf{r}_{ij}}{2} \times \left[\frac{\partial}{\partial \boldsymbol{\omega}_i} + \frac{\partial}{\partial \boldsymbol{\omega}_j}\right]\right) \tag{C.63}$$

Then together with Lioville operator the Fokker-Planck equation is expressed as;

$$\frac{\partial p}{\partial t} = \left(L^C + L^D + L^R\right) p \tag{C.64}$$

when one seeks the steady solution the transient terms vanish and if Boltzmann distribution is

assumed i.e.

$$p_{eq} = \frac{1}{Z}\exp\left[-\beta H\right] = \frac{1}{Z}\exp\left[-\beta\left(\sum_i\left(\frac{mv_i^2}{2}+\frac{I\omega_i^2}{2}\right)+U(r)\right)\right] \tag{C.65}$$

as in the DPD $L^C[p_{eq}] = 0$. This forces;

$$\mathbf{L}_{ij}^T p_{eq} = 0$$
$$\mathbf{L}_{ij}^R p_{eq} = 0;$$

also note that $\frac{\partial p_{eq}}{\partial \mathbf{v}_i} = -\beta \mathbf{v}_i p_e q$ and $\frac{\partial p_{eq}}{\partial \omega_i} = -\beta\omega_i p_{eq}$. This enforce similar to DPD two conditions;

$$\sigma = \sqrt{2\gamma k_b T} \tag{C.66}$$
$$\mathbf{M}^T(\mathbf{r}_{ij}) = \mathbf{T}_{ij} \tag{C.67}$$
$$\mathbf{M}^R(\mathbf{r}_{ij}) = \mathbf{T}_{ij} \tag{C.68}$$

if one picks

$$\mathbf{M}^T = \mathbf{M}^R = A(r)\mathbf{I} + B(r)\mathbf{e}_{ij}\otimes\mathbf{e}_{ij} \tag{C.69}$$

and recasts the A and B according to the SDPD;

$$A(r) = 4\left(\frac{5\eta}{3}-\xi\right)\frac{F_{ij}}{\rho_i\rho_j} \tag{C.70}$$
$$B(r) = 10\left(\xi-\frac{2\eta}{3}\right)\frac{F_{ij}}{\rho_i\rho_j} \tag{C.71}$$
$$\tag{C.72}$$

and recalls

$$\mathbf{T}_{ij} = \left(\frac{1}{2}\left(\tilde{A}^2+\tilde{C}^2\right)\mathbf{I} + \left(\left(\frac{1}{2}-\frac{1}{D}\right)\tilde{A}^2 + \frac{1}{D}\tilde{B}^2 - \frac{1}{2}\tilde{C}^2\right)(\mathbf{e}_{ij}\otimes\mathbf{e}_{ij})\right) \tag{C.73}$$

Then the detailed balance dictates;

$$A(r) = \frac{1}{2}\left(\tilde{A}(r)^2+\tilde{C}(r)^2\right) \tag{C.74}$$
$$B(r) = \frac{1}{2}\left(\tilde{A}(r)^2-\tilde{C}(r)^2\right) + \frac{1}{3}\left(\tilde{B}(r)^2-\tilde{A}(r)^2\right) \tag{C.75}$$

if $\tilde{C} = 0$ then;

$$\tilde{A}(r_{ij}) = \left(2\left(\frac{20\eta}{3} - 4\xi_b\right)\frac{F_{ij}}{r_{ij}^2}\right)^{1/2} \tag{C.76}$$

$$\tilde{B}(r_{ij}) = \left(2\left(\frac{17\xi_b - 40\eta}{3}\right)\frac{F_{ij}}{r_{ij}^2}\right)^{1/2} \tag{C.77}$$

Then the SDPD forces can be written of the form;

$$\mathbf{F}_{ij}^C = \left(\frac{p_i}{\rho_i^2} + \frac{p_j}{\rho_j^2}\right) F_{ij}\mathbf{r}_{ij} \tag{C.78}$$

$$\mathbf{F}_{ij}^D = -\gamma_{ij}^a \left(\mathbf{v}_{ij} + \mathbf{e}_{ij}\left(\mathbf{e}_{ij}\cdot\mathbf{v}_{ij}\right)\right)\frac{1}{3} - 2\gamma_{ij}^b \mathbf{e}_{ij}\left(\mathbf{e}_{ij}\cdot\mathbf{v}_{ij}\right) \tag{C.79}$$

$$\mathbf{F}_{ij}^R = -\gamma_{ij}^a \frac{\mathbf{e}_{ij}}{2} \times \left(\omega_i + \omega_j\right) \tag{C.80}$$

$$\tilde{\mathbf{F}}_{ij} = \left(\sigma_{ij}^a dW_{ij}^S + \sigma_{ij}^b \frac{1}{3}\mathrm{tr}[dW_{ij}]\mathbf{I}\right)\cdot \mathbf{e}_{ij}\frac{1}{dt} \tag{C.81}$$

where $\mathbf{F}_{ij}^C$, $\mathbf{F}_{ij}^D$ and $\mathbf{F}_{ij}^R$ are the deterministic force and stands for conservative, dissipative and rotational forces respectively whereas $\tilde{\mathbf{F}}_{ij}$ is the random force. The coefficients appearing in the above equation set and the constraints reads;

$$\gamma_{ij}^a = \left(\frac{20\eta}{3} - 4\xi_b\right)\frac{F_{ij}}{\rho_i\rho_j} \tag{C.82}$$

$$\gamma_{ij}^b = \left(\frac{17\xi_b - 40\eta}{3}\right)\frac{F_{ij}}{\rho_i\rho_j} \tag{C.83}$$

$$\sigma_{ij}^{a,b} = 2\sqrt{k_B T \gamma_{ij}^{a,b}} \tag{C.84}$$

$$\frac{2\eta}{3} \leq \xi \leq \frac{5\eta}{3} \tag{C.85}$$

$$\tag{C.86}$$

D Appendix D

There are some conventions, that are used in this appendix relevant to tensor algebra. They are explained in Appendix A. In this appendix derivation of the mechanicstic forces that govern the membrane of red cells and platelets will be derived. For the sake of clarity some information in the text will be repeated. It is worth to mention that accurate representation of membrane forces encapsulates the following features.

- Shear Elasticity
- Bending Resistance
- Area Conservation
- Volume Conservation

It is known that the red cell is encapsulated by a bilayer attached to the red cell's cytoskeleton. Bilayer by its nature resists to bending and the spectrin network induces shear elasticity. Moreover the bilayer resists to area changes and due to inner cytosol, the red cell resists volume changes. Upon discretization of the membrane surface, arising set of nodes are triangulated. This forms a graph and has edges, enclosed area via the edges. Two enclosed area makes an angle with each other. Geometrically speaking the graph is characterized with certain parameters. The N_v stands for the number of nodes which creates $3(N_v - 2)$ edges. These $3(N_v - 2)$ edges enclose $2(N_v - 2)$ triangles and create $3(N_v - 2)$ couples of triangles which can be characterized by the angle between them. Specifically the triangle couples are so called as dihedrals.

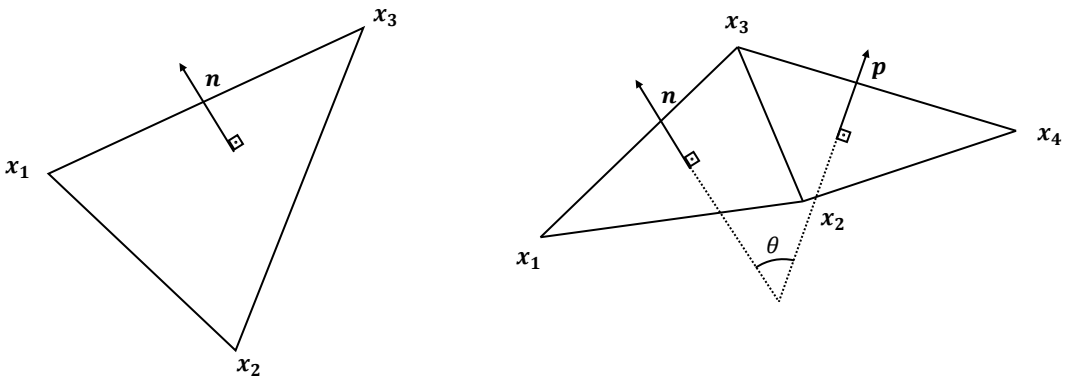

Figure D.33: (left) A representative triangular surface enclosed by three edges and its normal $\mathbf{n}$. (right) A representative dihedral composed of two triangles. Their normal $\mathbf{n}$, $\mathbf{p}$ and the angle in between them θ.

Figure D.33(left) shows a representative triangle which is indexed by i having the area A_i and normal $\mathbf{n}_i$. The normal is given by

$$\mathbf{n}_i = \left(\mathbf{x}_2^i - \mathbf{x}_1^i\right) \times \left(\mathbf{x}_3^i - \mathbf{x}_1^i\right),$$

and the area is

$$A_i = \frac{\sqrt{\mathbf{n}_i \cdot \mathbf{n}_i}}{2}.$$

For the sake of simplicity the triangle superscripts from the local nodes are removed that means $\mathbf{x}_1 = \mathbf{x}_1^i$. Same figure right hand side shows a representative dihedral with normals $\mathbf{n}$ and $\mathbf{p}$ with the angle θ in between them.

On this graph via the nodes, one defines various potentials to induce the aforementioned features to the membrane. The two body potentials are composed of a worm like chain potential and a power law spring. The reason of this selection was discussed in the main text in depth therefore will be skipped here. Moreover the derivation of forces from the potentials is straightforward therefore they will be only given here for the sake of clarity.

$$U_{\mathrm{WLC}} = \sum_j \left[\frac{k_B T\, l_m \left(3x_j^2 - 2x_j^3\right)}{4p\left(1 - x_j\right)} \right] \tag{D.1}$$

where l_j is the length of the spring j, l_m is the maximum spring extension, $x_j = \frac{l_j}{l_m}$, p is the persistance length, and k_p is the spring constant. The summation runs over all the edges. The corresponding force is

$$\mathbf{f}_{ij}^{\mathrm{WLC}} = -\frac{k_B T}{p} \left[\frac{1}{4(1 - x_j)^2} - \frac{1}{4} + x_j \right] \mathbf{e}_{ij} \tag{D.2}$$

The repulsive power law potential reads;

$$U_{\mathrm{POW}} = \sum_j \frac{-k_p}{1 - \alpha} l_j^{(1-\alpha)} \tag{D.3}$$

$$\mathbf{f}_{ij}^{\mathrm{POW}} = \frac{k_p}{l^m} \mathbf{e}_{ij} \tag{D.4}$$

where $\alpha \neq 1$ is a positive number and k_p is the repulsive coefficient. The summation again runs over all the edges.

The area and volume conservation are induced by the following harmonic potentials of the form;

$$U_{\mathrm{area}} = k_a \frac{(A - A_0)^2}{2A_0} + \sum_j k_d \frac{(A_j - A_j^0)^2}{2A_j^0} \tag{D.5}$$

$$U_{\mathrm{volume}} = k_v \frac{(V - V_0)^2}{2V_0} \tag{D.6}$$

The summation in the above equations run over all the triangles of the membrane. The area force on node i reads;

$$\mathbf{f}_i = -\nabla_{\mathbf{x}_i} U_{\text{area}} = -\nabla_{\mathbf{x}_i}\left(k_a \frac{(A-A_0)^2}{2A_0}\right) - \nabla_{\mathbf{x}_i}\left(\sum_j k_d \frac{(A_j - A_j^0)^2}{2A_j^0}\right) \tag{D.7}$$

$$\begin{aligned}
-\nabla_{\mathbf{x}_i}\left(k_a \frac{(A-A_0)^2}{2A_0}\right) &= -k_a \frac{A-A_0}{A_0}\nabla_{\mathbf{x}_i} A \\
&= -k_a \frac{A-A_0}{A_0}\sum_j \nabla_{\mathbf{x}_i} A_j \\
&= -k_a \frac{A-A_0}{A_0}\frac{1}{2}\nabla_{\mathbf{x}_i}\sqrt{\mathbf{n}_i \cdot \mathbf{n}_i} \\
&= -k_a \frac{A-A_0}{A_0}\frac{1}{2}\frac{1}{\sqrt{\mathbf{n}_i \cdot \mathbf{n}_i}}\mathbf{n}_i \nabla_{\mathbf{x}_i}\mathbf{n}_i \\
&= k_a \frac{A-A_0}{A_0}\frac{1}{4A_i}(-\mathbf{n}_i \nabla_{\mathbf{x}_i}\mathbf{n}_i) \\
&= \beta_a(-\mathbf{n}_i \nabla_{\mathbf{x}_i}\mathbf{n}_i)
\end{aligned} \tag{D.8}$$

$$\begin{aligned}
-\nabla_{\mathbf{x}_i}\left(\sum_j k_d \frac{(A_j - A_j^0)^2}{2A_j^0}\right) &= k_d \frac{A_i - A_i^0}{A_i^0}\frac{1}{4A_i}(-\mathbf{n}_i \nabla_{\mathbf{x}_i}\mathbf{n}_i) \\
&= \beta_d(-\mathbf{n}_i \nabla_{\mathbf{x}_i}\mathbf{n}_i)
\end{aligned} \tag{D.9}$$

$$\begin{aligned}
\mathbf{f}_1 &= (\beta_a + \beta_d)\,(-\mathbf{n}\nabla_{\mathbf{x}_1}\mathbf{n}) \\
\mathbf{f}_2 &= (\beta_a + \beta_d)\,(-\mathbf{n}\nabla_{\mathbf{x}_2}\mathbf{n}) \\
\mathbf{f}_3 &= (\beta_a + \beta_d)\,(-\mathbf{n}\nabla_{\mathbf{x}_3}\mathbf{n})
\end{aligned}$$

where

$$\begin{aligned}
\beta_a &= k_a \frac{A-A_0}{4A_0 A_i} \\
\beta_d &= k_d \frac{A_i - A_i^0}{4A_i^0 A_i}
\end{aligned}$$

$$-\mathbf{n}\nabla_{\mathbf{x}_1}\mathbf{n} = -\mathbf{n}\nabla_{\mathbf{x}_1}\left[(\mathbf{x}_2 - \mathbf{x}_1)\times(\mathbf{x}_3 - \mathbf{x}_1)\right] \tag{D.10}$$

Using $\nabla(\mathbf{u}\times\mathbf{v}) = \nabla\mathbf{u}\times\mathbf{v} + \mathbf{u}\times\nabla\mathbf{v}$, one gets;

$$\begin{aligned}
-\mathbf{n}\nabla_{\mathbf{x}_1}\mathbf{n} &= -\mathbf{n}\left[\nabla_{\mathbf{x}_1}(\mathbf{x}_2 - \mathbf{x}_1)\times(\mathbf{x}_3 - \mathbf{x}_1) + (\mathbf{x}_2 - \mathbf{x}_1)\times\nabla_{\mathbf{x}_1}(\mathbf{x}_3 - \mathbf{x}_1)\right] \\
&= -\mathbf{n}\left[-\mathbf{I}\times(\mathbf{x}_3 - \mathbf{x}_1) - (\mathbf{x}_2 - \mathbf{x}_1)\times\mathbf{I}\right]
\end{aligned} \tag{D.11}$$

and similarly;

$$-\mathbf{n}\nabla_{\mathbf{x}_2}\mathbf{n} = -\mathbf{n}\left[\mathbf{I}\times(\mathbf{x}_3-\mathbf{x}_1)\right] \tag{D.12}$$

$$-\mathbf{n}\nabla_{\mathbf{x}_3}\mathbf{n} = -\mathbf{n}\left[(\mathbf{x}_2-\mathbf{x}_1)\times\mathbf{I}\right] \tag{D.13}$$

The above set of equations are used to show the skew-symmetry of the term $\nabla\mathbf{n}$. For the sake of clarity the original definition will be retained.

The terms $\mathbf{I}\times\mathbf{u}$ and $\mathbf{u}\times\mathbf{I}$ and their properties can be found in [211]. For example $\mathbf{I}\times\mathbf{u} = (\delta_{mn}(\mathbf{e}_m\otimes\mathbf{e}_n))\times v_i\mathbf{e}_i = \delta_{mn}v_i(\mathbf{e}_m\otimes(\mathbf{e}_n\times\mathbf{e}_i)) = \delta_{mn}v_i\epsilon_{nik}\mathbf{e}_m\otimes\mathbf{e}_k = v_i\epsilon_{mik}\mathbf{e}_m\otimes\mathbf{e}_k$ which is skew-symmetric. Here one defines a generic skew-symmetric tensor $\mathbf{W}$ with the following property. $\mathbf{W}$ satisfies $\mathbf{W} = -\mathbf{W}^T$ and $\mathbf{W} = \mathbf{I}\times\mathbf{w} = \mathbf{w}\times\mathbf{I}$. Here $\mathbf{w}$ is the axial vector and satisfies $\mathbf{uW} = \mathbf{u}\times\mathbf{w}$, $\mathbf{Wv} = \mathbf{w}\times\mathbf{v}$ for any vector $\mathbf{u}$ and $\mathbf{v}$ and it is given by $\mathbf{w} = -\frac{1}{2}\epsilon : \mathbf{W}$ where ϵ is the third order permutation tensor. One realizes the terms inside the parentheses in Equations (D.11),(D.12),(D.13) are skew-symmetric and can be written as;

$$-\mathbf{n}\nabla_{\mathbf{x}_1}\mathbf{n} = -\mathbf{n}\mathbf{W}_1 = -\mathbf{n}\times\mathbf{w}_1 \tag{D.14}$$

$$-\mathbf{n}\nabla_{\mathbf{x}_2}\mathbf{n} = -\mathbf{n}\mathbf{W}_2 = -\mathbf{n}\times\mathbf{w}_2 \tag{D.15}$$

$$-\mathbf{n}\nabla_{\mathbf{x}_3}\mathbf{n} = -\mathbf{n}\mathbf{W}_3 = -\mathbf{n}\times\mathbf{w}_3 \tag{D.16}$$

using $\epsilon : \nabla\mathbf{u} = \nabla\times\mathbf{u}$

$$\mathbf{w}_1 = -\frac{1}{2}\epsilon : \nabla_{\mathbf{x}_1}\mathbf{n} = -\frac{1}{2}\nabla_{\mathbf{x}_1}\times(\mathbf{u}\times\mathbf{v})$$
$$\mathbf{w}_2 = -\frac{1}{2}\epsilon : \nabla_{\mathbf{x}_2}\mathbf{n} = -\frac{1}{2}\nabla_{\mathbf{x}_2}\times(\mathbf{u}\times\mathbf{v})$$
$$\mathbf{w}_3 = -\frac{1}{2}\epsilon : \nabla_{\mathbf{x}_3}\mathbf{n} = -\frac{1}{2}\nabla_{\mathbf{x}_3}\times(\mathbf{u}\times\mathbf{v})$$

where $\mathbf{u} = \mathbf{x}_2 - \mathbf{x}_1$ and $\mathbf{v} = \mathbf{x}_3 - \mathbf{x}_1$. Furthermore the expression $\nabla\times(\mathbf{u}\times\mathbf{v}) = (\nabla\cdot\mathbf{v})\,\mathbf{u} - (\nabla\cdot\mathbf{u})\,\mathbf{v} + (\nabla\mathbf{u})\cdot\mathbf{v} - (\nabla\mathbf{v})\cdot\mathbf{u}$ gives.

$$\mathbf{w}_1 = -\frac{1}{2}\left(-3(\mathbf{x}_2-\mathbf{x}_1) + 3(\mathbf{x}_3-\mathbf{x}_1) - \mathbf{I}(\mathbf{x}_3-\mathbf{x}_1) + \mathbf{I}(\mathbf{x}_2-\mathbf{x}_1)\right) = \mathbf{x}_2-\mathbf{x}_3 \tag{D.17}$$

$$\mathbf{w}_2 = \mathbf{x}_3-\mathbf{x}_1 \tag{D.18}$$

$$\mathbf{w}_3 = \mathbf{x}_1-\mathbf{x}_2 \tag{D.19}$$

where for example $\nabla_{\mathbf{x}_1} \cdot \mathbf{x}_1 = 3$ and $\nabla_{\mathbf{x}_1}\mathbf{x}_1 = \mathbf{I}$. Therefore

$$\mathbf{f}_1 = (\beta_a + \beta_d)\left(\mathbf{n} \times (\mathbf{x}_3 - \mathbf{x}_2)\right) \tag{D.20}$$

$$\mathbf{f}_2 = (\beta_a + \beta_d)\left(\mathbf{n} \times (\mathbf{x}_1 - \mathbf{x}_3)\right) \tag{D.21}$$

$$\mathbf{f}_3 = (\beta_a + \beta_d)\left(\mathbf{n} \times (\mathbf{x}_2 - \mathbf{x}_1)\right) \tag{D.22}$$

The volume conservation force yields with the definition of the volume of a triangular patch $V_i = \frac{1}{6}\left(\mathbf{n}_i \cdot \bar{\mathbf{x}}_i\right)$ where $\bar{\mathbf{x}} = \frac{\mathbf{x}_1+\mathbf{x}_2+\mathbf{x}_3}{3}$;

$$\begin{aligned}
-\nabla_{\mathbf{x}_i}\left(k_v\frac{(V-V_0)^2}{2V_0}\right) &= -k_v\frac{V-V_0}{V_0}\nabla_{\mathbf{x}_i}V \\
&= -k_v\frac{V-V_0}{V_0}\sum_j \nabla_{\mathbf{x}_i}V_j \\
&= -k_v\frac{V-V_0}{V_0}\frac{1}{6}\left(\nabla_{\mathbf{x}_i}\mathbf{n}_i\bar{\mathbf{x}}_i + \mathbf{n}_i\nabla_{\mathbf{x}_i}\bar{\mathbf{x}}_i\right) \\
&= -k_v\frac{V-V_0}{V_0}\frac{1}{6}\left(\frac{\mathbf{n}_i}{3} + \nabla_{\mathbf{x}_i\mathbf{n}_i}\bar{\mathbf{x}}_i\right) \\
&= \beta_v\left(\frac{\mathbf{n}_i}{3} + \nabla_{\mathbf{x}_i}\mathbf{n}_i\bar{\mathbf{x}}_i\right)
\end{aligned} \tag{D.23}$$

$$\begin{aligned}
\mathbf{f}_1 &= \beta_v(\frac{\mathbf{n}}{3} + \nabla_{\mathbf{x}_1}\mathbf{n}\bar{\mathbf{x}}) \\
\mathbf{f}_2 &= \beta_v(\frac{\mathbf{n}}{3} + \nabla_{\mathbf{x}_2}\mathbf{n}\bar{\mathbf{x}}) \\
\mathbf{f}_3 &= \beta_v(\frac{\mathbf{n}}{3} + \nabla_{\mathbf{x}_3}\mathbf{n}\bar{\mathbf{x}})
\end{aligned}$$

where

$$\beta_v = -k_v\frac{V-V_0}{6V_0}$$

$$\begin{aligned}
\nabla_{\mathbf{x}_1}\mathbf{n}\bar{\mathbf{x}} = \mathbf{W}_1\bar{\mathbf{x}} = \mathbf{w}_1 \times \bar{\mathbf{x}} = (\mathbf{x}_2 - \mathbf{x}_3) \times \bar{\mathbf{x}} = \bar{\mathbf{x}} \times (\mathbf{x}_3 - \mathbf{x}_2) \\
\nabla_{\mathbf{x}_2}\mathbf{n}\bar{\mathbf{x}} = \mathbf{W}_2\bar{\mathbf{x}} = \mathbf{w}_2 \times \bar{\mathbf{x}} = (\mathbf{x}_3 - \mathbf{x}_1) \times \bar{\mathbf{x}} = \bar{\mathbf{x}} \times (\mathbf{x}_1 - \mathbf{x}_3) \\
\nabla_{\mathbf{x}_3}\mathbf{n}\bar{\mathbf{x}} = \mathbf{W}_3\bar{\mathbf{x}} = \mathbf{w}_3 \times \bar{\mathbf{x}} = (\mathbf{x}_1 - \mathbf{x}_2) \times \bar{\mathbf{x}} = \bar{\mathbf{x}} \times (\mathbf{x}_2 - \mathbf{x}_1)
\end{aligned}$$

$$\mathbf{f}_1 = \beta_v(\frac{\mathbf{n}}{3} + \bar{\mathbf{x}} \times (\mathbf{x}_3 - \mathbf{x}_2)) \tag{D.24}$$

$$\mathbf{f}_2 = \beta_v(\frac{\mathbf{n}}{3} + \bar{\mathbf{x}} \times (\mathbf{x}_1 - \mathbf{x}_3)) \tag{D.25}$$

$$\mathbf{f}_3 = \beta_v(\frac{\mathbf{n}}{3} + \bar{\mathbf{x}} \times (\mathbf{x}_2 - \mathbf{x}_1)) \tag{D.26}$$

The bending potential is defined based on the angle between two adjacent triangles with indices

i and j. Their normals yield;

$$\mathbf{n}_i = \left(\mathbf{x}_2^i - \mathbf{x}_1^i\right) \times \left(\mathbf{x}_3^i - \mathbf{x}_1^i\right), \quad \mathbf{p}_i = \left(\mathbf{x}_3^j - \mathbf{x}_4^j\right) \times \left(\mathbf{x}_2^j - \mathbf{x}_4^j\right),$$

and the corresponding areas

$$A_i = \frac{1}{2}\sqrt{\mathbf{n}_i \cdot \mathbf{n}_i}, \quad A_j = \frac{1}{2}\sqrt{\mathbf{p}_j \cdot \mathbf{p}_j}.$$

Bending potential, between two adjacent triangles making an angle θ between their normals are given by;

$$U_{\text{bend}} = \sum_j k_b(1 - \cos\left(\theta_j - \theta_0\right) \tag{D.27}$$

The force reads on node $\mathbf{x}_i$ reads;

$$\begin{aligned} \mathbf{f}_i &= -\nabla_{\mathbf{x}_i}\left(k_b(1 - \cos\left(\theta_i - \theta_0\right)\right) \\ &= -k_B \sin\left(\theta_i - \theta_0\right) \nabla_{\mathbf{x}_i}\theta \end{aligned} \tag{D.28}$$

Furthermore, the angle θ_i is related to the normals with $\cos\theta_i = \left(\frac{\mathbf{n}}{\|\mathbf{n}\|} \cdot \frac{\mathbf{p}}{\|\mathbf{p}\|}\right)$ and $\sin\theta = \pm\sqrt{1 - \cos^2\theta}$. If $(\mathbf{n} - \mathbf{p}) \cdot (\bar{\mathbf{x}}_1 - \bar{\mathbf{x}}_2) \geq 0$ then the positive sign is used and negative otherwise. Again $\bar{\mathbf{x}}_i$ is the center of mass of the ith triangle.

$$\begin{aligned} \nabla_{\mathbf{x}_i}\theta &= \nabla_{\mathbf{x}_i} \arccos\left(\frac{\mathbf{n}}{\|\mathbf{n}\|} \cdot \frac{\mathbf{p}}{\|\mathbf{p}\|}\right) \\ &= -\frac{1}{\sqrt{1 - \cos^2\theta}} \nabla_{\mathbf{x}_i}\left(\frac{\mathbf{n}}{\|\mathbf{n}\|} \cdot \frac{\mathbf{p}}{\|\mathbf{p}\|}\right) \\ &= -\frac{1}{\sqrt{1 - \cos^2\theta}}\left[\nabla_{\mathbf{x}_i}\frac{\mathbf{n}}{\|\mathbf{n}\|}\frac{\mathbf{p}}{\|\mathbf{p}\|} + \frac{\mathbf{n}}{\|\mathbf{n}\|}\nabla_{\mathbf{x}_i}\frac{\mathbf{p}}{\|\mathbf{p}\|}\right] \end{aligned} \tag{D.29}$$

$$\nabla_{\mathbf{x}_i}\left(\frac{\mathbf{n}}{n} \cdot \frac{\mathbf{p}}{p}\right) = \frac{\mathbf{p}}{p}\nabla_{\mathbf{x}_i}\left(\frac{\mathbf{n}}{n}\right) + \frac{\mathbf{n}}{n}\nabla_{\mathbf{x}_i}\left(\frac{\mathbf{p}}{p}\right) \tag{D.30}$$

$$\tag{D.31}$$

where for example;

$$\nabla_{\mathbf{x}_i}\frac{\mathbf{n}}{n} = \frac{1}{n}\left[\nabla_{\mathbf{x}_i}\mathbf{n} - \frac{\mathbf{n} \otimes (\mathbf{n}\nabla_{\mathbf{x}_i}\mathbf{n})}{n^2}\right] \tag{D.32}$$

then;

$$\nabla_{\mathbf{x}_i}\left(\frac{\mathbf{n}}{n} \cdot \frac{\mathbf{p}}{p}\right) = \frac{1}{pn}\left[\mathbf{p}\nabla_{\mathbf{x}_i}\mathbf{n} - \frac{(\mathbf{p} \cdot \mathbf{n})(\mathbf{n}\nabla_{\mathbf{x}_i}\mathbf{n})}{n^2}\right] + \frac{1}{pn}\left[\mathbf{n}\nabla_{\mathbf{x}_i}\mathbf{p} - \frac{(\mathbf{p} \cdot \mathbf{n})(\mathbf{p}\nabla_{\mathbf{x}_i}\mathbf{p})}{n^2}\right] \tag{D.33}$$

then for example $\mathbf{f}_1$ reads and noting $\nabla_{\mathbf{x}_1}\mathbf{p} = \mathbf{0}$;

$$\mathbf{f}_1 = k_B \sin(\theta - \theta_0) \frac{1}{\sqrt{1-\cos^2\theta}} \frac{1}{pn} \left(\mathbf{p} \times \mathbf{x}_{23} - \frac{\mathbf{p}\cdot\mathbf{n}}{n^2} \mathbf{n} \times \mathbf{x}_{23} \right) \tag{D.34}$$

here for the sake of simplicity following coefficients will be defined;

$$\begin{aligned} \beta_b &= \frac{k_B \sin(\theta - \theta_0)}{\sqrt{1-\cos^2\theta}} \\ b_{11} &= -\frac{\beta_b \cos\theta}{n^2} \\ b_{12} &= \frac{\beta_b}{pn} \\ b_{22} &= \frac{-\beta_b \cos\theta}{n^2} \end{aligned} \tag{D.35}$$

then the the forces read;

$$\mathbf{f}_1 = b_{11}(\mathbf{n} \times (\mathbf{x}_2 - \mathbf{x}_3)) + b_{12}(\mathbf{p} \times (\mathbf{x}_2 - \mathbf{x}_3)),$$

$$\mathbf{f}_2 = b_{11}(\mathbf{n} \times (\mathbf{x}_3 - \mathbf{x}_1)) + b_{12}(\mathbf{p} \times (\mathbf{x}_4 - \mathbf{x}_3) + \mathbf{p} \times (\mathbf{x}_1 - \mathbf{x}_3)) + b_{22}(\mathbf{p} \times (\mathbf{x}_4 - \mathbf{x}_3)),$$

$$\mathbf{f}_3 = b_{11}(\mathbf{n} \times (\mathbf{x}_1 - \mathbf{x}_2)) + b_{12}(\mathbf{p} \times (\mathbf{x}_2 - \mathbf{x}_4) + \mathbf{p} \times (\mathbf{x}_1 - \mathbf{x}_2)) + b_{22}(\mathbf{p} \times (\mathbf{x}_2 - \mathbf{x}_4)),$$

$$\mathbf{f}_4 = b_{12}(\mathbf{n} \times (\mathbf{x}_3 - \mathbf{x}_2)) + b_{22}(\mathbf{p} \times (\mathbf{x}_3 - \mathbf{x}_2)).$$

Bibliography

[1] M. Abkarian, M. Faivre, and A. Viallat. Swinging of Red Blood Cells under Shear Flow. *Physical Review Letters*, 98(18):188302, Apr. 2007.

[2] M. Abkarian, C. Lartigue, and A. Viallat. Tank Treading and Unbinding of Deformable Vesicles in Shear Flow: Determination of the Lift Force. *Physical Review Letters*, 88(6):068103, Jan. 2002.

[3] M. Abkarian, C. Lartigue, and A. Viallat. Tank treading and unbinding of deformable vesicles in shear flow: determination of the lift force. *Phys. Rev. Lett.*, 88:068103, 2002.

[4] M. Abkarian, M. A. Mader, V. Vitkova, A. Viallat, and T. Podgorski. Dynamics of viscous vesicles in shear flow. *The European Physical Journal E*, 19(4):389–397, Apr. 2006.

[5] M. Abkarian and A. Viallat. Dynamics of Vesicles in a Wall-Bounded Shear Flow. *Biophysical Journal*, 89(2):1055–1066, Aug. 2005.

[6] P. Ahlrichs and B. Dünweg. Simulation of a single polymer chain in solution by combining lattice Boltzmann and molecular dynamics. *J. Chem. Phys.*, 111:8225–8239, 1999.

[7] C. K. Aidun and J. R. Clausen. Capsule dynamics and rheology in shear flow: Particle pressure and normal stress. *Physics of Fluids*, 22(12):123302, Dec. 2010.

[8] A. Alexander-Katz and R. R. Netz. Surface-enhanced unfolding of collapsed polymers in shear flow. *Europhys. Lett.*, 80:18001, 2007.

[9] A. Alexander-Katz and R. R. Netz. Dynamics and instabilities of collapsed polymers in shear flow. *Macromolecules*, 41:3363–3374, 2008.

[10] A. Alexander-Katz, M. F. Schneider, S. W. Schneider, A. Wixforth, and R. R. Netz. Shear-flow-induced unfolding of polymeric globules. *Phys. Rev. Lett.*, 97:138101, 2006.

[11] P. Bagchi. Mesoscale Simulation of Blood Flow in Small Vessels. *Biophysical Journal*, 92(6):1858–1877, Mar. 2007.

[12] P. Bagchi, D. Cordasco, and A. Yazdani. Comparison of erythrocyte dynamics in shear flow under different stress-free configurations. *Physics of Fluids*, 26(4):041902, Apr. 2014.

[13] P. Bagchi and R. M. Kalluri. Dynamics of nonspherical capsules in shear flow. *Physical Review E*, 80(1):016307, July 2009.

[14] P. Bagchi, K. Vahidkhah, and S. L. Diamond. Hydrodynamic Interaction Between a Platelet and an Erythrocyte: Effect of Erythrocyte Deformability, Dynamics, and Wall Proximity. *Journal of Biomechanical Engineering*, 135(5):051002, May 2013.

[15] P. Bagchi and A. Yazdani. Three-dimensional numerical simulation of vesicle dynamics using a front-tracking method. *Physical Review E*, 85(5):056308, May 2012.

[16] P. Bagchi and A. Z. K. Yazdani. Phase diagram and breathing dynamics of a single red blood cell and a biconcave capsule in dilute shear flow. *Physical Review E*, 84(2):026314, Aug. 2011.

[17] P. Bagchi and A. Z. K. Yazdani. Analysis of membrane tank-tread of nonspherical capsules and red blood cells. *The European Physical Journal E*, 35(10):103, Oct. 2012.

[18] P. Bagchi, A. Z. K. Yazdani, and R. M. Kalluri. Tank-treading and tumbling frequencies of capsules and red blood cells. *Physical Review E*, 83(4):046305, Apr. 2011.

[19] N. M. Bagheri, G. Závodszky, and A. G. Hoekstra. The impact of clot permeability on platelet fluxes toward its surface. *PloS one*, page e0317828, 2025.

[20] A. Barg, R. Ossig, T. Goerge, M. F. Schneider, H. Schillers, H. Oberleithner, and S. W. Schneider. Soluble plasma-derived von Willebrand factor assembles to a haemostatically active filamentous network. *Thromb. Haemost.*, 97:514–526, 2007.

[21] D. Barthés-Biesel. Role of interfacial properties on the motion and deformation of capsules in shear flow. *Physica A: Statistical Mechanics and its Applications*, 172(1-2):103–124, Mar. 1991.

[22] D. Barthès-Biesel. Motion and Deformation of Elastic Capsules and Vesicles in Flow. *Annual Review of Fluid Mechanics*, 48(1):25–52, Jan. 2016.

[23] D. Barthès-Biesel, E. Lac, and A. Morel. Hydrodynamic interaction between two identical capsules in simple shear flow. *Journal of Fluid Mechanics*, 573:149–169, Feb. 2007.

[24] W. S. Beck. *Hematology*. MIT Press, 1991.

[25] G. I. Bell. Models for the specific adhesion of cells to cells. *Science*, 200:618–627, 1978.

[26] A. V. Belyaev and Y. K. Kushchenko. Biomechanical activation of blood platelets via adhesion to von willebrand factor studied with mesoscopic simulations. *Biomechanics and Modeling in Mechanobiology*, 22(3):785–808, 2023.

[27] E. S. Bershadsky, D. A. Ermokhin, V. A. Kurattsev, M. A. Panteleev, and D. Y. Nechipurenko. Force balance ratio is a robust predictor of arterial thrombus stability. *Biophysical Journal*, pages 464–477, 2024.

[28] E. S. Bershadsky, D. A. Ermokhin, V. A. Kurattsev, M. A. Panteleev, and D. Y. Nechipurenko. Force balance ratio is a robust predictor of arterial thrombus stability. *Biophysical Journal*, 123(4):464–477, 2024.

[29] M. Bessis, W. Groner, and N. Mohandas. New optical technique for measuring erythrocyte deformability with the ektacytometer. *Clinical Chemistry*, 26(10):1435–1442, Sept. 1980.

[30] M. Bitbol. Red blood cell orientation in orbit c= 0. *Biophysical journal*, 49(5):1055–1068, 1986.

[31] M. Bryckaert, J.-P. Rosa, C. V. Denis, and P. J. Lenting. Of von willebrand factor and platelets. *Cellular and Molecular Life Sciences*, pages 307–326, 2015.

[32] P. B. Canham and A. C. Burton. Distribution of Size and Shape in Populations of Normal Human Red Cells. *Circulation Research*, 22(3):405–422, Mar. 1968.

[33] I. Cantat and C. Misbah. Lift force and dynamical unbinding of adhering vesicles under shear flow. *Phys. Rev. Lett.*, 83:880–883, 1999.

[34] L. Casa, S. Gillespie, S. Meeks, and D. Ku. Relative contributions of von willebrand factor and platelets in high shear thrombosis. *J Hematol Thrombo Dis*, pages 1–8, 2016.

[35] K. B. Chandran, T. AlMomani, H. S. Udaykumar, and J. S. Marshall. Micro-scale Dynamic Simulation of Erythrocyte–Platelet Interaction in Blood Flow. *Annals of Biomedical Engineering*, 36(6):905–920, June 2008.

[36] H. Chen, M. A. Fallah, V. Huck, J. I. Angerer, A. J. Reininger, S. W. Schneider, M. F. Schneider, and A. Alexander-Katz. Blood-clotting-inspired reversible polymer-colloid composite assembly in flow. *Nat. Commun.*, 4:1333, 2013.

[37] S. Choudhary, K. Sharma, and P. K. Singh. Von willebrand factor: A key glycoprotein involved in thrombo-inflammatory complications of covid-19. *Chemico-Biological Interactions*, page 109657, 2021.

[38] T. V. Colace, R. W. Muthard, and S. L. Diamond. Thrombus growth and embolism on tissue factor-bearing collagen surfaces under flow: role of thrombin with and without fibrin. *Arteriosclerosis, thrombosis, and vascular biology*, pages 1466–1476, 2012.

[39] B. S. Coller. Blood at 70: İts roots in the history of hematology and its birth. *Blood*, 126(24):2548–2560, Dec. 2015.

[40] G. Coupier, L. Bureau, and T. Salez. Lift at low Reynolds number. *The European Physical Journal E*, 46(11):111, Nov. 2023.

[41] K. De Ceunynck, S. F. De Meyer, and K. Vanhoorelbeke. Unwinding the von Willebrand factor strings puzzle. *Blood*, 121:270–277, 2013.

[42] M. Dembo, D. C. Torney, K. Saxman, and D. Hammer. The reaction-limited kinetics of membrane-to-surface adhesion and detachment. *Proc. R. Soc. Lond. B*, 234:55–83, 1988.

[43] T. A. Doggett, G. Girdhar, A. Lawshé, D. W. Schmidtke, I. J. Laurenzi, S. L. Diamond, and T. G. Diacovo. Selectin-like kinetics and biomechanics promote rapid platelet adhesion in flow: the GPIbα-vWF tether bond. *Biophys. J.*, 83:194–205, 2002.

[44] D. Doyle. William Hewson (1739–74): The father of haematology. *British Journal of Haematology*, 133(4):375–381, May 2006.

[45] P. Español and M. Revenga. Smoothed dissipative particle dynamics. *Phys. Rev. E*, 67:026705, 2003.

[46] P. Espanol. Fluid particle model. *Physical Review E*, 57(3):2930, 1998.

[47] P. Español and M. Ellero. Everything you always wanted to know about SDPD$\star$ ($\star$but were afraid to ask). *Applied Mathematics and Mechanics*, 39(1):103–124, Jan. 2018.

[48] P. Español and M. Revenga. Smoothed dissipative particle dynamics. *Physical Review E*, 67(2):026705, Feb. 2003.

[49] P. Español and P. Warren. Statistical Mechanics of Dissipative Particle Dynamics. *Europhysics Letters (EPL)*, 30(4):191–196, May 1995.

[50] E. Evans and N. Mohandas. Mechanical Properties of the Red Cell Membrane in Relation to Molecular Structure and Genetic Defects. *Annual Review of Biophysics*, 23:787–818, 1994.

[51] D. A. Fedosov and D. Alizadehrad. Static and dynamic properties of smoothed dissipative particle dynamics. *Journal of Computational Physics*, 356:303–318, Mar. 2018.

[52] D. A. Fedosov, B. Caswell, and G. E. Karniadakis. A Multiscale Red Blood Cell Model with Accurate Mechanics, Rheology, and Dynamics. *Biophysical Journal*, 98(10):2215–2225, May 2010.

[53] D. A. Fedosov, B. Caswell, and G. E. Karniadakis. A multiscale red blood cell model with accurate mechanics, rheology, and dynamics. *Biophys. J.*, 98:2215–2225, 2010.

[54] D. A. Fedosov, B. Caswell, and G. E. Karniadakis. Systematic coarse-graining of spectrin-level red blood cell models. *Computer Methods in Applied Mechanics and Engineering*, 199(29-32):1937–1948, June 2010.

[55] D. A. Fedosov, B. Caswell, and G. E. Karniadakis. Systematic coarse-graining of spectrin-level red blood cell models. *Comput. Meth. Appl. Mech. Eng.*, 199:1937–1948, 2010.

[56] D. A. Fedosov, B. Caswell, A. S. Popel, and G. E. Karniadakis. Blood flow and cell-free layer in microvessels. *Microcirculation*, 17:615–628, 2010.

[57] D. A. Fedosov, B. Caswell, A. S. Popel, and G. E. Karniadakis. Blood Flow and Cell-Free Layer in Microvessels: Blood Flow and Cell-Free Layer in Microvessels. *Microcirculation*, 17(8):615–628, Nov. 2010.

[58] D. A. Fedosov, A. K. Dasanna, J. Mauer, and G. Gompper. Importance of Viscosity Contrast for the Motion of Erythrocytes in Microcapillaries. *Frontiers in Physics*, 9:666913, May 2021.

[59] D. A. Fedosov, J. Fornleitner, and G. Gompper. Margination of white blood cells in microcapillary flow. *Phys. Rev. Lett.*, 108:028104, 2012.

[60] D. A. Fedosov and G. E. Karniadakis. Triple-decker: Interfacing atomistic-mesoscopic-continuum flow regimes. *J. Comput. Phys.*, 228:1157–1171, 2009.

[61] D. A. Fedosov, D. Katanov, and G. Gompper. Microvascular blood flow resistance: Role of red blood cell migration and dispersion. *Microvascular Research*, 99:57–66, May 2015.

[62] D. A. Fedosov, L. Lanotte, J. Mauer, S. Mendez, J.-M. Fromental, V. Claveria, F. Nicoud, G. Gompper, and M. Abkarian. Red cells' dynamic morphologies govern blood shear thinning under microcirculatory flow conditions. *Proceedings of the National Academy of Sciences*, 113(47):13289–13294, Nov. 2016.

[63] D. A. Fedosov, H. Lei, B. Caswell, and G. E. Karniadakis. Blood flow in small tubes: Quantifying the transition to the non-continuum regime. *Journal of Fluid Mechanics*, 722:214–239, May 2013.

[64] D. A. Fedosov, H. Lei, B. Caswell, and G. E. Karniadakis. Blood flow in small tubes: Quantifying the transition to the non-continuum regime. *Journal of Fluid Mechanics*, 722:214–239, May 2013.

[65] D. A. Fedosov, J. Mauer, S. Mendez, L. Lanotte, F. Nicoud, M. Abkarian, and G. Gompper. Flow-Induced Transitions of Red Blood Cell Shapes under Shear. *Physical Review Letters*, 121(11):118103, Sept. 2018.

[66] D. A. Fedosov, K. Müller, and G. Gompper. Smoothed dissipative particle dynamics with angular momentum conservation. *Journal of Computational Physics*, 281:301–315, Jan. 2015.

[67] D. A. Fedosov, W. Pan, B. Caswell, G. Gompper, and G. E. Karniadakis. Predicting human blood viscosity in silico. *Proceedings of the National Academy of Sciences*, 108(29):11772–11777, July 2011.

[68] D. A. Fedosov, W. Pan, B. Caswell, and G. E. Karniadakis. Predicting dynamics and rheology of blood flow: A comparative study of multiscale and low-dimensional models of red blood cells. *Microvascular Research*, 82(2):163–170, Sept. 2011.

[69] D. A. Fedosov, M. Peltomäki, and G. Gompper. Deformation and dynamics of red blood cells in flow through cylindrical microchannels. *Soft Matter*, 10(24):4258–4267, 2014.

[70] D. A. Fedosov, F. Reichel, J. Mauer, A. A. Nawaz, G. Gompper, and J. Guck. High-Throughput Microfluidic Characterization of Erythrocyte Shapes and Mechanical Variability. *Biophysical Journal*, 117(1):14–24, July 2019.

[71] T. Fischer and H. Schmid-Schönbein. Tank Tread Motion of Red Cell Membranes in Viscometric Flow: Behavior of Intracellular and Extracellular Markers (with Film). In M. Bessis, S. B. Shohet, and N. Mohandas, editors, *Red Cell Rheology*, pages 347–361. Springer Berlin Heidelberg, Berlin, Heidelberg, 1978.

[72] T. M. Fischer. Shape Memory of Human Red Blood Cells. *Biophysical Journal*, 86(5):3304–3313, May 2004.

[73] T. M. Fischer. Tank-Tread Frequency of the Red Cell Membrane: Dependence on the Viscosity of the Suspending Medium. *Biophysical Journal*, 93(7):2553–2561, Oct. 2007.

[74] T. M. Fischer, M. Stöhr-Liesen, and H. Schmid-Schönbein. The Red Cell as a Fluid Droplet: Tank Tread-Like Motion of the Human Erythrocyte Membrane in Shear Flow. *Science*, 202(4370):894–896, Nov. 1978.

[75] W. E. Fowler, L. J. Fretto, K. K. Hamilton, H. P. Erickson, and P. A. McKee. Substructure of human von Willebrand factor. *J. Clin. Invest.*, 76:1491–1500, 1985.

[76] J. B. Freund. Numerical Simulation of Flowing Blood Cells. *Annual Review of Fluid Mechanics*, 46(1):67–95, Jan. 2014.

[77] H. Fu, Y. Jiang, D. Yang, F. Scheiflinger, W. P. Wong, and T. A. Springer. Flow-induced elongation of von Willebrand factor precedes tension-dependent activation. *Nat. Comm.*, 8:324, 2017.

[78] S. Gekle, B. Becic, and K. Gräßel. Origin of red blood cell slippers in confined geometries. *Physical Review Fluids*, 10(6):L061101, June 2025.

[79] A. Giri and S. Tamgadge. Red blood cells in health and disease. *Journal of Microscopy and Ultrastructure*, pages 10–4103, 2024.

[80] R. Glowinski, L. Shi, and T.-W. Pan. Deformation of a single red blood cell in bounded Poiseuille flows. *Physical Review E*, 85(1):016307, Jan. 2012.

[81] R. Glowinski, L. Shi, and T.-W. Pan. Numerical simulation of lateral migration of red blood cells in Poiseuille flows. *International Journal for Numerical Methods in Fluids*, 68(11):1393–1408, Apr. 2012.

[82] H. Goldsmith, J. Marlow, and F. C. MacIntosh. Flow behaviour of erythrocytes-i. rotation and deformation in dilute suspensions. *Proceedings of the Royal Society of London. Series B. Biological Sciences*, 182(1068):351–384, 1972.

[83] H. L. Goldsmith and S. Spain. Margination of leukocytes in blood flow through small tubes. *Microvasc. Res.*, 27:204–222, 1984.

[84] G. Gompper, S. Meßlinger, B. Schmidt, and H. Noguchi. Dynamical regimes and hydrodynamic lift of viscous vesicles under shear. *Physical Review E*, 80(1):011901, July 2009.

[85] G. Gompper and H. Noguchi. Fluid Vesicles with Viscous Membranes in Shear Flow. *Physical Review Letters*, 93(25):258102, Dec. 2004.

[86] G. Gompper and H. Noguchi. Dynamics of fluid vesicles in shear flow: Effect of membrane viscosity and thermal fluctuations. *Physical Review E*, 72(1):011901, July 2005.

[87] G. Gompper and H. Noguchi. Shape transitions of fluid vesicles and red blood cells in capillary flows. *Proceedings of the National Academy of Sciences*, 102(40):14159–14164, Oct. 2005.

[88] G. Gompper and H. Noguchi. Swinging and Tumbling of Fluid Vesicles in Shear Flow. *Physical Review Letters*, 98(12):128103, Mar. 2007.

[89] M. D. Graham and A. Kumar. Mechanism of Margination in Confined Flows of Blood and Other Multicomponent Suspensions. *Physical Review Letters*, 109(10):108102, Sept. 2012.

[90] X. Grandchamp, G. Coupier, A. Srivastav, C. Minetti, and T. Podgorski. Lift and Down-Gradient Shear-Induced Diffusion in Red Blood Cell Suspensions. *Physical Review Letters*, 110(10):108101, Mar. 2013.

[91] N. G. Gutierrez, D. Mukherjee, and D. Bark Jr. Decoding thrombosis through code: a review of computational models. *Journal of Thrombosis and Haemostasis*, pages 35–47, 2024.

[92] S. I. Hajdu. The Discovery of Blood Cells. *Annals of Clinical & Laboratory Science*, 33(2):237, 2003.

[93] Y. Hao, G. Závodszky, C. Tersteeg, M. Barzegari, and A. G. Hoekstra. Image-based flow simulation of platelet aggregates under different shear rates. *PLoS Computational Biology*, page e1010965, 2023.

[94] P. J. Hoogerbrugge and J. M. V. A. Koelman. Simulating Microscopic Hydrodynamic Phenomena with Dissipative Particle Dynamics. *Europhysics Letters (EPL)*, 19(3):155–160, June 1992.

[95] M. Hoore, K. Rack, D. A. Fedosov, and G. Gompper. Flow-induced adhesion of shear-activated polymers to a substrate. *J. Phys.: Condens. Matter*, 30:064001, 2018.

[96] V. Huck, M. F. Schneider, C. Gorzelanny, and S. W. Schneider. The various states of von Willebrand factor and their function in physiology and pathophysiology. *J. Thromb. Haemost.*, 111:598–609, 2014.

[97] V. Huck, M. F. Schneider, C. Gorzelanny, and S. W. Schneider. The various states of von willebrand factor and their function in physiology and pathophysiology. *Thrombosis and haemostasis*, pages 598–609, 2014.

[98] B. Huisman, M. Hoore, G. Gompper, and D. A. Fedosov. Modeling the cleavage of von willebrand factor by adamts13 protease in shear flow. *Medical engineering & physics*, 48:14–22, 2017.

[99] B. Huisman, M. Hoore, G. Gompper, and D. A. Fedosov. Modeling the cleavage of von Willebrand factor by ADAMTS13 protease in shear flow. *Med. Eng. Phys.*, 48:14–22, 2017.

[100] T. Ishikawa, T. Omori, D. Barthès-Biesel, A.-V. Salsac, J. Walter, Y. Imai, and T. Yamaguchi. Comparison between spring network models and continuum constitutive laws: Application to the large deformation of a capsule in shear flow. *Physical Review E*, 83(4):041918, Apr. 2011.

[101] T. Ishikawa, T. Omori, Y. Imai, and T. Yamaguchi. Shear-induced diffusion of red blood cells in a semi-dilute suspension. *Journal of Fluid Mechanics*, 724:154–174, June 2013.

[102] S. P. Jackson, W. S. Nesbitt, and E. Westein. Dynamics of platelet thrombus formation. *J. Thromb. Haemost.*, 7:17–20, 2009.

[103] G. B. Jeffery. The motion of ellipsoidal particles immersed in a viscous fluid. *Proceedings of the Royal Society of London. Series A, Containing Papers of a Mathematical and Physical Character*, 102(715):161–179, 1922.

[104] V. Kantsler and V. Steinberg. Orientation and Dynamics of a Vesicle in Tank-Treading Motion in Shear Flow. *Physical Review Letters*, 95(25):258101, Dec. 2005.

[105] V. Kantsler and V. Steinberg. Transition to Tumbling and Two Regimes of Tumbling Motion of a Vesicle in Shear Flow. *Physical Review Letters*, 96(3):036001, Jan. 2006.

[106] Z. S. Kaplan and S. P. Jackson. The role of platelets in atherothrombosis. *Hematology 2010, the American Society of Hematology Education Program Book*, 2011.

[107] G. E. Karniadakis and I. V. Pivkin. Accurate Coarse-Grained Modeling of Red Blood Cells. *Physical Review Letters*, 101(11):118105, Sept. 2008.

[108] D. A. Kim, K. J. Ashworth, J. Di Paola, and D. N. Ku. Platelet α-granules are required for occlusive high-shear-rate thrombosis. *Blood advances*, pages 3258–3267, 2020.

[109] D. A. Kim and D. N. Ku. Structure of shear-induced platelet aggregated clot formed in an in vitro arterial thrombosis model. *Blood Advances*, pages 2872–2883, 2022.

[110] J. Kim, C.-Z. Zhang, X. Zhang, and T. A. Springer. A mechanically stabilized receptor-ligand flex-bond important in the vasculature. *Nature*, 466:992–995, 2010.

[111] F. Kong, A. J. García, A. P. Mould, M. J. Humphries, and C. Zhu. Demonstration of catch bonds between an integrin and its ligand. *J. Cell. Biol.*, 185:1275–1284, 2009.

[112] D. N. Ku. BLOOD FLOW IN ARTERIES. *Annual Review of Fluid Mechanics*, 1997.

[113] V. V. Lebedev, K. S. Turitsyn, and S. S. Vergeles. Dynamics of Nearly Spherical Vesicles in an External Flow. *Physical Review Letters*, 99(21):218101, Nov. 2007.

[114] H. Lei, D. A. Fedosov, and G. E. Karniadakis. Time-dependent and outflow boundary conditions for dissipative particle dynamics. *J. Comput. Phys.*, 230:3765–3779, 2011.

[115] H. H. Lipowsky. Microvascular rheology and hemodynamics. *Microcirculation*, 12:5–15, 2005.

[116] G. Lippi, E. Favaloro, M. Franchini, and G. Guidi. Milestones and Perspectives in Coagulation and Hemostasis. *Seminars in Thrombosis and Hemostasis*, 35(01):009–022, Feb. 2009.

[117] Z. L. Liu, C. Bresette, C. K. Aidun, and D. N. Ku. Sipa in 10 milliseconds: Vwf tentacles agglomerate and capture platelets under high shear. *Blood advances*, pages 2453–2465, 2022.

[118] Z. L. Liu, D. N. Ku, and C. K. Aidun. Mechanobiology of shear-induced platelet aggregation leading to occlusive arterial thrombosis: A multiscale in silico analysis. *Journal of Biomechanics*, page 110349, 2021.

[119] J. A. Lopez, R. K. Andrews, V. Afshar-Kharghan, and M. C. Berndt. Bernard-soulier syndrome. *Blood*, pages 4397–4418, 1998.

[120] B. Lorz, R. Simson, J. Nardi, and E. Sackmann. Weakly adhering vesicles in shear flow: Tanktreading and anomalous lift force. *Europhysics Letters (EPL)*, 51(4):468–474, Aug. 2000.

[121] Z. Y. Luo, S. Q. Wang, L. He, F. Xu, and B. F. Bai. Inertia-dependent dynamics of three-dimensional vesicles and red blood cells in shear flow. *Soft Matter*, 9(40):9651, 2013.

[122] Y. Matsumoto, R. Hatakenaka, and S. Takagi. Orientation and internal flow of a vesicle in tank-treading motion in shear flow. *Physical Review E*, 84(2):026324, Aug. 2011.

[123] Y. Matsumoto, S. Takagi, T. Yamada, and X. Gong. The Deformation of a Vesicle in a Linear Shear Flow. *Journal of Applied Mechanics*, 76(2):021207, Mar. 2009.

[124] H. Meiselman, C. Pfafferott, and G. Nash. Red blood cell deformation in shear flow. Effects of internal and external phase viscosity and of in vivo aging. *Biophysical Journal*, 47(5):695–704, May 1985.

[125] J. Meletis and K. Konstantopoulos. The Beliefs, Myths, and Reality Surrounding the Word Hema (Blood) from Homer to the Present. *Anemia*, 2010:1–6, 2010.

[126] G. L. Mendolicchio and Z. M. Ruggeri. New perspectives on von Willebrand factor functions in hemostasis and thrombosis. *Semin. Hematol.*, 42:5–14, 2005.

[127] S. Messlinger, B. Schmidt, H. Noguchi, and G. Gompper. Dynamical regimes and hydrodynamic lift of viscous vesicles under shear. *Phys. Rev. E*, 80:011901, 2009.

[128] A. D. Michelson. *Platelets*. Academic Press, second edition edition, 2007.

[129] C. Misbah. Vacillating Breathing and Tumbling of Vesicles under Shear Flow. *Physical Review Letters*, 96(2):028104, Jan. 2006.

[130] C. Misbah, O. Aouane, A. Farutin, M. Thiébaud, A. Benyoussef, and C. Wagner. Hydrodynamic pairing of soft particles in a confined flow. *Physical Review Fluids*, 2(6):063102, June 2017.

[131] C. Misbah, O. Aouane, M. Thiébaud, A. Benyoussef, and C. Wagner. Vesicle dynamics in a confined Poiseuille flow: From steady state to chaos. *Physical Review E*, 90(3):033011, Sept. 2014.

[132] C. Misbah, J. Beaucourt, F. Rioual, T. Séon, and T. Biben. Steady to unsteady dynamics of a vesicle in a flow. *Physical Review E*, 69(1):011906, Jan. 2004.

[133] C. Misbah and T. Biben. Tumbling of vesicles under shear flow within an advected-field approach. *Physical Review E*, 67(3):031908, Mar. 2003.

[134] C. Misbah, T. Biben, and A. Farutin. Three-dimensional vesicles under shear flow: Numerical study of dynamics and phase diagram. *Physical Review E*, 83(3):031921, Mar. 2011.

[135] C. Misbah and I. Cantat. Lift Force and Dynamical Unbinding of Adhering Vesicles under Shear Flow. *Physical Review Letters*, 83(4):880–883, July 1999.

[136] C. Misbah, G. Coupier, A. Farutin, C. Minetti, and T. Podgorski. Shape Diagram of Vesicles in Poiseuille Flow. *Physical Review Letters*, 108(17):178106, Apr. 2012.

[137] C. Misbah, G. Coupier, B. Kaoui, and T. Podgorski. Noninertial lateral migration of vesicles in bounded Poiseuille flow. *Physics of Fluids*, 20(11):111702, Nov. 2008.

[138] C. Misbah and G. Danker. Rheology of a Dilute Suspension of Vesicles. *Physical Review Letters*, 98(8):088104, Feb. 2007.

[139] C. Misbah, G. Danker, and P. M. Vlahovska. Vesicles in Poiseuille Flow. *Physical Review Letters*, 102(14):148102, Apr. 2009.

[140] C. Misbah and A. Farutin. Symmetry breaking of vesicle shapes in Poiseuille flow. *Physical Review E*, 84(1):011902, July 2011.

[141] C. Misbah and A. Farutin. Squaring, Parity Breaking, and S Tumbling of Vesicles under Shear Flow. *Physical Review Letters*, 109(24):248106, Dec. 2012.

[142] C. Misbah and A. Farutin. Analytical and Numerical Study of Three Main Migration Laws for Vesicles Under Flow. *Physical Review Letters*, 110(10):108104, Mar. 2013.

[143] C. Misbah and A. Farutin. Symmetry breaking and cross-streamline migration of three-dimensional vesicles in an axial Poiseuille flow. *Physical Review E*, 89(4):042709, Apr. 2014.

[144] C. Misbah, A. Farutin, and O. Aouane. Vesicle dynamics under weak flows: Application to large excess area. *Physical Review E*, 85(6):061922, June 2012.

[145] C. Misbah, A. Farutin, and T. Biben. Analytical progress in the theory of vesicles under linear flow. *Physical Review E*, 81(6):061904, June 2010.

[146] C. Misbah, G. Ghigliotti, H. Selmi, and L. E. Asmi. Why and how does collective red blood cells motion occur in the blood microcirculation? *Physics of Fluids*, 24(10):101901, Oct. 2012.

[147] C. Misbah, P.-Y. Gires, A. Srivastav, T. Podgorski, and G. Coupier. Pairwise hydrodynamic interactions and diffusion in a vesicle suspension. *Physics of Fluids*, 26(1):013304, Jan. 2014.

[148] C. Misbah, B. Kaoui, and G. Biros. Why Do Red Blood Cells Have Asymmetric Shapes Even in a Symmetric Flow? *Physical Review Letters*, 103(18):188101, Oct. 2009.

[149] C. Misbah, B. Kaoui, G. H. Ristow, I. Cantat, and W. Zimmermann. Lateral migration of a two-dimensional vesicle in unbounded Poiseuille flow. *Physical Review E*, 77(2):021903, Feb. 2008.

[150] C. Misbah, J. Lyu, P. G. Chen, A. Farutin, M. Jaeger, and M. Leonetti. Swirling of vesicles: Shapes and dynamics in Poiseuille flow as a model of RBC microcirculation. *Physical Review Fluids*, 8(2):L021602, Feb. 2023.

[151] C. Misbah, M.-A. Mader, H. Ez-Zahraouy, and T. Podgorski. On coupling between the orientation and the shape of a vesicle under a shear flow. *The European Physical Journal E*, 22(4):275–280, Apr. 2007.

[152] C. Misbah, A. Nait-Ouhra, A. Guckenberger, A. Farutin, H. Ez-Zahraouy, A. Benyoussef, and S. Gekle. Lateral vesicle migration in a bounded shear flow: Viscosity contrast leads to off-centered solutions. *Physical Review Fluids*, 3(12):123601, Dec. 2018.

[153] C. Misbah, N. Tahiri, T. Biben, H. Ez-Zahraouy, and A. Benyoussef. On the problem of slipper shapes of red blood cells in the microvasculature. *Microvascular Research*, 85:40–45, Jan. 2013.

[154] C. Misbah, P. M. Vlahovska, and T. Podgorski. Vesicles and red blood cells in flow: From individual dynamics to rheology. *Comptes Rendus. Physique*, 10(8):775–789, Nov. 2009.

[155] D. M. Monroe and M. Hoffman. What does it take to make the perfect clot? *Arterioscler. Thromb. Vasc. Biol.*, 26:41–48, 2006.

[156] K. Müller, D. A. Fedosov, and G. Gompper. Margination of micro- and nano-particles in blood flow and its effect on drug delivery. *Sci. Rep.*, 4:4871, 2014.

[157] K. Müller, D. A. Fedosov, and G. Gompper. Smoothed dissipative particle dynamics with angular momentum conservation. *J. Comput. Phys.*, 281:301–315, 2015.

[158] National Health Service (NHS). Red blood cell count, 2024. Accessed: 2025-02-09.

[159] D. Y. Nechipurenko, A. M. Shibeko, A. N. Sveshnikova, and M. A. Panteleev. In silico hemostasis modeling and prediction. *Hämostaseologie*, pages 524–535, 2020.

[160] J. A. Neder. Cardiovascular and pulmonary interactions: Why Galen's misconceptions proved clinically useful for 1,300 years. *Advances in Physiology Education*, 44(2):225–231, June 2020.

[161] H. Noguchi and G. Gompper. Shape transitions of fluid vesicles and red blood cells in capillary flows. *Proc. Natl. Acad. Sci. USA*, 102:14159–14164, 2005.

[162] P. Olla. The lift on a tank-treading ellipsoidal cell in a shear flow. *Journal de Physique II*, 7(10):1533–1540, 1997.

[163] Y. Oya and T. Kawakatsu. Onsager's variational principle for the dynamics of a vesicle in a Poiseuille flow. *The Journal of Chemical Physics*, 148(11):114905, Mar. 2018.

[164] T. G. Papaioannou, C. Stefanadis, et al. Vascular wall shear stress: basic principles and methods. *Hellenic J Cardiol*, 46(1):9–15, 2005.

[165] Y. V. Pereverzev, O. V. Prezhdo, M. Forero, E. V. Sokurenko, and W. E. Thomas. The two-pathway model for the catch-slip transition in biological adhesion. *Biophys. J.*, 89:1446–1454, 2005.

[166] A. S. Popel and P. C. Johnson. MICROCIRCULATION AND HEMORHEOLOGY. *Annual Review of Fluid Mechanics*, 37(1):43–69, Jan. 2005.

[167] A. S. Popel and P. C. Johnson. Microcirculation and hemorheology. *Annu. Rev. Fluid Mech.*, 37:43–69, 2005.

[168] A. R. Pries, D. Neuhaus, and P. Gaehtgens. Blood viscosity in tube flow: Dependence on diameter and hematocrit. *American Journal of Physiology-Heart and Circulatory Physiology*, 263(6):H1770–H1778, Dec. 1992.

[169] K. Rack, V. Huck, M. Hoore, D. A. Fedosov, S. W. Schneider, and G. Gompper. Margination and stretching of von willebrand factor in the blood stream enable adhesion. *Scientific reports*, 7(1):14278, 2017.

[170] K. Rack, V. Huck, M. Hoore, D. A. Fedosov, S. W. Schneider, and G. Gompper. Margination and stretching of von Willebrand factor in the blood stream enable adhesion. *Sci. Rep.*, 7:14278, 2017.

[171] A. J. Reininger. Function of von Willebrand factor in haemostasis and thrombosis. *Haemophilia*, 14:11–26, 2008.

[172] A. J. Reininger, H. F. G. Heijnen, H. Schumann, H. M. Specht, W. Schramm, and Z. M. Ruggeri. Mechanism of platelet adhesion to von Willebrand factor and microparticle formation under high shear stress. *Blood*, 107:3537–3545, 2006.

[173] D. Ribatti. William Harvey and the discovery of the circulation of the blood. *Journal of Angiogenesis Research*, 1(1):3, 2009.

[174] F. Risso, F. Collé-Paillot, and M. Zagzoule. Experimental investigation of a bioartificial capsule flowing in a narrow tube. *Journal of Fluid Mechanics*, 547:149–173, Jan. 2006.

[175] F. Römer and D. A. Fedosov. Dense brushes of stiff polymers or filaments in fluid flow. *Europhys. Lett.*, 109:68001, 2015.

[176] Z. M. Ruggeri, J. N. Orje, R. Habermann, A. B. Federici, and A. J. Reininger. Activation-independent platelet adhesion and aggregation under elevated shear stress. *Blood*, 108:1903–1910, 2006.

[177] J. E. Sadler. New concepts in von Willebrand disease. *Annu. Rev. Med.*, 56:173–191, 2005.

[178] J. E. Sadler, U. Budde, J. C. J. Eikenboom, E. J. Favaloro, F. G. H. Hill, L. Holmberg, J. Ingerslev, C. A. Lee, D. Lillicrap, P. M. Mannucci, C. Mazurier, D. Meyer, W. L. Nichols, M. Nishino, I. R. Peake, F. Rodeghiero, R. Schneppenheim, Z. M. Ruggeri, A. Srivastava, R. R. Montgomery, and A. B. Federici. Update on the pathophysiology and classification of von Willebrand disease: a report of the subcommittee on von Willebrand factor. *J. Thromb. Haemost.*, 4:2103–2114, 2006.

[179] K. S. Sakariassen, L. Orning, and V. T. Turitto. The impact of blood shear rate on arterial thrombus formation. *Future Science OA*, 1:FSO30, 2015.

[180] K. Sarkar and A. R. Malipeddi. Shear-induced gradient diffusivity of a red blood cell suspension: Effects of cell dynamics from tumbling to tank-treading. *Soft Matter*, 17(37):8523–8535, 2021.

[181] B. Savage, F. Almus-Jacobs, and Z. M. Ruggeri. Specific synergy of multiple substrate-receptor interactions in platelet thrombus formation under flow. *Cell*, 94:657–666, 1998.

[182] B. Savage, E. Saldivar, and Z. M. Ruggeri. Initiation of platelet adhesion by arrest onto fibrinogen or translocation on von Willebrand factor. *Cell*, 84:289–297, 1996.

[183] B. Savage, J. J. Sixma, and Z. M. Ruggeri. Functional self-association of von Willebrand factor during platelet adhesion under flow. *Proc. Natl. Acad. Sci. USA*, 99:425–430, 2002.

[184] M. F. Schneider, M. A. Fallah, C. Mess, T. Obser, R. Schneppenheim, A. Alexander-Katz, S. W. Schneider, and V. Huck. Platelet adhesion and aggregate formation controlled by immobilised and soluble vwf. *BMC molecular and cell biology*, 2020.

[185] S. W. Schneider, S. Nuschele, A. Wixforth, C. Gorzelanny, A. Alexander-Katz, R. R. Netz, and M. F. Schneider. Shear-induced unfolding triggers adhesion of von Willebrand factor fibers. *Proc. Natl. Acad. Sci. USA*, 104:7899–7903, 2007.

[186] R. Schneppenheim and U. Budde. *von Willebrand disease and von Willebrand factor*. UNI-MED Verlag AG, Bremen, 2008.

[187] B. Sebastian and P. S. Dittrich. Microfluidics to Mimic Blood Flow in Health and Disease. *Annual Review of Fluid Mechanics*, 50(1):483–504, Jan. 2018.

[188] T. W. Secomb. Blood Flow in the Microcirculation. *Annual Review of Fluid Mechanics*, 2017.

[189] T. W. Secomb and J. M. Skotheim. Red Blood Cells and Other Nonspherical Capsules in Shear Flow: Oscillatory Dynamics and the Tank-Treading-to-Tumbling Transition. *Physical Review Letters*, 98(7):078301, Feb. 2007.

[190] U. Seifert. Configurations of fluid membranes and vesicles. *Advances in Physics*, 46(1):13–137, Feb. 1997.

[191] U. Seifert. Fluid membranes in hydrodynamic flow fields: Formalism and an application to fluctuating quasispherical vesicles in shear flow. *The European Physical Journal B*, 8(3):405–415, Apr. 1999.

[192] U. Seifert. Hydrodynamic Lift on Bound Vesicles. *Physical Review Letters*, 83(4):876–879, July 1999.

[193] U. Seifert, D. Abreu, M. Levant, and V. Steinberg. Fluid vesicles in flow. *Advances in Colloid and Interface Science*, 208:129–141, June 2014.

[194] U. Seifert, S. Kessler, and R. Finken. Swinging and tumbling of elastic capsules in shear flow. *Journal of Fluid Mechanics*, 605:207–226, June 2008.

[195] U. Seifert, R. Lipowsky, M. Kraus, and W. Wintz. Fluid Vesicles in Shear Flow. *Physical Review Letters*, 77(17):3685–3688, Oct. 1996.

[196] U. Seifert and S. Sukumaran. Influence of shear flow on vesicles near a wall: A numerical study. *Physical Review E*, 64(1):011916, June 2001.

[197] C. Sendner and R. R. Netz. Shear-induced repulsion of a semiflexible polymer from a wall. *Europhys. Lett.*, 81:54006, 2008.

[198] R. S. Seymour, Q. Hu, and E. P. Snelling. Blood flow rate and wall shear stress in seven major cephalic arteries of humans. *Journal of Anatomy*, 236(3):522–530, Mar. 2020.

[199] E. S. G. Shaqfeh, V. Narsimhan, and H. Zhao. Coarse-grained theory to predict the concentration distribution of red blood cells in wall-bounded Couette flow at zero Reynolds number. *Physics of Fluids*, 25(6):061901, June 2013.

[200] E. S. G. Shaqfeh, A. P. Spann, and H. Zhao. Loop subdivision surface boundary integral method simulations of vesicles at low reduced volume ratio in shear and extensional flow. *Physics of Fluids*, 26(3):031902, Mar. 2014.

[201] E. S. G. Shaqfeh and H. Zhao. The dynamics of a vesicle in simple shear flow. *Journal of Fluid Mechanics*, 674:578–604, May 2011.

[202] E. S. G. Shaqfeh, H. Zhao, and A. P. Spann. The dynamics of a vesicle in a wall-bound shear flow. *Physics of Fluids*, 23(12):121901, Dec. 2011.

[203] R. Skalak and P. I. Brånemark. Deformation of Red Blood Cells in Capillaries. *Science*, 164(3880):717–719, May 1969.

[204] R. Skalak and S. R. Keller. Motion of a tank-treading ellipsoidal particle in a shear flow. *Journal of Fluid Mechanics*, 120:27–47, July 1982.

[205] M. Soutani, Y. Suzuki, N. Tateishi, and N. Maeda. Quantitative evaluation of flow dynamics of erythrocytes in microvessels: İnfluence of erythrocyte aggregation. *American Journal of Physiology-Heart and Circulatory Physiology*, 268(5):H1959–H1965, May 1995.

[206] T. A. Springer. Biology and physics of von Willebrand factor concatamers. *J. Thromb. Haemost.*, 9:130–143, 2011.

[207] T. A. Springer. von Willebrand factor, Jedi knight of the bloodstream. *Blood*, 124:1412–1425, 2014.

[208] V. Steinberg, J. Deschamps, and V. Kantsler. Phase Diagram of Single Vesicle Dynamical States in Shear Flow. *Physical Review Letters*, 102(11):118105, Mar. 2009.

[209] V. Steinberg, M. Levant, J. Deschamps, and E. Afik. Characteristic spatial scale of vesicle pair interactions in a plane linear flow. *Physical Review E*, 85(5):056306, May 2012.

[210] V. Steinberg, N. J. Zabusky, E. Segre, J. Deschamps, and V. Kantsler. Dynamics of vesicles in shear and rotational flows: Modal dynamics and phase diagram. *Physics of Fluids*, 23(4):041905, Apr. 2011.

[211] P. Steinmann. Geometrical foundations of continuum mechanics. *Lecture Notes in Applied Mathematics and Mechanics*, 2, 2015.

[212] Y. Sui, H. T. Low, Y. T. Chew, and P. Roy. Tank-treading, swinging, and tumbling of liquid-filled elastic capsules in shear flow. *Physical Review E*, 77(1):016310, Jan. 2008.

[213] S. Suresh, M. Dao, and J. Li. Molecularly based analysis of deformation of spectrin network and human erythrocyte. *Materials Science and Engineering: C*, 26(8):1232–1244, Sept. 2006.

[214] S. Suresh, J. Li, M. Dao, and C. Lim. Spectrin-Level Modeling of the Cytoskeleton and Optical Tweezers Stretching of the Erythrocyte. *Biophysical Journal*, 88(5):3707–3719, May 2005.

[215] N. Takeishi, H. Yamashita, T. Omori, N. Yokoyama, and M. Sugihara-Seki. Axial and Nonaxial Migration of Red Blood Cells in a Microtube. *Micromachines*, 12(10):1162, Sept. 2021.

[216] C. Teeraratkul, Z. Irwin, S. C. Shadden, and D. Mukherjee. Computational investigation of blood flow and flow-mediated transport in arterial thrombus neighborhood. *Biomechanics and Modeling in Mechanobiology*, pages 701–715, 2021.

[217] C. Teeraratkul and D. Mukherjee. Microstructure aware modeling of biochemical transport in arterial blood clots. *Journal of Biomechanics*, page 110692, 2021.

[218] C. Teeraratkul, M. Tomaiuolo, T. J. Stalker, and D. Mukherjee. Investigating clot-flow interactions by integrating intravital imaging with in silico modeling for analysis of flow, transport, and hemodynamic forces. *Scientific Reports*, page 696, 2024.

[219] W. Thomas, M. Forero, O. Yakovenko, L. Nilsson, P. Vicini, E. Sokurenko, and V. Vogel. Catch-bond model derived from allostery explains force-activated bacterial adhesion. *Biophys. J.*, 90:753–764, 2006.

[220] W. E. Thomas, E. Trintchina, M. Forero, V. Vogel, and E. V. Sokurenko. Bacterial adhesion to target cells enhanced by shear force. *Cell*, 109:913–923, 2002.

[221] W. E. Thomas, V. Vogel, and E. V. Sokurenko. Biophysics of catch bonds. *Annu. Rev. Biophys.*, 37:399–416, 2008.

[222] M. Tomaiuolo, T. J. Stalker, J. D. Welsh, S. L. Diamond, T. Sinno, and L. F. Brass. A systems approach to hemostasis: 2. computational analysis of molecular transport in the thrombus microenvironment. *Blood, The Journal of the American Society of Hematology*, 124:1816–1823, 2014.

[223] A. Topuz, M. Hoore, G. Gompper, and D. A. Fedosov. Reversible formation of von-willebrand-factor-platelet aggregates in microvascular blood flow. *PNAS nexus*, page pgaf375, 2025.

[224] A. Tosenberger, F. Ataullakhanov, N. Bessonov, M. Panteleev, A. Tokarev, and V. Volpert. Modelling of thrombus growth in flow with a dpd-pde method. *Journal of theoretical biology*, pages 30–41, 2013.

[225] R. Tran-Son-Tay, S. Sutera, and P. Rao. Determination of red blood cell membrane viscosity from rheoscopic observations of tank-treading motion. *Biophysical Journal*, 46(1):65–72, July 1984.

[226] H. Ulrichts, M. Udvardy, P. J. Lenting, I. Pareyn, N. Vandeputte, K. Vanhoorelbeke, and H. Deckmyn. Shielding of the A1 domain by the D'D3 domains of von Willebrand factor modulates its interaction with platelet glycoprotein Ib-IX-V. *J. Biol. Chem.*, 281:4699–4707, 2006.

[227] A. van Leeuwenhoek. Letter 42 in arcana naturae detecta. Delft: Henrik van Kroonevelt; accessed online via Lens on Leeuwenhoek, 1695. Accessed: 2025-12-18.

[228] B. Van Rooij, G. Závodszky, V. Azizi Tarksalooyeh, and A. Hoekstra. Identifying the start of a platelet aggregate by the shear rate and the cell-depleted layer. *Journal of the Royal Society Interface*, page 20190148, 2019.

[229] B. Van Rooij, G. Závodszky, A. Hoekstra, and D. Ku. Haemodynamic flow conditions at the initiation of high-shear platelet aggregation: a combined in vitro and cellular in silico study. *Interface Focus*, page 20190126, 2021.

[230] S. Varchanis, Y. Dimakopoulos, C. Wagner, and J. Tsamopoulos. How viscoelastic is human blood plasma? *Soft Matter*, 14(21):4238–4251, 2018.

[231] A. Vázquez-Quesada, M. Ellero, and P. Español. Consistent scaling of thermal fluctuations in smoothed dissipative particle dynamics. *J. Chem. Phys.*, 130:034901, 2009.

[232] H. H. Versteeg, J. W. M. Heemskerk, M. Levi, and P. H. Reitsma. New fundamentals in hemostasis. *Physiol. Rev.*, 93:327–358, 2013.

[233] P. M. Vlahovska and R. S. Gracia. Dynamics of a viscous vesicle in linear flows. *Physical Review E*, 75(1):016313, Jan. 2007.

[234] J. Waeterschoot, W. Gosselé, Š. Lemež, and X. Casadevall i Solvas. Artificial cells for in vivo biomedical applications through red blood cell biomimicry. *Nature communications*, 15(1):2504, 2024.

[235] A. Walter, H. Rehage, and H. Leonhard. Shear induced deformation of microcapsules: Shape oscillations and membrane folding. *Colloids and Surfaces A: Physicochemical and Engineering Aspects*, 183–185:123–132, July 2001.

[236] P. B. Warren and R. D. Groot. Dissipative particle dynamics: Bridging the gap between atomistic and mesoscopic simulation. *The Journal of Chemical Physics*, 107(11):4423–4435, Sept. 1997.

[237] C. T. Watson, S. C. Ward, S. A. Rizzo, A. Redaelli, and K. B. Manning. Influence of hematocrit level and integrin αiibβiii function on vwf-mediated platelet adhesion and shear-induced platelet aggregation in a sudden expansion. *Cellular and Molecular Bioengineering*, pages 49–65, 2024.

[238] P. J. Wellings and D. N. Ku. Mechanisms of platelet capture under very high shear. *Cardiovascular Engineering and Technology*, pages 161–170, 2012.

[239] J. D. Welsh, T. J. Stalker, R. Voronov, R. W. Muthard, M. Tomaiuolo, S. L. Diamond, and L. F. Brass. A systems approach to hemostasis: 1. the interdependence of thrombus architecture and agonist movements in the gaps between platelets. *Blood, The Journal of the American Society of Hematology*, pages 1808–1815, 2014.

[240] A. Wendelboe and J. I. Weitz. Global health burden of venous thromboembolism. *Arteriosclerosis, thrombosis, and vascular biology*, 44(5):1007–1011, 2024.

[241] J. Westerweel, P. Vennemann, and R. Lindken. In vivo whole-field blood velocity measurement techniques. *Experiments in Fluids*, 42(4):495–511, Apr. 2007.

[242] T. Yago, J. Lou, T. Wu, J. Yang, J. J. Miner, L. Coburn, J. A. López, M. A. Cruz, J.-F. Dong, L. V. McIntire, R. P. McEver, and C. Zhu. Platelet glycoprotein Ibα forms catch bonds with human WT vWF but not with type 2B von Willebrand disease vWF. *J. Clin. Invest.*, 118:3195–3207, 2008.

[243] T. Ye, H. Shi, N. Phan-Thien, and C. T. Lim. The key events of thrombus formation: platelet adhesion and aggregation. *Biomechanics and Modeling in Mechanobiology*, pages 943–955, 2020.

[244] T. Ye, X. Zhang, G. Li, and S. Wang. Biomechanics in thrombus formation from direct cellular simulations. *Physical Review E*, page 042410, 2020.

[245] X. Zheng, A. Yazdani, H. Li, J. D. Humphrey, and G. E. Karniadakis. A three-dimensional phase-field model for multiscale modeling of thrombus biomechanics in blood vessels. *PLoS computational biology*, page e1007709, 2020.

[246] M. Zhussupbekov, R. M. Rojano, W.-T. Wu, and J. F. Antaki. von willebrand factor unfolding mediates platelet deposition in a model of high-shear thrombosis. *Biophysical journal*, pages 4033–4047, 2022.

[247] M. Zurita-Gotor, J. Bławzdziewicz, and E. Wajnryb. Layering Instability in a Confined Suspension Flow. *Physical Review Letters*, 108(6):068301, Feb. 2012.

Deceleration of Authorship

According to the doctoral regulations of University of Cologne, Faculty of Mathematics and Natural Sciences, the contributions of the author of this thesis to publications must be declared.

Chapter 2 has been published in PNAS Nexus, in 2025 [223], with the title *Reversible formation of von-Willebrand-factor-platelet aggregates in microvascular blood flow* written by Alper Topuz (first author), Masoud Hoore (second author), Gerhard Gompper (third author), Dmitry A. Fedosov (fourth author). Alper Topuz is also the author of this thesis. In this work, the author of this thesis has performed the simulations, data analysis and manuscript preparation, under the supervision of Dmitry A. Fedosov. Dmitry A. Fedosov and Gerhard Gompper designed the project, supervised the work. Masoud Hoore conducted the initial simulations, participated in the writing of the manuscript.

Chapter 3 serves as the framework of the publication under a different name *Primary hemostasis and dynamics of clot formation after vascular injury* **to be published in the future**. Alper Topuz is the first author of the corresponding paper, Gerhard Gompper (second author) and Dmitry A. Fedosov (third author). Dmitry A. Fedosov and Gerhard Gompper designed the project and supervised Alper Topuz. Alper Topuz conducted all the simulations and data analysis. All participants contributed to the writing of the paper, which is under preperation.

Eidesstattliche Versicherung

Hiermit versichere ich an Eides statt, dass ich die vorliegende Dissertation selbstständig und ohne die Benutzung anderer als der angegebenen Hilfsmittel und Literatur angefertigt habe. Alle Stellen, die wörtlich oder sinngemäß aus veröffentlichten und nicht veröffentlichten Werken dem Wortlaut oder dem Sinn nach entnommen wurden, sind als solche kenntlich gemacht. Ich versichere an Eides statt, dass diese Dissertation noch keiner anderen Fakultät oder Universität zur Prüfung vorgelegen hat; dass sie – abgesehen von unten angegebenen Teilpublikationen und eingebundenen Artikeln und Manuskripten – noch nicht veröffentlicht worden ist sowie, dass ich eine Veröffentlichung der Dissertation vor Abschluss des Prüfungsverfahrens der Promotion nicht vornehmen werde. Die Bestimmungen der Promotionsordnung der Mathematisch-Naturwissenschaftlichen Fakultät der Universität zu Köln sind mir bekannt. Darüber hinaus erkläre ich hiermit, dass ich die Ordnung zur Sicherung guter wissenschaftlicher Praxis und zum Umgang mit wissenschaftlichem Fehlverhalten der Universität zu Köln gelesen und sie bei der Durchführung der der Dissertation zugrundeliegenden Arbeiten und der schriftlich oder elektronisch verfassten Dissertation beachtet habe, und verpflichte mich hiermit, die dort genannten Vorgaben bei allen wissenschaftlichen Tätigkeiten zu beachten und umzusetzen.
Teilpublikationen :

Topuz, Alper, et al. "Reversible formation of von-Willebrand-factor-platelet aggregates in microvascular blood flow." PNAS nexus (2025): pgaf375.

Alper Topuz

Jülich, den 22.02.2026

Decleration for Doctoral Thesis

I hereby declare that I have prepared the present dissertation independently and without using any aids or literature other than those indicated. All passages that have been taken verbatim or in substance from published or unpublished works, in wording or in meaning, are identified as such. I declare under oath that this dissertation has not previously been submitted to any other faculty or university for examination; that it — apart from the publications and embedded articles and manuscripts listed below — has not yet been published, and that I will not publish the dissertation before the conclusion of the doctoral examination procedure. I am aware of the terms of the doctoral degree regulations of the Faculty of Mathematics and Natural Sciences of the University of Cologne. Furthermore, I hereby declare that I have read the regulations on ensuring good scientific practice and on dealing with scientific misconduct of the University of Cologne, and that I have complied with them in carrying out the work underlying this dissertation and in preparing this dissertation in written or electronic form, and I hereby undertake to observe and implement the rules set out therein in all my scientific activities.

Partial publications of the thesis :

Topuz, Alper, et al. "Reversible formation of von-Willebrand-factor-platelet aggregates in microvascular blood flow." PNAS nexus (2025): pgaf375.

Alper Topuz

Jülich, 22.02.2026